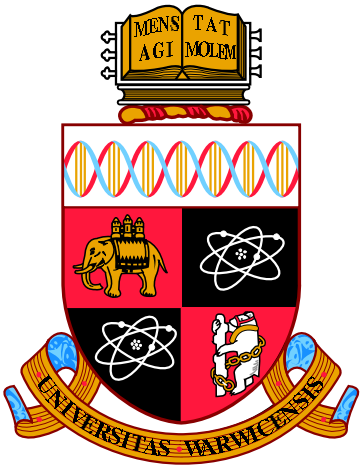

Behaviour of an axi-symmetric jet in the rotating reference frame

by

I. U. Atthanayake

Thesis

Submitted to the University of Warwick

for the degree of

Doctor of Philosophy

School of Engineering

....

THE UNIVERSITY OF WARWICK

Contents

List of Figures **iv**

List of Tables **xvi**

Acknowledgments **xvii**

Abstract **xix**

Nomenclature **xx**

Chapter 1 Introduction **1**

1.1 Objectives 4

1.2 Structure of the Thesis 4

Chapter 2 Literature Review **6**

2.1 Jets and Plumes 7

2.2 Jets in Rotating Reference Frame 11

2.2.1 Centrifugal Instability 17

2.3 Particle Image Velocimetry 19

Chapter 3 Theory **22**

3.1 Coordinate System and Governing Equations 22

3.2 Equations for Estimating Physical Quantities Required for the Flow Analysis 24

3.3 Non Dimensional Numbers 27

3.4 Particle Image Velocimetry 27

3.5 Proper Orthogonal Decomposition (POD) 32

3.6 Instability Criteria 35

3.7 Hilbert-Huang Transformation 36
3.7.1 Hilbert Transformation 39

Chapter 4 Methodology **41**
4.1 Experimental Set up 41
4.2 PIV system set up 43
4.2.1 Horizontal $(r-\theta)$ Plane Measurements 44
4.2.2 Vertical $(r-z)$ Plane Measurements 47
4.2.3 Stability of the Turntable 49
4.3 Analysis of PIV Images 49
4.4 Experimental Arrangement for Plumes 52

Chapter 5 Jets without Background Rotation **54**
5.1 Longitudinal Velocity Profiles 55
5.1.1 Radial Velocity Profiles 57
5.1.2 Turbulent Intensities 58
5.1.3 Reynolds Stress 61
5.1.4 Turbulent Viscosity 63
5.1.5 Volume Flow 64
5.1.6 Entrainment Coefficient 66

Chapter 6 Jets in the Presence of Background Rotation **69**
6.1 Qualitative Observations 69
6.2 Vertical Velocities 72
6.3 Temporal Development of the Radial and Azimuthal Velocities 80
6.3.1 Near to the Source $(z/d = 0.5)$ 80
6.3.2 Horizontal Plane at Height $z/d = 10$ 87
6.3.3 Horizontal Plane at Height $z/d = 15$ 93
6.4 Kinetic Energy Associated with the Radial and Azimuthal Velocity Components 94
6.4.1 Algorithm for Finding the Centre of the Vortices 94
6.4.2 Definition of the Radial Cut-off Radius 98
6.4.3 Kinetic Energy Associated with the Azimuthal Velocity 100
6.4.4 Kinetic Energy Associated with the Radial Velocity . . 108
6.4.5 Azimuthal Wave Number 110

6.4.6 Local Rossby Number 114
6.5 Behaviour of the Jet in the Horizontal Plane after Continuation of the Jet for Long Time 121

Chapter 7 Proper Orthogonal Decomposition Analysis 129
7.1 Introduction 129
7.2 POD Modes of the Jet with Background Rotation 130
7.2.1 Horizontal Plane 130
7.2.2 Vertical Plane 141
7.3 Image Reconstruction Using the POD Modes 145

Chapter 8 Centrifugal Instability 152

Chapter 9 Forced Plumes in the Presence of Background Rotation 174
9.1 Behaviour in the Horizontal Plane 174
9.2 First POD Mode 182
9.3 The Precession Frequency of the Plume 188

Chapter 10 Conclusion 196

Appendix A 200
A.I Limits of instability criterion χ_1 200
A.II Limits of instability criterion χ_2 201
A.III Evaluation of instability criterion χ_2 202

List of Figures

2.1 High Reynolds number turbulent jet produced by a test of a rocket (Lee & Chu, 2012). 8
2.2 Instantaneous three dimensional view of a horizontal axisymmetric jet issuing from a circular nozzle (photo courtesy: J. Kurima, N. Kasagi and M. Hirata, Turbulence and heat transfer laboratory, University of Tokyo.). 8
2.3 Variation of non-dimensionalised mean axial velocity (U/U_c) with non-dimensionalised radial coordinate ($r/(x-x_0)$) by Hussein *et al.* (1994): SHW- stationary hot wire, LDA - Laser Doppler Anemometry, FHW - Flying hot wire. 11
2.4 Instantaneous snapshots of a thermal with and without background rotation (Wilkins *et al.*, 1969). 14

3.1 Schematic diagram of a jet through a fluid at rest. 23
3.2 Schematic diagram of a PIV experimental arrangement (Raffel *et al.*, 2007). 28
3.3 (a) Single frame with single exposure of light to the camera lens, (b) Single frame with multi exposures of light to the camera lens (Raffel *et al.*, 2007). 29
3.4 Schematic diagram of analysing a PIV image pair (Raffel *et al.*, 2007). 29
3.5 A typical PIV calibration image (Quénot *et al.*, 2001). 31
3.6 Interrogation windows with a 50% overlap. 31
3.7 Interrogation windows in an image pair with respective interrogation window in second image has an offset. 32

3.8 Examples for a (a) stationary process and a (b) non stationary process (Kam, 2014). 37
3.9 The data $x(t)$ (blue) upper and lower envelopes (green) defined by the local maxima and minima, respectively, and the mean value of the upper and lower envelopes given in red (Huang *et al.*, 1998). 39
3.10 Repeated sifting steps with $h1(t)$ (Huang *et al.*, 1998). 40
3.11 A typical IMF obtained after 12 steps of sifting original data (Huang *et al.*, 1998). 40

4.1 Technical drawing of the large-scale rotating-tank facility. . . . 42
4.2 Ejector box. 43
4.3 Schematic diagram of the experimental set up for horizontal plane measurements. 45
4.4 Arrangement of the mirror and the camera for the horizontal plane measurements. 46
4.5 The Calibration Plate in the Horizontal Plane. 46
4.6 Schematic diagram of the experimental arrangement for vertical plane measurements. 47
4.7 Plan view of the experimental arrangement for the vertical plane measurements. 48
4.8 The calibration plate in the vertical plane. 48
4.9 Velocity vectors (a) Horizontal plane and (b) Vertical plane. . . 50
4.10 An original PIV image in the vertical plane. 51
4.11 PIV image with sub divided interrogation areas. 51
4.12 Two PIV images taken at time (a) t and (b) $t + \triangle t$: $\triangle t = 0.01$ s. 52
4.13 Velocity vector field obtained by analysing a PIV image pair. . 52

5.1 Velocity vectors of the jets with velocity profiles for $5 \leq z/d \leq 25$, for different Reynolds numbers: (a) 1800, (b) 2000, (c) 3000, (d) 3500 (the negative values of r/d indicates the change of direction). 56

5.2 Non-dimensionalised radial velocity profiles of longitudinal velocity for $5 \leq z/d \leq 25$, for different Reynolds numbers: (a) 1800, (b) 2000, (c) 3000, (d) 3500 (the negative values of r/b indicates the change of direction.). 58
5.3 Non-dimensionalised radial profiles of vertical turbulent intensity (I_w) for $5 \leq z/d \leq 25$, for different Reynolds numbers: (a) 1800, (b) 2000, (c) 3000, (d) 3500 (the negative values of r/b indicates the change of direction). 60
5.4 Non-dimensionalised radial profiles of radial turbulent intensity (I_u) for $5 \leq z/d \leq 25$, for different Reynolds numbers: (a) 1800, (b) 2000, (c) 3000, (d) 3500 (the negative values of r/b indicates the change of direction). 61
5.5 Non-dimensionalised radial profiles of the Reynolds stress for $5 \leq z/d \leq 25$, for different Reynolds numbers: (a) 1800, (b) 2000, (c) 3000, (d) 3500 (the negative values of r/b indicates the change of direction). 63
5.6 Non-dimensionalised radial profiles of turbulent kinematic viscosity for different Reynolds numbers: (a) 1800, (b) 2000, (c) 3000, (d) 3500 (the negative values of r/b indicates the change of direction). 64
5.7 Variation of non-dimensionalised vertical, volumetric flow rate for different Reynolds numbers: (a) 1800, (b) 2000, (c) 3000, (d) 3500. 66
5.8 Variation of the entrainment coefficient with vertical height for different Reynolds numbers: (a) 1800, (b) 2000, (c) 3000, (d) 3500. 68

6.1 Dye visualisation of jets for different background rotations. Each photo shows the jet at an instant of five seconds after liquid ejection from the nozzle had commenced. The rotation rates, in units of rad s^{-1}, associated with the photos are: (a) 0, (b) 0.1, (c) 0.2, (d) 0.31, (e) 0.41, (f) 0.52, (g) 0.63, (h) 0.73, (i) 0.83, (j) 0.94, (k) 1.05. 70

6.2 Fluorescein visualisation of the stem of a jet revealing the two cyclonically upwards spiralling helical strands for $Re_0 = 2300$ at $\Omega = 0.21$ rad s^{-1}. 71
6.3 Fluorescein visualisation of the cross section of the stem of a jet with $Re_0 = 2300$ at $\Omega = 0.21$ rad s^{-1} at times t for (a) 6 s, (b) 10 s, (c) 14 s, (d) 18 s, (e) 22 s, (f) 26 s, (g) 30 s, (h) 34 s. . 72
6.4 Instantaneous vector fields of the vertical velocity component, $w(r)$ for a jet with $Re_0 = 2300$ at $\Omega = 0.21$ rad s^{-1} at times. . . 73
6.4 Continued. 74
6.5 Instantaneous vector fields of the vertical velocity component, $w(r)$ for a jet with $Re_0 = 2300$ at $\Omega = 0.84$ rad s^{-1} at times t for (a) 0.5 s, (b) 1.5 s, (c) 2.5 s, (d) 3.5 s, (e) 4.5 s, (f) 5.5 s, (g) 6.5 s, (h) 7.5 s, (i) 8.5 s, (j) 9.5 s, (k) 10.5 s, (l) 11.5 s, (m) 12.5 s, (n) 13.5 s, (o) 14.5 s, (p) 15.5 s. 77
6.5 Continued. 78
6.6 Variation of mean axial velocity with nondimensional height for a jet with $Re_o = 2300$. 79
6.8 Temporal variation of the maximum velocity, in the horizontal plane at a height $z/d = 0.5$, for a jet with $Re_0 = 2300$ at $\Omega = 0.21$ rad s^{-1}. 82
6.9 Temporal variation of the maximum vorticity in the horizontal plane at a height $z/d = 0.5$, for a jet with $Re_0 = 2300$ at $\Omega = 0.21$ rad s^{-1}. 82
6.7 Instantaneous vector fields of the velocity components, v_r and v_θ for a jet with $Re_0 = 2300$ at $\Omega = 0.21$ rad s^{-1}. 83
6.7 Continued. 84
6.7 Continued 85
6.10 Temporal variation of instantaneous radial position of the instantaneous values of the maximum velocity in the horizontal plane, at height $z/d = 0.5$, for a jet with $Re_0 = 2300$ and $\Omega = 0.21$ rad s^{-1}. 86

6.11 Temporal variation of instantaneous radial position of the instantaneous values of the maximum vorticity in the horizontal plane, at height z/d = 0.5, for a jet with Re_0 = 2300 and Ω = 0.21 rad s^{-1}. 87
6.12 Instantaneous vector fields of the velocity components, v_r and v_θ for a jet with Re_0 = 2300 at Ω = 0.21 rad s^{-1} at times t for z/d = 10. 89
6.12 Continued. 90
6.12 Continued. 91
6.13 Spatio-temporal variation of the iso-surfaces of the 'highest velocity' at z/d = 10, for a jet with Re_0 = 2300 at Ω = 0.21 rad s^{-1} 92
6.14 Instantaneous vector fields of the velocity components, u_r & u_θ for a jet with Re_0 = 2300 at Ω = 0.21 rad s^{-1} at times t at z/d = 15. 95
6.14 Continued. 96
6.14 Continued. 97
6.15 Two examples illustrating the performance of the centre-finding process of Graftieaux *et al.* (2001) applied to flow fields from the current experiments for Re_0 = 2300, at Ω = 0.21 rad s^{-1}, with (a) Γ_1 = 0.87, (b) Γ_1 = 0.66. 99
6.16 Profiles of the circumferentially-averaged azimuthal velocity component $\overline{v}_\theta$ as as a function of the distance r/d from the centre for different instances in time, for a jet with Re = 2300 at Ω = 0.21 rad s^{-1}, z/d = 0.5. 99
6.17 Profiles of the circumferentially-averaged azimuthal velocity component $\overline{v}_\theta$ as as a function of the distance r/d from the centre for different instances in time, for a jet with Re = 2300 at Ω = 0.21 rad s^{-1}, z/d = 5. 101
6.18 Profiles of the circumferentially-averaged azimuthal velocity component $\overline{v}_\theta$ as as a function of the distance r/d from the centre for different instances in time, for a jet with Re = 2300 at Ω = 0.21 rad s^{-1}, z/d = 10. 101

6.19 Temporal variation of kinetic energy associated with azimuthal velocity for different background rotations rates, for a jet with Re_0 = 2300 at z/d = 0.5 ; the rotation rates, in units of rad s^{-1}, associated with sub figures are: (a) 0.21, (b) 0.31, (c) 0.41, (d) 0.52, (e) 0.63, (f) 0.73, (g) 0.83, (h) 0.94, (i) 1.05. 104
6.20 Fourier spectra for the temporal variation of $K.E_{(v_\theta)}$ for different background rotations rates for a jet with Re_0 = 2300; the rotation rates, in units of rad s^{-1}, associated with sub figures are: (a) 0.2, (b) 0.31, (c) 0.41, (d) 0.52, (e) 0.63, (f) 0.73, (g) 0.83, (h) 0.94, (i) 1.05. 107
6.21 Formation-breakdown frequency, f_θ, of the jets as a function of the background-rotation frequency, $f_T = \Omega/2\pi$, of the turntable. 107
6.22 Temporal variation of the kinetic energy associates with the radial velocity component for different background rotations rates, for a jet with Re_0 = 2300 at z/d = 0.5; the rotation rates, in units of rad s^{-1}, associated with the photos which are: (a) 0.2, (b) 0.31, (c) 0.41, (d) 0.52, (e) 0.63, (f) 0.73, (g) 0.83, (h) 0.94, (i) 1.05. 110
6.23 Temporal variation of magnitude of the instantaneous velocity for a jet with Re_0 = 2300 at z/d = 0.5 and Ω = 0.21 rad s^{-1} for times: (a) 6 s, (b) 10 s, (c) 14 s, (d) 18 s,(e) 22 s, (f) 26 s, (g) 30 s, (h) 34 s 111
6.24 Variation of azimuthal wave number, at z/d = 0.5, for eight radial locations, $0.5 \leqslant r/d \leqslant 4$, for a jet with Re_0 = 2300 at Ω = 0.21 rad s^{-1} for times: (a) 6 s, (b) 10 s, (c) 14 s, (d) 18 s, (e) 22 s, (f) 26 s, (g) 30 s, (h) 34 s. 112
6.24 Continued. 113
6.25 Variation of the instantaneous, local Rossby number Ro_l with time for a jet with Re = 2300, at z/d = 0.5, with different background rotations rates; the rotation rates, in units of rad s^{-1}, associated with the sub figures are: (a) 0.2, (b) 0.31, (c) 0.41, (d) 0.52, (e) 0.63, (f) 0.73, (g) 0.83, (h) 0.94, (i) 1.05. 117

6.26 Variation of the mean maximum and minimum local Rossby number with background rotation for a jet with Re = 2300, at z/d = 0.5. 118
6.27 Variation of the mean local Rossby number $\overline{Ro_l}$ with background rotation for a jet with Re = 2300, at z/d = 0.5, z/d = 5 & z/d = 10. 119
6.28 The mean values of the maximum and minimum local Rossby number, Ro_l^U and Ro_l^L, as a function of the global Rossby number, Ro_0 at height z/d = 0.5 above the source. For Re_0 = 2300: Upper Limit, ■, −, $Ro_l^U = 0.011Ro_0 - 4$; Lower Limit, □, −−, $Ro_l^L = 0.05Ro_0 - 0.21$. For Re_0 = 16000, $Ro_0 \leq 850$: Upper Limit, •, −..−, $Ro_l^U = 0.0015Ro_0 + 2.27$; Lower Limit, ∘, .−., $Ro_l^L = 0.002Ro_0 + 0.27$. 120
6.29 Instantaneous vector fields of the velocity components, u_r & u_θ for a jet with Re_0 = 2300 at Ω = 0.21 rad s^{-1} at times t for (a) 1800 s, (b) 1804 s, (c) 1808 s, (d) 1812 s, (e) 1816 s, (f) 1820 s, (g) 1824 s, (h) 1828 s, (i) 1832 s, (j) 1836 s, (k) 1840 s, (l) 1844 s, (m) 1848 s, (n) 1852 s, (o) 1856 s, (p) 1860 s at z/d = 5. 124
6.30 Instantaneous vector fields of the velocity components, u_r & u_θ for a jet with Re_0 = 2300 at Ω = 0.63 rad s^{-1} at times t for at z/d = 15. 126
6.30 Continued. 127
6.30 Continued. 128

7.1 Velocity vector fields of the first POD mode: the rotation rates, in units of rad s^{-1}, associated with sub figures are: (a) 0.2, (b) 0.31, (c) 0.41, (d) 0.52, (e) 0.63, (f) 0.73, (g) 0.83, (h) 0.94, (i) 1.05. 134
7.2 Temporal coefficients of POD mode 1: the rotation rates, in units of rad s^{-1}, associated with sub figures are: (a) 0.2, (b) 0.31, (c) 0.41, (d) 0.52, (e) 0.63, (f) 0.73, (g) 0.83, (h) 0.94, (i) 1.05. 135
7.3 Velocity vectors and vorticity field of (a) first, (b) second and (c) third POD mode for a jet with Re_0 = 2300, at Ω = 0.21 rad s^{-1}, for z/d = 0.5. 136

7.4 Fourier spectra for the time coefficient, $c_1(t)$, of the first POD mode for a jet with Re = 2300 for different rotation rates;the rotation rates, in units of rad s^{-1}, associated with sub figures are: (a) 0.2, (b) 0.31, (c) 0.41, (d) 0.52, (e) 0.63, (f) 0.73, (g) 0.83, (h) 0.94, (i) 1.05. 138
7.5 Formation-breakdown frequency, f_θ, of the jets as a function of the background-rotation frequency, $f_T = \Omega/2\pi$, of the turntable. 139
7.6 Formation-breakdown frequency, f_θ, of the jets as a function of the background-rotation frequency, $f_T = \Omega/2\pi$, of the turntable; $\bullet, -, Re$ = 2300, $f_\theta = 0.84 f_T$; $\circ, --, Re$ = 16000, $f_\theta = 1.57 f_T$. The dotted lines in the immediate vicinity of the two least-squares interpolations in this figure are the corresponding data interpolations from figure 6.21 obtained from the analysis of kinetic energy of the azimuthal component. 140
7.7 The first POD mode at each nondimensionalised vertical height of the jet for a jet with Re = 2300, and background rotation 0.21 rad $^{-1}$. 142
7.8 Variation of formation-breakdown frequency, f_θ, of the jets as a function of the Reynolds number Re_0 143
7.9 First POD mode in the vertical plane for jet with Re_0 = 2300 and z/d = 0.5. The rotation rates, in units of rad s^{-1}, associated with sub figures are: (a) 0.21, (b) 0.31, (c) 0.41, (d) 0.52, (e) 0.73, (f) 0.83. 145
7.10 Time characteristics of first POD mode in the vertical plane (a) for jet with Re_0 = 2300 and z/d = 0.5. The rotation rates, in units of rad s^{-1}, associated with sub figures are: (a) 0.21, (b) 0.31, (c) 0.41, (d) 0.52, (e) 0.73, (f) 0.83. 146
7.11 (a) The original vector field in the horizontal plane after $40s$ of the jet development and (b) reconstructed vector fields using first 5 POD modes, for jet with Re = 2300 and z/d = 0.5 d, $-5 \leqslant x/d \leqslant 5$ and $-5 \leqslant y/d \leqslant 5$ 148

7.12 (a) The original vector field in the horizontal plane after $40s$ of the jet development and (b) reconstructed vector fields using first 5 POD modes, for jet with Re = 2300 and z/d = 0.5 d, $-15 \leqslant x/d \leqslant 15$ and $-15 \leqslant y/d \leqslant 15$ 148
7.13 (a) Original vector field in the horizontal plane after $40s$ of jet development and (b) reconstructed vector fields using first 30 POD modes, for jet with Re = 2300 and $z/d = 0.5d$, $-10 \leqslant x/d \leqslant 10$ and $-10 \leqslant y/d \leqslant 10$. 149
7.14 (a) Original vector field in the horizontal plane after $40s$ of jet development and (b) reconstructed vector fields using first 30 POD modes, for jet with Re = 2300 and $z/d = 0.5d$, $-40 \leqslant x/d \leqslant 40$ and $-40 \leqslant y/d \leqslant 40$. 149
7.15 (a) The original vector field in the vertical plane after $2s$ of jet development and (b) reconstructed vector fields using first 30 POD modes, for a jet with Re = 2300. 150
7.16 Variation of cumulative percentage of kinetic energy with POD mode number in the: (a) vertical plane (b) horizontal plane for a jet with Re = 2300. 151

8.1 Variation of $d(\overline{v_\theta}r)^2/dr$ with time and r/d at z/d = 0.5, for a jet with Re_0 = 2300 at Ω = 0.21 rad s^{-1}. 154
8.2 Variation of $d(\overline{v_\theta}r)^2/dr$ with time and r/d at z/d = 5, for a jet with Re_0 = 2300 at Ω = 0.21 rad s^{-1}. 155
8.3 Variation of $d(\overline{v_\theta}r)^2/dr$ with time and r/d at z/d = 10, for a jet with Re_0 = 2300 at Ω = 0.21 rad s^{-1}. 156
8.4 Variation of $d(\overline{v_\theta}r + \Omega r^2)^2/dr$ with time and r/d at z/d = 0.5, for a jet with Re_0 = 2300 at Ω = 0.21 rad s^{-1}. 157
8.5 Variation of $d(\overline{v_\theta}r + \Omega r^2)^2/dr \leq 0$ with time and r/d at z/d = 5, for a jet with Re_0 = 2300 at Ω = 0.21 rad s^{-1}. 158
8.6 Variation of $d(\overline{v_\theta}r + \Omega r^2)^2/dr \leq 0$ with time and r/d at z/d = 10, for a jet with Re_0 = 2300 at Ω = 0.21 rad s^{-1}. 159
8.7 Variation of χ_1 with time and r/d at z/d = 10, for a jet with Re_0 = 2300 at Ω = 0.21 rad s^{-1}. 161

8.8 Variation of χ_2 with time and r/d at z/d = 10, for a jet with Re_0 = 2300 at Ω = 0.21 rad s^{-1}. 162
8.9 Variation of $d(\overline{v_\theta}r)^2/dr$ with time and r/d at z/d = 0.5, for a jet with Re_0 = 2300 at Ω = 0.83 rad s^{-1}. 163
8.10 Variation of $d(\overline{v_\theta}r)^2/dr$ with time and r/d at z/d = 5, for a jet with Re_0 = 2300 at Ω = 0.83 rad s^{-1}. 164
8.11 Variation of $d(\overline{v_\theta}r)^2/dr$ with time and r/d at z/d = 10, for a jet with Re_0 = 2300 at Ω = 0.83 rad s^{-1}. 165
8.12 Variation of $d(\overline{v_\theta}r+\Omega r^2)^2/dr$ with time and r/d at z/d = 0.5, for a jet with Re_0 = 2300 at Ω = 0.83 rad s^{-1}. 166
8.13 Variation of $d(\overline{v_\theta}r+\Omega r^2)^2/dr$ with time and r/d at z/d = 5, for a jet with Re_0 = 2300 at Ω = 0.83 rad s^{-1}. 167
8.14 Variation of $d(\overline{v_\theta}r+\Omega r^2)^2/dr0$ with time and r/d at z/d = 10, for a jet with Re_0 = 2300 at Ω = 0.83 rad s^{-1}. 168
8.15 Variation of χ_1 with time and r/d at z/d = 10, for a jet with Re_0 = 2300 at Ω = 0.83 rad s^{-1}. 169
8.16 Variation of χ_2 with time and r/d at z/d = 10, for a jet with Re_0 = 2300 at Ω = 0.83 rad s^{-1}. 170
8.17 (a) Phase synchronized, mean radial velocity component $\overline{v}_\theta$ obtained for two separate experimental runs from $\theta - r$ plane and from $r - z$ plane; (b) circumferentially and radially averaged mean circulation $\overline{\Gamma}_{\theta-r}$ (c) radially averaged mean vertical flow component $\overline{w}_{\theta-r}$; (d) parameter χ_1, from (3.45) & (e) parameter χ_2, from (3.46) , for instability criterion of Nagarathinam *et al.* (2015) for a jet with Re_0 = 2300, at Ω = 0.21 rad s^{-1}, for z/d = 10, Ro_0 = 302. 172

9.2 Profiles of the circumferentially-averaged azimuthal velocity component $\overline{v}_\theta$ as a function of nondimensionalised distance r/d from the centre for different instances in time, for a plume with Re_0 = 1800 at Ω = 0.52 rad s^{-1}, z/d = 10. 176
9.1 Instantaneous vector fields of the velocity components, u_r & u_θ for a plume with Re_0 = 1800 at Ω = 0.21 rad s^{-1} at times t for at z/d = 10 177

9.1 Continued 178
9.1 Continued 179
9.3 Instantaneous velocity vectors field of the plume at (a) 20 s, (b) 26 s (c) 32 s (d) 38 s (e) 44 (f) 50 s (g) 56 s (h) 62 s (i) 68 s (j) 74 s (k) 80 s (l) 86 s (m) 92 s (n) 98 s (o) 104 s for a plume with $Re_0 = 1800$, at $\Omega = 0.52$ rad s^{-1}, for $z/d = 10$. 180
9.4 Temporal variation of the nondimensionalised radial coordinate for the location of the maximum velocity for the plume of $Re_0 = 1800$ at $z/d = 10$ at background rotation 0.52 rad s^{-1}. 181
9.5 Temporal variation of the nondimensionalised radial coordinate for the location of the maximum vorticity for the plume ($Re_0 = 1800$) at height $z/d = 10$ with background rotation 0.52 rad s^{-1}. 182
9.6 Velocity vectors of first POD mode: the rotation rates, in units of rad s^{-1}, associated with sub figures are: (a) 0.2, (b) 0.31, (c) 0.41, (d) 0.52, (e) 0.63, (f) 0.73, (g) 0.83, (h) 0.94, (i) 1.05. 186
9.7 Velocity vectors and vorticity field of (a) first, (b) second and (c) third POD mode for a plume with $Re_0 = 1800$, at $\Omega = 0.21$ rad s^{-1}, for $z/d = 10$. 187
9.8 Velocity vectors and vorticity field of (a) first, (b) second and (c) third POD mode for a jet with $Re_0 = 2300$, at $\Omega = 0.21$ rad s^{-1}, for $z/d = 10$. 187
9.9 Variation of the time coefficient of the first POD mode: the rotation rates, in units of rad s^{-1}, associated with sub figures are: (a) 0.2, (b) 0.31, (c) 0.41, (d) 0.52, (e) 0.63, (f) 0.73, (g) 0.83, (h) 0.94, (i) 1.05. 188
9.10 Splines for extrema and mean for the time characteristics (C_1) of POD mode 1 of the plume at background rotation 0.52 rad $^{-1}$. 191
9.11 Splines for extrema and mean for the time characteristic (C_1) of POD mode 1 of the plume after first sifting, at background rotation 0.52 rad $^{-1}$ 191

9.12 IMF_1 calculated from the time characteristic (C_1) of POD mode 1 of the plume after twenty siftings. Splines for extrema and mean is shown in yellow and purple lines respectively. The background rotation associate with data is 0.52 rad s^{-1}. 192
9.13 IMF_2 calculated from the time characteristic (C_1) of POD mode 1 of the plume after ten siftings. Splines for extrema and mean is shown in yellow and purple lines respectively. The background rotation associate with data is 0.52 rad s^{-1}. 192
9.14 All IMFs calculated from the time characteristic (C_1) of POD mode 1 of the plume. The background rotation associate with data is 0.52 rad s^{-1}. 193
9.15 All IMFs calculated from the time characteristic (C_1) of POD mode 1 of the plume. The background rotation associate with data is 0.52 rad s^{-1}. 193
9.16 Variation of the instantaneous frequency with time for the plume at $\Omega = 0.52$ rad s^{-1}, for $z/d = 0.5$: (a) IMF_1, (b) IMF_2, (c) IMF_3, (d) IMF_4, (e) IMF_5, (f) IMF_6. 194
9.17 Variation of the plume precession rate ω_p with background rotation rate Ω. 195
9.18 Mean plume precession frequency $\overline{\omega}$ as a function of the rotation rate of the environment Ω by Frank *et al.* (2017). 195

List of Tables

2.1 Previous findings on entrainment coefficient of jets and plumes; J : Jet, P : Plumes. 9

5.1 Previous Studies on Jets and measured values on entrainment coefficient α, HW : hot wire anemometry, LDA : laser-droppler anemometry, PIV: Particle image velocimetry. 55

5.2 Comparison of peak values for I_w and I_u for the data of the present study with corresponding data of other authors. 62

Acknowledgments

I would like to express my sincere gratitude to my supervisor Dr. Yongmann M. Chung, specially for getting me a tuition fee waiver from the school of Engineering, University of Warwick, and for the continuous support throughout my PhD. I would like to extend my sincere gratitude to my co-supervisor, the most wonderful person I have ever met in my life, Prof. Peter J. Thomas, not only for his guidance but also for his incredible, invaluable patience during my PhD journey. My sincere thanks also goes to Dr. Petr Denissenko, the person behind the scene, for his insightful comments and encouragement. His hard questions broadened my research from various perspectives. I am also grateful to Prof. David Towers for providing PIV analysis software, the most important tool used during my studies. My sincere gratitude also goes to my examiners, Prof. Gary Hunt from the department of Engineering, University of Cambridge and Prof. Duncan Lockerby from the school of Engineering, University of Warwick. I would like to express my deepest gratitude to precision engineer, Mr. Paul Hackett, for the excellent technical support received during the experimental work. Without his precious support it would not be possible to conduct this research.

I take this opportunity to thank the school of Engineering, University of Warwick for granting me a tuition fee waiver and for the other benefits that I received throughout my PhD studentship. I am also grateful to University

Grant commission of Sri Lanka and The Open university Sri Lanka for granting partial funding for my studies. I really appreciate the support given by ffwG (funds for woman graduates) in my final year of PhD. I take this opportunity to thank Dr. N. S. Senanayake and Mr. P.D. Sarathchandra for writing recommendation letters to accompany with my PhD application to University of Warwick. Further I would like to thank Mrs. P. R. Dedigamuwa for helping me to getting to an academic position at The Open university of Sri Lanka.

I take this opportunity to say thank you for my dearest friend and mentor Mrs. T.M.D.N. Medagedara for encouraging me throughout my study. I greatly appreciate the support I received by my wonderful friends Gayani Yapa, Shiroma Basnayake, Chaturika Silva. I would also like to extend my gratitude to Mr. Devapriya Perera and Dr. Shyamalie Bopitiya for their continuous support during my stay in the UK.

There are no words to explain the constant and unconditional support I received from my mother. I am greatly indebted to her for everything she has done for me. I would also like to thank my mothers sister Mrs. M. G. Gunasili Silva and her daughter Miss Dilini Buddhika for their very honest support towards completing my goals.

I am grateful to my husband for playing both roles of mum and dad for my two daughters during these years. I had a great relief during my study since my kids were in safe hands whenever I was away from home. Finally and without hesitation I would like to thank, my two daughters, Dinadi and Minadi, the two wonderful souls in my life, for their belief in me. They were always with the hope that mum would finish her studies one day and get a proper job.

Abstract

Experimental results from comprehensive PIV measurements investigating the dynamics of turbulent jets in a rotating fluid are presented. It is observed that background system rotation induces a time-periodic formation-breakdown cycle of the jets. The flow dynamics associated with this process are studied in detail. It is found that the frequency of the cycle increases linearly with the background rotation rate. The data show that the onset of the breakdown phase and of the reformation phase of the cycle can be characterized in terms of a local Rossby number employing an internal velocity and length scale of the jet. The critical values for this local Rossby number, for onset of breakdown and reformation, scale linearly with a global Rossby number based on the flow conditions at the source. The analysis of the experimental data in terms of relevant stability criteria suggests that the formation-breakdown cycle is due to centrifugal instability and that the temporally fluctuating axial flow plays a prominent role in the process. The development of a turbulent plume subject to background rotation was also briefly investigated by means of PIV, in order to compare its behaviour with the jets. It was revealed that unlike the jets, the plume precesses around the axis of rotation of the background. It was also observed that the mean precession frequency of the plume increases linearly with the rate of background rotation.

Nomenclature

b	Width of the jet
d	Diameter of the source or nozzle
f	Coriolis parameter
k	Axial wave number
m	Azimuthal wave number
r	Radius of the jet
u	Velocity component in the radial direction
v	Velocity component in the azimuthal direction
w	Velocity component in the vertical/axial direction
z	Vertical height measured from the source
$\overline{u}$	Time averaged velocity component in the radial direction
$\overline{v}$	Time averaged velocity component in the azimuthal direction
$\overline{v_\theta}$	Maximum circumferentially averaged azimuthal velocity
$\overline{w}$	Time averaged velocity component in the vertical/axial direction
u'	Fluctuating velocity component in the radial direction

w' Fluctuating velocity component in the vertical/axial direction

$u_{r.m.s}$ Root mean square value of the fluctuating velocity component in the radial direction

$w_{r.m.s}$ Root mean square value of the fluctuating velocity component in the vertical/axial direction

w_m Time averaged/mean centreline velocity

u_e Entrainment velocity

u_0 Vertical velocity of the jet at the source

B Buoyancy flux

M Momentum flux

N Buoyancy frequency

P Cauchy principal value

Q Volume flux

R Cut off radius

B_0 Buoyancy flux at the source

M_0 Momentum flux at the source

Q_0 Volume flux at the source

$\widehat{R}$ Rossby deformation radius

Re_0 Ejection Reynolds number

Ro_0 Ejection Rossby number

Ro_l	Local Rossby number
$\overline{Ro_l}$	Average of local Rossby number
Ro_l^U	Mean value of maxima of local Rossby number
Ro_l^L	Mean value of minima of local Rossby number
$K.E_{v_\theta}$	Kinetic energy associates with azimuthal velocity component
$K.E_{v_r}$	Kinetic energy associates with radial velocity component
ϕ	Azimuthal angle
ν	Kinematic viscosity of the jet liquid
ν_T	Kinematic turbulent viscosity
$\widehat{\nu_T}$	Non-dimensionalised kinematic turbulent viscosity
α	Entrainment coefficient
Ω	Rate of background rotation
ρ	Density of the ambient environment
ρ'	Density of the ambient environment
Γ	Plume Richardson number
Γ_1	Dimensionless scalar
$\mathcal{H}$	Hilbert transform

Chapter 1

Introduction

The present study is involved with the investigation of the effects of background system rotation on the fluid dynamics of jets and plumes. The main focus of the project is on the dynamics of jets. Plumes will be briefly considered near the end of the thesis since a publication on this topic (Frank *et al.*, 2017) appeared in the literature during the final phase of the current investigation and described some observations which were believed to possibly be connected to certain results described here.

Turbulent jets and plumes are a class of turbulent flows produced by continues momentum and buoyancy sources respectively (Lee & Chu, 2012). More generally a fluid motion is called a jet when its primary source of kinetic energy and momentum flux is a pressure drop through an orifice. A fluid motion whose main source of kinetic energy and momentum flux is body forces is called a plume. Flows whose motion is in transition from a jet to a plume, are called a forced plume or a buoyant jet (List, 1982). The appearance of a jet is similar to that of a plume although the turbulent motions in the two flows are produced by different mechanisms. Jet flows are also a subset of general flows known as free shear flows where free indicates that the shear arises in the absence of a boundary (wall) and instead results from a maintained velocity difference. These types of flows are prevalent in nature and technology and this has motivated numerous studies in this area. The efflux of waste water into lakes and oceans and the discharge of toxic fumes into the atmosphere through smoke stacks are examples for jets and plumes related to technology (Baines

& Chu, 1996) while volcanic eruptions and sea floor hydrothermal vents are examples for such flows in the natural environment (Helfrich & Battisti, 1991).

Many flows in nature and technology are subject to background system rotation (Vanyo, 1993; Cushman-Roisin, 1994; Pedlosky, 1987). Background system rotation can substantially alter the dynamics of flows in comparison to their non-rotating counterparts and it leads to effects that can appear counter-intuitive such as, for instance, the Taylor-Proudman theorem (Greenspan, 1968). In technology rotating flows appear in the context of rotating machinery whereas in nature it is the rotation of the earth that can affect flows. The earth's rotation does for instance affect the dynamics of large scale turbulent jets and plumes. It is also a problem of interest in a wide variety of geophysical problems, including deep ocean mixing induced by either surface cooling in the open ocean or freezing events in the earth's atmosphere (John & Andrew, 1998). Examples of industrial applications where jets and plumes are emerging into a rotating environment are for instance associated with combustion chambers, chemical mixing processes and cooling towers. An important non-dimensional number in the context of rotating flows is the Rossby number Ro . The Rossby number characterizes the ratio of inertial forces to Coriolis forces and it is named for Carl-Gustav Arvid Rossby. Effects of rotation become important when the Rossby number is sufficiently small, that is typically when $Ro < 1$, as is the case in many industrial and large scale geophysical and astrophysical flows (Mininni *et al.*, 2009).

The present study investigates the effect of background rotation on turbulent jets and plumes, with the focus being on the dynamics of jets. The jets considered here are generated within a system, rotating at angular velocity Ω, that is the liquid is ejected into ambient water which is in solid-body rotation. The direction of jet ejection is aligned parallel with the axis of rotation. For the case of jets there is no density difference between the ejected water and the ambient water. For the case of plumes fresh water is released at the bottom of a tank filled with salt water of higher density.

The motivation for the current study was a preliminary short set of exper-

iments conducted by an undergraduate student project as part of a project funded through the Undergraduate Research Support Scheme (URSS) of the University of Warwick (Thomas, 2014). During this undergraduate project approximately fifty to one hundred small jets in close proximity were released from a manifold. It was observed that the speed at which the common front of the jets propagated upwards, after liquid ejection at the source had commenced, substantially reduced with an increasing value Ω of the background rotation rate. However, these experiments were based on dye visualisations and could only provide some very preliminary, mostly qualitative, data. At the start of the current project it was decided that a natural strategy to conduct a comprehensive, in-depth investigation was to begin with experiments involving a single jet rather than many interacting jets emerging from a manifold.

The present study goes substantially beyond qualitative dye-visualization experiments only. To the best of our knowledge the current investigation represents the first study of jets in rotating systems for which Particle Image Velocimetry (PIV) measurements were conducted and analyzed. Therefore we initially performed PIV measurements on jets in non-rotating environments to ensure that we were able to qualitatively reproduce relevant PIV data for non-rotating jets of previous authors such as results contained in Carazzo *et al.* (2006); Hussein *et al.* (1994); Ezzamel *et al.* (2015). Thereafter we began to perform experiments on jets subject to background rotation. As will be seen in the remainder the main focus of the study will become the experimental corroboration of the existence of a formation-breakdown cycle of jets in rotating systems that had been described by Lawrie *et al.* (2011) in a short publication summarizing computational simulations of jets developing subject to background rotation. The final part of the thesis will briefly discuss the related case of the effects of background rotation on plumes. The experiments for this part of the project were conducted during the very late phase of the overall project after we had become aware of the results of Frank *et al.* (2017) that had just become available in the literature. Frank *et al.* (2017) report an oscillatory flow behaviour they observed in dye visualizations involving plumes in rotating systems and we suspected that this behaviour of the plumes could re-

flect a phenomenon corresponding to the formation-breakdown cycle observed in the current investigation on jets.

1.1 Objectives

- Investigate the dynamics of a jet in the presence of background rotation.
- Compare and contrast the jet dynamics with the jet in the absence of background rotation.
- Investigate the effect of variation of background rotation on the dynamics of the jet.
- Investigate the effect of the variation of source momentum flow on dynamics of the jet. (Reynolds number effect).
- Establish a relationship between the relevant quantified parameters and background rotation.
- Investigate the behaviour of a plume in the presence of background rotation.
- Compare the behaviour of the plume with the jet subjected to background rotation.

1.2 Structure of the Thesis

This thesis consists of ten chapters. Chapter 2 covers a wide range of literature in order to critically assess the published work related to the current study. Chapter 3 explains the theory and equations used throughout the thesis. In Chapter 4, the methodology used for experiments and analysis is explained. Chapter 5 of the thesis presents the results related to the jets in the absence of background rotation. The main results of the study that shows the behaviour of the jet in the presence of background rotation are presented in chapter 6. Chapter 7 discusses the results obtained using proper orthogonal decomposition analysis for the jets with background rotation. Chapter 8 takes up

the issue of the centrifugal instability that develops when the jet propagates in background rotating environment. In chapter 9, a short study on forced plumes with background rotation is included. The conclusions of the study is discussed in chapter 10.

Chapter 2

Literature Review

This chapter summarises the published research results related to the current study. The focus of the present investigation is on jets and plumes developing subject to background rotation. However, a review of the literature regarding these flow structures in the absence of rotation is included to facilitate appreciating the fundamental issues associated with the subject. Thereafter the focus will become the behaviour of jets and plumes in the presence of background rotation with the goal to outline the current state of knowledge regarding Coriolis effects on the primary flow.

The effect of rotation on a flow can significantly alter its nature. A dominant effect of rotation is to produce waves and flows that are themselves rotating relative to a frame of reference fixed to the Earth. In a rotating frame dynamic effects arise from the virtual Coriolis force. The action of the Coriolis force results, for instance, in the Taylor-Proudman (Taylor, 1917; Proudman, 1916) theorem. This theorem states that, in a Cartesian coordinate system x, y, z with rotation around the z axis, the derivative δ/dz of the components of the flow velocity in the x and y directions vanish. Fluid columns are therefore set in motion like solid bodies, and the flow may be considered to be two-dimensional, although the vertical velocity component not necessarily vanishes, and can behave as a convected scalar (Greenspan, 1968). Therefore in rotating flow experiments the observed flow phenomena often do not match our expectations and intuition. Consequently careful detailed measurements, such as PIV studies, are required to reveal the actual flow behaviour in such

flow arrangements. Since the present study is the first experimental study that uses PIV for jets in a rotating fluid it can be expected that the analysis of the data to be obtained will substantially extend our knowledge regarding the effects of the action of the Coriolis force on jet flow subject to background rotation.

2.1 Jets and Plumes

Jets and plumes are frequently seen in both environmental and industrial applications (Carazzo *et al.*, 2006). A jet is a flow produced by a continuous source of momentum while a plume is a flow produced by a continuous source of buoyancy (Lee & Chu, 2012). Figure 2.1 shows a jet produced during a test of a rocket which is an example for a jet flow in an industrial application. More examples for jets and plumes in industry include smokestack emissions, sewage discharges, thermal effluents from power stations, and ocean dumping of sludge (Papanicolaou & List, 1988). Jet/Plume like flow in nature can be seen in volcanic eruptions, deep sea vents and thermals.

Whenever a moving fluid enters a quiescent body of miscible liquid, a velocity shear is created between the entering and ambient fluids, causing turbulence and mixing. Figure 2.2 shows an instantaneous three dimensional view of a horizontal axisymmetric jet issuing from a circular nozzle photographed shortly after fluid ejection has commenced. The photo clearly illustrates the existence of coherent flow structures in the downstream flow region. After exiting the orifice and while propagating downstream, approximately an axial distance equal to five diameters, the jet begins to entrain ambient fluid resulting in a radial spreading. The details of the downstream jet development depend on many parameters such as the initial conditions at the source, the boundary conditions associated with the ambient liquid, including possibly effects of geometric confinement, as well as the exact nature of the forces acting on the fluid.

Therefore the dynamics of jets and plumes have been the focus of numerous studies over the past years. The classical theoretical approach to turbulent en-

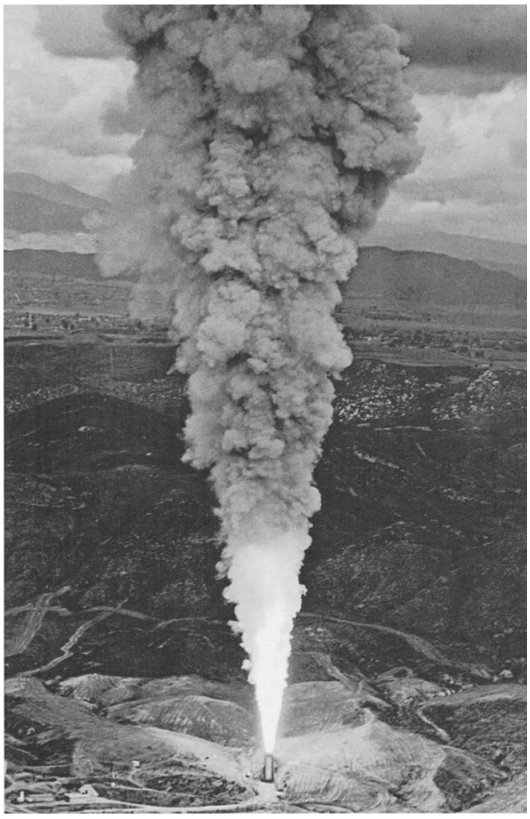

Figure 2.1: High Reynolds number turbulent jet produced by a test of a rocket (Lee & Chu, 2012).

Figure 2.2: Instantaneous three dimensional view of a horizontal axisymmetric jet issuing from a circular nozzle (photo courtesy: J. Kurima, N. Kasagi and M. Hirata, Turbulence and heat transfer laboratory, University of Tokyo.).

trainment of jets and plumes was developed by Zel'dovich (1937), Priestley & Ball (1955) and Morton *et al.* (1956). Their analysis is based on conservation equations for fluxes of mass, momentum and buoyancy. They proposed that the entrainment rate at the edge of the jet or plume was proportional to the average vertical centreline velocity. The constant of proportionality is referred to as the entrainment coefficient.

Numerous experimental studies have presented different values for the entrainment coefficient. Table 2.1 shows examples of values previously obtained by various authors for the entrainment coefficient of jets and plumes.

Authors	Flow	α
Forstall & Gaylord (1955)	J	0.070
Rosensweig *et al.* (1961)	J	0.076
Papanicolaou & List (1988)	J	0.074
Panchapakesan & Lumley (1993)	J	0.095
Wang & Law (2002)	J	0.075
Ezzamel *et al.* (2015)	J	0.045
George *et al.* (1977)	P	0.159
Papanicolaou & List (1988)	P	0.130
Shabbir & George (1994)	P	0.154
Wang & Law (2002)	P	0.124
Ezzamel *et al.* (2015)	P	0.075

Table 2.1: Previous findings on entrainment coefficient of jets and plumes; J : Jet, P : Plumes.

The comprehensive review by Carazzo *et al.* (2006) states that for jets/plumes with Gaussian velocity profiles the entrainment coefficient for pure jets is in the range of 0.045 to 0.056 while it adopts values in the range of 0.07 to 0.11 for pure plumes. The higher values of the entrainment coefficient of plumes are likely due to buoyancy-enhanced turbulence (List, 1982; Kaminsky *et al.*, 2005). The spread of the values among jets and among plumes are not fully explained. However, differences between measurement techniques, the nature of the fluids and the shapes of nozzles were suggested as reasons for the dis-

crepancies (Carazzo *et al.*, 2006). Richards & Pitts (1993) studied the effects of source conditions on jets. They carried out a number of experiments by changing the jet injecting nozzle type. But the results did not show any dependence on the initial conditions of the jet. On the other hand Mi *et al.* (2013) performed experiments on a free jet using two different types of nozzle. They found differences in the flow characteristics for different types of the nozzles.

Apart from the entrainment coefficient there are many other important flow characteristics of jets and plumes that have been investigated and presented. Examples include mean velocities, the jet centreline velocity profile, Reynolds stresses and turbulence intensities including second, third and fourth order moments. Wygnanski & Fiedler (1969) presented various statistics of jet flow such as mean velocities and turbulence fluctuations and their data became a frequent reference for jet studies. Figure 2.3 shows the variation of the mean axial velocity profiles, normalised by the mean centreline velocity, with the non dimensional radial coordinate for a jet as presented in Hussein *et al.* (1994). The data in the figure illustrate how different measurement methods can affect the results obtained. Figure 2.3 displays corresponding results they sampled by means of a stationary hot wire (SHW), a flying hot wire (FHW) and Laser Doppler Anemometry (LDA) in comparison to some previous results obtained by Wygnanski & Fiedler (1969).

Panchapakesan & Lumley (1993) performed experiments on a turbulent round jet of air discharging into quiescent air and they analysed turbulent characteristics to second and third moments and reported in great detail. These results are in good agreement with the results presented later by Wang & Law (2002) and (Ezzamel *et al.*, 2015). As regards the mean velocity profiles at the nozzle exit it is accepted that the profile is determined by the source geometry. A nozzle, pipe or sharp-edged orifice will produce a top-hat, power-law-type, or complex converging-diverging flow profile, respectively (Ball *et al.*, 2012). Moreover Uddin & Pollard (2007) confirmed that the axial expansion of the effective jet width depends on the shape of the initial jet velocity profile.

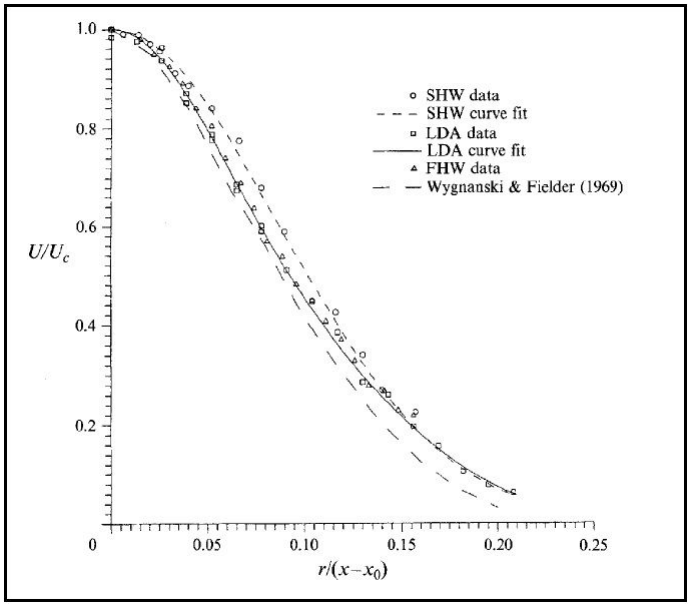

Figure 2.3: Variation of non-dimensionalised mean axial velocity (U/U_c) with non-dimensionalised radial coordinate ($r/(x - x_0)$) by Hussein *et al.* (1994): SHW- stationary hot wire, LDA - Laser Doppler Anemometry, FHW - Flying hot wire.

2.2 Jets in Rotating Reference Frame

Fluid flows subjected to effects of background rotation have received much attention over the years (Greenspan, 1968; Vanyo, 1993; Chia *et al.*, 1982; Hopfinger & Linden, 1990; Cambon, 1994; Afanasyev *et al.*, 2009). The influence of the Earth's rotation on the dynamics of turbulent plumes and jets is also of interest in a wide variety of geophysical problems, including deep ocean mixing induced by either surface cooling in the open ocean or freezing events in the Earth's atmosphere (John & Andrew, 1998). The presence of jets in the atmosphere and oceans points to the importance of the investigation of free jets in a rotating reference frame. The nondimensional Rossby number (Ro) is used to characterise flows subjected to background rotation. The Rossby number is defined as $v/(\Omega l)$ where v is the velocity scale, l is the characteristic length scale associated with the flow and Ω is the background rotation of the system.

Experiments on jets in a rotating system generally fall into one of two cate-

gories. Studies either consider jets where the direction of flow is aligned with (in the direction of) the axis of rotation or, alternatively, where the flow direction of the jet is orientated perpendicular to the axis of rotation. The present study considers the former case where the jet motion is aligned with the axis of rotation. Therefore the literature on the latter case where the flow direction is perpendicular to the rotational axis will not be discussed here further.

The first study related to the vertical jets in a rotating reference frame was reported by Barcilon (1967b). In order to mimic the same flow phenomena as in jets with background rotation, Barcilon (1967b) considered a flow field of steady columnar vortex with a constant angular momentum and a thermal boundary layer at the bottom. Due to thermal convection, fluid particles move axially upwards inside the columnar vortex which creates a jet like flow in the middle of the vortex. Barcilon (1967b) developed a theoretical model to predict the behaviour of this flow by extending the work of Morton *et al.* (1956). This model predicted that a discontinuous transition or a vortex breakdown can occur in the flow when $Ro > 1$. The main questionable point here is that the model was developed by assuming that the entrainment coefficient is constant throughout the axial height regardless of the vortex flow surrounded by. He also conducted some experiments that involved a jet flow surrounded by a coaxial cylinder. In order to create the surrounding vortex flow the cylinder was made to rotate slowly. He observed that, as the jet rises axially, the vortex pressure eroded the supply of vertical momentum until it brings the jet to a stop at a finite height.

Wilkins *et al.* (1969) also conducted laboratory experiments on instantaneous source thermals in rotating fluid. They compared the behaviour of these thermals with the thermals in non rotating fluid. Both enhancement and suppression of vertical velocity have been observed experimentally as effects induced by rotation. Figure 2.4 shows a series of instantaneous snapshots which compare the thermals in rotating and non rotating fluid. It can be seen that the thermal had laterally expanded more when the rotation is present. This observation is consistent with the qualitative observations of the present study even though the present study consider a jet in rotating fluid.

Wilkins *et al.* (1971a,b) further performed a series of experiments to investigate the effect of background rotation on successive thermals, that is thermals which are released successively from the same source but separated by short time intervals. They used three successive thermals and reported that the effects of rotation are a downward tilt of the outer portion of the thermal, generation of counter circulations and reversals in the direction of vertical velocity. They also reported that there is a tendency of formation of a 'Taylor column' when there is sufficiently strong interaction between the thermals and the background rotating fluid. The study of Wilkins *et al.* (1969) motivated Niino (1978, 1980) to extend their work theoretically and experimentally. He considered the cases of instantaneous and maintained liquid releases and, in particular, Niino (1978, 1980) addressed the case which is the subject of the current study where there exists no density difference between the ejected and the ambient liquid.

Niino (1978) conducted experiments by injecting a jet downwards in a rotating fluid. He reported that the advancing velocity of the lower end of the jet is smaller than that in a static fluid. He further discussed that an upward motion appears when the injection of the source fluid is stopped and the secondary circulation induced by the jet does not penetrate far below the lower end. For a two dimensional laminar jet Niino (1978) used linear theory to qualitatively explain the suppression of the vertical velocities caused by the upward pressure gradient force which is generated by the entrainment of the rotating ambient fluid. The linear analysis was further extended by Niino (1980) for the two cases of jets with continues and finite momentum flow rate at the source. Niino (1980) writes that, as soon as the jet starts, the fluid particles near the origin are most strongly accelerated. Therefore the vertical velocity is comparatively larger than that far downstream. This structure in the vertical velocity results in horizontal divergence which, in turn, induces anticyclonic azimuthal velocity. As the divergence always vanishes very near to the source, the azimuthal velocity is zero at that level. Thus, the azimuthal velocity field has a vertical gradient. Hence, the pressure field which is in geostrophic balance in the radial direction has a vertical gradient. Therefore the vertical velocity

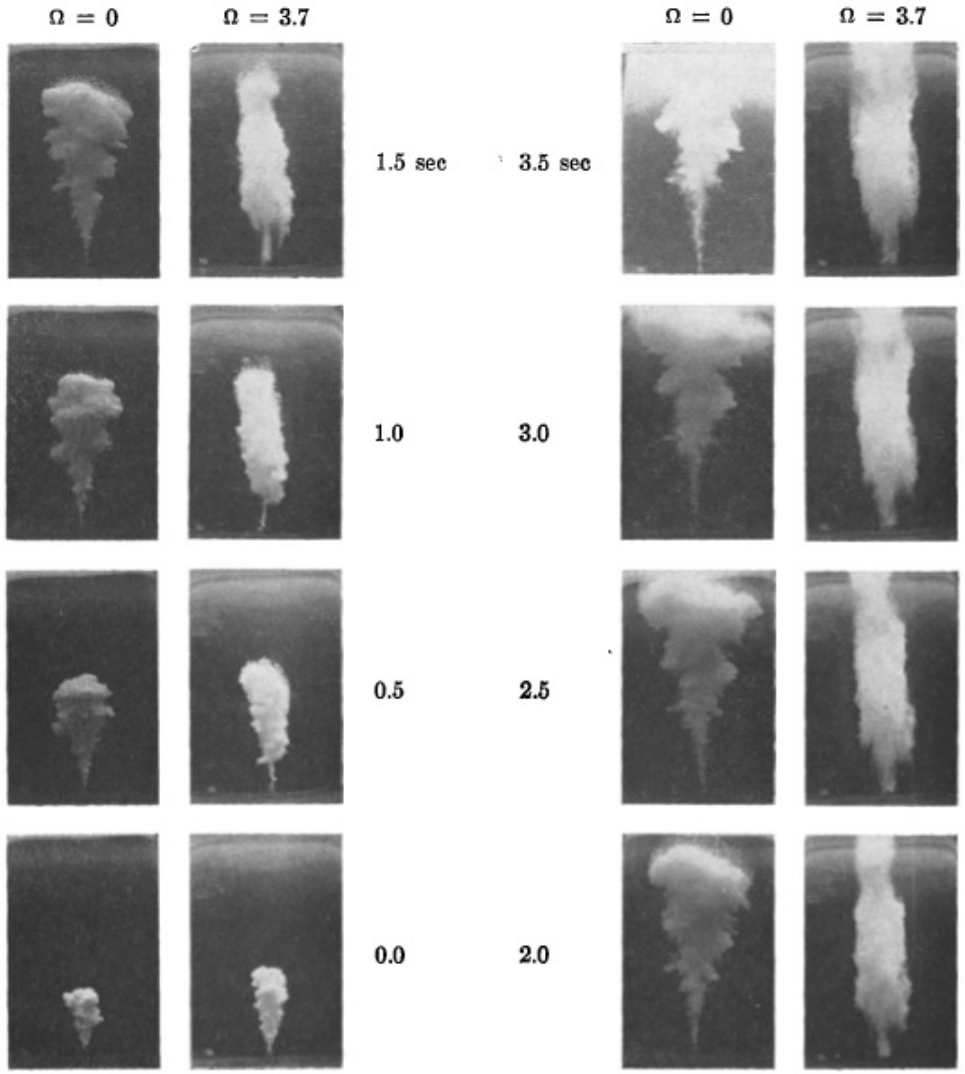

Figure 2.4: Instantaneous snapshots of a thermal with and without background rotation (Wilkins *et al.*, 1969).

is reversed thus flow is reversed. However, Niino (1980) does not refer to any time periodic features that could be related to the formation-breakdown cycle for the continuous jets which is the subject of the current investigation. Nevertheless, for forcing of finite duration, but longer than a certain critical limit, the computations of Niino (1980) revealed damped, continuous oscillations near the forcing region, with a period of about π/Ω, after the forcing has been terminated. Niino (1980) discusses that these oscillations are associated with reverse flow in the forcing regions at large times but he does not state whether he had indeed observed these oscillations in the earlier experiments (Niino, 1978) that motivated his subsequent computations.

Elrick (1979) conducted experiments on negatively buoyant thermals in a rotating fluid. He showed that vortex forming interaction occurs over a considerable range of buoyancies and rotation rates. Helfrich & Battisti (1991) performed laboratory experiments to examine the combined effects of rotation and stratification on the structure and the stability of hydrothermal plumes. The experimental results showed that buoyant plumes in rotating systems result in the formation of a baroclinic vortex. The spreading level and the maximum penetration level of the plume are larger than predicted by the standard plume theory. The plume vortices are destabilized by rotation leading to the unsteady production of isolated baroclinic vortices, which are able to propagate away from the source regions. They observed an instability of the flow and concluded that the instability results from the interaction of cyclonic circulation of ambient fluid around the rising plume (driven by entrainment into the plume) and anticyclonic circulation in the spreading plume fluid at the neutral buoyancy level.

Fernando *et al.* (1998) also carried out laboratory experiments to investigate the effects of rotation on turbulent convection. They considered the evolution turbulent plume that is released from a point source located at the free surface of a homogeneous fluid layer in the presence of background rotation. They also observed the same vertical velocity suppression as in previous studies and found that the rotational effects become important after the plume has risen to a vertical distance given by $3.3(B/\Omega^3)^{0.25}$, where B is the specific

buoyancy flux. Fernando *et al.* (1998) further concluded that the rotational effects inhibit the lateral growth of the plume when the maximum plume width is $1.4(B/\Omega^3)^{0.25}$. A similar type of experiment was also carried out by Bush & Woods (1998). As they stated, they mainly examined the influence of the bounding geometry and rotation on the discharge of buoyant fluid from a turbulent axisymmetric plume in an open-ended channel. Having considered both non stratified and stratified ambient environments, they found that the onset of time dependence in the flow is brought on by instability of the anticyclonic vortex overlying the source, either a columnar vortex in the homogeneous environment, or a lenticular neutral cloud in the stratified case. Bush & Woods (1998) further observed a pulsatile flow regime in their experiments which is consistent with observations by Niino (1980). But Bush & Woods (1998) have discussed that criterion for the transition between steady and pulsatile flows depends on the relative magnitudes of the channel width and the maximum radius attainable by the plume structure.

Numerical Studies on Jets

Numerical studies on jets and plumes with background rotation have received much attention recently. Lawrie *et al.* (2011) conducted a numerical study investigating an axisymmetric jet in a rotating reference frame by means of their MOBILE software. Lawrie et al. (2011, p. 2) discuss that they observed that the jets develop a helical instability, whereby the jet initially grows, entrains ambient fluid and that this leads to helical displacement of the jet from the axis. It is reported that at large displacement amplitudes the jet beaks down upon which the associated entrainment ceases. It is argued that with nothing to drive further radial convergence of material contours, the azimuthal velocity decays sufficiently for the jet to reform and thereby establishing a periodic formation-breakdown cycle. Deremble (2016) numerically investigated the effects of background rotation on convective plumes and concluded that the rotation strongly affects classical convection patterns of the plume, that the plume is confined at the intrusion level by the establishment of geostrophic balance and that non-trivial swirl speed develops in and around the plume. Tomàs *et al.* (2016) also carried out a numerical study to investigate the effects of rotation on the turbulent dynamics of thermally driven buoyant plumes in

stratified environments at large Rossby numbers. Their simulations revealed that the primary response to the adverse pressure gradient is an off-axis deflection of the plume that evolves into a robust, organized anticyclonic radial precession about the buoyancy source.

Except Niino (1980) and Lawrie *et al.* (2011), all other published studies on jets subjected to background rotation include buoyancy effects or stratification in the ambient environment. The damped oscillations predicted theoretically by Niino (1980) have hitherto not been verified experimentally. Moreover the existence of the formation breakdown cycle of jets in rotating systems that has been observed by Lawrie *et al.* (2011) in their numerical simulation has also not yet been corroborated experimentally. To the best of author's knowledge the present study is the first experimental validation of existence of this formation breakdown cycle. Moreover, the present study is the first experimental work that uses PIV for investigating the behaviour of jets in a rotating fluid. A substantial number of previous experimental studies have reported different flow instabilities associated with jets and plumes that are subjected to background rotation. However, none of these studies tested any quantitative instability criteria in order to shed light on the underlying physical origins of any observed instabilities. One main reason for this absence of quantitative instability tests is, evidently, the fact that all the past experimental studies on jets and plumes in rotating flow only involved dye visualisation experiments and these can generally not produce the required data for a thorough quantitative analysis. Since the present study used 2D PIV for carrying out measurements it was possible to test some quantitative instability criteria. The relevant, most recent instability criteria tested here are those developed by Nagarathinam *et al.* (2015) for centrifugal instability.

2.2.1 Centrifugal Instability

The experimental data to be described in the remainder will show that jets subject to background rotation undergo a continuous formation-breakdown cycle. The literature on centrifugal instability is reviewed for two reasons. Firstly, it was suggested in many past studies that vortices in a rotating fluid become

unstable due to centrifugal instability (Afanasyev & Peltier, 1998; Gallaire & Chomaz, 2003a). Secondly, it is known that vortices with axial flow experience centrifugal instability as the axial flow gets stronger (Leblanc & Cambon, 1998; Mathur *et al.*, 2014) and the flow investigated here resembles this type of flow. Therefore studies addressing centrifugal instability of vortices in a rotating fluid with axial flow are relevant in the present context.

The original investigation into the stability of swirling flow motion was performed by Rayleigh (1917). For inviscid flow Rayleigh derived a necessary and sufficient condition for centrifugal instability. This condition or criterion is now known as 'Rayleighs instability criteria'. The criterion states that if the square of the circulation of the flow does not decrease in the direction of increasing radial distance anywhere within the flow then the flow is stable to axisymmetric instabilities.

In its original formulation the Rayleigh criterion was derived for the vortices without axial flow and without background rotation. The criterion is robust and simple but yet important in many types of turbulent flows. Bayly (1988) extended Rayleighs centrifugal instability criterion to general inviscid two dimensional flows. He further concluded that a sufficient condition for centrifugal instability is that the streamlines should be convex closed curves in the considered region of the flow and with the magnitude of the circulation decreasing outwards. Leibovich & Stewartson (1983) generalized the Rayleigh criterion to axisymmetric vortex flow that involves axial flow. But the criterion developed by Leibovich & Stewartson (1983) is valid only for large azimuthal wave numbers.

Kloosterzielt & Heijst (1991) modified the Rayleighs instability criterion in order to accommodate the effects of background rotation. From the laboratory experiments performed they concluded that in a rotating fluid only very weak anticyclonic, barotropic vortices are centrifugally stable, and very strong cyclonic, barotropic vortices are centrifugally unstable. Leblanc & Cambon (1998); Potylitsin & Peltier (1999); Godeferd *et al.* (2001) have shown that centrifugal instability is a potential reason for instability in anticyclonic vor-

tices for Stuart vortices with background rotation.

Mathur *et al.* (2014) proposed a heuristic criterion and applied it in the context of a stability analysis of Stuart vortices with axial flow. They found that the elliptic and hyperbolic instabilities, that exist in Stuart vortices with no axial flow, were shown to get suppressed in the presence of a sufficiently strong axial flow. They also concluded that further increase in the axial flow triggers the development of a new branch of centrifugal instability. Mathur *et al.* (2014) further concluded that their new criterion is shown to describe the onset of centrifugal instability very accurately.

Nagarathinam *et al.* (2015) developed the first instability criterion that accommodates both background rotation and axial flow. They solved local stability equations analytically for a axisymmetric vortex at the first instance. The resulting sufficient criterion for centrifugal instability in an axisymmetric vortex is then heuristically extended to non-axisymmetric vortices and written in terms of integral quantities and their derivatives with respect to the stream function on a streamline. The also developed a new criterion for non-axisymmetric vortices that converges to the exact criterion of Bayly (1988) in the absence of background rotation and axial flow. Nagarathinam *et al.* (2015) validated their criterion by comparisons with numerically calculated growth rates for two different anticyclonic vortices namely Stuart vortex and TaylorGreen vortex. In the present study their criterion is tested, probably for the first time, using experimental data.

2.3 Particle Image Velocimetry

An important advancement in the area of flow-diagnostics measurement methodologies for modern experimental fluid mechanics is the invention and development of techniques for the measurement of whole, instantaneous fields of scalars and vectors (Adrian, 1991). These techniques include tomographic interferometry (Hesselink, 1988), planar laser-induced fluorescence for scalars (Hassa *et al.*, 1987) and planar laser-induced fluorescence, laser-speckle velocimetry, particle-tracking velocimetry (Lloyd *et al.*, 1995; Cowen & Moni-

smith, 1997; Muste *et al.*, 1998) and particle image velocimetry for velocity fields. The ability to make 'global' velocity measurements has elevated particle image velocimetry (PIV) to a special status in fluid mechanics. PIV is a non-intrusive measuring technique. It involves seeding the flow with tracer particles and following their displacement as they are carried along with the flow (Raffel *et al.*, 2007). From such recordings comparisons of successive image frames enable the calculation of velocity vector fields based on instantaneous images taken at known time intervals. The velocity is estimated based on sophisticated algorithms that evaluate the extent that particles in the images move within the time interval. The number of velocity vectors that can be obtained depends on the resolution of the images. The crucial, important feature of PIV is that it provides whole-field velocity measurements.

A typical PIV image displays light reflection of the tracer particles carried along with the flow at the instant the image was taken at their locations within the light sheet used to illuminate the flow region under consideration. As part of the PIV data analysis the recorded images are divided into small sub areas known as 'interrogation areas'. Then the cross correlation of the interrogation area with respect to the same interrogation area of the successive image is calculated in order to quantify the velocities this procedure was first proposed by Adrian & Yao (1984) and Sutton *et al.* (1983). As in most other fields of life the development of computer technology has substantially benefited the computationally intensive PIV data analysis procedures. In the early stages of the development of PIV photographic and opto-mechanical processing steps were inherent to the method (Willert & Gharib, 1991). The technique became known as digital particle image velocimetry (DPIV) when it became possible to use digitally recorded video images and analyse them computationally (Willert & Gharib, 1991). Nowadays the method is normally just referred to as PIV despite it relying crucially on digital methodologies. Two dimensional DPIV/PIV has been enormously rewarding in revealing fundamental aspects of the structure of turbulence and many other flows aspects (Adrian, 2005) for many years. More recently PIV technique has been improved to measure three velocity components (Nishino *et al.*, 1989; Prasad & Adrian, 1993; Gaydon *et al.*, 1997) by mean of Stereoscopic PIV. In this technique one laser light

sheet and two cameras are used to view the laser plane from different angles and capture particle displacement images. By means of this stereoscopic observation mode it is then possible to also infer the third velocity component from the measurements. The most recent development in the general area of PIV is tomographic PIV. This technique makes use of several simultaneous views of the illuminated particles and their 3D reconstruction as a light intensity distribution by means of optical tomography (Elsinga *et al.*, 2006). The measurements conducted for the present study were conducted with a 2D PIV measurement system.

Chapter 3

Theory

This chapter summarises the main theoretical concepts required for the analysis of the Particle Image Velocimetry (PIV) measurements for both the jets with and without background rotation. The topics to be addressed include technical aspects of the PIV methodology itself, aspects of the proper orthogonal decomposition (POD) data analysis technique applied to the PIV data as well as the fundamental theoretical issues associated with the particular instability criteria tested as part of the data analysis.

Figure 3.1 shows a schematic diagram illustrating the flow of a fluid jet through ambient fluid at rest. In the region of the potential core, the centreline velocity is equal to the outlet velocity of the jet at the circular source. The height of this region is less than $5d$ where d is the diameter of the nozzle from which the jets is ejected. In the regions surrounding and above the potential core the jet entrains ambient fluid.

3.1 Coordinate System and Governing Equations

The flow is described in cylindrical polar coordinates r, ϕ and z with associated velocity components of, respectively, u, v and w. The axial velocity profile $w(r, z)$ develops a Gaussian nature as indicated in figure 3.1. The flow is governed by the continuity and the Navier-Stokes (momentum) equations

displayed in equation (3.1) and equation (3.2). Note that equation (3.2) only shows the momentum equation for the vertical component, w, of the flow velocity since rotational symmetry around the vertical z- axis is assumed.

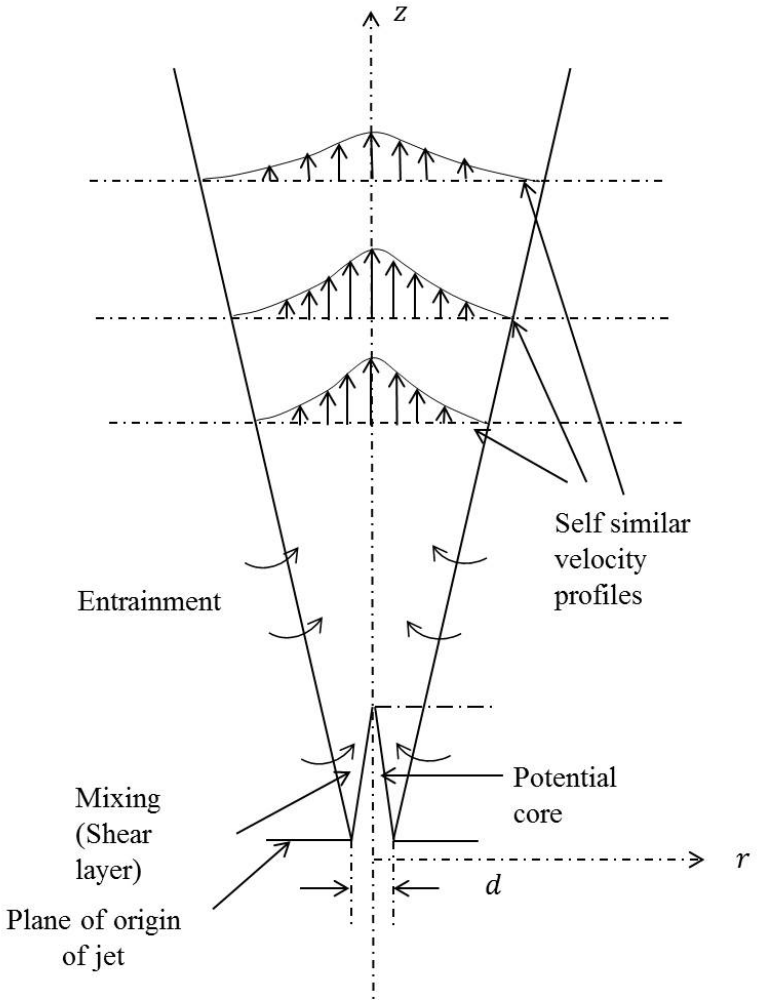

Figure 3.1: Schematic diagram of a jet through a fluid at rest.

$$\frac{1}{r}\frac{\partial(ru)}{\partial r} + \frac{1}{r}\frac{\partial v}{\partial \phi} + \frac{\partial w}{\partial z} = 0, \tag{3.1}$$

$$\frac{\partial w}{\partial t} + u\frac{\partial w}{\partial r} + \frac{1}{r}\frac{\partial w}{\partial \phi} + w\frac{\partial w}{\partial z} = -\frac{1}{\rho}\frac{\partial p}{\partial z} + \nu\nabla^2 w. \tag{3.2}$$

When analysing jets developing without background rotation, time averaged quantities are considered. Therefore equations (3.1) and (3.2) can be written in such a way that the required velocity quantities $(\overline{u}, \overline{w})$ represent time averaged

data and we use primes to characterize the fluctuating velocity contributions u' and v'. The azimuthal velocity component (v) is neglected assuming axisymmetry of the jet.

$$\frac{1}{r}\frac{\partial(r\overline{u})}{\partial r} + \frac{\partial \overline{w}}{\partial z} = 0, \tag{3.3}$$

$$\frac{1}{r}\frac{\partial(r\overline{uw})}{\partial r} + \frac{\partial \overline{w}^2}{\partial z} + \frac{1}{r}\frac{\partial(r\overline{u'w'})}{\partial r} + \frac{\partial \overline{w'^2}}{\partial z} = -\frac{1}{\rho}\frac{\partial \overline{p}}{\partial z} + \nu\nabla^2\overline{w}, \tag{3.4}$$

where

$$u = \overline{u} + u', \tag{3.5}$$

$$w = \overline{w} + w'. \tag{3.6}$$

Equations (3.3) and (3.4) represent the basic expressions governing the flow field for non-rotating jets. For the case when the jets are subject to background rotation the Coriolis force has to be added as a body force on the right-hand side of the Navier-Stokes equation. However, neither the Navier-Stokes equation for the non-rotating case nor that for the the rotating case will be solved as part of this study. Therefore we refer the reader to books such as (Greenspan, 1968; Cushman-Roisin, 1994; Pedlosky, 1987).

3.2 Equations for Estimating Physical Quantities Required for the Flow Analysis

Before analyzing the effects of background rotation on the jet, dynamics of jets in non-rotating systems will be considered to corroborate that our experimental set up and our measurement techniques are suitable for the main part of the study. To this end we will initially compare experimental data from the present study for a jet in a non-rotating environment to some corresponding recent data of Ezzamel *et al.* (2015). In this context we follow Morton *et al.*

(1956) and Ezzamel *et al.* (2015) and define the specific mass flux $Q(z)$ and the momentum flux $M(z)$ at any axial height z above the source as

$$Q(z) = 2\pi \int_0^\infty \overline{w}(r,z) r dr, \tag{3.7}$$

$$M(z) = 2\pi \int_0^\infty \overline{w}^2(r,z) r dr. \tag{3.8}$$

The values of these two quantities at the source where $z = 0$ are defined as

$$Q_0 = \frac{\pi d^2}{4} u_0, \tag{3.9}$$

$$M_0 = \frac{\pi d^2}{4} u_0^2, \tag{3.10}$$

where u_0 is the velocity of the jet at the source. In chapter 9 we will briefly consider results for plumes and, in this context, we will moreover require the buoyancy flux $B(z)$ which we define following Morton *et al.* (1956) and Ezzamel *et al.* (2015) as

$$B(z) = 2\pi \int_0^\infty \overline{w} g'(r,z) r dr, \tag{3.11}$$

$$g' = \frac{g(\rho - \rho')}{\rho}. \tag{3.12}$$

In equations (3.11) and (3.12) ρ' is the density of the fluid of the plume and ρ is the uniform density of the ambient environment. The Buoyancy flux at the source (B_0) is defined as

$$B_0 = \frac{\pi d^2}{4} g' u_0. \tag{3.13}$$

As already discussed above in the context of introducing figure 3.1 the time averaged vertical velocity profile $\overline{w}(r,z)$ of the jet is known to be of Gaussian nature (Morton *et al.*, 1956) and this can be described by

$$\frac{\overline{w}(r,z)}{w_m(z)} = e^{\frac{-r^2}{b^2(z)}}. \tag{3.14}$$

Non-dimensionalised root mean square values of the fluctuating velocities I_u and I_w respectively in the radial direction and the vertical direction are defined

by

$$I_w = \frac{w_{r.m.s}}{w_m}, \tag{3.15}$$

$$I_u = \frac{u_{r.m.s}}{w_m}, \tag{3.16}$$

where $u_{r.m.s} = \sqrt{\overline{u'^2}}$ and $w_{r.m.s} = \sqrt{\overline{w'^2}}$. The Reynolds stress, $\overline{u'w'}$, is characterized by the fluctuating velocities in the radial and the axial direction and, by using the Reynolds stress, we define the kinematic turbulent viscosity, ν_T, as

$$\nu_T = \frac{\overline{-u'w'}}{\frac{\partial w}{\partial r}}. \tag{3.17}$$

The entrainment coefficient (α) is defined as

$$\alpha = \frac{u_e}{w_m}, \tag{3.18}$$

where w_m is the mean vertical centreline velocity, u_e is the entrainment velocity and b, from equation (3.14), is the width of the jet at each height. The volume flow rate at each height can be found by using equation (3.19) assuming axisymmetry of the jet

$$Q(z) = 2\pi \int_0^b w(r,z) r dr. \tag{3.19}$$

The volume of liquid entrained by the jet from the surrounding at each small vertical height dz can be written as

$$\frac{dQ}{dz} = 2\pi b u_e = 2\pi b \alpha w_m. \tag{3.20}$$

On the basis of equations (3.19) and (3.20) the entrainment coefficient α can be obtained from the experimental data.

3.3 Non Dimensional Numbers

The experimental conditions for each run of the experiment are characterized in terms of an ejection Reynolds number and an ejection Rossby number. These two non dimensional numbers are defined as

$$Re_0 = \frac{u_0 d}{\nu}, \tag{3.21}$$

$$Ro_0 = \frac{u_0}{\Omega d}, \tag{3.22}$$

where u_0 is the velocity of the jet at the source, ν is the kinematic viscosity of the jet liquid. Moreover a local Rossby number dependent on the height above the source is used. This local Rossby number is based on the azimuthal velocity and it is defined by

$$Ro_l = \frac{\overline{v}_\theta}{\Omega l}, \tag{3.23}$$

where $\overline{v}_\theta$ is the maximum circumferentially averaged azimuthal velocity and l is the radius at which it occurs.

Following Hunt & Kaye (2001) a source parameter, or Richardson Number, (Γ) for the plumes at the source is defined as

$$\Gamma = \frac{5Q_0^2 B_0}{4\alpha M_0^{5/2}}, \tag{3.24}$$

where B_0, M_0 and Q_0 are Buoyancy, Momentum and Volume flux at the source.

3.4 Particle Image Velocimetry

PIV is a non-intrusive, laser-based, optical measurement technique. Figure 3.2 shows a schematic diagram of a typical experimental PIV arrangement. As illustrated in the figure a basic PIV measuring system consists of a CCD (charge couple device) camera to record images of the flow, a laser device to illuminate the flow, optics to create a light sheet and PIV tracer particles for seeding the flow. Figure 3.2 illustrates how images of the seeded flow are

recorded by means of the CCD camera. The underlying rationale of the PIV measurement technique requires that the seeding particles faithfully follow the flow. Information regarding the flow-field velocities can then be obtained by filming the the particle motion in the illuminated plane of the light sheet and a subsequent analysis of these recordings.

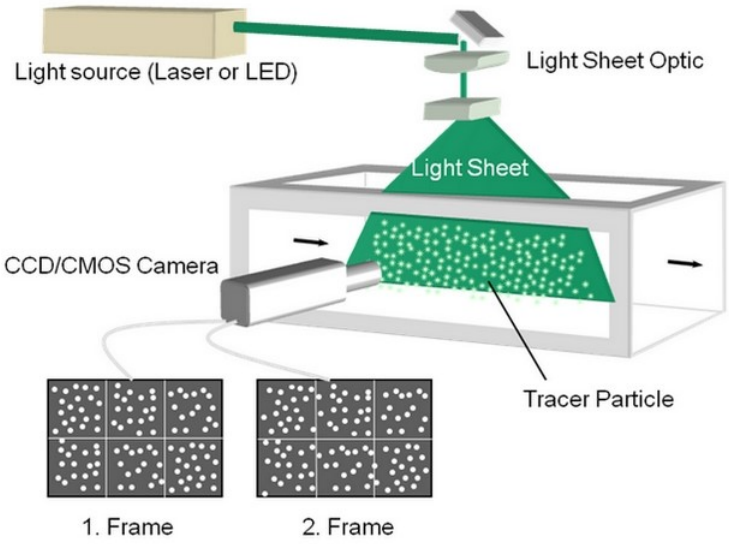

Figure 3.2: Schematic diagram of a PIV experimental arrangement (Raffel *et al.*, 2007).

There are two techniques that can be used to record images, namely single frame/multi exposure technique and the multi frame/single exposure technique. Figure 3.3 illustrates the way that images get recorded when these two techniques are used. Both techniques rely on information of the particle velocities being available for successive instants, t, in time separated by short intervals Δt.

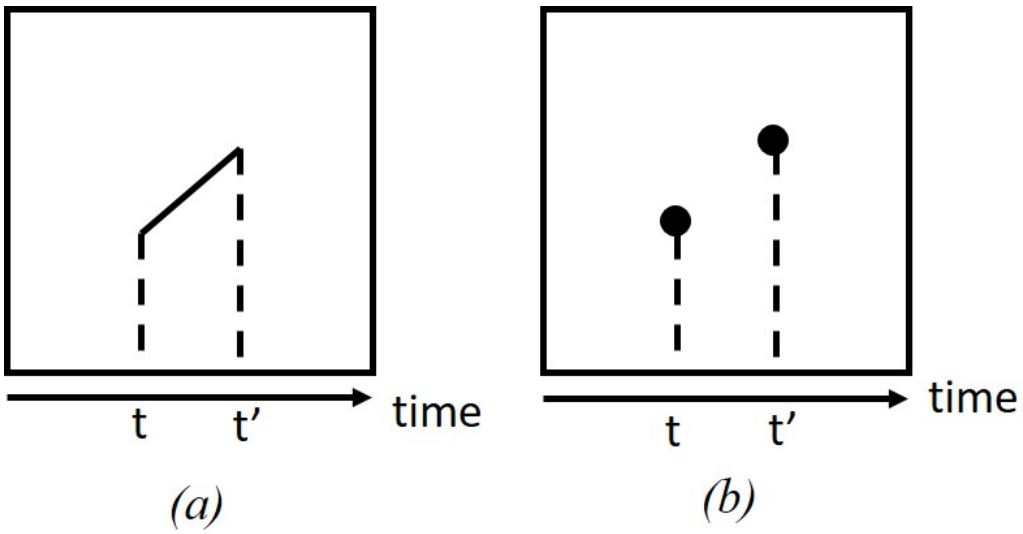

Figure 3.3: (a) Single frame with single exposure of light to the camera lens, (b) Single frame with multi exposures of light to the camera lens (Raffel *et al.*, 2007).

In modern PIV, the data analysis is conducted using dedicated computer packages and the terminology Digital Particle Image Velocimetry (DPIV) is now common. For DPIV the pixel array representing an image is divided into smaller areas referred to as 'interrogation areas'.

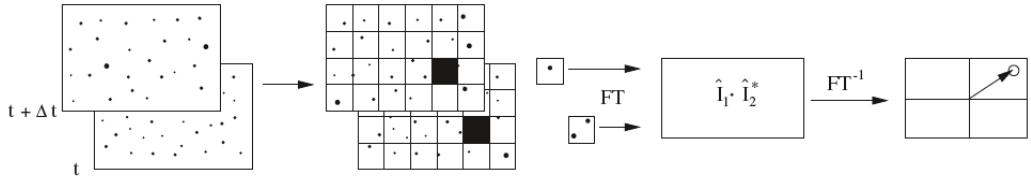

Figure 3.4: Schematic diagram of analysing a PIV image pair (Raffel *et al.*, 2007).

As illustrated in figure 3.4 image pairs at time t and $t' = t + \Delta t$ are taken into consideration. Each image is then subdivided into a number of small interrogation regions. The interrogation regions have to be small enough such that it can be assumed that all particles within each interrogation move homogeneously as a whole. These interrogation areas are the key factor that define the desired density of the vector field obtained after processing the images. For the data analysis one interrogation area from the first image (image taken

at time t) is selected and the respective interrogation area of the second image (image taken at time t') is shifted with respect to the first. The cross correlation of the image densities at each pixel is calculated. Then the peak of the correlation map shows the degree of match between the two interrogation areas and hence can be used to estimate the particle displacement. Most of the software packages use fast Fourier transform to calculate the cross correlation.

In order to find the velocity vectors, the particle displacement has to be quantified. This is achieved by means of an image calibration. Image calibration provides a conversion factor that relates the distance in terms of pixels to its corresponding real-world distance in units of length. For the calibration process a calibration image is used. Figure 3.5 displays a typical calibration image which, in this particular case, consists of rows of black circles of constant radius on a white background. The radius of the circles and the distance between their centres represent known reference lengths. Once the real distance of particle displacement is known a velocity vector for the considered interrogation area is determined. A velocity vector map over the whole image area is obtained by repeating the above explained procedure for each interrogation area over the image pair. In order to increase the spatial resolution, a technique called 'overlapping of interrogation areas' can be used. Figure 3.6 shows, three interrogation windows and, as it can be seen, the interrogation window 2 has a 50% overlap with the interrogation window 1. Also the interrogation window 3 has a 50% overlap with the interrogation window 2. Since one velocity vector is assigned for one interrogation window, the overlapping of interrogation windows increases the spatial resolution of the vector field. Another technique of improving the results of PIV is offsetting the interrogation windows. Figure 3.7 shows two interrogation windows in an image pair. The cross correlation is calculated by comparing the interrogation window 1 in image 1 shown in the figure with the interrogation window 1 in image 2. As it can be observed in the figure the position of the interrogation window in image 2 has a slight offset when compared with the position of the interrogation area in image 1. The offset has to be carefully chosen to improve the results obtain from PIV images - for details refer to Westerweel *et al.* (1997).

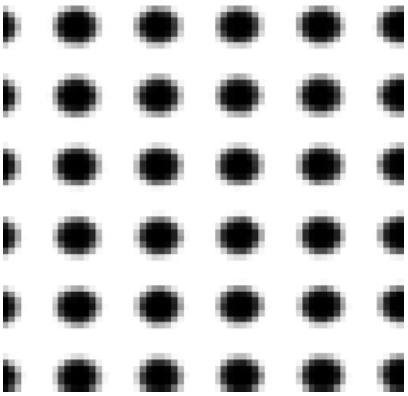

Figure 3.5: A typical PIV calibration image (Quénot *et al.*, 2001).

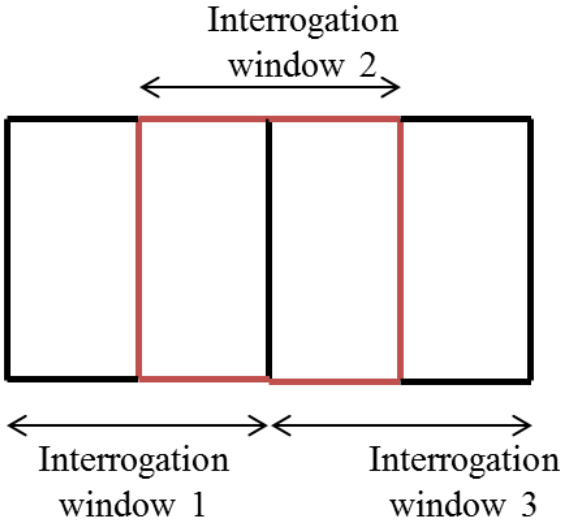

Figure 3.6: Interrogation windows with a 50% overlap.

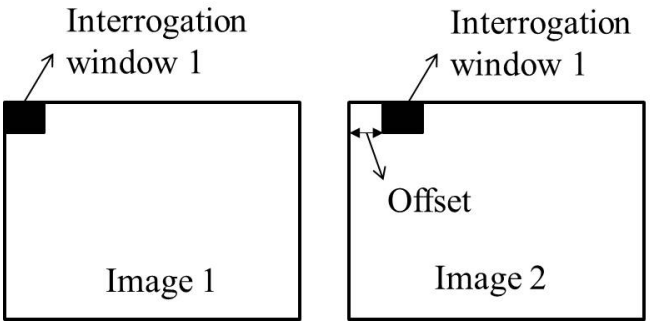

Figure 3.7: Interrogation windows in an image pair with respective interrogation window in second image has an offset.

3.5 Proper Orthogonal Decomposition (POD)

Proper Orthogonal Decomposition (POD) represents a tool to identify coherent structures in turbulent flow - see, for instance, Patte-Rouland *et al.* (2001) and Vanierschot *et al.* (2014). POD was first used for the study of turbulent flows by Lumley (1967) - it is also known as Principal Component Analysis (PCA). The method is described in detail in, for instance, Joliffe (2002). In the context of the current study POD will be applied to sequences of captured PIV images to extract information regarding the temporal variability of coherent structures in the flow field of the jets.

For the POD analysis a given set of images will be decomposed with the intention to represent the images as a sum of base functions. The strategy for the selection of the proper base functions relies on maximising the energy content of each mode. Consider a case where a flow field was captured at N consecutive time intervals (N being the number of snap shots).

$$u(x, y, t) = \overline{u}(x, y) + u'(x, y, t). \tag{3.25}$$

Any instantaneous velocity field can be decomposed into two parts as in equation (3.25), where $\overline{u}(x, y)$ is the time averaged mean velocity and $u'(x, y, t)$ is the fluctuating velocity of the flow. The concept of POD relies on representing the fluctuating part of the flow by linear combinations of POD modes $\phi_i(x, y)$ with associated time-varying modal coefficients $C_i(t)$ as identified in equation (3.26). The time-varying modal coefficients are referred to as the

time coefficients hereafter in this thesis.

$$u(x,y,t) = \overline{u}(x,y) + \sum_{i=1}^{n} C_i(t)\phi_i(x,y). \tag{3.26}$$

Note that $u(x,y,t)$ is a vector containing a number M of real entries arising from the spatial resolution. Therefore the velocity field u^i at any time instant, t^i, can be expressed as

$$u^i = [u_1, u_2, ...u_j..u_M]^T, \tag{3.27}$$

where T denotes the transpose of the matrix. More generally u^i is a column vector that contains M rows. Since there exist a number N of snapshots, all the data can be composed into a single matrix as indicated below

$$U = [u^1 u^2 .....u^N], \tag{3.28}$$

where matrix U has dimensions $M \times N$.

Then the fluctuating part of the velocity field is calculated by subtracting the time velocity mean from the velocity field as

$$U' = U - \frac{1}{N}\sum_{i=1}^{N} u^i. \tag{3.29}$$

Now i^{th} column of the matrix U' contains the fluctuating velocities of the snapshot taken at time t^i (refer equation (3.30)).

$$U' = [u^{1'} u^{2'} .....u^{N'}]. \tag{3.30}$$

Then the eigenvalue value problem for the snapshot POD method is defined by

$$CH = \lambda H, \tag{3.31}$$

where

$$C = \langle U'^T U' \rangle. \tag{3.32}$$

By definition C is the time correlation matrix of dimension $N \times N$ and $\langle\rangle$ indicates the ensemble average. The solution of equation (3.31) gives H which is

a matrix of dimension $N \times N$ and where each column consists of eigenvectors. Corresponding eigenvalues are given by matrix λ. The eigenvectors are arranged such that their corresponding eigenvalues are in order where $\lambda_{i+1} > \lambda_i$. The new eigenvalue matrix is H' where each column consists of base for POD modes. In order to obtain non-normalised POD modes, the computation of equation (3.33) is performed.

$$\Phi^* = U'H', \tag{3.33}$$

where U' is a matrix with dimension $M \times N$ and H' is a matrix with dimension $N \times N$. Then the matrix Φ^* has the dimension $M \times N$. Each column consists of vectors of each POD mode as in equation (3.34) and $*$ indicates that quantities are not normalised yet.

$$\Phi^* = [\phi^{1^*}\phi^{2^*}...\phi^{i^*}...\phi^{N^*}]. \tag{3.34}$$

$$\phi^{i^*} = [v_1, v_2...v_j...v_M]. \tag{3.35}$$

Every POD mode is normalized as indicated in equation 3.36. Note that after normalising the POD modes, the matrix is denoted by Φ.

$$\phi^i = \sqrt{v_1^2 + v_2^2 + ... + v_j^2 + ... + v_M^2}. \tag{3.36}$$

From the definition it is known that

$$u'(x, y, t) = \sum_{i=1}^{n} C_i(t)\phi^i(x, y). \tag{3.37}$$

$$u^{i'} = \Phi C^i. \tag{3.38}$$

In matrix notation

$$U' = \Phi C, \tag{3.39}$$

where

$$C = [C^1C^2...C^i...C^N]. \tag{3.40}$$

$$C = \Phi^{-1}U'. \tag{3.41}$$

C is a matrix of dimension $N \times N$ of which the rows give the time characteristics of each POD mode. Since all the POD modes have already been calculated, C can be obtained from equation (3.41). Since Φ is an orthogonal matrix $\Phi^{-1} = \Phi^T$, and then

$$C = \Phi^T U'. \tag{3.42}$$

Once all the modes and time characteristics have been calculated image reconstruction can be conducted using the required number of modes in order to check the accuracy of the POD calculation.

3.6 Instability Criteria

For the jets considered in this study the effects of shear between the liquid forming the jet and the ambient are small compared to the case of a swirling jet in a non-rotating environment. Therefore we suspected that the formation-breakdown cycle discussed herein might arise as a consequence of centrifugal instability. Four instability criteria were considered in the present study.

$$d(\overline{v}_\theta r)^2/dr \leqslant 0. \tag{3.43}$$

$$d(\overline{v}_\theta r + \Omega r^2)^2/dr \leqslant 0. \tag{3.44}$$

The first one shown in equation (3.43), is the Rayleigh instability criterion for vortex flow in the absence of background rotation and second one shown in equation (3.44) is the modified Rayleigh's instability criterion to include background rotation, by Kloosterzielt & Heijst (1991). According to the Rayleigh's instability criterion, which is valid only for inviscid fluids, the square of the circulation of a vortex must increase continuously in passing from the inner to the outer radius. The modified Rayleigh instability criterion includes the effect of background rotation on the circulation. In other words the absolute

circulation.

$$\chi_1 = \left(\frac{4w'^2(r\Omega + \overline{v}_\theta)^2}{(r\overline{v}'_\theta - \overline{v}_\theta)^2 + r^2 w'^2} - 2\Big(\frac{\overline{v}_\theta}{r} + \Omega\Big)\Big(\overline{v}'_\theta + \frac{\overline{v}_\theta}{r} + 2\Omega\Big) \right). \tag{3.45}$$

$$\chi_2 = \left(\frac{4(dw/d\psi)^2(\Omega + 2\pi/T)^2}{(\Gamma/T^3)(dT/d\psi)^2 + (dw/d\psi)^2} - 2\Big(\frac{2\pi}{T} + \Omega\Big)\Big(\frac{1}{T}\frac{d\Gamma}{d\psi} + 2\Omega\Big) \right), \tag{3.46}$$

where $\Gamma = 2\pi r\overline{v}_\theta$ is the circulation and $\mathrm{T} = 2\pi r/\overline{v}_\theta$.

The third criterion, by Nagarathinam *et al.* (2015), was derived for testing the centrifugal instability of axisymmetric vortices in the presence of both background rotation and axial flow. The the third criterion is given in equation (3.45). The fourth criterion is given in equation (3.46). This criterion is specially derived for testing the centrifugal instability of non-axisymmetric vortices in the presence of background rotation and axial flow.

3.7 Hilbert-Huang Transformation

The Hilbert-Huang transform (HHT) is NASA's designated name for a combination of empirical mode decomposition (EMD) and the Hilbert spectral analysis (HSA). In the present study for the data analysis of the jets the Fourier transformation was used as an analytical technique wherever appropriate. However, according to Huang & Wu (2008) Fourier analysis can only yield meaningful interpretations for linear and stationary processes whereas its application to data from nonlinear and non stationary processes is often problematic. A stationary process is a process whose statistical properties, such as the mean, variance and autocorrelation are all constant over time. Hence, a non-stationary process is a process, where statistical properties change over time. Figures 3.8 (a) and (b), show examples for a stationary process and a non stationary process, respectively.

The data generated from PIV measurements on plumes showed a non stationary behaviour. Therefore the Hilbert-Huang transformation is used in part of

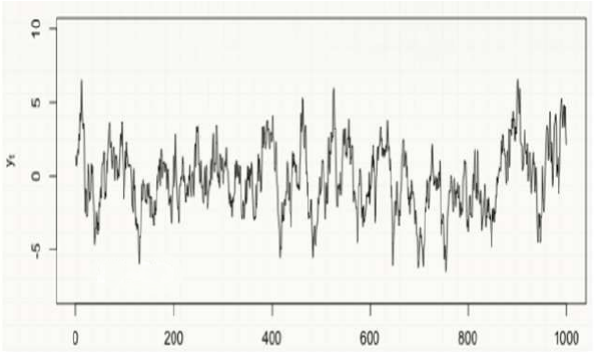

(a)

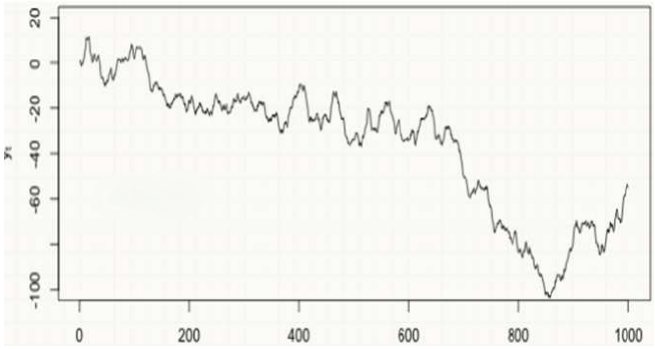

(b)

Figure 3.8: Examples for a (a) stationary process and a (b) non stationary process (Kam, 2014).

the data analysis. The Hilbert-Huang transformation consists of two parts. The first part is referred to as the empirical mode decomposition (EMD) and second one is a Hilbert spectral analysis (HSA). For the EMD process it is assumed that fluctuating data consists of different simple intrinsic modes of oscillations which are represented by intrinsic mode function (IMF)s. According to Huang *et al.* (1996), an IMF has two features. The first being that in the whole data set of an IMF the number of extrema and the number of zero-crossings must either be equal or differ at most by one. The second feature is, at any point, the mean value of the envelope defined by the local maxima and the envelope defined by the local minima is zero. Finding IMFs in a data set is referred to as the sifting process and this must be continued until all required IMFs are found. For the sifting process, for any raw data set $x(t)$ all local extrema, that is maxima and minima, are identified. Thereafter all local maxima are connected by means of a cubic spline and, similarly, all minima are connected by a another cubic spline as illustrated in figure 3.9. Then the local mean value ($m1(t)$) between the two splines is calculated. Then new data set ($h1(t)$) is generated by subtracting $m1(t)$ from $x(t)$ as in 3.47. Upon completion ($h1(t)$) is considered as new data set and same procedure as explained above is repeated. Figure 3.11 shows the two splines for the maxima and the minima together with the mean ($m2(t)$). The sifting procedure is then repeated until a data set that represents an IMF is found (i.e. a data set for that the number of extrema and the number of zero-crossings must either be equal or differ at most by one and the second feature is, at any point, the mean value of the envelope defined by the local maxima and the envelope defined by the local minima is zero.). Once an IMF is found through sifting, a new data set is generated by subtracting a data set of IMF from the raw data ($x(t)$). Then the same sifting procedure is adopted for the new data set until a new IMF is found. At the end the required IMFs are chosen to calculate frequencies. A typical IMF is shown in figure 3.11.

$$h1(t) = x(t) - m1(t). \tag{3.47}$$

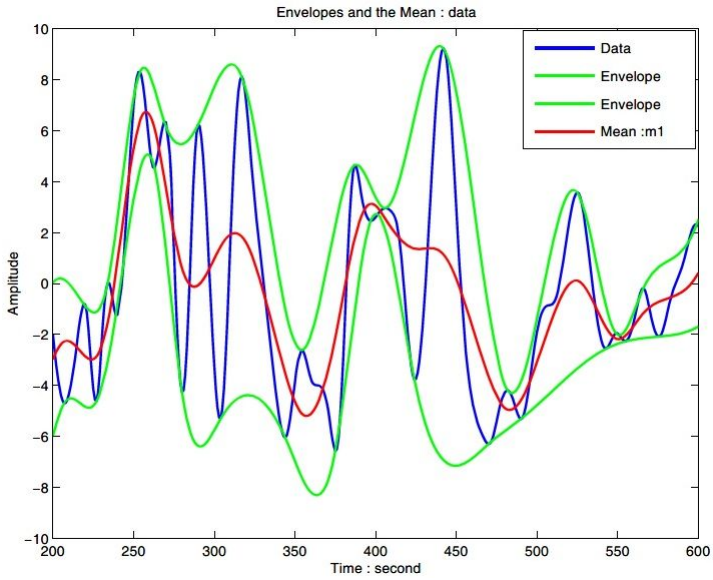

Figure 3.9: The data $x(t)$ (blue) upper and lower envelopes (green) defined by the local maxima and minima, respectively, and the mean value of the upper and lower envelopes given in red (Huang *et al.*, 1998).

3.7.1 Hilbert Transformation

The Hilbert transformation is used to calculate the time dependent frequency of each IMF obtained using EMD. A Hilbert transform $\mathcal{H}(f(t))$ of a function $f(t)$ is expressed by

$$\mathcal{H}(f(t)) = \frac{1}{\pi} P \int_{-\infty}^{\infty} \frac{f(\tau)}{t-\tau} d\tau, \tag{3.48}$$

where P denotes the Cauchy principal value. Hilbert transforms convert any signal to an analytical signal where amplitude and phase can be determined at every single point. Then the time dependent frequency can be calculated via the rate of change of the phase of the signal.

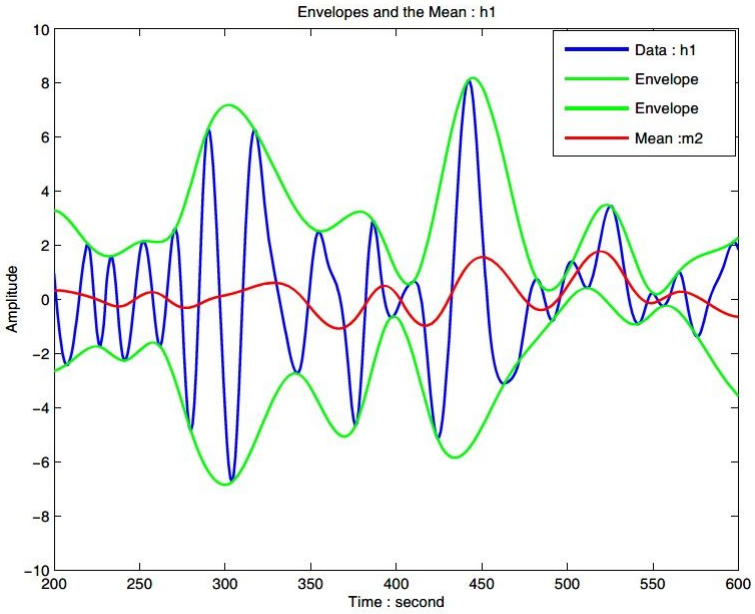

Figure 3.10: Repeated sifting steps with $h1(t)$ (Huang *et al.*, 1998).

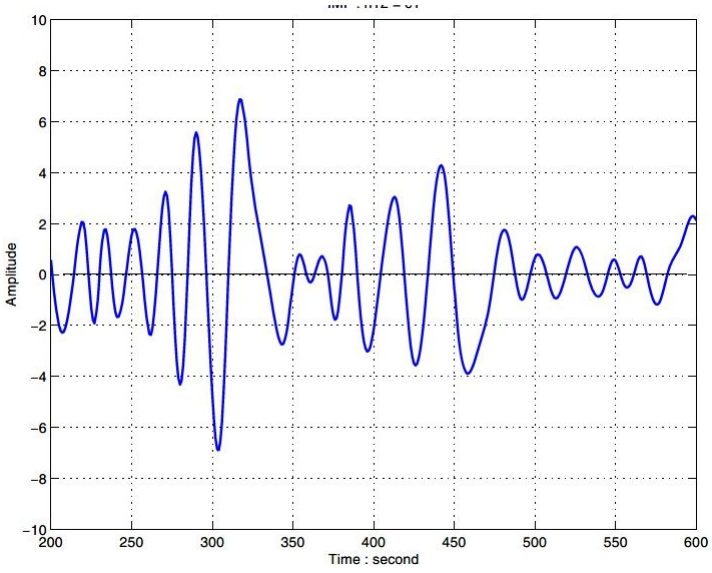

Figure 3.11: A typical IMF obtained after 12 steps of sifting original data (Huang *et al.*, 1998).

Chapter 4

Methodology

4.1 Experimental Set up

The experiments were conducted on Warwick's rotating-tank facility illustrated in figure 4.1. The set up constitutes a tank of height 2.5 m, with octagonal cross-section and across width of 1 m, which is mounted on top of a rotating turntable. The overall height of the facility, from the floor to the top of the support structure, is over 5.7 m. The jets studied were released vertically upwards from an exit nozzle embedded flush within the top surface of an acrylic ejector box as illustrated in figure 4.2. The ejector box had a diameter of 500 mm and it was placed at the bottom of the rotating tank. The center of the exit nozzle was aligned to coincide with the rotational axis of the turntable. The diameter of the exit nozzle, from which the jets were ejected, was $d = 6$ mm. Thus, the ratio of tank width to source diameter was approximately 167. This ensured that effects from the surrounding walls of the tank, induced on the flow during the experiments, can be assumed to be negligible.

The inside of the ejector box which is shown in 4.2, was filled with a honeycomb-structured plastic material through which the supplied water had to flow on its path to the exit nozzle. The purpose of the honeycomb material was to suppress large-scale rotary flow structures developing inside the ejector box before reaching the nozzle exit and, therewith, potentially biasing the flow condition through induced swirl within the exit nozzle.

A controlled, continuous supply of water, at prescribed volumetric flow rate, q_0, was provided via rotary joints through the hollow central axis of the turntable facility. In preparation for the experiments the water inside the tank was allowed to settle for at least 4 hours after the turntable had been accelerated to its required rotational speed. This ensured that the liquid was in a state of solid-body rotation when the experiments commenced. The two-dimensional velocity field measurements in the vertical and horizontal planes were obtained. The data are analysed in terms of cylindrical polar coordinates, r, ϕ, z. The z-axis coincides with the rotational axis of the turntable and $z = 0$ corresponds to the centre of the exit nozzle at the surface of the ejector box.

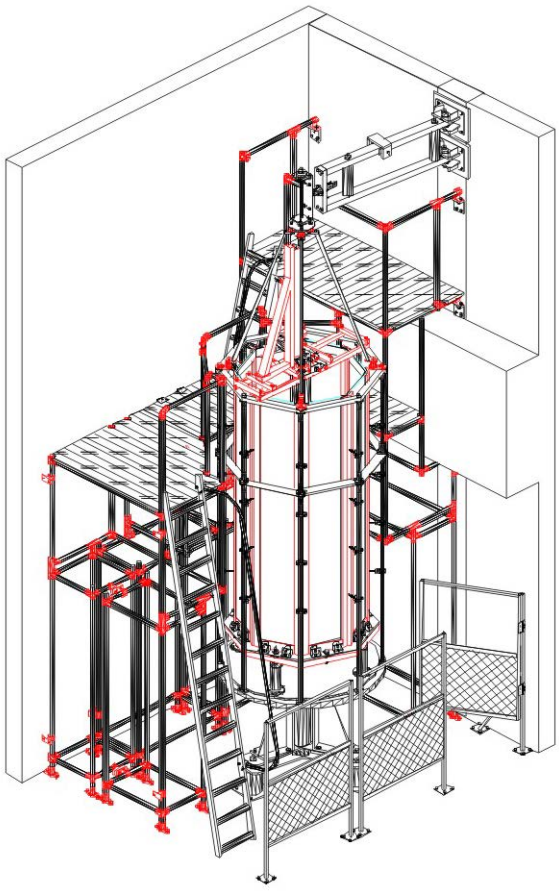

Figure 4.1: Technical drawing of the large-scale rotating-tank facility.

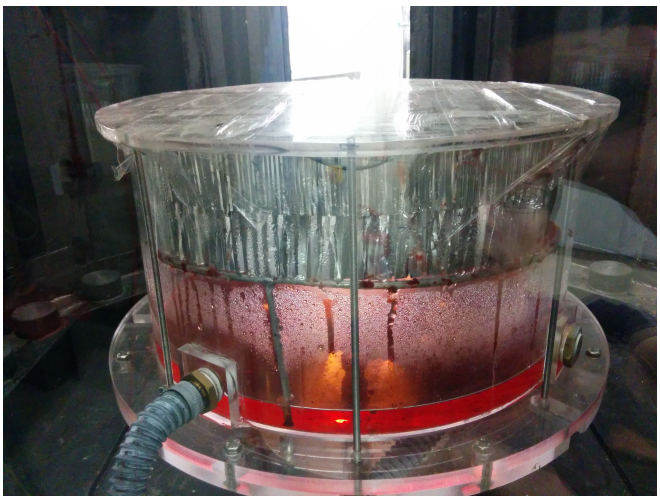

Figure 4.2: Ejector box.

The laboratory in which the turntable facility is housed is fully air conditioned. Moreover, there exist a number of additional fans distributed throughout the laboratory facilitating agitation and mixing of the ambient air in the laboratory. This ensures that the possibility of vertical temperature gradients developing over long time periods within the liquid inside the tank is minimized.

4.2 PIV system set up

The entire PIV system which consists of laser & optics and CCD camera, was mounted on the rotating turntable, that is within the rotating frame of reference. The PIV frames were acquired using a Point grey USB 3.0 camera at a rate of 90 frames per second and with a resolution 1024×1024 pixels. The tracer particles used for the PIV measurements were Dantec, 10 μm diameter silver coated, neutrally buoyant, hollow glass spheres. The flow was illuminated by Green colour, wave length of 532 nm, continuous laser. Several optics were used to get the required height and width of the laser sheet. The PIV measurements carried out for the velocity field calculation can be divided into two, depending on the plane of measurement, namely $r-\theta$ (horizontal) plane $r-z$ (vertical) plane. The laser sheet and the camera arrangement in each plane is discussed in following sections.

4.2.1 Horizontal ($r-\theta$) Plane Measurements

In order to calculate the velocities in the cross sections, of vertically emerging jets, measurements were carried out at the cross sections at selected heights from the source. A schematic diagram for the experimental arrangement for the horizontal plane measurements, is shown in figure 4.3. As it can be seen in the figure, the cross sectional plane of the jet at the required height from the source was illuminated by a horizontally spread laser sheet. The plane of the laser sheet is perpendicular to the $r-z$ plane. A mirror was fixed at the top of the tank facing downwards of the tank, at an angle 45^0. The focussed images of illuminated particles, in the $r-\theta$ plane was obtained by viewing through the mirror. Figure 4.4 shows the actual experimental arrangement of the camera and the mirror.

Cross sectional velocity vector fields were obtained at heights of $0.5d$, $5d$, $10d$, $15d$ above the source of the jet. Before conducting any experiment the calibration plate was aligned with the horizontal laser sheet at the required plane and few images were taken for calibration purpose. Four strings were used to place the horizontal calibration plate on the required horizontal plane as shown in figure 4.5. After recording the calibration images, the tank was spun until it attains solid body rotation. When the tank was spinning as a solid body (approximately after four hours from the start), the jet was started and the PIV measurements were carried out. The camera was switched on before the jet starts emerging to the ambient environment, which ensured that the required measurements were taken from the start of the jet flow.

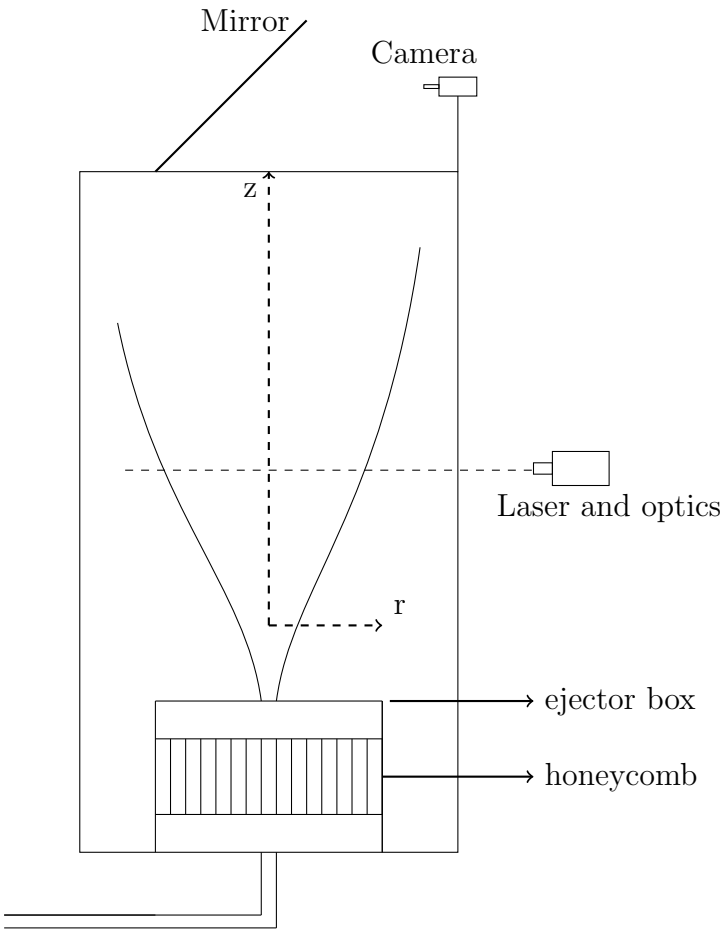

Figure 4.3: Schematic diagram of the experimental set up for horizontal plane measurements.

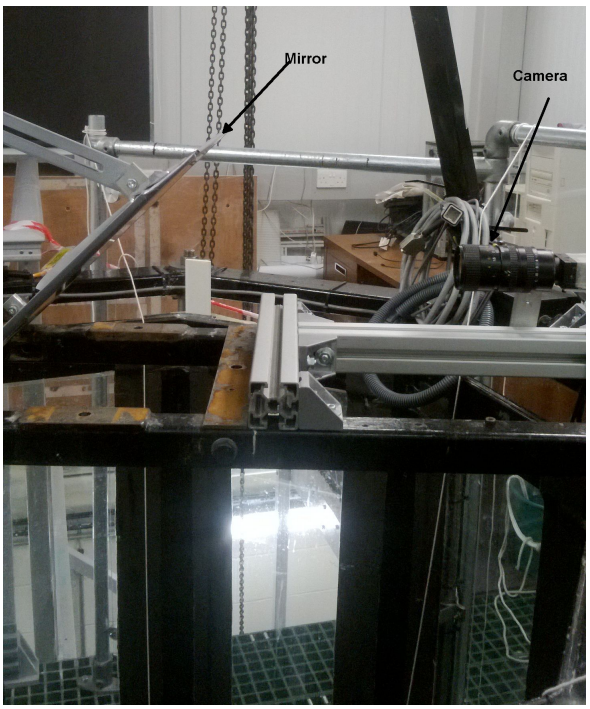

Figure 4.4: Arrangement of the mirror and the camera for the horizontal plane measurements.

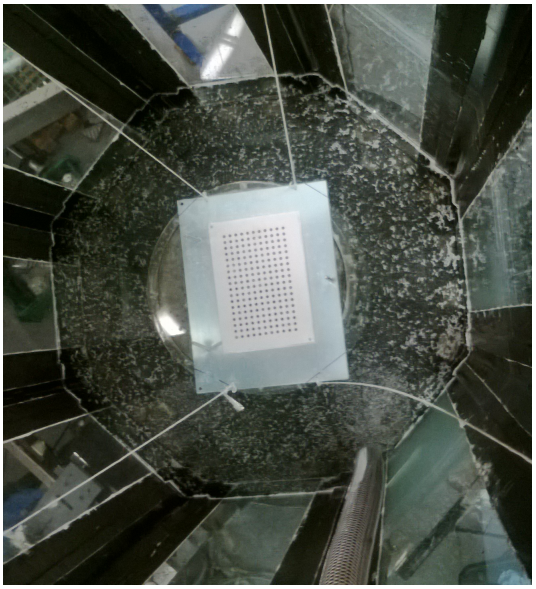

Figure 4.5: The Calibration Plate in the Horizontal Plane.

4.2.2 Vertical ($r - z$) Plane Measurements

The measurements in the vertical plane lead to calculate the velocity in $r - z$ plane, that is the axial velocity and the entrainment velocity. PIV particles in the plane were illuminated by a vertical laser sheet. A schematic diagram of the experimental set up is shown in figure 4.6. The camera was fixed perpendicular to the plane of the laser sheet. Figure 4.7 shows the plan view of the schematic diagram shown in figure 4.6. Prior to spinning the tank, the calibration images were recorded. In order to do this the calibration plate which is shown in figure 4.8, was placed at the middle of the tank and was aligned with the laser sheet which is already set at the required plane. Afterwards the calibration images were recorded.

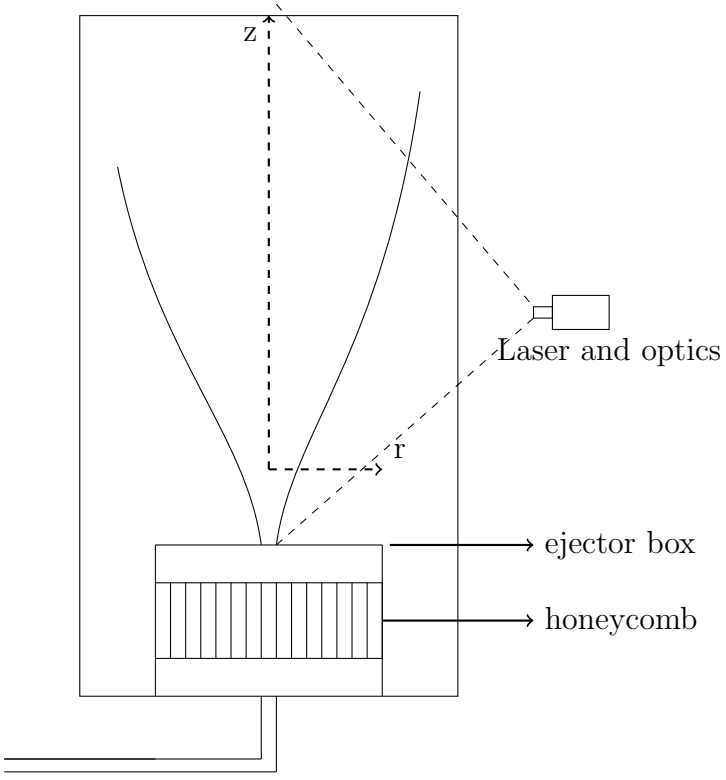

Figure 4.6: Schematic diagram of the experimental arrangement for vertical plane measurements.

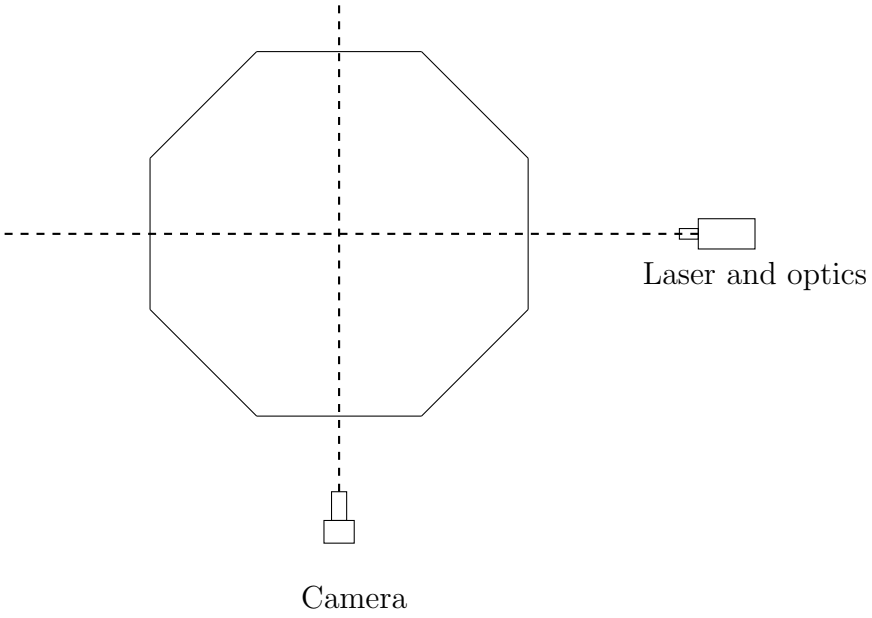

Figure 4.7: Plan view of the experimental arrangement for the vertical plane measurements.

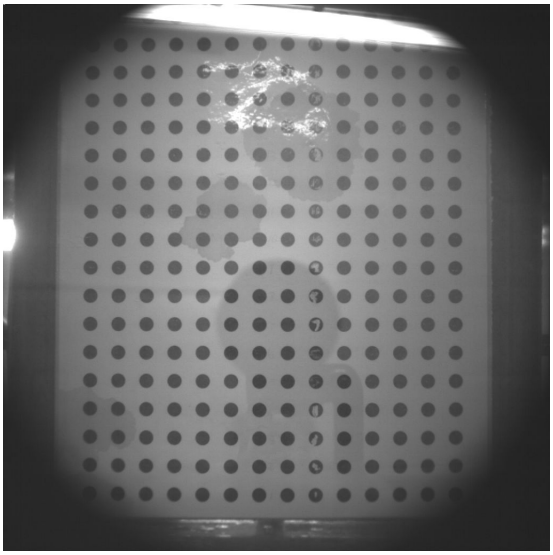

Figure 4.8: The calibration plate in the vertical plane.

4.2.3 Stability of the Turntable

Before starting any experiment that involves background rotation, a stability check for the turntable was carried out. The tank was spun around at 2rpm (0.21 rad s^{-1}), until it attains a solid body rotation. Then the PIV measurements were carried out in both the vertical plane and the horizontal plane without the jet. If the tank is spinning as a solid body, there should not be any movement of water, relative to the tank. Since the PIV system is also mounted on the tank, there should not be any velocities recorded if the turntable is perfectly stable. Figures 4.9 (a) & (b) show time average velocity vector field in both horizontal and vertical plane obtained after analysing the PIV images. The vector fields were averaged over 100 seconds. There are no significantly large velocity fields thus the stability of the turntable and the tank are guaranteed.

4.3 Analysis of PIV Images

All the PIV images were analysed using Lavision Davis 7.2 software. It is assumed that the seeding particles are homogeneously distributed, that they follow flow perfectly and uniform displacement within interrogation region. Figure 4.10 shows a typical PIV image taken during measurements in the vertical plane. Moreover in figure 4.10, the camera was focused to the area in the middle of the image (area of interest) where the particles can be seen properly and the particles near to the edges of the image are blurred. The area where, the particles are blurred does not affect the measurements because only vectors in the area of interest are considered for further calculation of the flow field. As shown in figure 4.11, PIV images were divided into interrogation areas as required (ex. 16×16 pixels or 32×32 pixels). Then image pairs were made by choosing two consecutive instantaneous images, that were taken with a time separation of Δt. Figures 4.12 (a) and (b) show such an image pair. The time separation Δt for the two images shown in figures 4.12 (a) and (b) is 0.01 s. The respective interrogation areas of the image pair are taken into consideration where the interrogation area of second image(image taken at time $t + \Delta t$) is shifted with respect to that of first and cross correlation of the

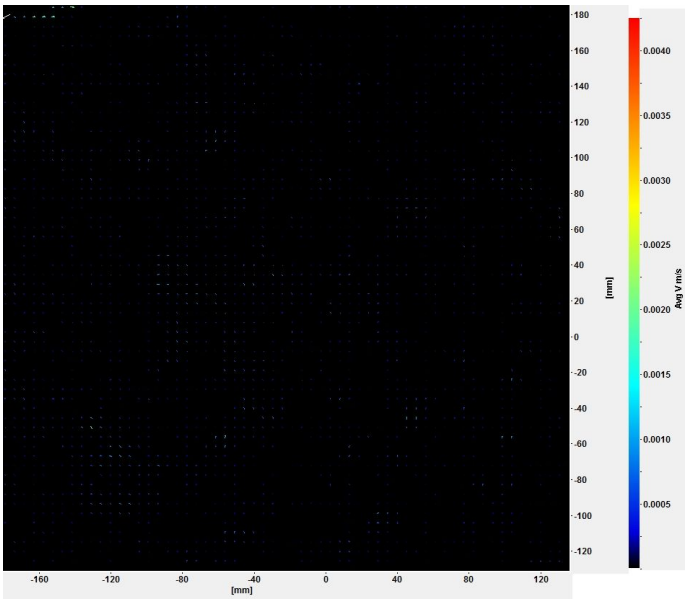

(a)

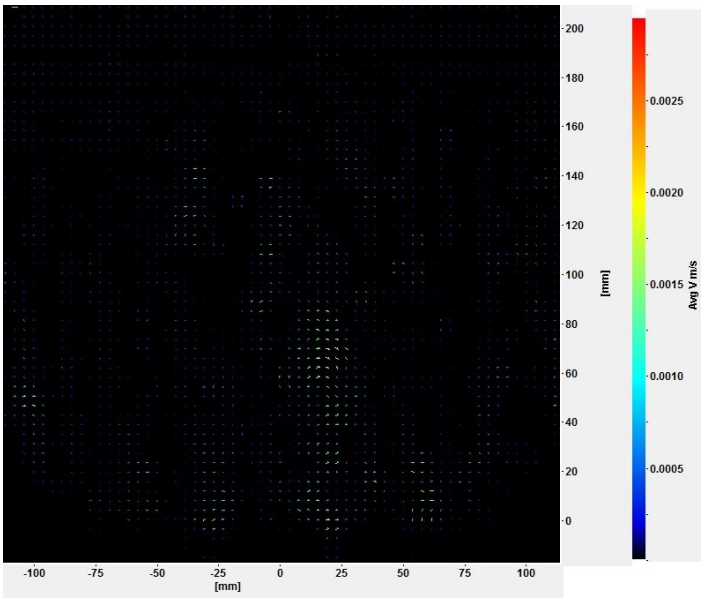

(b)

Figure 4.9: Velocity vectors (a) Horizontal plane and (b) Vertical plane.

image densities at each pixel are calculated. With the help of the calibration images velocity vector for each interrogation area is estimated. Figure 4.13 shows a typical velocity vector field calculated from a PIV image pair. For the calculation of the vector field shown in figure 4.13, the interrogation areas of 32×32 pixels with 75 % overlap were used. This configuration led to a spatial resolution 2.8 mm.

Figure 4.10: An original PIV image in the vertical plane.

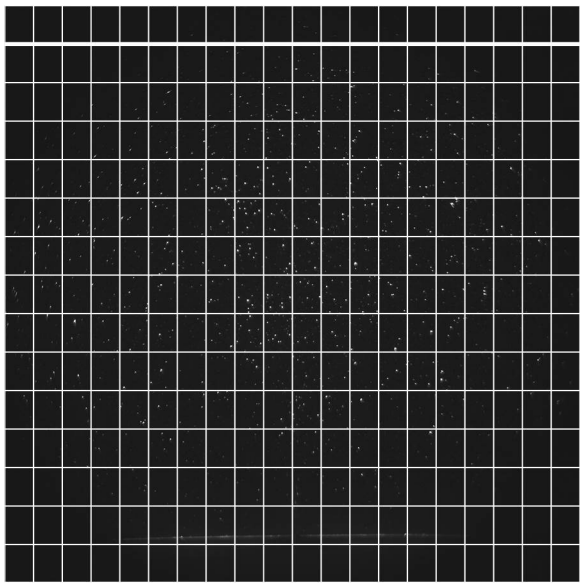

Figure 4.11: PIV image with sub divided interrogation areas.

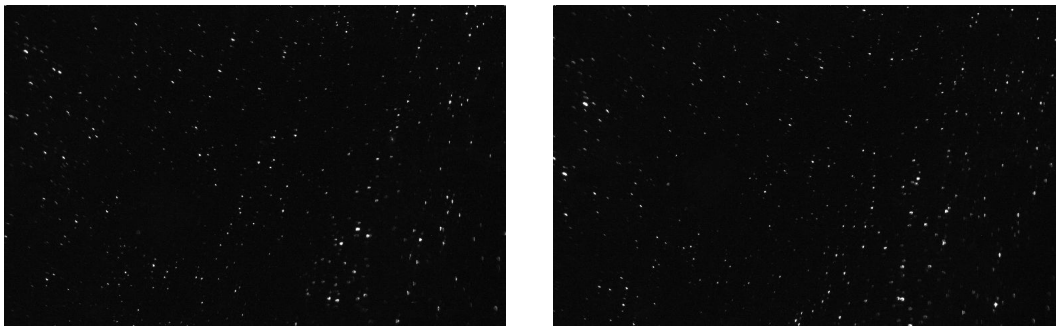

(a) (b)

Figure 4.12: Two PIV images taken at time (a) t and (b) $t + \triangle t$: $\triangle t = 0.01$ s.

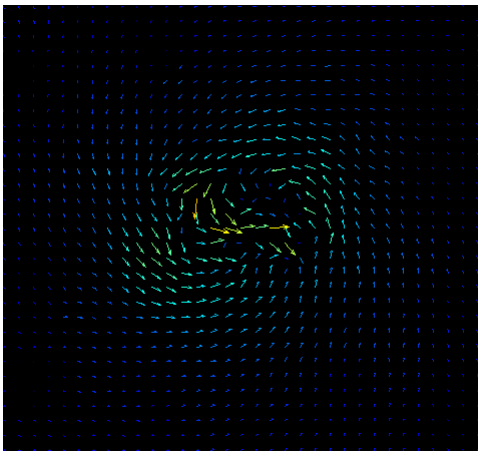

Figure 4.13: Velocity vector field obtained by analysing a PIV image pair.

4.4 Experimental Arrangement for Plumes

In the experimental arrangement for plumes, lower density fluid was ejected through the ejector box into an ambient environment of higher density fluid that was in solid body rotation . Therefore the tank was filled with salt water of percentage salinity 0.2%. This was achieved by adding salt water of predetermined concentration, to the tank. It was revealed recently by Frank *et al.* (2017), that after approximately one period of background rotation, the plumes tilted laterally and started to precess anticyclonically. Therefore only horizontal plane measurements were carried out for the plumes. The momentum flow rate was 0.5×10^{-3} m^3 for all of the plume experiments that were

conducted and the background rotation rate varied from 2 rpm (0.21 rad s^{-1}) to 10 rpm (1.05 rad s^{-1}) with 1 rpm interval. The experimental arrangement for the plume for the horizontal plane measurements were the same as that for the jets as shown in figure 4.3. The plume Richardson number at the source was 0.003.

Chapter 5

Jets without Background Rotation

The main objective of this chapter is to evaluate the reliability and accuracy of the experimental jet apparatus and the PIV measurement system. Preliminary experiments on jets ejected into non-rotating environments were conducted for the purpose of comparison of the results obtained with experimental data by other authors. At the same time it is expected to find the entrainment coefficient of moderately low Reynolds number jets. Note again that the Reynolds number was calculated based on the velocity of the jets at the source. As part of this explicit references will be made to figures from the very recent study by Ezzamel *et al.* (2015). However, results corresponding to those to be discussed are also contained in other earlier studies by, for instance, Hussein *et al.* (1994), Shabbir & George (1994) or Wang & Law (2002).

Ezzamel *et al.* (2015) presented experimental measurements conducted on freely propagating, turbulent, steady buoyant air plumes. Thus, in contrast to the present study the density within their thermal air plumes was different than the density of the ambient air. However, they conducted experiments for conditions ranging from momentum-flux dominated, jet-like releases to pure plume releases characterized by a balance between momentum, volume and buoyancy fluxes at the source. They focus on the discussion of three different sets of conditions referred to as cases J, F and P in their paper. Of these three cases the conditions of case J are for jet-like flow conditions for which

buoyancy effects are small. Consequently it is required that the nature and the quality of the experimental data obtained here must mirror those for case J of Ezzamel *et al.* (2015). Table 5.1 shows the previous studies on jets and findings for range of Reynolds number flows.

Authors	Method of measurements	Re	α
Forstall and Gaylord (1955)	HW	-	0.070
Rosensweig *et al.*(1961)	HW	26200	0.076
Papanicolaou and List (1988)	LDA	2460-10900	0.074
Panchapakesan and Lumley (1993)	HW	11000	0.095
Wang and Law (2002)	LDA	12700	0.075
Ezzamel *et al.* (2015)	PIV	7700	0.045

Table 5.1: Previous Studies on Jets and measured values on entrainment coefficient α, HW : hot wire anemometry, LDA : laser-droppler anemometry, PIV: Particle image velocimetry.

5.1 Longitudinal Velocity Profiles

Figures 5.1 (a), (b), (c) & (d) show vectors of vertical velocity component ($w(z)$) of jets with Re = 1800, Re = 2000,Re = 3000 & Re = 3500 respectively. For each Re number seven data sets at selected non dimensional heights z/d above the source, were plotted. They clearly show the radial dependence of the longitudinal velocity in each sub figure. Moreover they also show the Gaussian profile type behaviour of vertical velocity along the non dimensional radial direction (r/d). In figure 5.1 (b), velocity profiles within the heights $15 \leqslant z/d \leqslant 25$ are not perfectly symmetric around $r/d = 0$. This may be due to a disturbance occurred during the measurements.

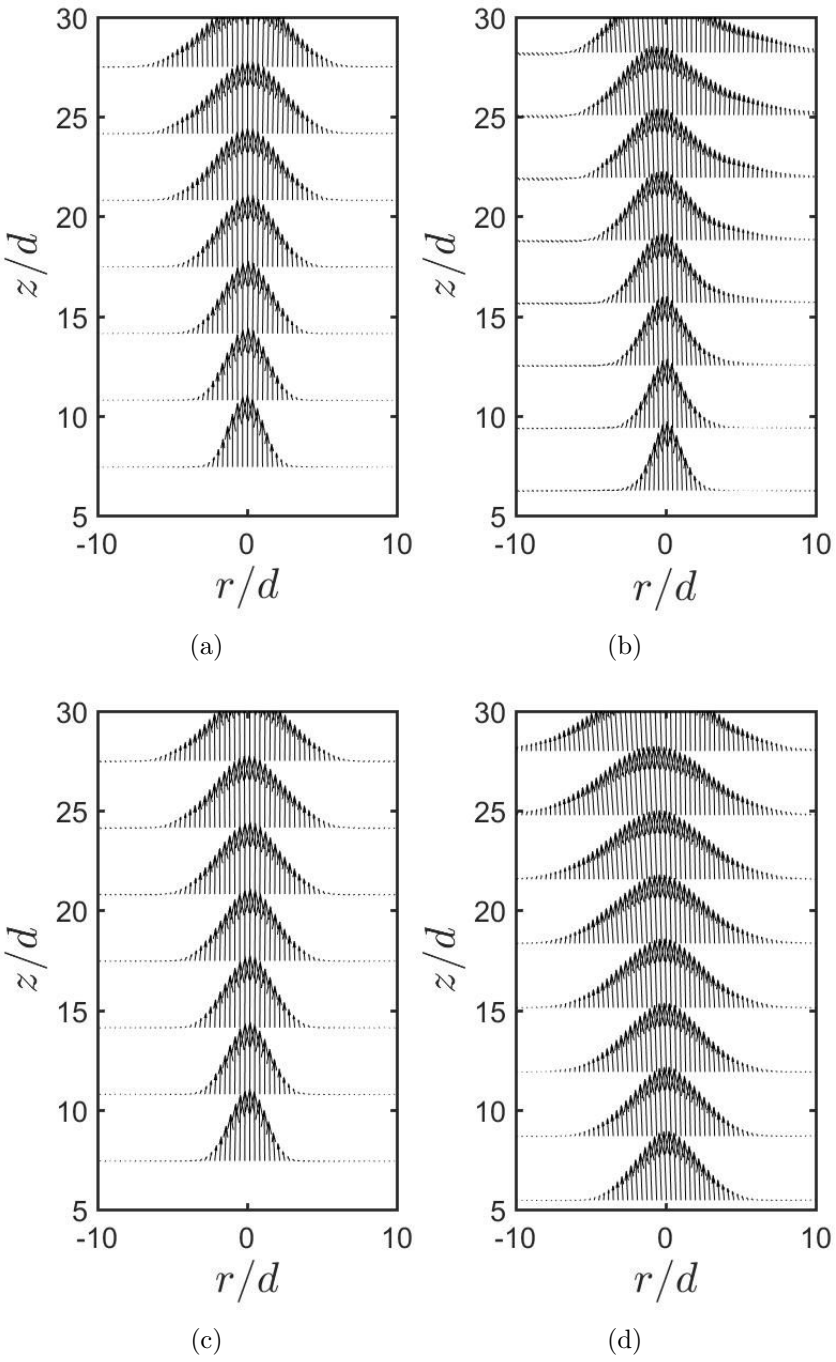

Figure 5.1: Velocity vectors of the jets with velocity profiles for $5 \leq z/d \leq 25$, for different Reynolds numbers: (a) 1800, (b) 2000, (c) 3000, (d) 3500 (the negative values of r/d indicates the change of direction).

5.1.1 Radial Velocity Profiles

In figures 5.1 (a), (b), (c) and (d), it can be clearly seen that, $w(z) \to 0$ when $r/d \to \infty$, for all the radial profiles of the vertical velocity component. Therefore a clear edge for the jet in the radial direction can not be identified. Hence to find the width of the jet at each height, a Gaussian profile of the form given in equation (3.14), centred on the middle of the jet ($r/d = 0$) was fitted for each radial profile. Radial profiles were obtained within the interval $5 \leq z/d \leq 25$ with a resolution $\Delta(z/d) = 2.8\text{mm}/6\text{mm}$, such that forty two profiles were available in total. For some z/d values it was found that the maximum velocity of the radial profile of vertical velocity was measured somewhat off-centre, that is not at $r = 0$. This was due to camera positioning and calibration plate uncertainties. Following Ezzamel *et al.* (2015), the maximum value of w was recorded and the coordinate system was translated to center the maximum velocity on the axis to achieve $w_m(z) = w(0, z)$. The purpose of this centring procedure was to avoid inaccuracies in the determination of the jet radius. After fitting Gaussian curves we obtained the velocity scale w_m and length scale b and non-dimensionalised radial profiles of the vertical velocity. Figure 5.2 (a), (b), (c) and (d) summarizes the forty two data interpolations in terms of $w(r)/w_m(z)$ as a function of r/b. Figure 5.2 clearly demonstrates that all profiles collapse onto a single curve for all four Re numbers and it reveals, therewith, the self-similarity of the profiles corresponding to the data for case J in figure 3(a) of Ezzamel *et al.* (2015). Note that the collapse of the velocity profiles for the present data in figure 5.1 are even slightly better than for the data in figure 3(a) of Ezzamel *et al.* (2015). The reason for this is probably due to the fact that their measurements for flow in air were most likely subject to larger disturbances caused by residual background motion in the ambient air environment.

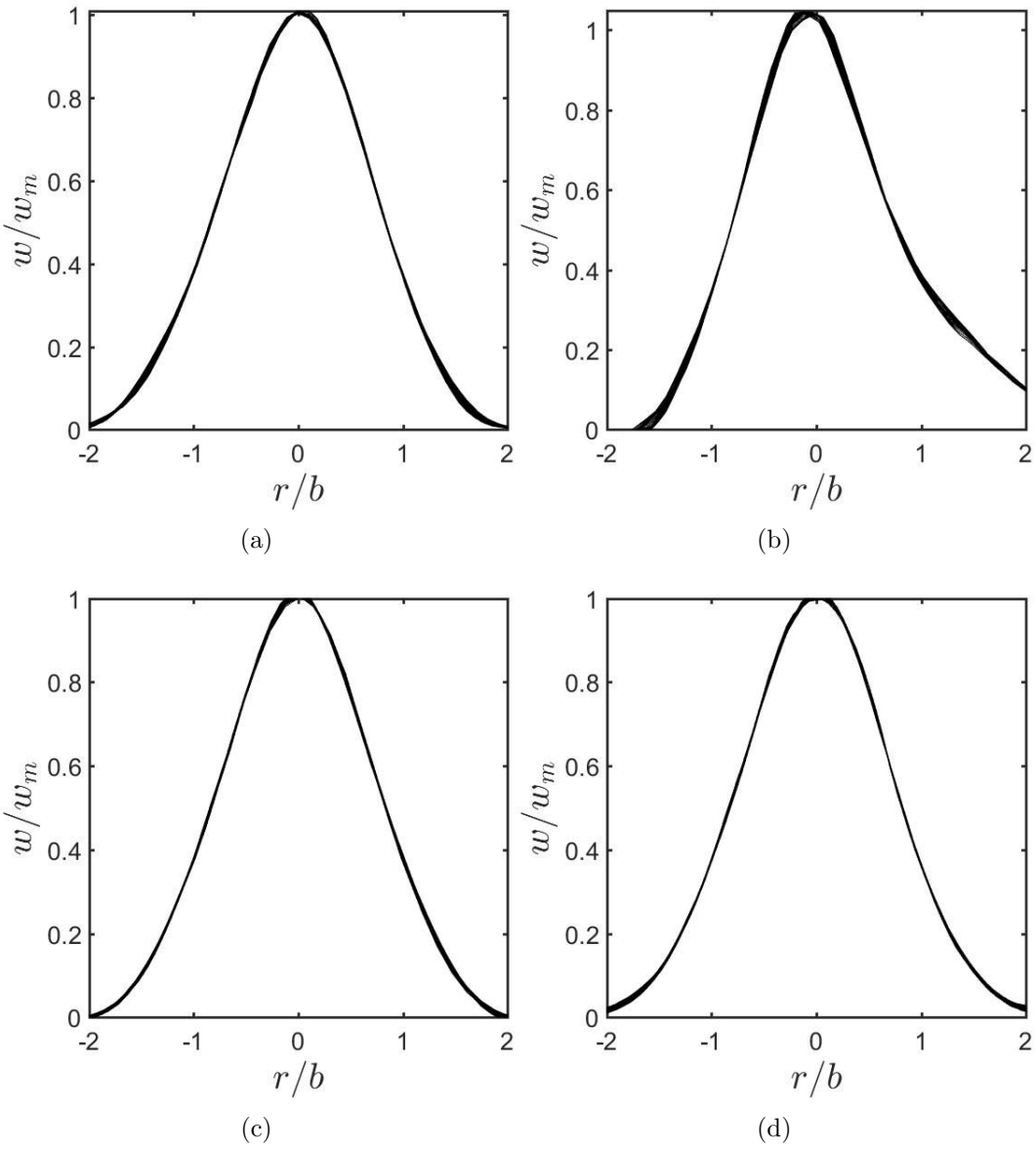

Figure 5.2: Non-dimensionalised radial velocity profiles of longitudinal velocity for $5 \leq z/d \leq 25$, for different Reynolds numbers: (a) 1800, (b) 2000, (c) 3000, (d) 3500 (the negative values of r/b indicates the change of direction.).

5.1.2 Turbulent Intensities

Figures 5.3 (a), (b), (c) and (d) show the non-dimensionalised radial profiles of the root mean square values of the vertical velocity (I_w) for four Reynolds numbers given in the figure caption. Moreover figures 5.4 (a), (b), (c) and (d)

show the non-dimensionalised radial profiles of the root mean square values of radial velocity (I_u) for the same four Reynolds numbers as in figure 5.3. When these two figures (5.3 and 5.4) are carefully inspected, one notices that the radial profiles of the r.m.s values of the radial velocity and that of the vertical velocity are qualitatively different. The radial profiles of I_u, in figure 5.3, have their peaks at the jet centre line. They show a Gaussian type behaviour where they decay monotonically from their peak values as the non-dimensionalised radius increases. But the radial profiles of I_w, in figure 5.3, have their peaks off the centreline of the jet. Since all radial profiles of I_w qualitatively collapse on to a single curve, local peaks are at the same non-dimensionalised radial location for each curve. These two non-dimensionalised radial locations are the points where maximum shear occurs within the jet and turbulence production is maximum. Since there is not much shear in the radial direction one can not see this type of local peaks in the radial profiles of I_u. The corresponding graphs for the turbulent intensities are shown in figure 9 (a) and (b) of Ezzamel *et al.* (2015). Figures 5.3 and 5.4 reveals a very good collapse of the current data for I_u and I_w collected in water. In fact, the comparison of the present data to those in Ezzamel *et al.* (2015), for plumes in air, reveals that the data collapse is indeed substantially better for our water-based system. Table 5.2 moreover displays additional comparisons of the peak values of I_w and I_u, from figures 5.3 and 5.4, with corresponding values obtained in other studies.

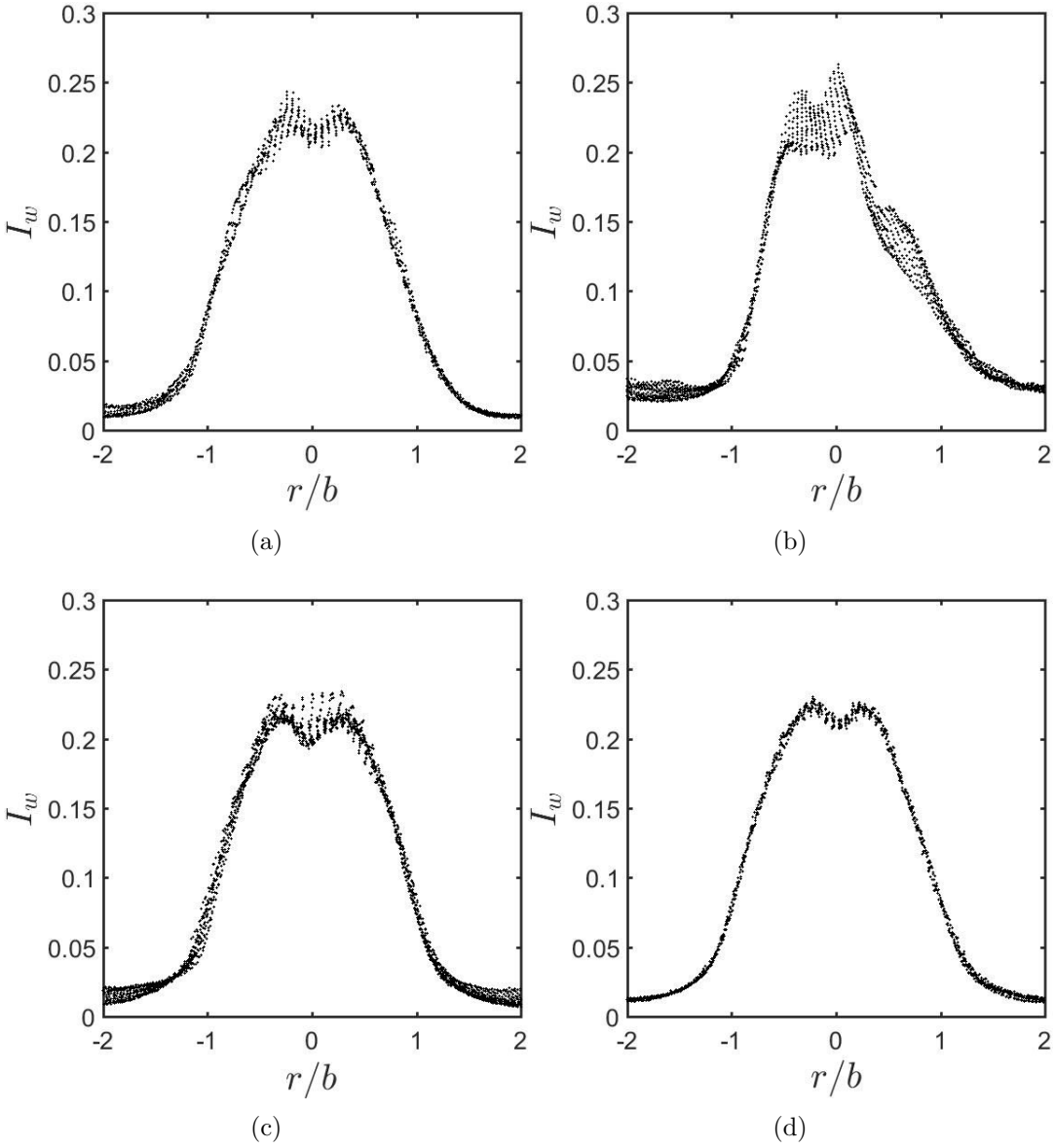

Figure 5.3: Non-dimensionalised radial profiles of vertical turbulent intensity (I_w) for $5 \leq z/d \leq 25$, for different Reynolds numbers: (a) 1800, (b) 2000, (c) 3000, (d) 3500 (the negative values of r/b indicates the change of direction).

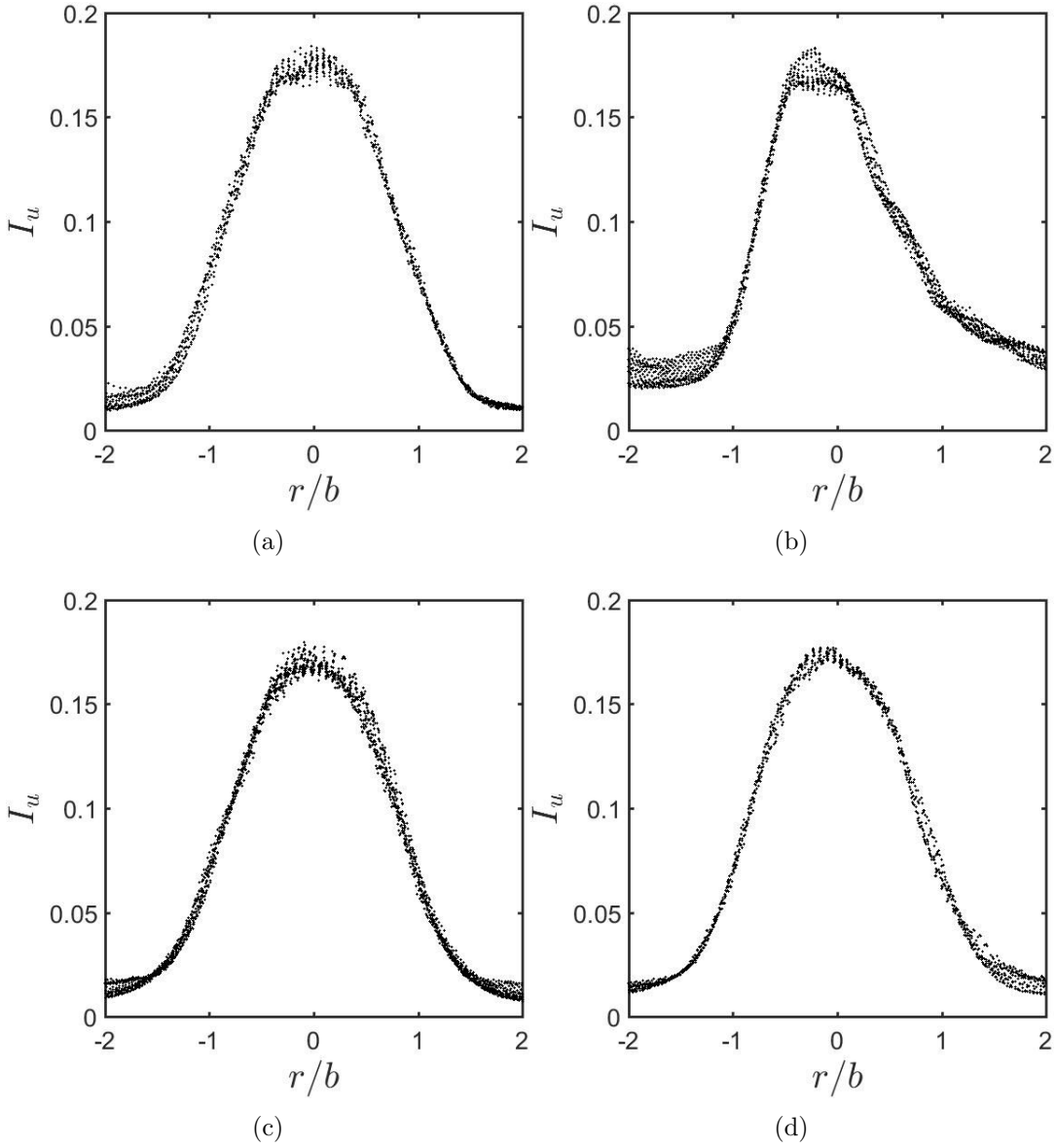

Figure 5.4: Non-dimensionalised radial profiles of radial turbulent intensity (I_u) for $5 \leq z/d \leq 25$, for different Reynolds numbers: (a) 1800, (b) 2000, (c) 3000, (d) 3500 (the negative values of r/b indicates the change of direction).

5.1.3 Reynolds Stress

Figures 5.5 (a)-(d) show the radial profiles of non-dimensionalised Reynolds stress $\overline{u'w'}$ for the four different Reynolds numbers. The respective Reynolds

Authors	peak value of I_w	peak value of I_u
Hussein *et al.* (1994)	0.27	0.22
Shabbir and George (1994)	0.32	0.19
Wang and Law (2002)	0.3	0.2
Ezzamel *et al.* (2015)	0.25	0.2
Present study	0.25 ~ 0.3	0.18

Table 5.2: Comparison of peak values for I_w and I_u for the data of the present study with corresponding data of other authors.

number is given in the caption of figure 5.5. These figures correspond to figure 10 (a) and (b) of Ezzamel *et al.* (2015). The present data for flow in water do, again, show a significantly better data collapse then the data for the air plumes of Ezzamel *et al.* (2015).

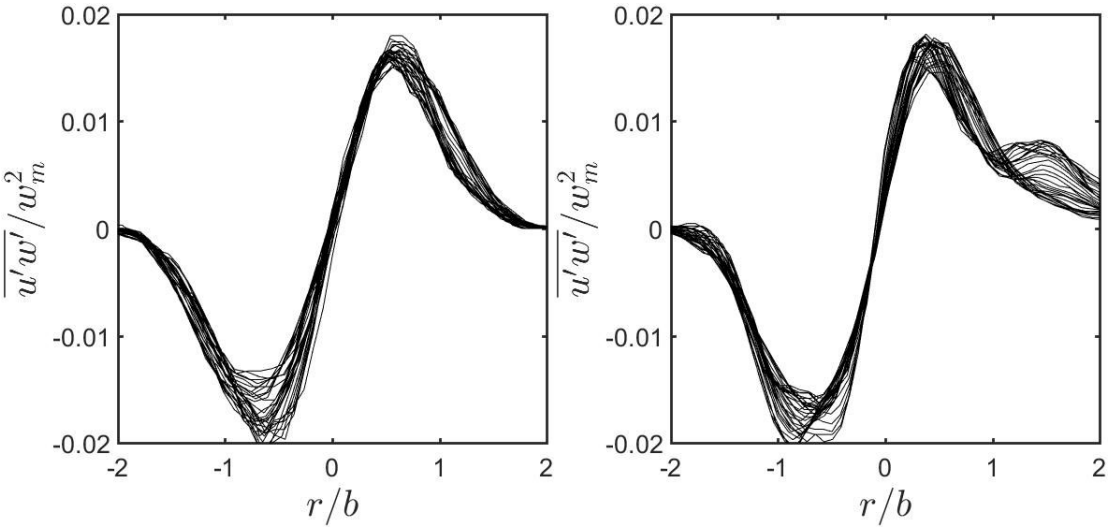

(a) (b)

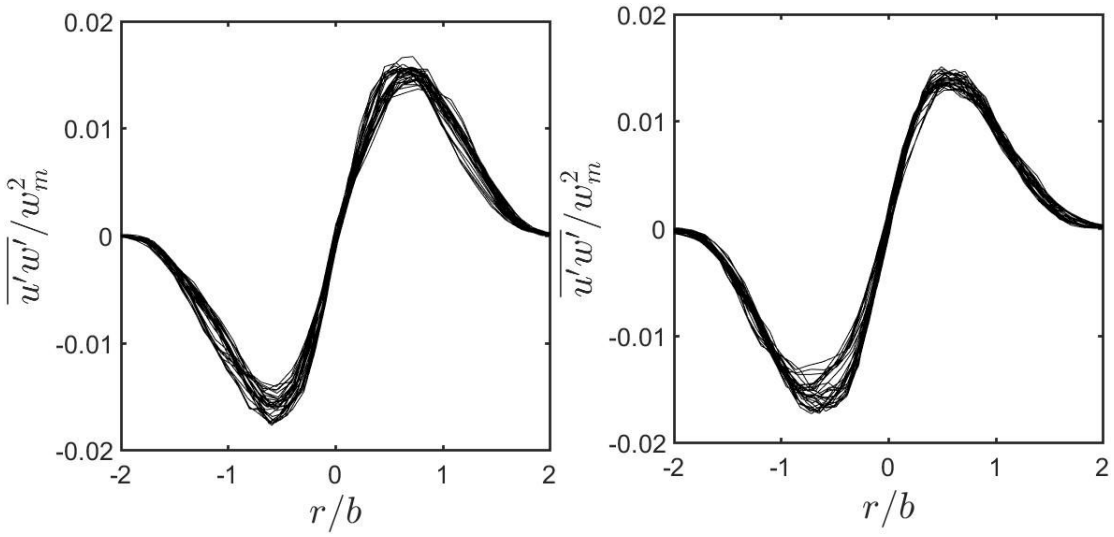

(c) (d)

Figure 5.5: Non-dimensionalised radial profiles of the Reynolds stress for $5 \leq z/d \leq 25$, for different Reynolds numbers: (a) 1800, (b) 2000, (c) 3000, (d) 3500 (the negative values of r/b indicates the change of direction).

5.1.4 Turbulent Viscosity

Figure 5.6 shows non-dimensionalised radial profiles of turbulent kinematic viscosity $\widehat{\nu_T}$ for four Reynolds numbers where $\widehat{\nu_T} = \nu_T/(w_m b)$. It can be seen that the value of $\widehat{\nu_T}$ has increased when Re number of the flow increased.

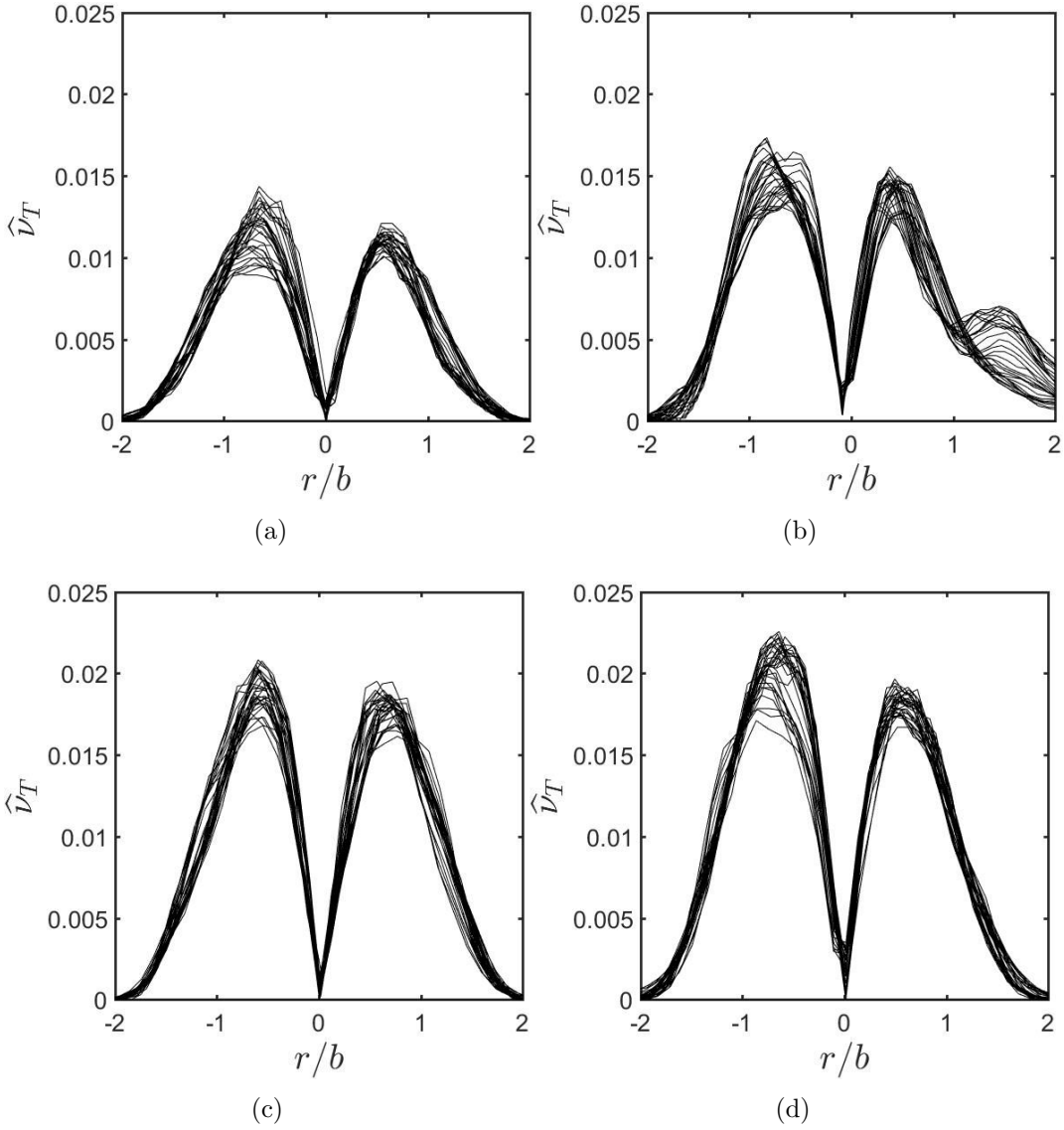

Figure 5.6: Non-dimensionalised radial profiles of turbulent kinematic viscosity for different Reynolds numbers: (a) 1800, (b) 2000, (c) 3000, (d) 3500 (the negative values of r/b indicates the change of direction).

5.1.5 Volume Flow

The volume flow at each non-dimensional height z/d was calculated using equation 3.7. Since the PIV measurements were taken only in one plane, we assume that the jet is axisymmetric. Figure 5.7 displays the variation of the non-dimensional vertical volume flux, $Q(z)/Q_0$, as a function of the

non-dimensional height, z/d, above the source. The data were interpolated by a linear least-squares interpolation as $Q(z)/Q_0 = kz/d + 1$ and the linear least-squares fit for each Reynolds number is also shown in figures 5.7 (a)-(d).

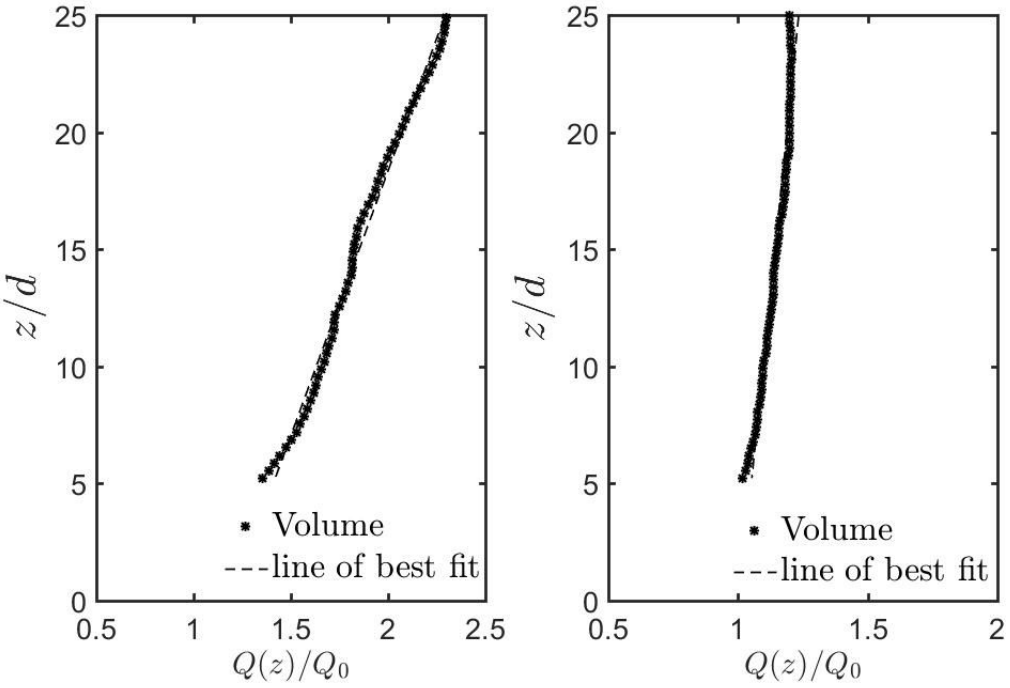

(a) (b)

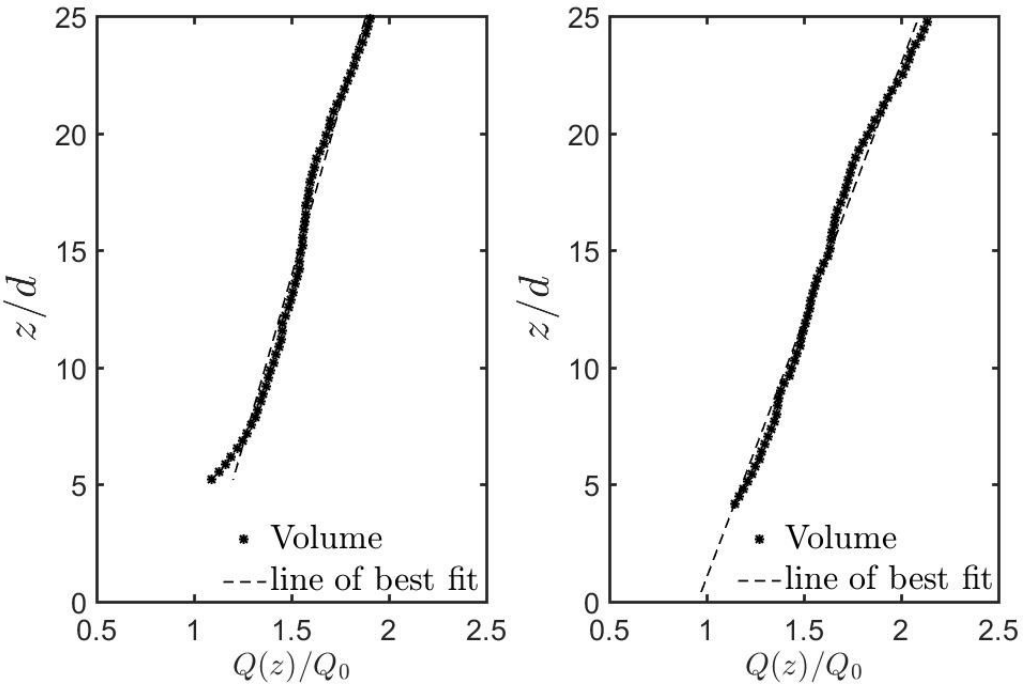

Figure 5.7: Variation of non-dimensionalised vertical, volumetric flow rate for different Reynolds numbers: (a) 1800, (b) 2000, (c) 3000, (d) 3500.

5.1.6 Entrainment Coefficient

The volume flux calculated in section 5.0.6 is related to the maximum upward velocity, w_m, measured on the central axis, and to the entrainment velocity $u_e = \alpha w_m$ through

$$dQ = 2\pi b u_e dz = 2\pi b \alpha w_m dz \ . \tag{5.1}$$

Therefore, the entrainment coefficient α is obtained, after finding the gradient $dQ(z)/dz$, from

$$\alpha = \frac{1}{2\pi b w_m} \frac{dQ}{dz}. \tag{5.2}$$

The gradient $d(Q(z)/Q_0)/d(z/d) = k$ implies that $dQ/dz = kQ_0/d$ in (5.2). Using the measured values $w_m(z)$ and the calculated values of respective b, one can now determine data for $\alpha(z)$ from (5.2). The results obtained are

displayed in figure 5.8(b) against the non-dimensional height above the source. Averaging the data in Figure 5.8 over the height yields a mean value α = 0.033 ± 0.001 , $\alpha = 0.025 \pm 0.001$, $\alpha = 0.033 \pm 0.001$, $\alpha = 0.041 \pm 0.001$ for the jets with $Re_0 = 1,800$, $Re_0 = 2000$, $Re_0 = 3000$ and $Re_0 = 3,500$ respectively. This mean value is compared to entrainment coefficients obtained by other authors in table 5.1. As the table shows, the entrainment coefficients that are available, correspond to comparatively higher Reynolds numbers than that of the jets considered in the present study. Therefore direct one-to-one comparisons of the entrainment coefficients are not possible. Nevertheless, in particular, the present value of $\alpha = 0.041$, for the jet with $Re_0 = 3,500$, for flow in water, is very close to the value $\alpha = 0.045$ which Ezzamel *et al.* (2015) obtained, at similar Reynolds number, for flow in air. On the other hand turbulent mixing enhances the entrainment and hence the entrainment coefficient can be higher for jets at high Reynolds number. Therefore in the present study we get comparatively lower entrainment coefficient values for the jets with comparatively lower Reynolds number.

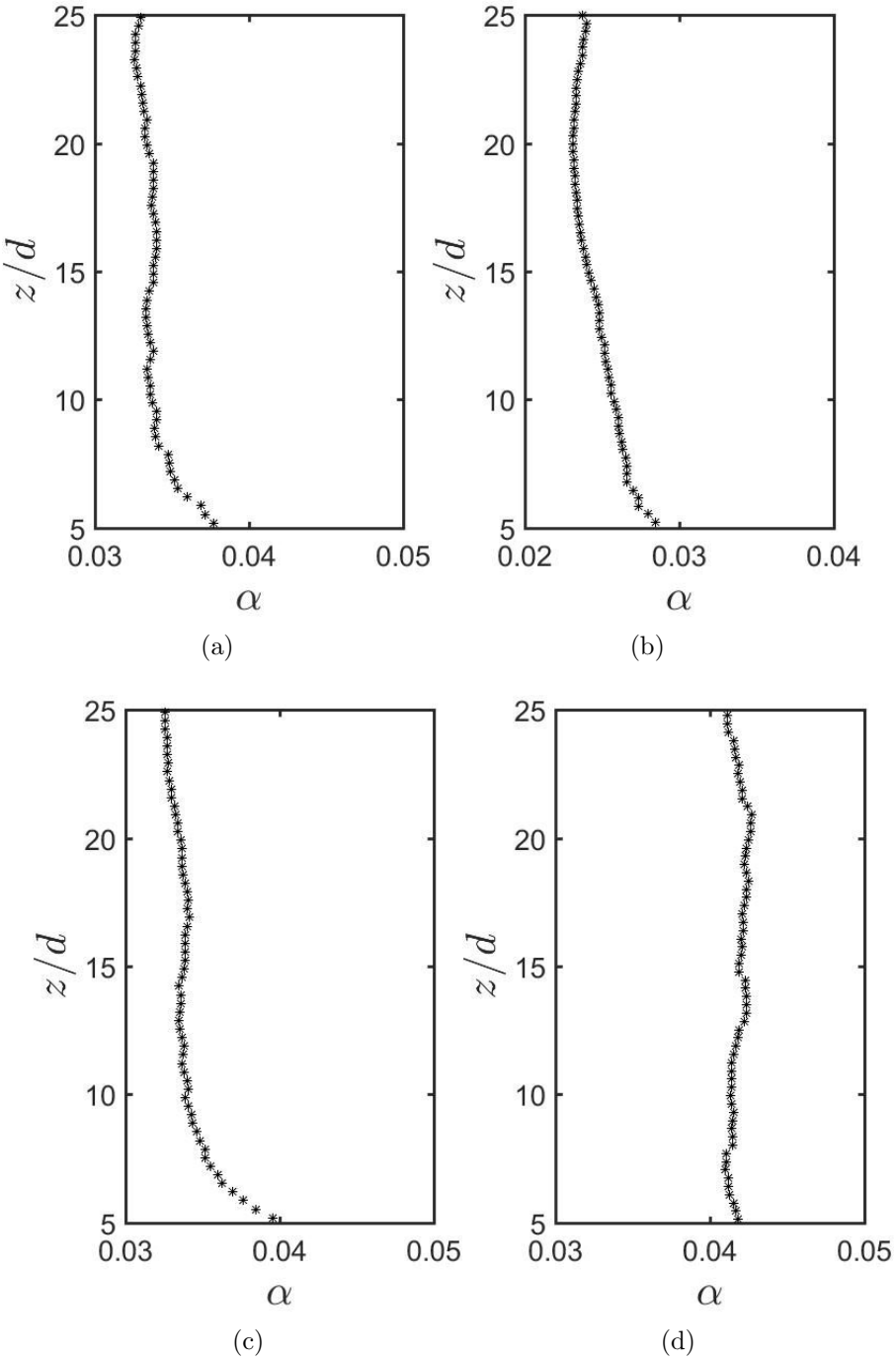

Figure 5.8: Variation of the entrainment coefficient with vertical height for different Reynolds numbers: (a) 1800, (b) 2000, (c) 3000, (d) 3500.

Chapter 6

Jets in the Presence of Background Rotation

In the present chapter, the behaviour of jets subject to different background rotation rates is discussed. Qualitative observations from dye-visualization (food colouring and Fluorescein) experiments and quantitative PIV measurements are reported.

6.1 Qualitative Observations

Figures 6.1 (a) - (k) display a series of dye visualisations which qualitatively illustrate some of the effects of background rotation on the jet development as revealed by the visual inspection of video recordings. Figures 6.1 (a) - (k) show images of the jets generated for a Reynolds number of Re_0 = 2300, but subject to different levels of background rotation. Figure 6.1 (a) shows the jet in the absence of background rotation while figures 6.1 (b) - (k) are for successively increasing background rotation rates as identified in the figure caption. Each image shows the jet, five seconds after the ejection of liquid at the source had commenced. The series of images in figure 6.1 illustrates that an increasing level of background rotation has a pronounced effect on the jet development and it changes the overall outline structure of the dyed jet region. The behaviour displayed here in figure 6.1 (a) - (k) corresponds to the change of the jet outline as illustrated in the hand-drawn sketches in Figure (16) in Wilkins *et al.* (1969) and the photos shown are similar to those

in Figure (2) of Niino (1978), Figure (3) in Wilkins *et al.* (1969) and Figure (2) of Etling & Fernando (1993). The conical jet structure which is observed in the absence of rotation changes into a more columnar structure for increasing levels of background rotation.

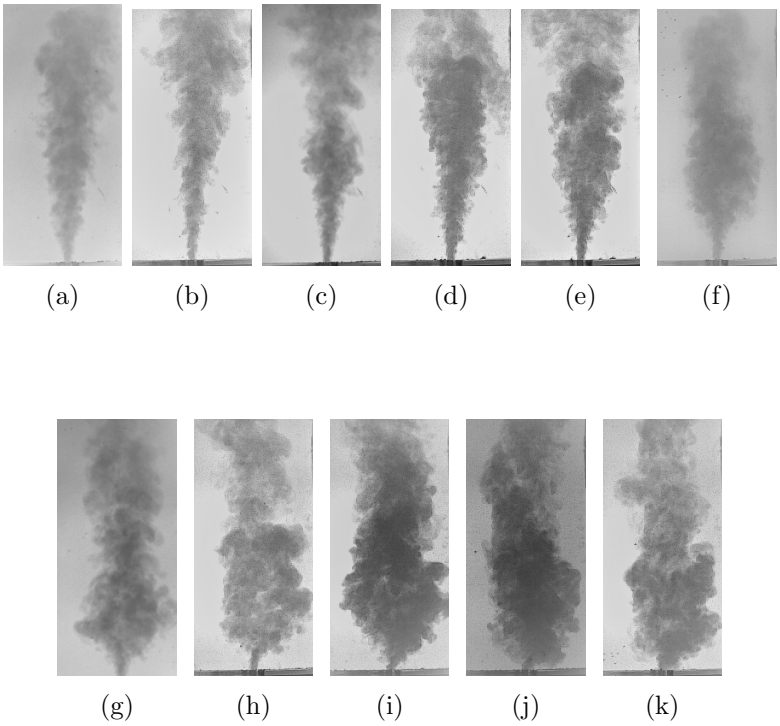

Figure 6.1: Dye visualisation of jets for different background rotations. Each photo shows the jet at an instant of five seconds after liquid ejection from the nozzle had commenced. The rotation rates, in units of rad s^{-1}, associated with the photos are: (a) 0, (b) 0.1, (c) 0.2, (d) 0.31, (e) 0.41, (f) 0.52, (g) 0.63, (h) 0.73, (i) 0.83, (j) 0.94, (k) 1.05.

Due to the complexity of the developing flow field, it is very difficult to describe further qualitative observations from dye visualisations. But close-up views of the stem region, such as that shown in figure 6.2, revealed that the stem region develops into two, sometimes sporadically three, separate strands. Induced by Coriolis forces these strands spiral helically upwards, in a cyclonic sense relative to the background rotation, before breaking down into a turbulent flow field. At breakdown, or shortly thereafter, the cyclonic spiralling motion appeared to very briefly switch into an anti-cyclonic rotation before the cyclonic sense

of swirl was readopted. Note that Fluorescein was used to do the visualisation of the stem region that is shown in figure 6.2. Further, figures 6.3 (a) - (h) show, instantaneous cross sectional view of the jet, taken closer to the source over a time period from 6 s to 34 s, after ejection of liquid had commenced. These photos were also taken by using Fluorescein as the visualising agent. The time interval in between these sub figures is 4 s. In figures 6.3 (a) - (d) the cross sectional structure of the jet consists of two strands, whereas in figures 6.3 (e) - (f) it consists of three strands. Even though the number of strands in figure 6.3 (g) is not clear, in figure 6.3 (h), again three strands can clearly be seen. The photos shown in the figure were taken by focusing the camera directly on the source from the top of tank, through the water. The water height above the source was approximately 1.5 m. Unlike PIV particles, the water mixed with Fluorescein does not emitting enough light. Therefore capturing clear images was difficult and improving the quality of the images was also not possible.

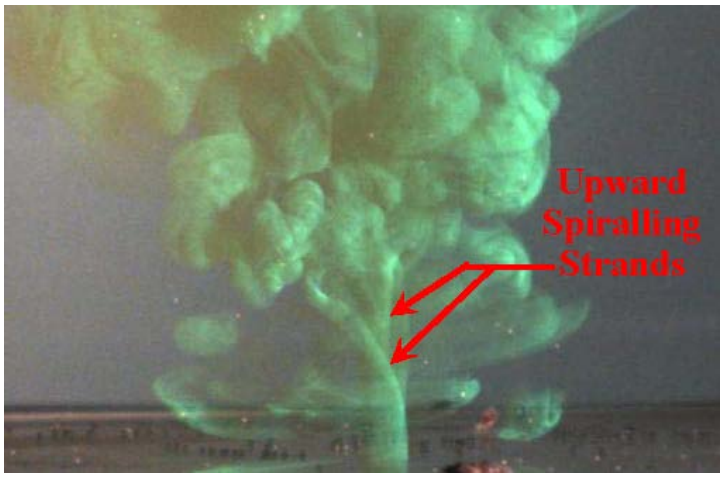

Figure 6.2: Fluorescein visualisation of the stem of a jet revealing the two cyclonically upwards spiralling helical strands for Re_0 = 2300 at Ω = 0.21 rad s^{-1}.

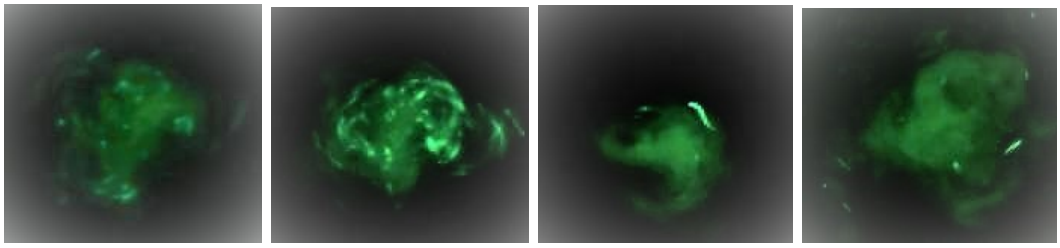

(a) (b) (c) (d)

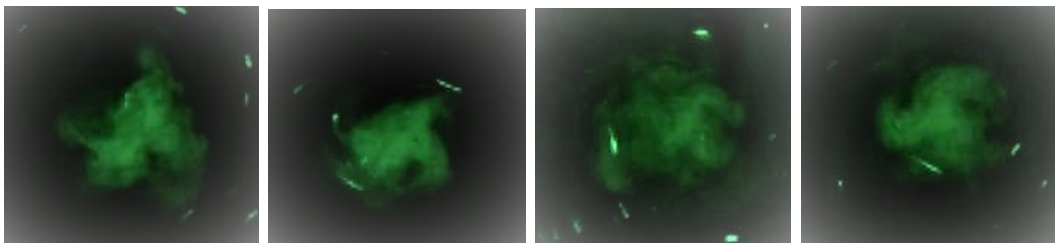

(e) (f) (g) (h)

Figure 6.3: Fluorescein visualisation of the cross section of the stem of a jet with Re_0 = 2300 at Ω = 0.21 rad s^{-1} at times t for (a) 6 s, (b) 10 s, (c) 14 s, (d) 18 s, (e) 22 s, (f) 26 s, (g) 30 s, (h) 34 s.

6.2 Vertical Velocities

Figures 6.4 (a) - (p) illustrate the development of the vertical velocity component, $w(r)$, at different heights, z/d, above the source, over a time interval of 68 s. Inspection reveals that the velocity profiles for the first 18 s, in figures 6.4 (a) - (d), are qualitatively similar to those for a jet in a non-rotating environment shown in figure 5.1 (a). However, after around 22 s to 26 s, in figures 6.4 (e) - (f), the flow velocity begins to reverse at radial positions $x/d \geqslant 5$ for heights around $30 \leqslant z/d \leqslant 40$. The vertical position where onset of the flow reversal is observed, then shifts downwards in the direction towards the source.

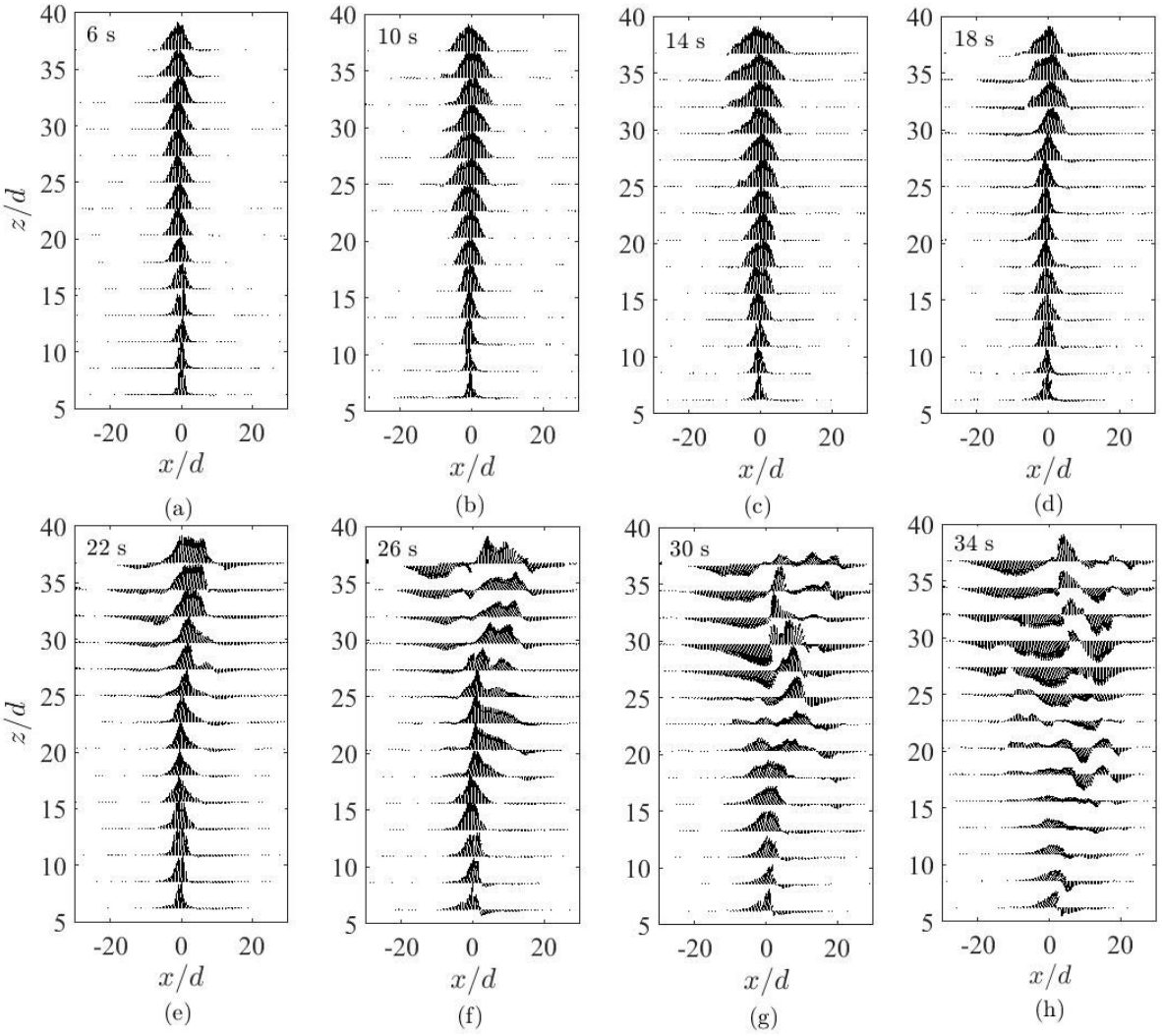

Figure 6.4: Instantaneous vector fields of the vertical velocity component, $w(r)$ for a jet with $Re_0 = 2300$ at $\Omega = 0.21$ rad s^{-1} at times.

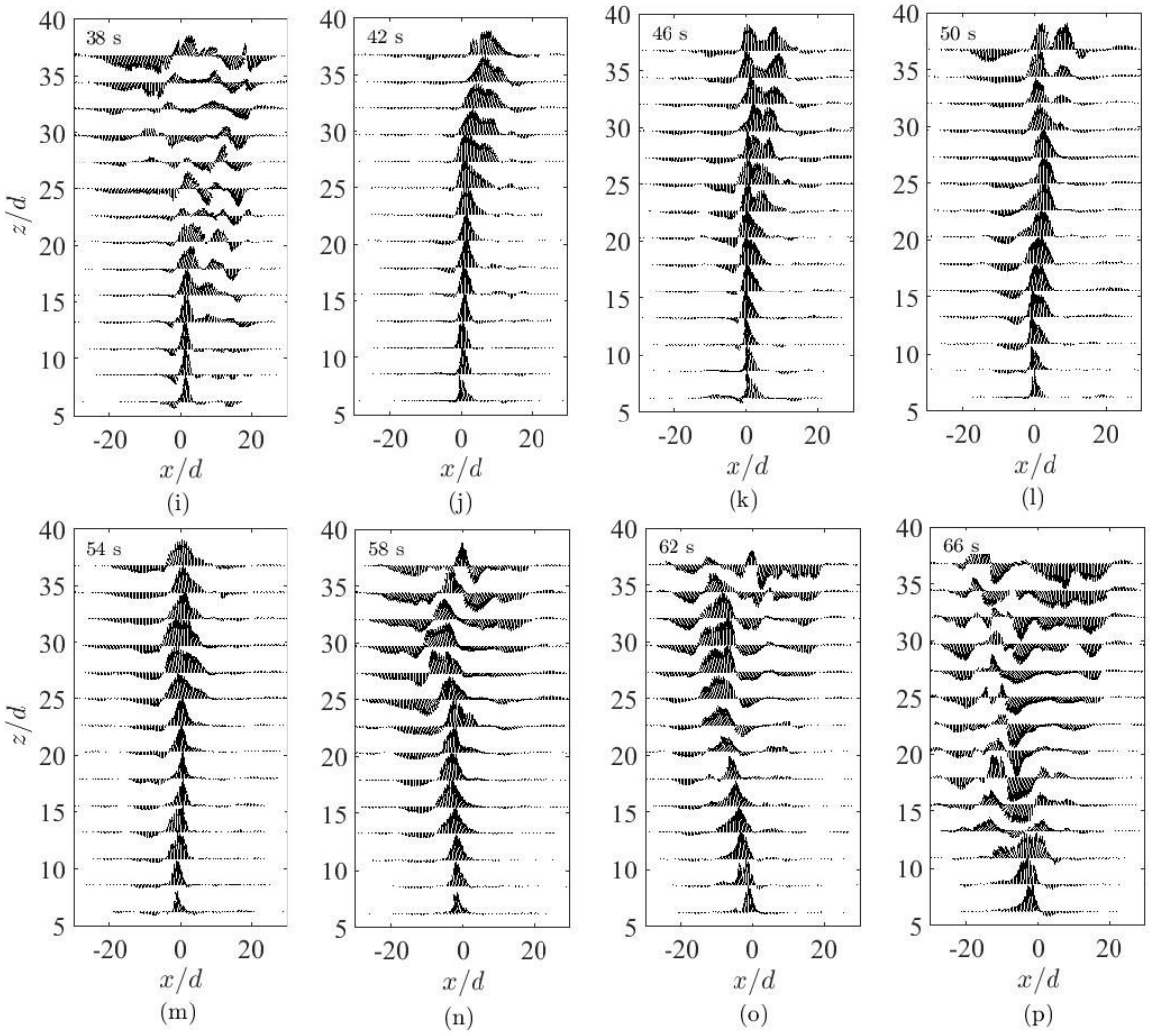

Figure 6.4: Continued.

For times between about 30 s to 38 s, in figures 6.4 (g) - (i), the initial Gaussian-like velocity profiles that were originally present in figures 6.4 (a)-(d) have broken down entirely and there are various regions of x/d across the diameter of the jet where the flow velocity has reversed and downward flow exists. Nevertheless, in the period between about 42 s and 54 s, in figures 6.4 (j) - (m), the jet recovers from its breakdown. After about 54 s, in figure 6.4 (m), the profiles at all heights have resumed the Gaussian-like shapes that were initially present at the start of the cycle in figures 6.4 (a) - (d). Thereafter, between about 58 s and 68 s, in figures 6.4 (n) - (p), a new breakdown cycle of the velocity profiles begins that mirrors the behaviour in figures 6.4 (e) - (i). The

breakdown-reformation cycle of the jet was observed for all tested Reynolds numbers $1600 \leq Re_0 \leq 16000$ and non-vanishing rotational speeds and, in each case, it continued to repeated itself periodically throughout the entire runs of the experiments until liquid ejection from the source was terminated. In the dye visualisations the downward propagating flow reversal of figures 6.4 revealed itself as accompanied by variations of the length, of the stem indicated in figure 6.1.

Figures 6.5 (a) - (p) show again development of the vertical velocity component for a jet with background rotation of 0.83 rad s^{-1}. Each sub plot in figure 6.5 shows instantaneous velocity vectors of the vertical velocity component over a time period of 15 s. The time interval in between these sub figures is 1 s. The jet shown in the figure subject to much higher background rotation rate than that of the jet shown in figure 6.4. Therefore a shorter time interval (1 s) in between sub plots compared to that of figure 6.4 was accommodated. Figure 6.5 (a) shows instantaneous velocity vectors of the vertical velocity of the jet at the instant 0.5 s after ejection of liquid from the source had commenced. At this instant the jet has propagated vertically upwards to a height of approximately $z/d = 25$ and the radial profiles of the vertical velocity are again qualitatively similar to those shown in figure 5.1 for the jets in a non rotating environment. As the jet propagates in the axial direction as shown in figure 6.5 (b), the flow velocity begins to reverse approximately at radial positions $\pm x/d \geqslant 3$ for heights around $5 \leqslant z/d \leqslant 15$. Approximately for heights $z/d \geqslant 15$, the jet propagates further in the stream-wise direction. After 2.5 s, in figure 6.5 (c), downward flow appears at radial positions $\pm x/d \geqslant 3$, for heights $5 \leqslant z/d \leqslant 30$. Moreover at times 3.5 s and 4.5 s, in figures 6.5 (d) - (e), the velocity vectors correspond to downward flow or reverse flow of the jet appears at the two edges of the jet for heights around $5 \leqslant z/d \leqslant 40$. If figures 6.5 (f) - (g), are carefully observed one can see that below $z/d = 15$, almost all the velocity vectors show downward flow. But above $z/d = 15$ the jet flow still continues in the streamwise, vertical direction. It can be suspected that this may be due to a slight precession of the jet. i.e. the part of the jet which propagates upwards, below $z/d = 15$, may have moved out of the laser plane when experiments were conducted. Therefore the vertical vectors corresponds to upward motion can

not be seen in the figures. As time passes, the downward flow dominates in the measurement plane until 11.5 s (refer figures 6.5 (h) - (l)). Then again at times 12.5 s, 13.5 s and 14.5 s, in figures 6.5 (m) - (o), streamwise or upward flow appears at radial locations slightly away from the temporal centreline of the jet. Note that due to highly turbulent nature of the jet, a proper centreline can not be defined. Moreover, in figures 6.5 (m) - (o), downward flow appears in the vicinity of the centreline of the jet or in other words in the middle of the jet, for the entire vertical height. The flow has become entirely reversed, below height $z/d = 20$ after 15.5 s, as in figure 6.5 (p). According to these figures, it is clear that when background rotation rate increases behaviour of the jet in the vertical plane is fully turbulent and time dependant. But still streamwise, vertical flow and reverse flow which correspond to the breakdown-reformation cycle can be observed.

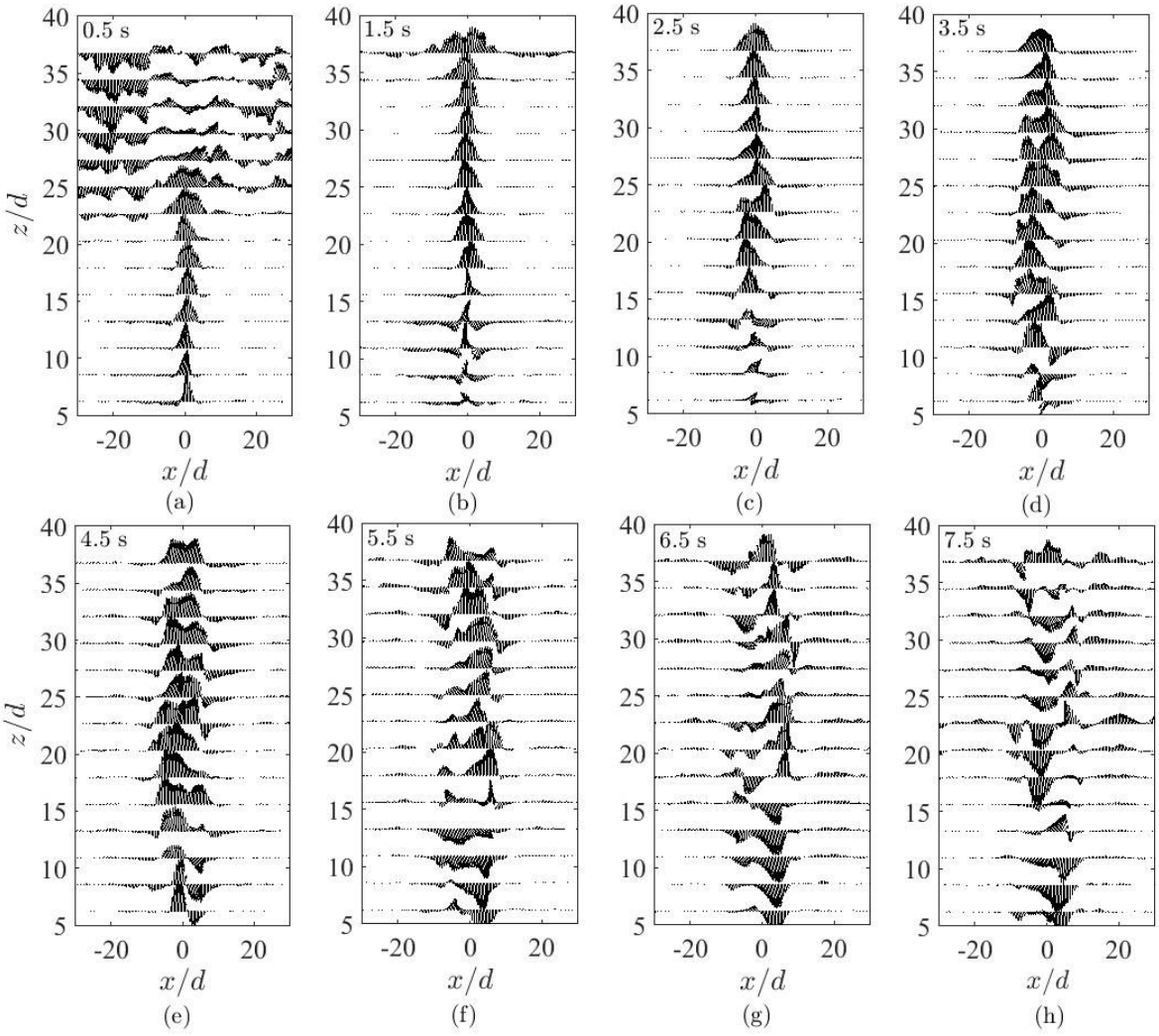

Figure 6.5: Instantaneous vector fields of the vertical velocity component, $w(r)$ for a jet with $Re_0 = 2300$ at $\Omega = 0.84$ rad s^{-1} at times t for (a) 0.5 s, (b) 1.5 s, (c) 2.5 s, (d) 3.5 s, (e) 4.5 s, (f) 5.5 s, (g) 6.5 s, (h) 7.5 s, (i) 8.5 s, (j) 9.5 s, (k) 10.5 s, (l) 11.5 s, (m) 12.5 s, (n) 13.5 s, (o) 14.5 s, (p) 15.5 s.

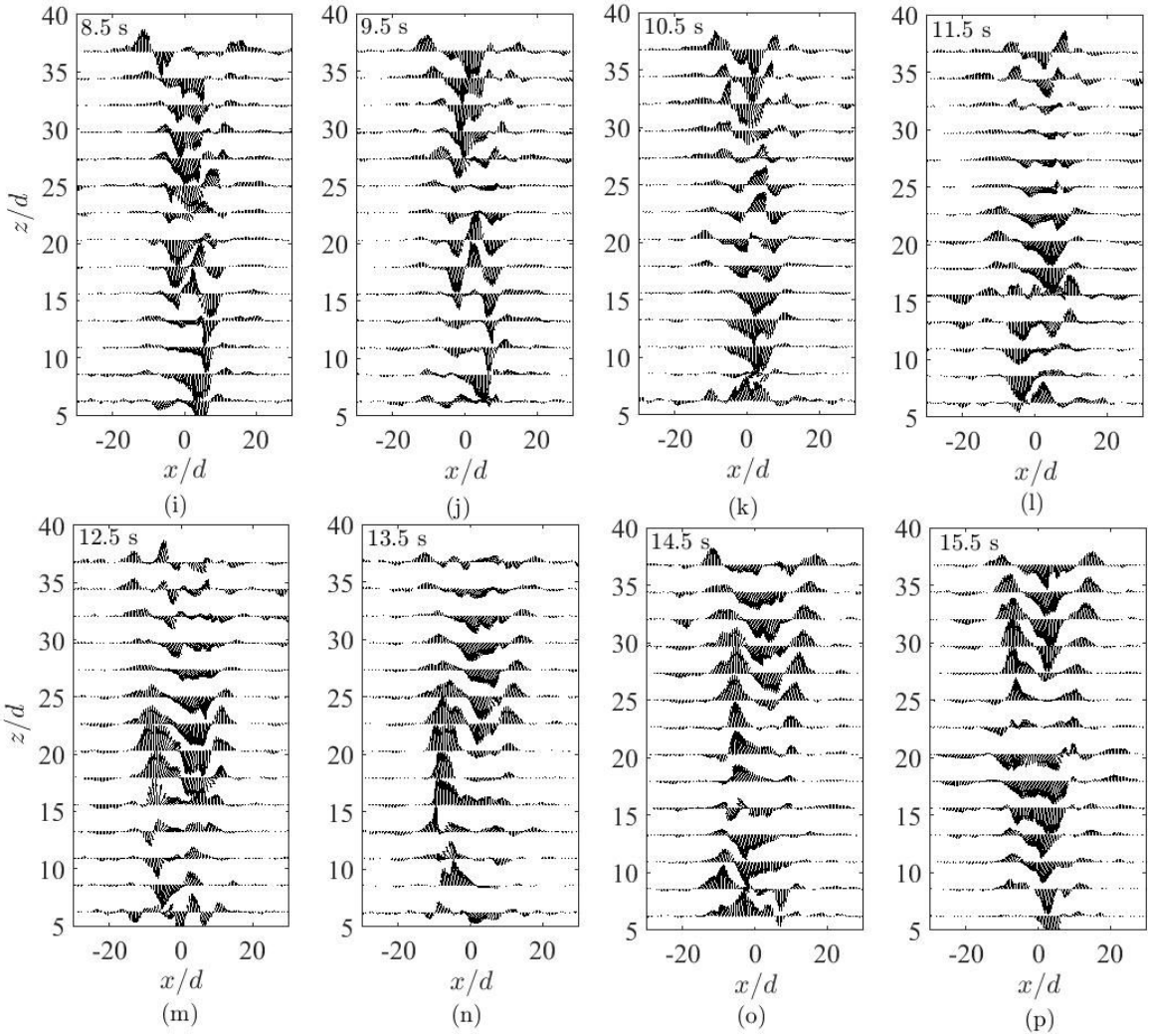

Figure 6.5: Continued.

In order to investigate behaviour of the mean flow in the vertical plane of the jet, the nondimensionalised mean axial centreline velocity of the jet ($\widehat{w}$), was plotted against nondimensional vertical height (z/d). Figure 6.6 shows the variation of $\widehat{w}$, with z/d for seven background rotations as identified in the legend, for $8 \leqslant z/d \leqslant 24$. The mean axial centreline velocities of the jet subject to background rotation were nondimensionalised using the mean axial velocity of the jet without background rotation at $z/d = 8$. The nondimensionalising of the mean axial velocities in this manner, directly allows to compare, values of $\widehat{w}$ of the jet subjected to different rates of background rotation, with that of the jet with no rotation. From figure 6.6, it is clear that the mean axial velocity

decreases, when background rotation rate increases. Also it can be clearly seen in the same figure that, when the background rotation rate increases, the velocity gradient in the vertical direction decreases. Therefore it can be suspected, that there is a tendency of forming a Taylor column at these heights ($8 \leqslant z/d \leqslant 24$). Also when background rotation rate increases, it was observed that the extent of height at which the jet reaches, decreases. Therefore one can conclude that at higher rotation rates, the flow field far from the source, is less disturbed. Note that the vertical height limit $z/d = 8$ was chosen for the lowest limit in the graph. This is because the vertical velocities near the source can not be resolved due to limitations of the experimental set up. Even though the shape of the velocity profiles can be observed at $z/d = 5$ qualitatively, the quantitative velocity measurements were more reliable from $z/d = 8$ and upwards.

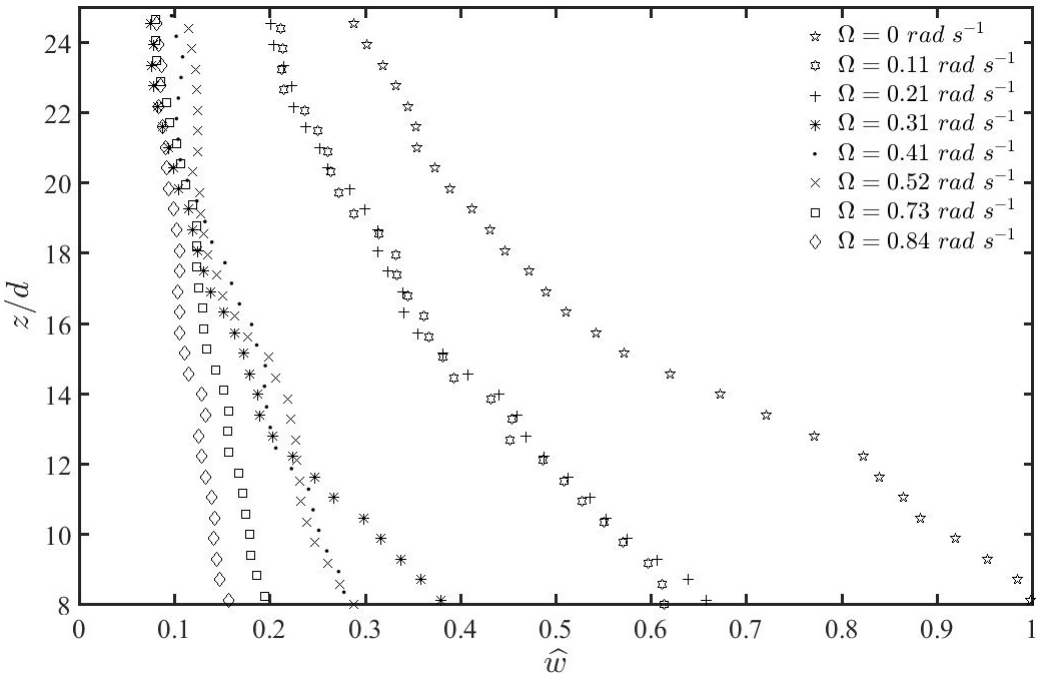

Figure 6.6: Variation of mean axial velocity with nondimensional height for a jet with $Re_o = 2300$.

6.3 Temporal Development of the Radial and Azimuthal Velocities

As discussed in section 6.2, due to a slight precession of the jet it is somewhat difficult to calculate any quantitative data with the vertical plane PIV measurements. Therefore velocity measurements were conducted at the cross sections of the jet at heights, z/d = 0.5, 10, 15 & 20, above the source. As explained in Chapter 4, these measurements were conducted with a horizontal laser sheet in order to capture the radial and azimuthal velocity components.

6.3.1 Near to the Source ($z/d = 0.5$)

Figures 6.7 (a) - (p) show the temporal development of the jet, in the horizontal plane. The horizontal plane is at height z/d = 0.5 above the source. Furthermore figures 6.7 (a) - (p) show instantaneous velocity vectors for the horizontal velocity component, over a time interval of 66 s for $-15 \leqslant x/d \leqslant 15$ and $-15 \leqslant y/d \leqslant 15$. The background rotation rate associated with the figures is 0.21 rad s^{-1} and figure 6.7 (q) shows the colour map for the velocity vectors. As the jet propagates upwards, it entrains fluid from the ambient environment and the entrainment velocity gets affected by the Coriolis force due to background rotation. Consequently swirling is starting to build up. As time passes, it can be seen from figures 6.7 (a) - (e), that a vortex is forming and the radius of the vortex increases with time. Note that the direction of the vortex flow is the same as the direction of the background rotation and hence this vortex is a cyclonic vortex. Also it can be seen that the velocity components in figures 6.7 (a) - (e), have higher azimuthal velocity component contribution than the radial velocity component contribution. After 26 s, in figure 6.7 (f), the flow starts developing radially outwards or in other words the flow is not purely azimuthal. When time passes, in figures 6.7 (g) - (h), the radial flow develops further throughout the outer circumference of the vortex and one can see a gradual unwinding of the vortex or a breaking of the vortex. It can be concluded that this vortex breakdown is due to the breakdown of the jet as explained in section 6.2. Then in figure 6.7 (i), after 38 s, azimuthal flow starts to build up, which implies that the jet recovers from its breakdown.

Followed by the azimuthal velocity built up, in figure 6.7 (i), the radial flow starts to develop. After 42 s, in figure 6.7 (k), the unwinding of the vortex can again be seen. In figures 6.7 (l) - (m), one can see that the unwinding of the vortex continues and hence the radius of the vortex decreases. After 58 s, in figure 6.7 (n), the vortex starts to reform. The reforming continues until 62 s, as in figure 6.7 (o) and again the vortex starts breaking around 66 s. In the long run of the experiments, this recurrent breaking and reforming nature of the vortex was observed in the horizontal plane. This repeated until the ejection of liquid had been stopped at the source. This time dependant flow behaviour in the horizontal plane is consistent with the flow behaviour observed in the vertical plane. Therefore one can conclude that when the jet breaks, as explained in section 6.1, the vortex breaks or unwinds and when the jet reforms, the vortex also reforms in the cross- sectional plane of the jet.

Furthermore figures 6.8 and 6.9 display temporal variation of instantaneous values of the maximum velocity v_{max} and the maximum vorticity ω_{max} respectively, in the horizontal plane, at height z/d = 0.5 above the source, for a jet with Re = 2300 and background rotation 0.21 rad s^{-1}. Figure 6.8 clearly shows a periodic behaviour of the maximum velocity whereas figure 6.9 shows a periodic behaviour of the maximum vorticity. Note that the maximum velocity in the considered horizontal plane corresponds to the entrainment velocity in that plane. When the jet starts to propagate, the entrainment of the liquid from ambient environment gradually increases and hence the entrainment velocity reaches its maximum value in the considered horizontal plane. If the jet propagates without any interruption the maximum entrainment velocity should not vary after it reaches its maximum value. But according to figure 6.8, the maximum entrainment velocity varies in between its maximum value (approximately 0.05 m s^{-1}) and the minimum value (approximately 0.035 m s^{-1}). Therefore one can conclude that when the jet breaks the maximum entrainment velocity decreases and when the jet reforms the maximum entrainment velocity gradually increases. Thus the behaviour of the maximum entrainment velocity is also consistent with the formation-breakdown cycle of the jet that was explained in section 6.1. A similar explanation can be given for the behaviour of the maximum vorticity which is shown in figure 6.9. When the jet

is propagating upwards, the maximum value of vorticity increases, whereas when the jet breaks, the maximum vorticity gradually decreases.

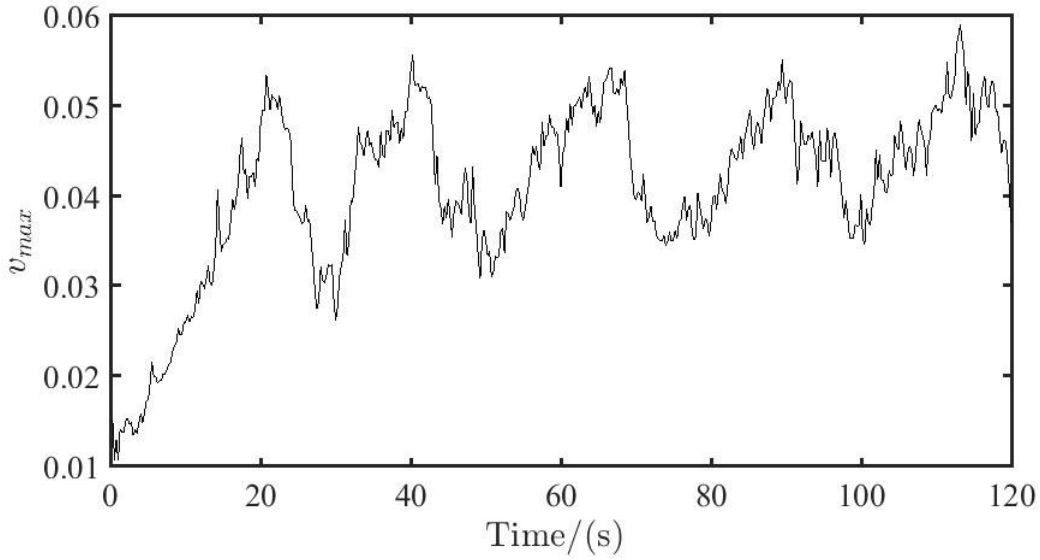

Figure 6.8: Temporal variation of the maximum velocity, in the horizontal plane at a height $z/d = 0.5$, for a jet with $Re_0 = 2300$ at $\Omega = 0.21$ rad s^{-1}.

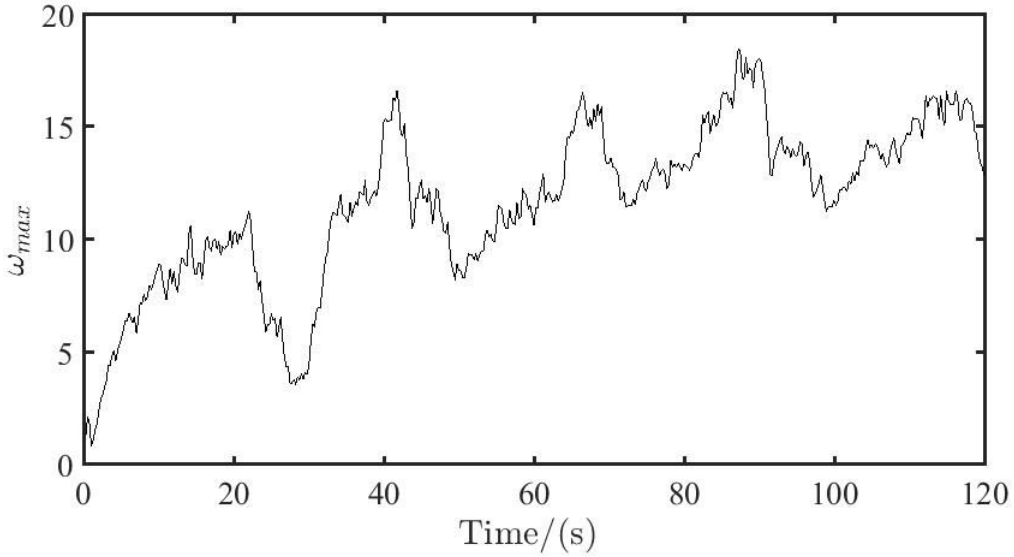

Figure 6.9: Temporal variation of the maximum vorticity in the horizontal plane at a height $z/d = 0.5$, for a jet with $Re_0 = 2300$ at $\Omega = 0.21$ rad s^{-1}.

Moreover the variation of the radial position of the instantaneous values of

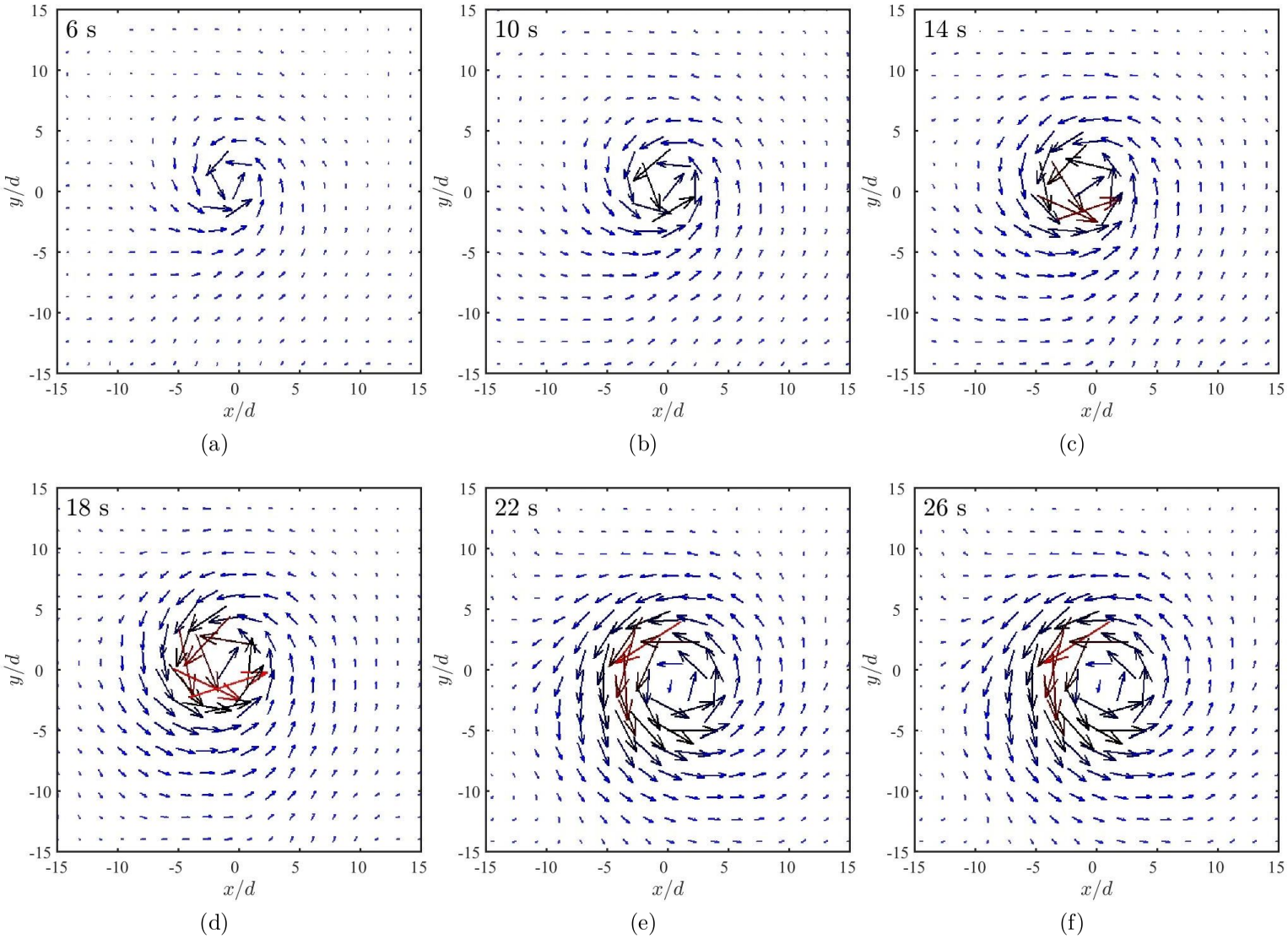

Figure 6.7: Instantaneous vector fields of the velocity components, v_r and v_θ for a jet with Re_0 = 2300 at Ω = 0.21 rad s^{-1}.

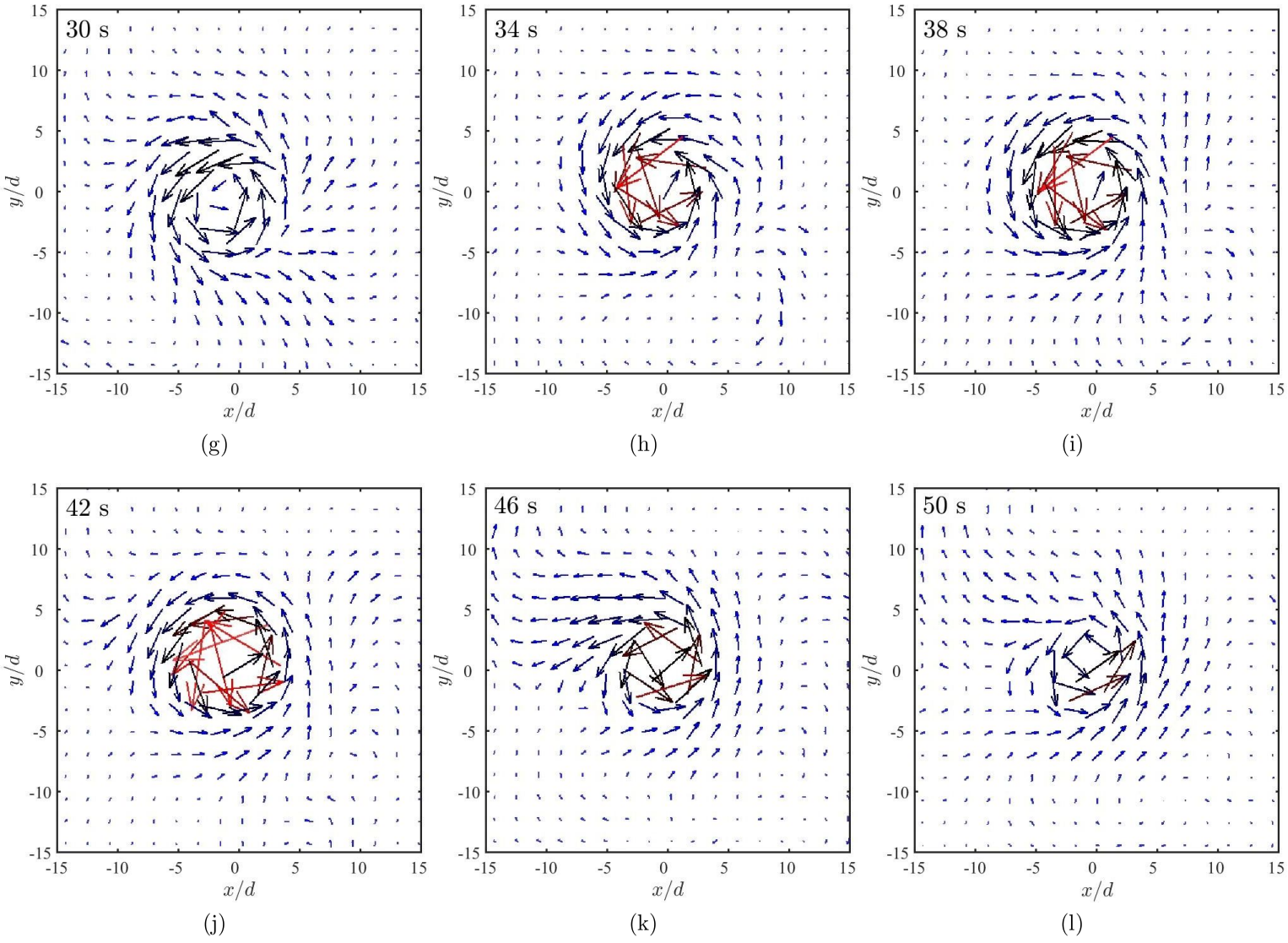

Figure 6.7: Continued.

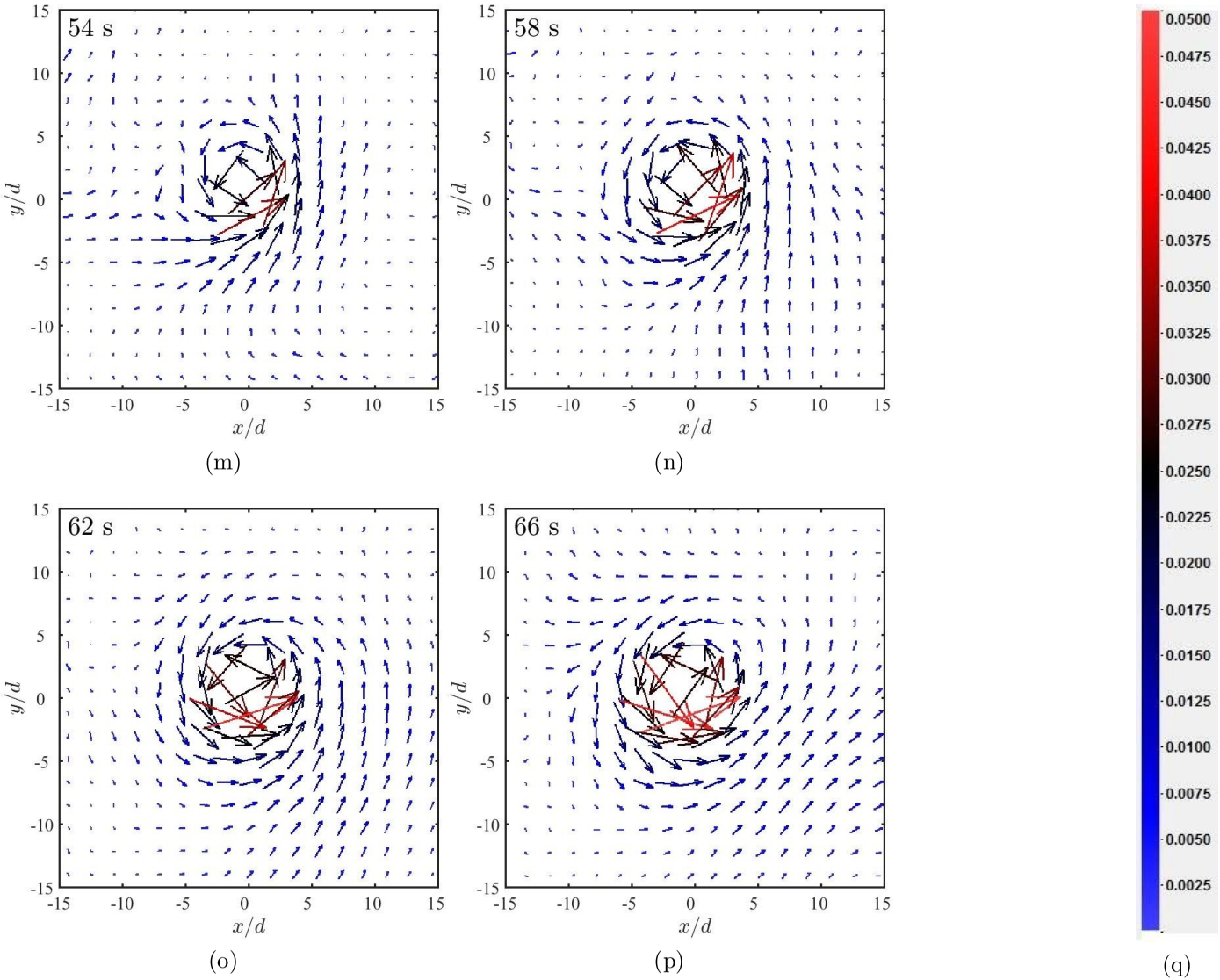

Figure 6.7: Continued

the maximum velocity and the maximum vorticity with time were calculated. Figures 6.10 and 6.11 display, respectively, the temporal variation of the nondimensionalised instantaneous radial position of the maximum velocity (v_{max}) and the maximum vorticity (ω_{max}). The background rotation rate associated with these two figures is 0.21 rad s^{-1}. According to figure 6.10, the radial position of the maximum velocity varies within $-2 \leq r/d \leq 2$ over time. Figure 6.11, shows that the radial position of the maximum vorticity varies within $-1 \leq r/d \leq 1$.

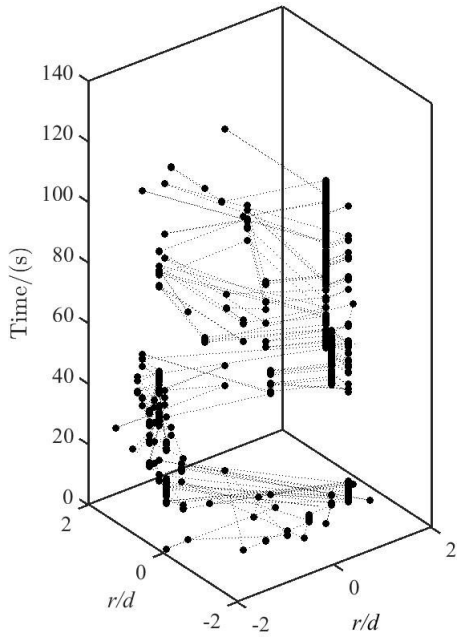

Figure 6.10: Temporal variation of instantaneous radial position of the instantaneous values of the maximum velocity in the horizontal plane, at height $z/d = 0.5$, for a jet with $Re_0 = 2300$ and $\Omega = 0.21$ rad s^{-1}.

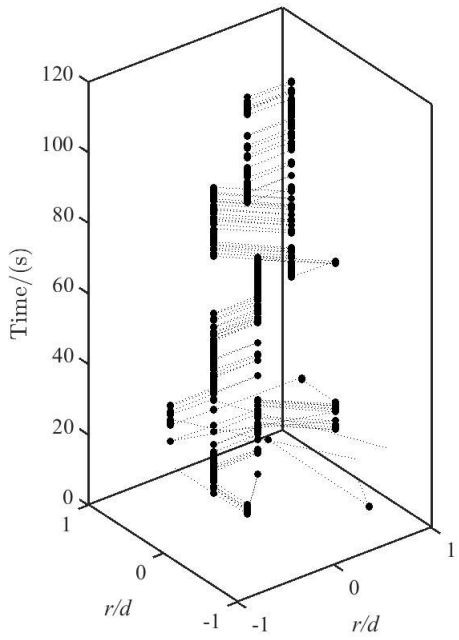

Figure 6.11: Temporal variation of instantaneous radial position of the instantaneous values of the maximum vorticity in the horizontal plane, at height $z/d = 0.5$, for a jet with $Re_0 = 2300$ and $\Omega = 0.21$ rad s^{-1}.

6.3.2 Horizontal Plane at Height $z/d = 10$

Figures 6.12 (a) - (p) display the temporal development of the jet ($Re_0 = 2300$) in the horizontal plane at height $z/d = 10$ above the source for a background rotation 0.21 rad s^{-1}. Figure 6.12 (q) shows the colour map for the velocity vectors. Note that the colour map used for velocity vectors in the figure is the same as that used for velocity vectors in figure 6.7. The red colour represents the velocity vectors of higher magnitude. If figures 6.12 (a) - (p) are carefully observed one can see that there are no red colour velocity vectors. Thus by comparing two figures (6.7 & 6.12), it is clear that, in general, the velocities in the horizontal plane at height $z/d = 10$ are lower than those in the horizontal plane at height $z/d = 0.5$. Figures 6.12 (a) - (e), clearly show formation of the cyclonic vortex and the gradual increment of the vortex radius with time. After about 26 s, in figure 6.12 (f), the formed vortex breaks from several consecutive radial points at the outer circumference. Further breaking of the vortex continues in figure 6.12 (g). Followed by the breaking up, the vortex starts reforming as shown in figures 6.12 (h) - (j). In figures 6.12 (k) - (m),

the vortex gradually breaks up again. At around 58 s, in figure 6.12 (n), the vortex starts to reform and the reforming continues until 66 s (refer figures 6.12 (o) - (p)). Thus, these figures provide an evidence for the periodic breaking and reforming of the jet in the horizontal plane at height $z/d = 10$.

Moreover figure 6.13 shows the spatio-temporal variation of the iso-surface correspond to the 'highest velocity' in the horizontal plane (at $z/d = 10$) that occurs within the considered time period. Note that the 'highest velocity' is not the local maximum velocity at a time instance. It is the maximum of all the instantaneous maximum velocities. Therefore the term 'highest velocity' is used to avoid confusion. As displayed in figure 6.13, it takes 10 s for the velocity in the horizontal plane to reach its highest velocity value and the radius of the iso-surface increases with time. Then after approximately 28 s, iso-surface is not present, which means there is no highest velocity component in the horizontal plane. But after 32 s, the iso-surface starts spreading radially until 48 s and it disappears afterwards. After approximately 52 s, the iso-surface reappears. The disappearance and the reappearance of the iso-surface continues to happen throughout the considered time period, which is 100 s. Therefore it is clear from figure 6.13 that the highest velocity is not present during some of the time intervals. The highest velocity corresponds to the highest entrainment velocity in the horizontal plane. When the jet is propagating in the streamwise (z) direction the entrainment velocity is present whereas when the jet is not propagating through the horizontal plane, the entrainment velocity is not present. This proves that the formation-breakdown cycle of the jet, where when the jet breaks down, there is no highest velocity in the considered horizontal plane (i.e. $z/d = 10$ for this case) and when the jet starts to reform the entrainment velocity or the velocity in the horizontal plane increases gradually to its maximum, until the jet breaks down. When the jet is first started the solid body rotation status of the tank gets disturbed and even though the jet breaks up, due to the background rotation there are some other velocity fields of comparatively small scale are present in the horizontal plane. Therefore the highest velocity was chosen for iso-surfaces, in order to make sure that the chosen velocity is only present when the jet is active.

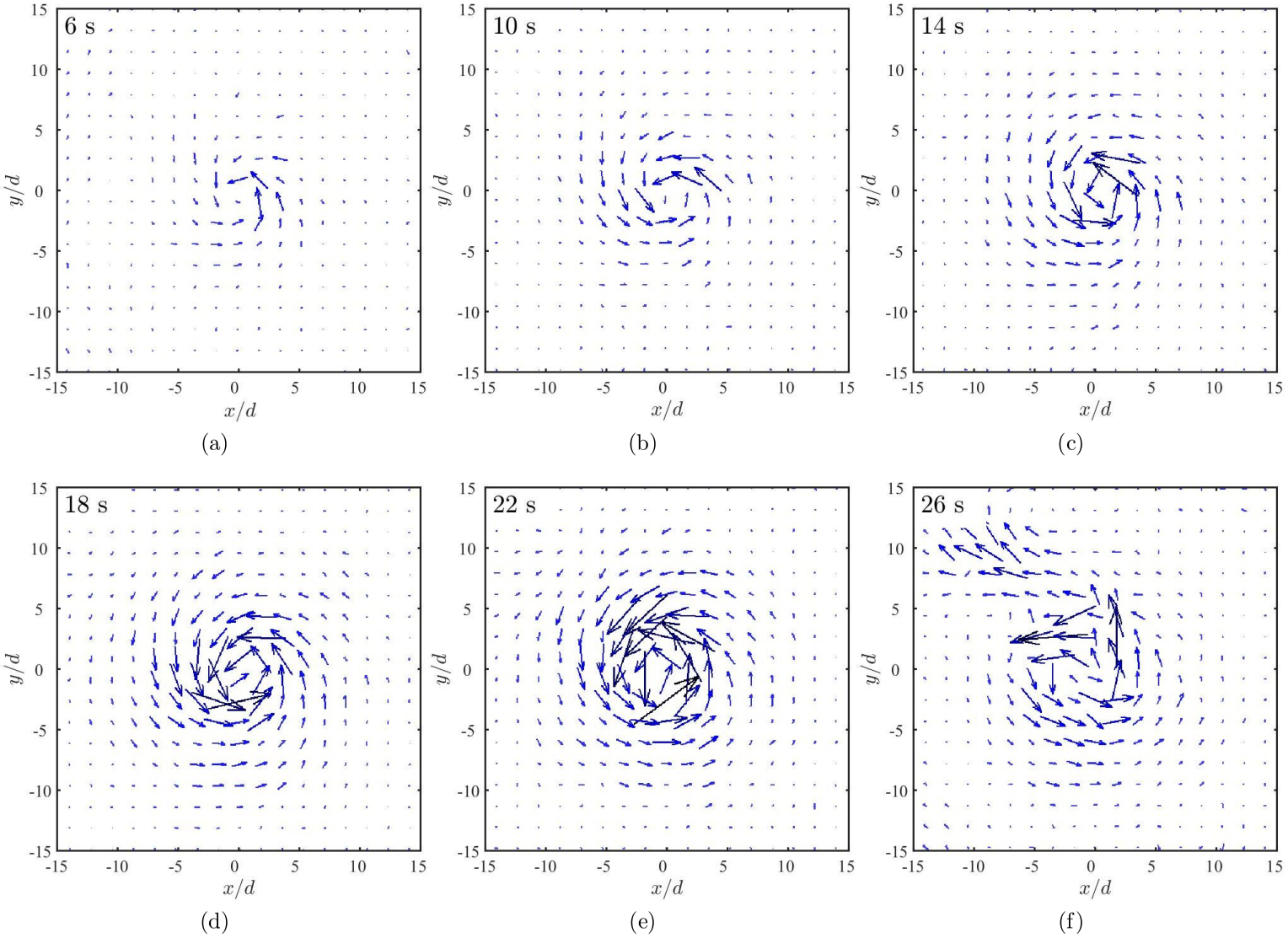

Figure 6.12: Instantaneous vector fields of the velocity components, v_r and v_θ for a jet with $Re_0 = 2300$ at $\Omega = 0.21$ rad s^{-1} at times t for $z/d = 10$.

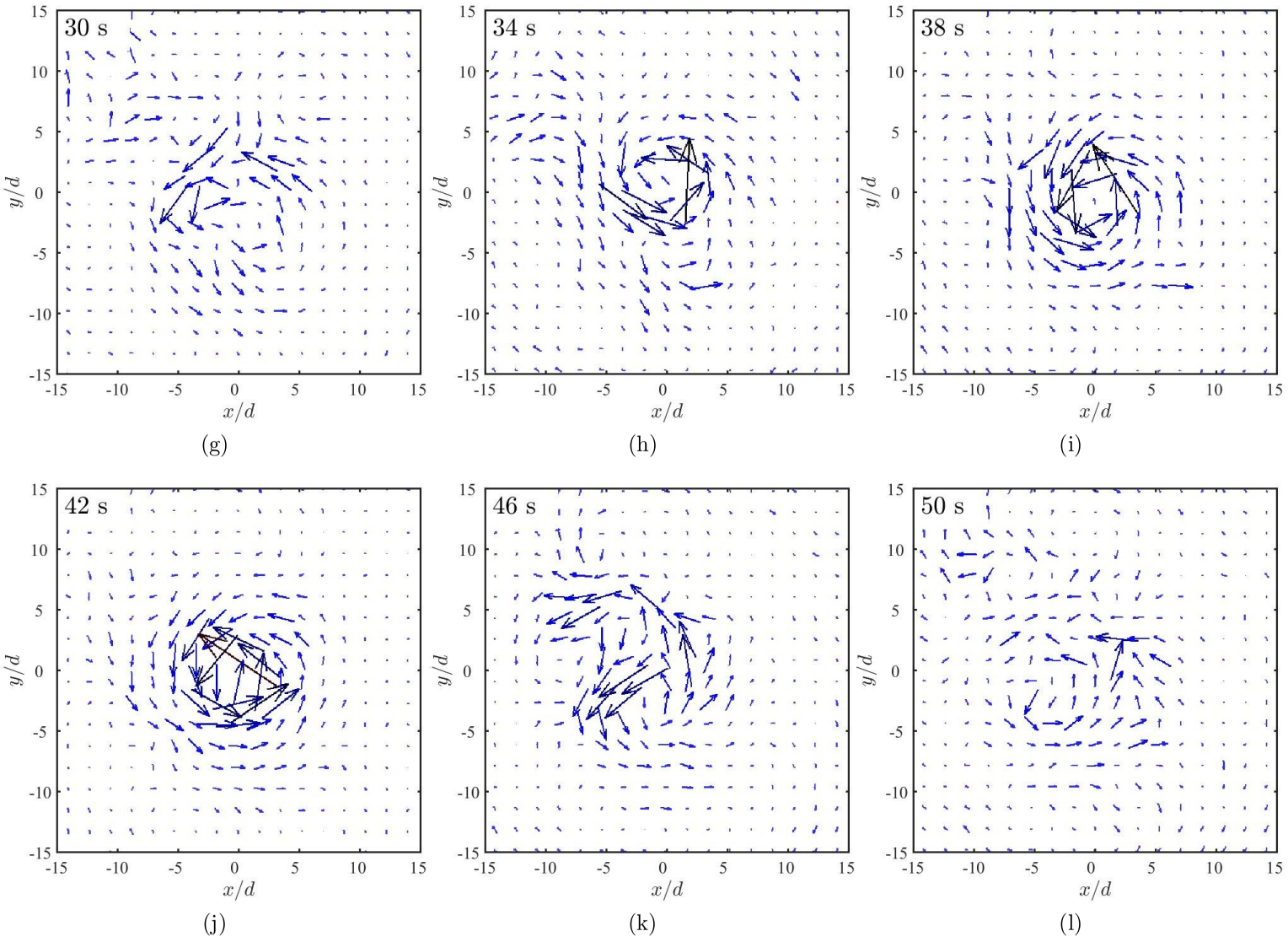

Figure 6.12: Continued.

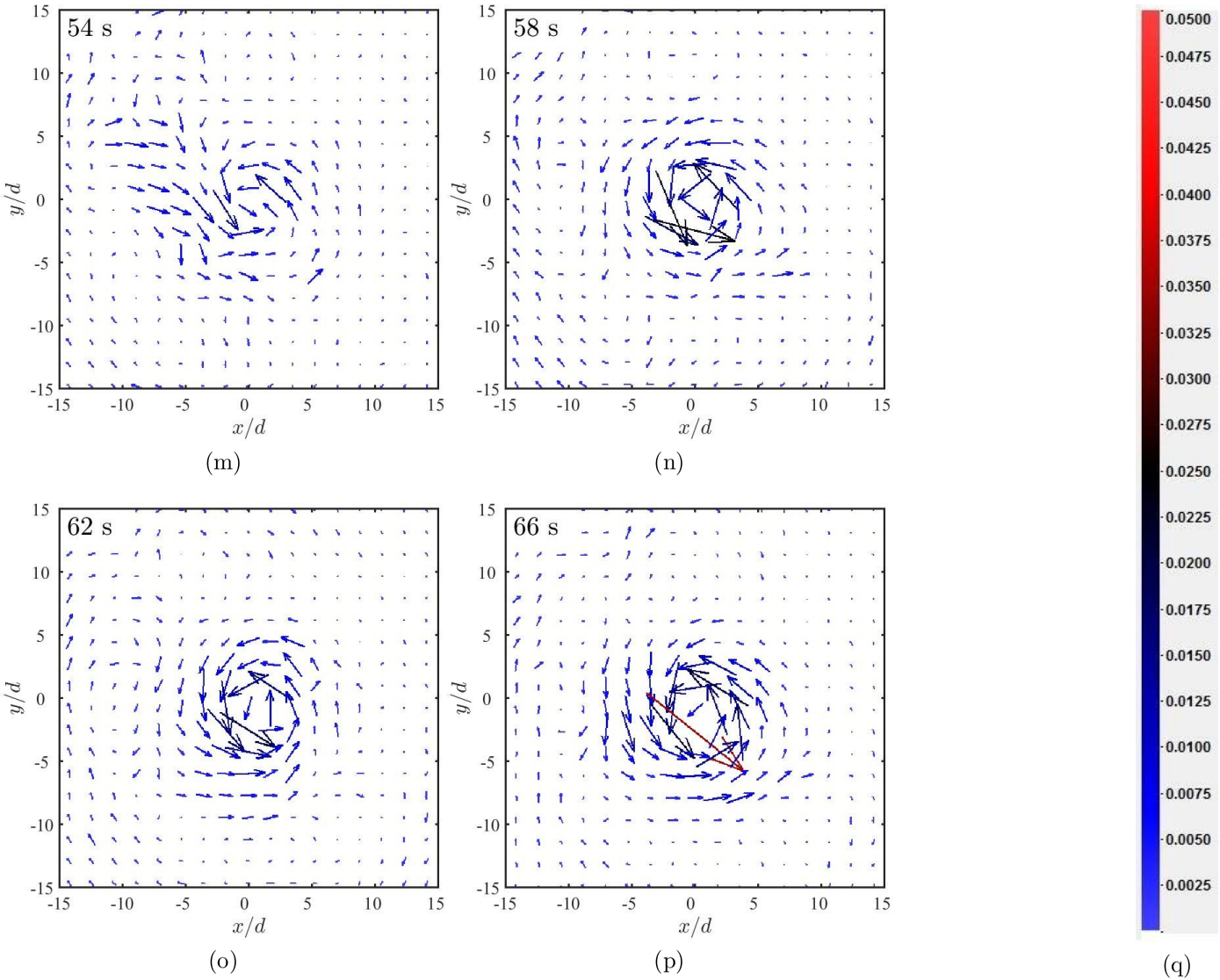

Figure 6.12: Continued.

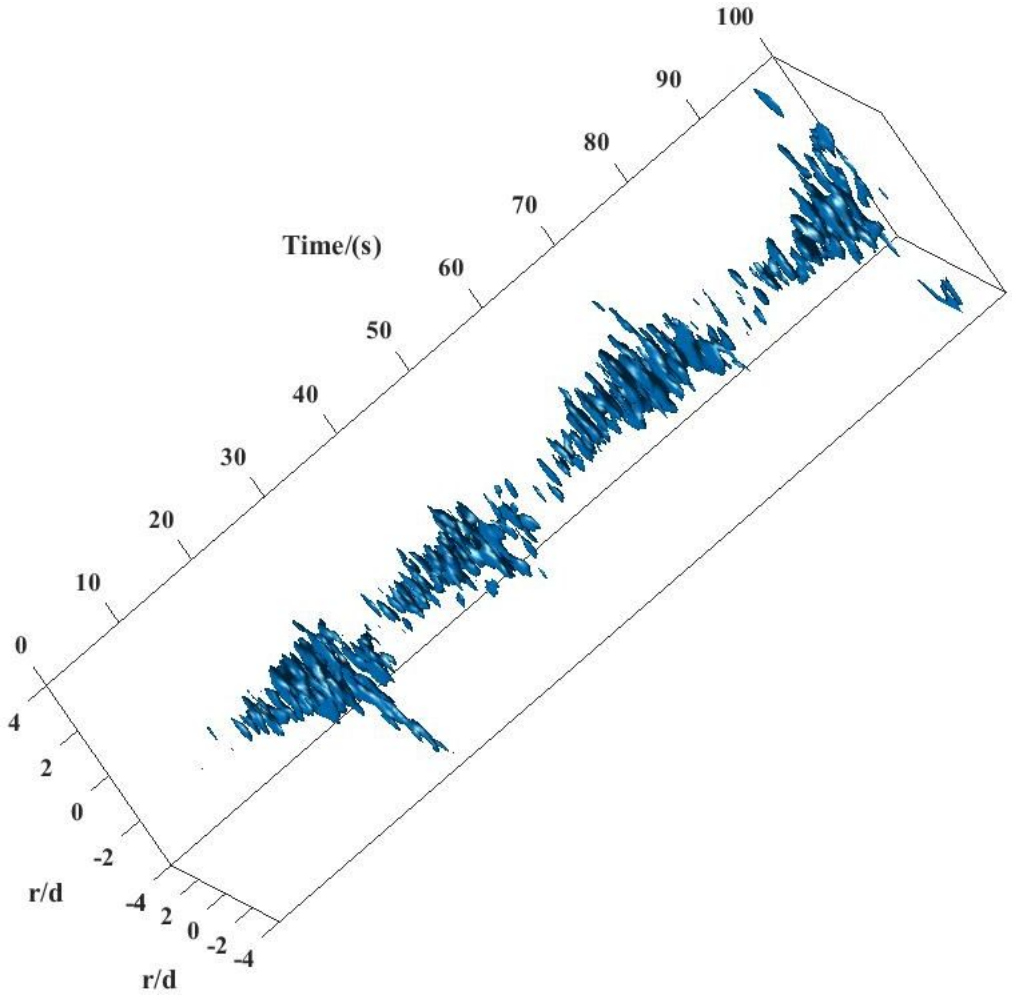

Figure 6.13: Spatio-temporal variation of the iso-surfaces of the 'highest velocity' at $z/d = 10$, for a jet with $Re_0 = 2300$ at $\Omega = 0.21$ rad s^{-1} .

6.3.3 Horizontal Plane at Height $z/d = 15$

Figures 6.14 (a) - (p) illustrate the velocity vectors of the jet ($Re_0 = 2300$) in the horizontal plane at height $z/d = 15$. The background rotation associate with the figures is $\Omega = 0.21$ rad s^{-1}. Note that the PIV measurements were started once the jet reached the height of the measurement plane (not at the instance of ejection of liquid at the source had started). Also note that the colour map for the velocity vectors shown in figure 6.14 (q) is the same as that for the velocity vectors in figures 6.7 & 6.12. Therefore when the two figures 6.7 & 6.14 are compared, one can see that the velocities are much higher in the horizontal plane, $z/d = 0.5$, which is near to the source, compared to the horizontal plane, $z/d = 15$, above the source.

Figure 6.14 (a) shows the instantaneous behaviour of the velocity vectors after 6 s. A cyclonic vortex appears due to the fact that the entrainment velocity is affected by the Coriolis force. Then, after 10 s, in figure 6.14 (b), the radius of the vortex has increased and the shape of the vortex is elliptical. After 14 s, in figure 6.14 (c), the velocity vectors appear in such a manner that they are trying to form two co-rotating vortices. In figure 6.14 (d), one can clearly see that two co-rotating vortices have formed. As time passes, the velocities are decreasing until 30 s, but still two co-rotating vortices can be seen (refer figures 6.14 (e) - (f)). It can be concluded that after 22 s, the jet is not propagating through the horizontal plane ($z/d = 15$), therefore the entrainment velocity is not that strong. In figure 6.14 (g), it can be observed that three co-rotating vortices have formed. Thereafter, between about 34 s and 38 s, in figures 6.14 (h) - (i), comparatively higher velocity vectors start appearing, which implies that the jet is reforming. But a single vortex formation that corresponds to reformation of the jet can not be observed. Therefore it can be suspected that the velocity vectors that appear in figures 6.14 (h) - (i) may correspond to fluid particles that move due to the pressure from underneath of the horizontal plane. Around 42 s & 46 s, in figures 6.14 (j) - (k), three co-rotating vortices can again be observed. Thereafter, in figures 6.14 (l) - (p) which correspond to time interval 54 s - 66 s, the velocity in the horizontal plane decreases and a significant structure can not be observed. Thus on the basis of evidence from figures 6.14 (a) - (p), it can be concluded that the jet

had reached, the horizontal plane at height, $z/d = 15$, only in one instance, that is after few seconds of the liquid ejection at the source had started. In other words, after the first break up of the jet, it had never reached the horizontal plane at height $z/d = 15$.

6.4 Kinetic Energy Associated with the Radial and Azimuthal Velocity Components

The method applied here involves analysing the temporal fluctuations of the kinetic energy associated with the circumferentially-averaged azimuthal flow velocity $v_\theta(r,t)$ and radial velocity $v_r(r,t)$. In order to infer this kinetic energy from our data it is initially required to define, and identify, the centre of the swirling flow field for each PIV frame. Then it is necessary to define a cut-off distance, R, for the radial extent of this flow structure in each frame. Thereafter a measure, $K.E_{v_\theta}(t)$ and $K.E_{v_r}(t)$, for the kinetic energy of the azimuthal flow and the radial flow components can be obtained by using equations (6.1) and (6.2).

$$K.E_{v_\theta}(t) = \int_0^R v_\theta^2(r,t) r dr. \tag{6.1}$$

$$K.E_{v_r}(t) = \int_0^R v_r^2(r,t) r dr. \tag{6.2}$$

6.4.1 Algorithm for Finding the Centre of the Vortices

In order to identify the centre of the swirling flow structure on the measurement domain, we followed Graftieaux *et al.* (2001) whose method proceeds as follows. Let S refer to the two-dimensional, discrete, rectangular PIV measurement domain containing N pixel sites. Aligned perpendicular to this domain is the unit vector $\vec{e}_z$ in the direction of the z-axis. Let P refer to the particular pixel site on which S is centred and denote the remaining locations on the measurement domain as M. Let $\vec{a}$ be the radius vector from P to M, let $\vec{U}_M$ denote velocity vector at M and let ϕ_M represent the angle between $\vec{a}$ and $\vec{U}_M$. Graftieaux *et al.* (2001) initially consider a dimensionless scalar function

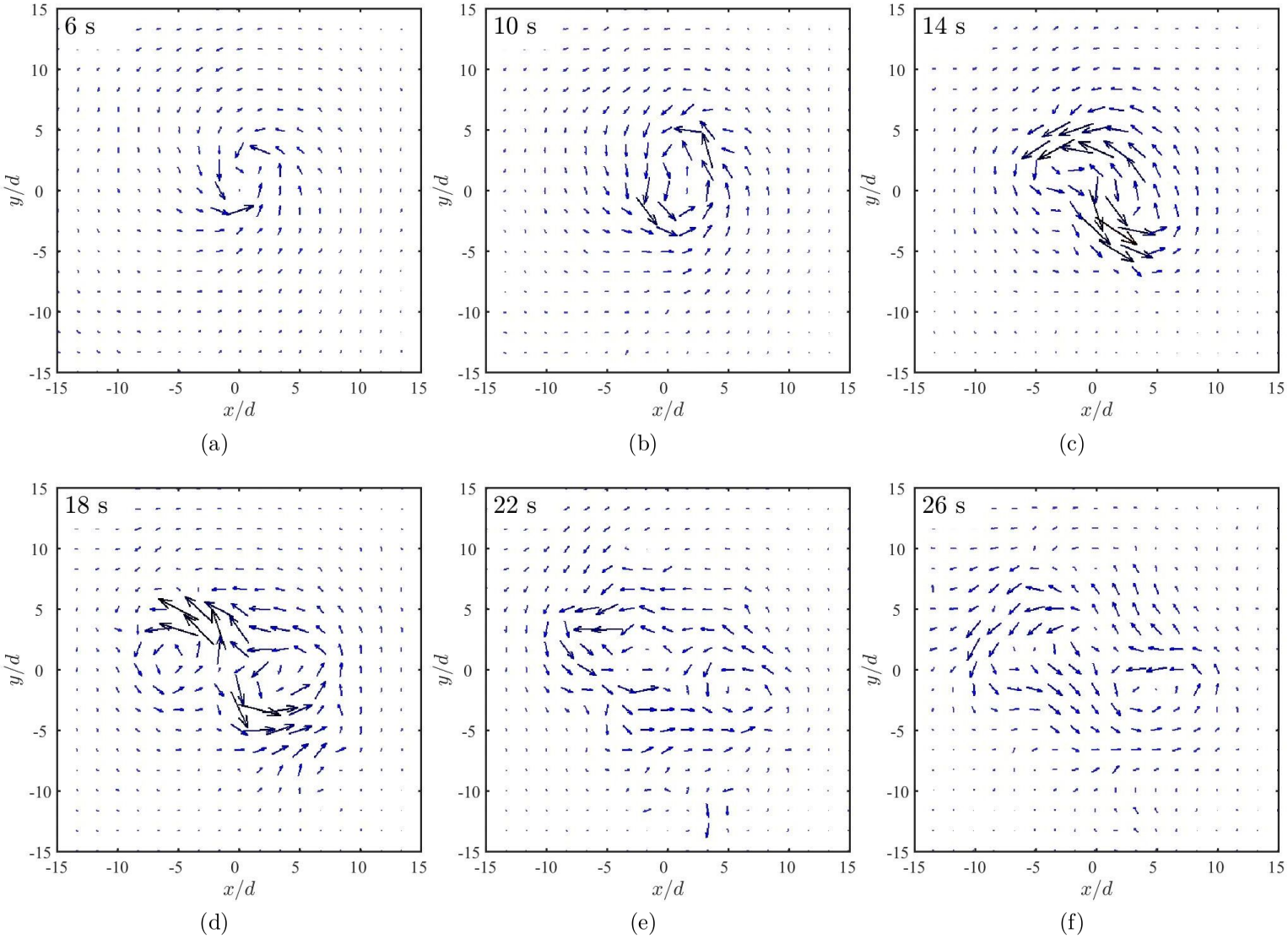

Figure 6.14: Instantaneous vector fields of the velocity components, u_r & u_θ for a jet with $Re_0 = 2300$ at $\Omega = 0.21$ rad s^{-1} at times t at $z/d = 15$.

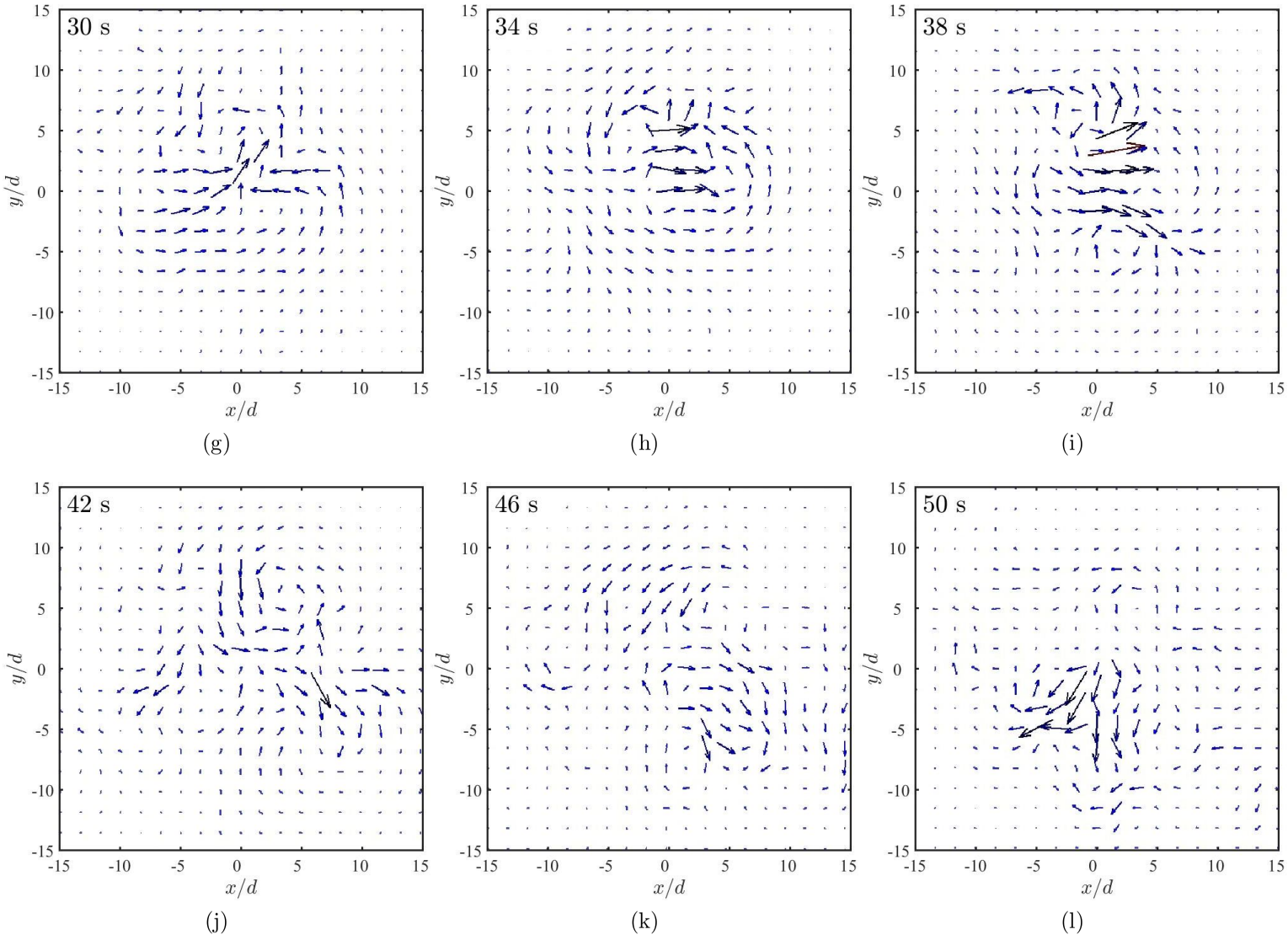

Figure 6.14: Continued.

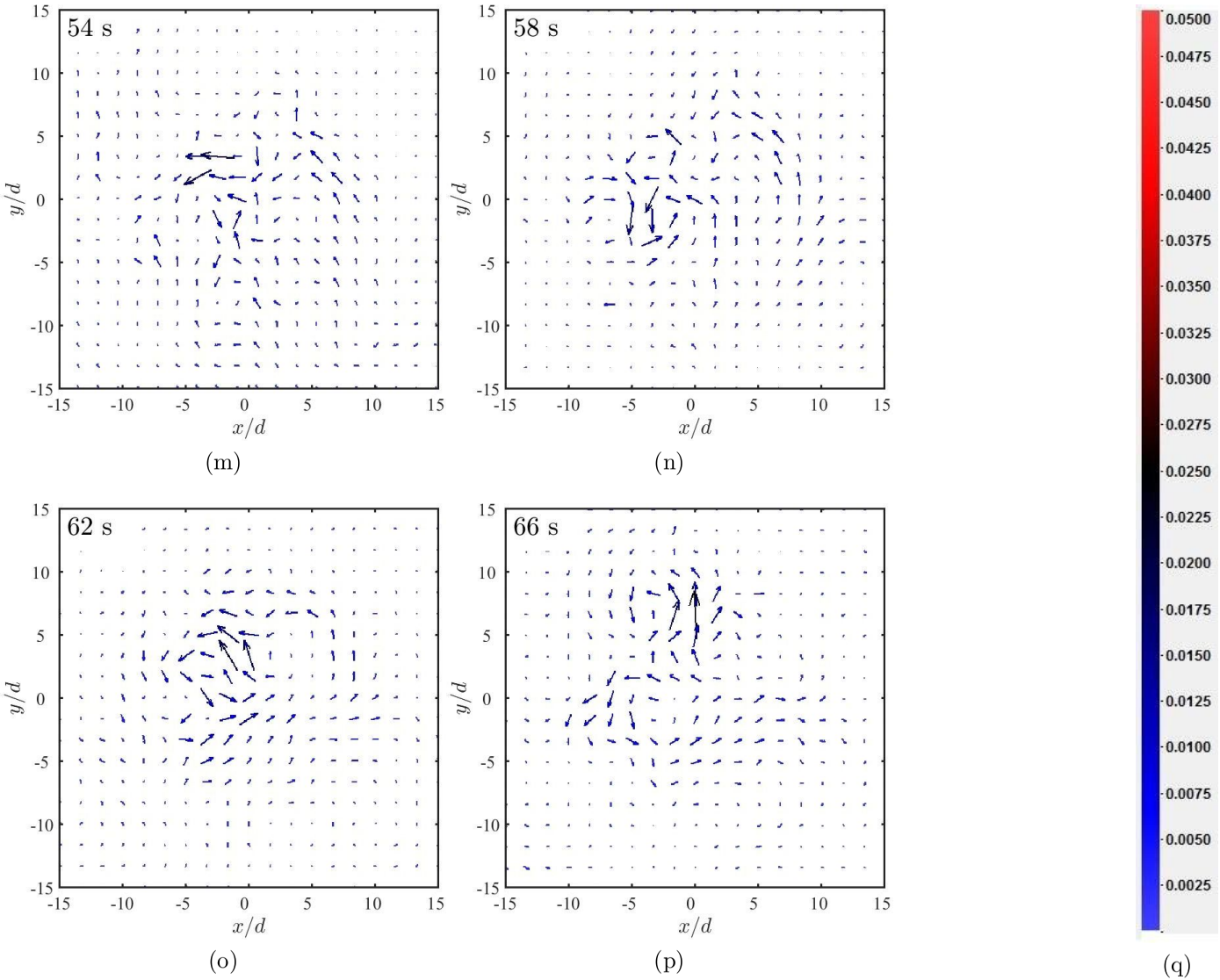

Figure 6.14: Continued.

$\Gamma_1(P)$ for a continuous domain S but which reduces for the discrete PIV measurement domain to,

$$\Gamma_1(P) = \frac{1}{N} \sum_S \frac{(\vec{a} \times \vec{U}_M) \cdot \vec{e}_z}{|\vec{a}\| \cdot \vec{U}_M|} = \frac{1}{n} \sum_S \sin(\phi_M) \ . \tag{6.3}$$

Thus, Γ_1 is a dimensionless scalar, with $|\Gamma_1| \leq 1$. When a vortex centre is located at P then $\vec{U}_M$ is perpendicular to $\vec{a}$ at all pixel sites. This implies that $\sin \phi_M = 1$ at all pixel sites and it follows, therewith, that $\Gamma_1(P)$ adopts its maximum value at P. Consequently, the strategy for identifying the vortex structure in the measurement domain is to determine the value of Γ_1 for all pixel sites and identify that particular site with the largest value for the parameter. Graftieaux *et al.* (2001) state that Γ_1 typically reaches values from 0.9 to 1 near the vortex centre, independent of the value of N - the current observations are consistent with this. Graftieaux *et al.* (2001) discuss, moreover, that N plays the role of a spatial filter and it is therewith possible to remove small-scale turbulent fluctuations through the selection of the particular value of N to be selected. Figure 6.15 displays examples of two PIV flow-field frames on which the centre, as identified by the centre-finding process of Graftieaux *et al.* (2001), is marked by a bold black cross. The inspection of the symmetric flow field in Figure 6.15 (a) reveals that the location of the centre of the flow structure corresponds well with the position one would have intuitively chosen based on a visual inspection only. However, when the flow field is less symmetric, that is during later stages of the formation-decay cycle of the jet, a centre location by visual inspection is, evidently, not that straightforward as is illustrated by considering figure 6.15 (b).

6.4.2 Definition of the Radial Cut-off Radius

The evaluation of temporal variation of the kinetic energy associated with the azimuthal flow velocity and the radial flow velocity, by means of equations 6.1 and 6.2, requires the cut-off value for the radial extent R to be defined. Figure 6.16 displays a series of profiles of the circumferentially-averaged, azimuthal velocity component, $\overline{v}_\theta$, as a function of the nondimensionalised radial position r/d at height $z/d = 0.5$ above the source. The figure shows eight data sets spanning a total interval of 34 s during a formation-breakdown cycle of

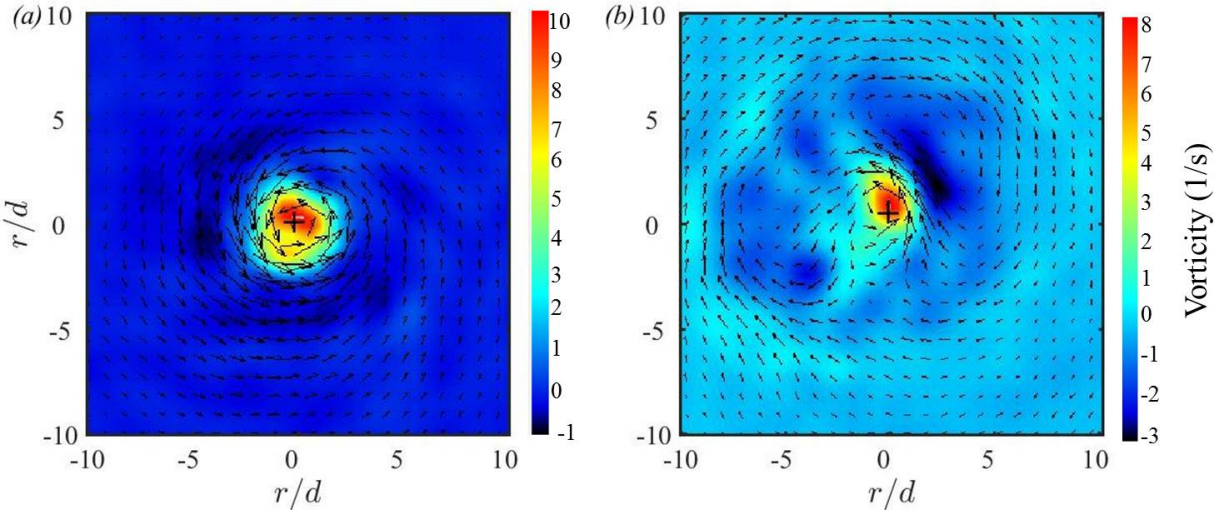

Figure 6.15: Two examples illustrating the performance of the centre-finding process of Graftieaux *et al.* (2001) applied to flow fields from the current experiments for Re_0 = 2300, at Ω = 0.21 rad s^{-1}, with (a) Γ_1 = 0.87, (b) Γ_1 = 0.66.

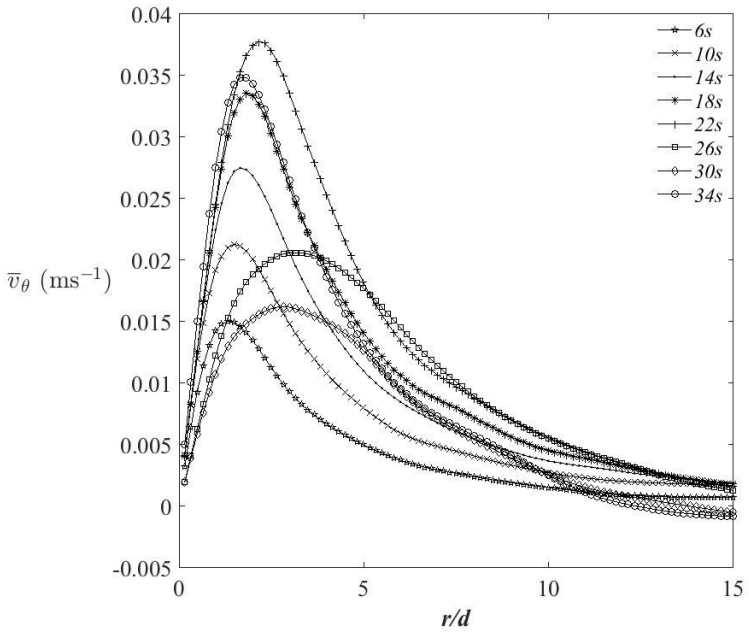

Figure 6.16: Profiles of the circumferentially-averaged azimuthal velocity component $\overline{v}_\theta$ as as a function of the distance r/d from the centre for different instances in time, for a jet with Re = 2300 at Ω = 0.21 rad s^{-1}, z/d = 0.5.

a jet with Re_0 = 2300 at Ω = 0.21 rad s^{-1}. The vector fields determined from the PIV measurements were acquired at a rate of 90 frames per second and then averaged over successive periods of Δt = 0.25 s before calculating the circumferentially-averaged velocity $\overline{v}_\theta$.

Figure 6.16 reveals, firstly, that for $r/d \to 0$ the profiles for all times satisfy the expected condition $\overline{v}_\theta \to 0$. This represents quantitative evidence for a good performance of the process described in section 6.4.1 to identify the centre of the flow field. The flow structures formed in the horizontal planes away from the source (i.e z/d = 5, z/d = 10) are more complex, specially when the jet is breaking down. Therefore the centre finding algorithm were used to find the centres of the flow structures in the horizontal planes, at heights, z/d = 5 and z/d = 10. Figures 6.17 & 6.18 illustrate the profiles of the circumferentially-averaged, azimuthal velocity component, at heights, z/d = 5 and z/d = 10 respectively. These two figures also qualitatively reveal that for $r/d \to 0$ the profiles for all times satisfy the expected condition $\overline{v}_\theta \to 0$, which again prove the reliability of the process used to identify the centre.

As regards the selection of the cut-off value for the radial extent R required to evaluate 6.1 and 6.2, Figures 6.16, 6.17 and 6.18 demonstrate that the azimuthal flow velocity approaches values $\overline{v}_\theta \approx 0$, for all profiles displayed, for radial locations $r/d \geq 15$. Therefore we have selected r/d = 15 as the cut-off location such that $R = 15d$ in 6.1 and 6.2. The precise choice for the value for R will not strongly affect the value of 6.1 and 6.2 as long as the bulk of the kinetic energy is captured by the integral - which is certainly the case for any choice of the cut-off value with $r/d \geq 10$.

6.4.3 Kinetic Energy Associated with the Azimuthal Velocity

Figures 6.19 (a) - (i) illustrate samples for the temporal variation of $K.E_{(v_\theta)}$ for a jet with Re_0 = 2300, at nine different rotation rates from 0.21 rad s^{-1} to 1.05 rad s^{-1}. It can be seen that the figures display very regular fluctuations of $K.E_{(v_\theta)}$ for all rotation rates. Comparison of the graphs in figure 6.19

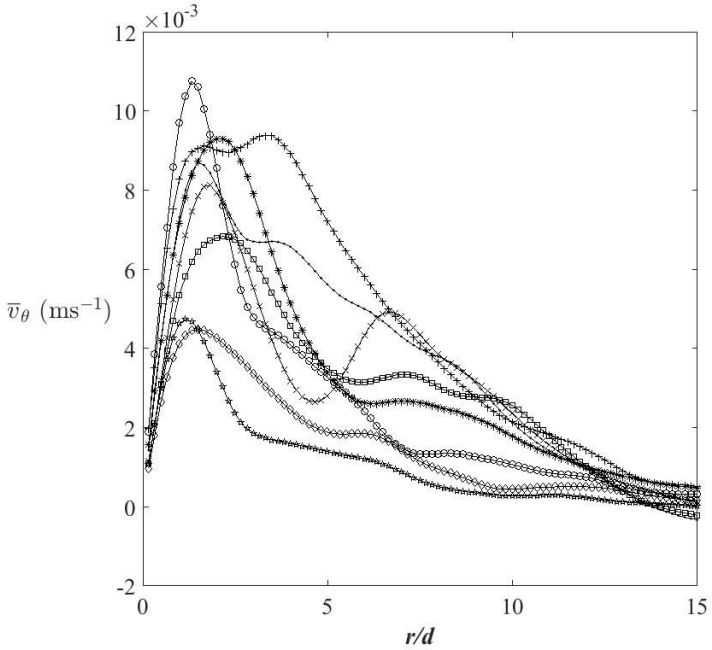

Figure 6.17: Profiles of the circumferentially-averaged azimuthal velocity component $\overline{v}_\theta$ as as a function of the distance r/d from the centre for different instances in time, for a jet with $Re = 2300$ at $\Omega = 0.21$ rad s^{-1}, $z/d = 5$.

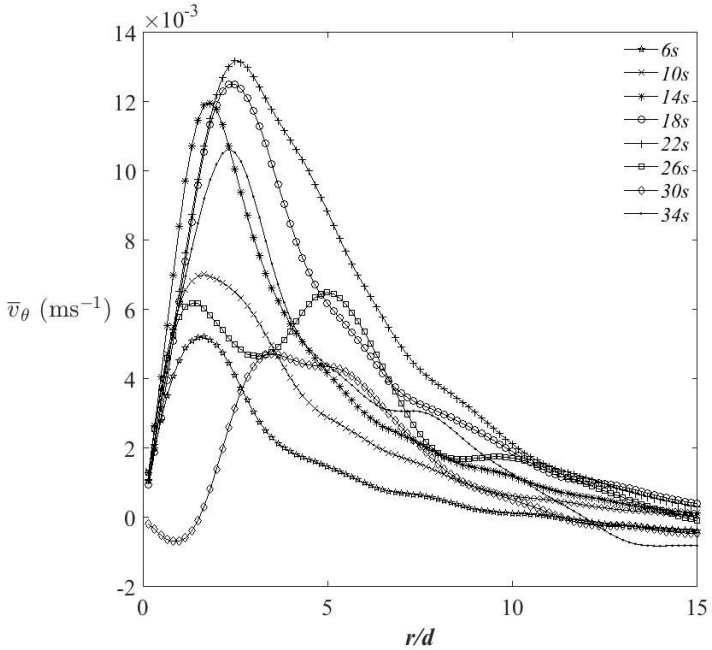

Figure 6.18: Profiles of the circumferentially-averaged azimuthal velocity component $\overline{v}_\theta$ as as a function of the distance r/d from the centre for different instances in time, for a jet with $Re = 2300$ at $\Omega = 0.21$ rad s^{-1}, $z/d = 10$.

moreover reveals, qualitatively, that the frequency of the temporal fluctuation of $K.E_{(v_\theta)}$ increases with increasing values of the background rotation. The azimuthal velocity in any considered horizontal plane gradually increases when the jet starts propagating through that plane. But if the jet is propagating without any interruption, the kinetic energy associated with the azimuthal velocity should either increase continuously throughout the considered time or it should increase to a certain value and remain constant within the considered time period. The latter corresponds to a jet that reached a steady state during the considered time period. Therefore the temporal fluctuations of $K.E_{(v_\theta)}$ correspond to the formation-breakdown phenomena of the jet. Thus the frequency associates with the temporal fluctuations of $K.E_{(v_\theta)}$, gives the formation-breakdown frequency, f_θ, for each rotation rate. The Fourier transform was used to calculate the frequencies.

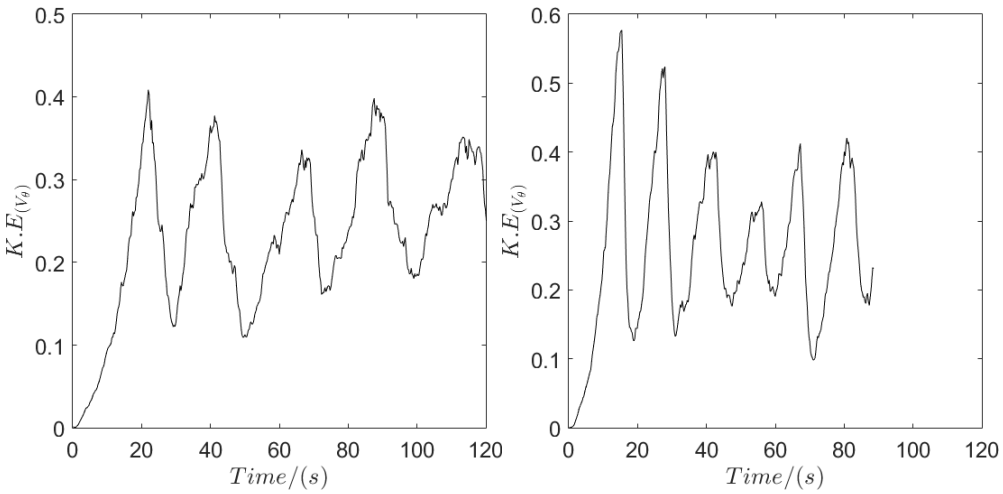

(a) (b)

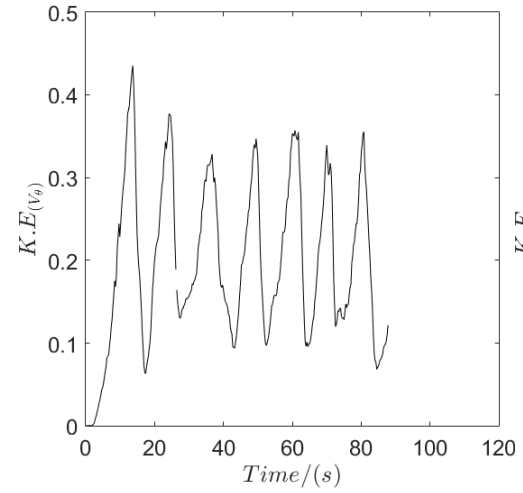
0.5
0.4
0.3
0.2
0.1
0
$K.E_{(V_\theta)}$
0
20
40
60
80
100
120
$Time/(s)$

(c)

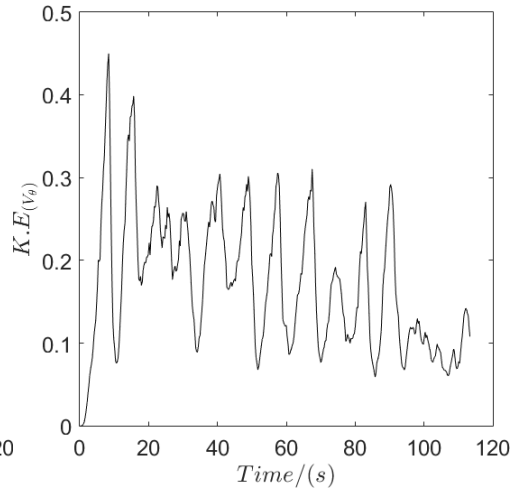
0.5
0.4
0.3
0.2
0.1
0
$K.E_{(V_\theta)}$
0
20
40
60
80
100
120
$Time/(s)$

(d)

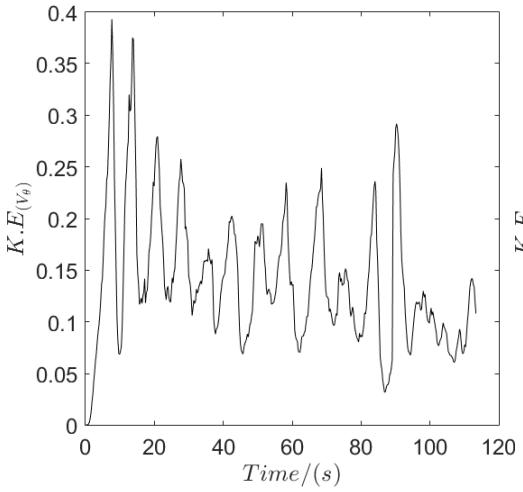
0.4
0.35
0.3
0.25
0.2
0.15
0.1
0.05
0
$K.E_{(V_\theta)}$
0
20
40
60
80
100
120
$Time/(s)$

(e)

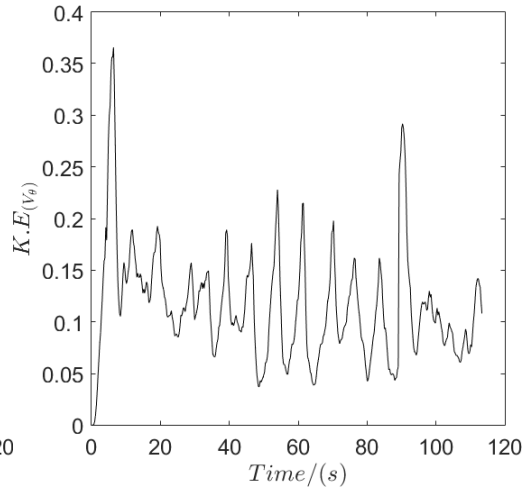
0.4
0.35
0.3
0.25
0.2
0.15
0.1
0.05
0
$K.E_{(V_\theta)}$
0
20
40
60
80
100
120
$Time/(s)$

(f)

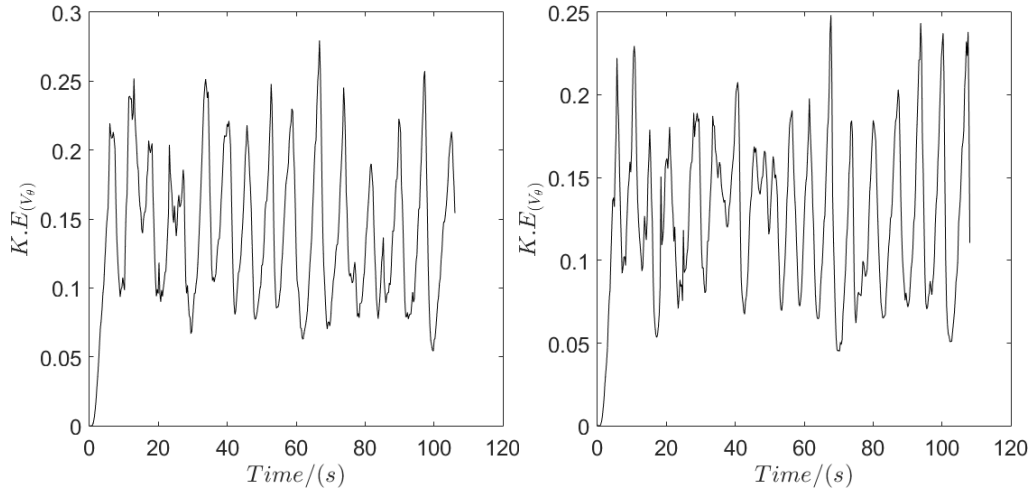

(g) (h)

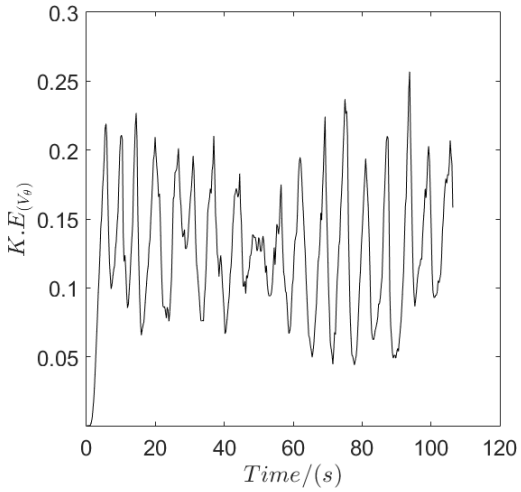

(i)

Figure 6.19: Temporal variation of kinetic energy associated with azimuthal velocity for different background rotations rates, for a jet with Re_0 = 2300 at z/d = 0.5 ; the rotation rates, in units of rad s^{-1}, associated with sub figures are: (a) 0.21, (b) 0.31, (c) 0.41, (d) 0.52, (e) 0.63, (f) 0.73, (g) 0.83, (h) 0.94, (i) 1.05.

The nine Fourier spectra associated with the data for $K.E_{(v_\theta)}$ in figure 6.19 are displayed in figure 6.20. The formation-breakdown frequency f_θ is associated with the dominant peak in the spectra. The frequencies for these peaks, for jets at Re_0 = 2300 and Re_0 = 16000, at different rotational frequencies f_T, are

displayed in figure 6.21. The two least-squares interpolations of the two data set for Re_0 = 2300 and Re_0 = 16000 are given by, respectively, $f_\theta = 0.84 f_T$ and $f_\theta = 1.57 f_T$ and they are identified by the solid line and the dashed line, respectively.

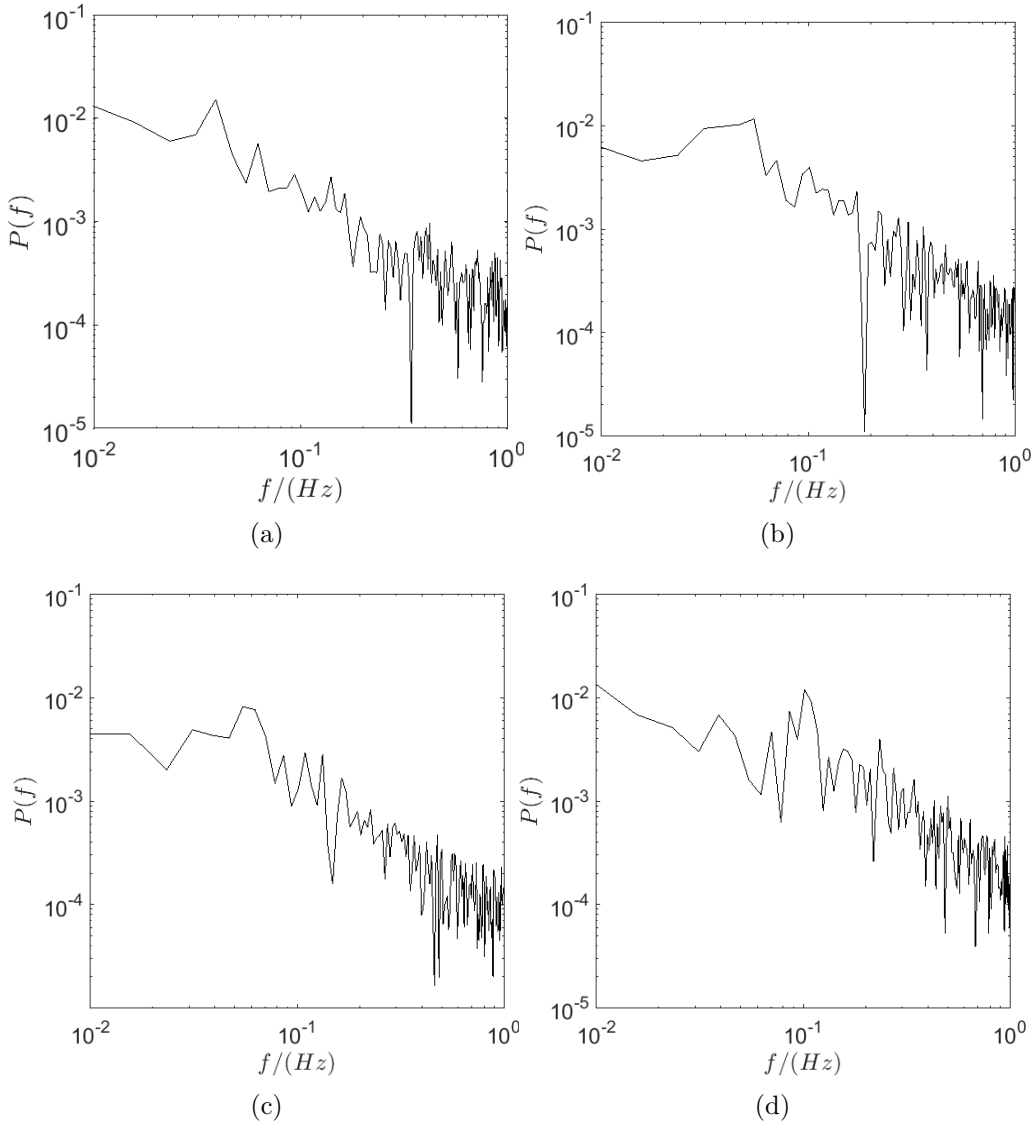

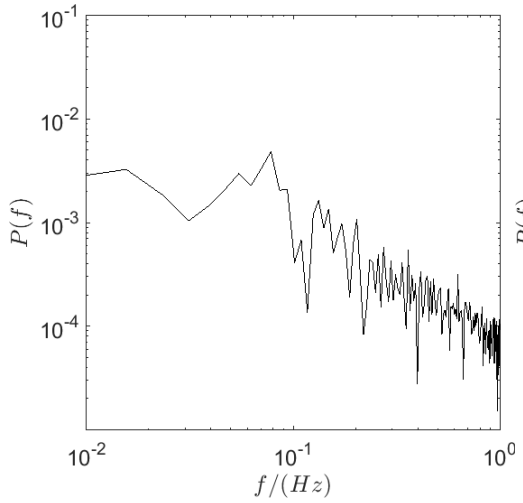
10^{-1}
10^{-2}
10^{-3}
10^{-4}
$P(f)$
10^{-2}
10^{-1}
10^{0}
$f/(Hz)$

(e)

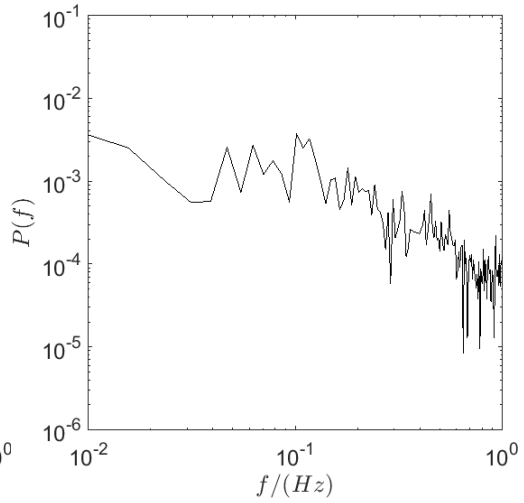
10^{-1}
10^{-2}
10^{-3}
10^{-4}
10^{-5}
10^{-6}
$P(f)$
10^{-2}
10^{-1}
10^{0}
$f/(Hz)$

(f)

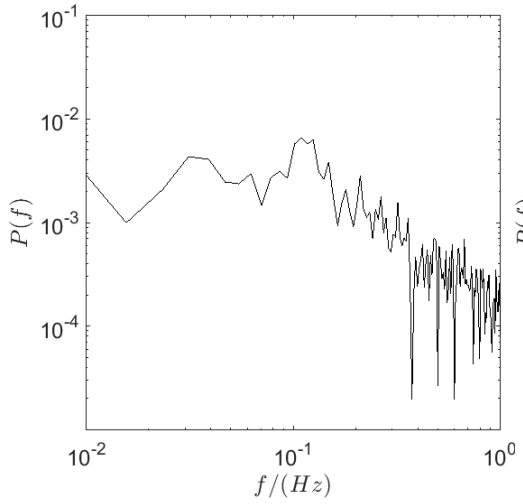
10^{-1}
10^{-2}
10^{-3}
10^{-4}
$P(f)$
10^{-2}
10^{-1}
10^{0}
$f/(Hz)$

(g)

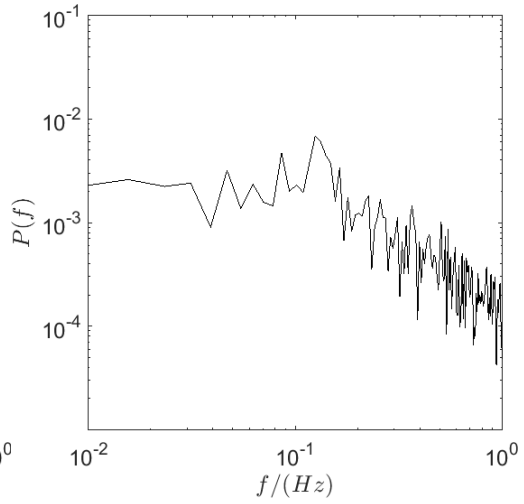
10^{-1}
10^{-2}
10^{-3}
10^{-4}
$P(f)$
10^{-2}
10^{-1}
10^{0}
$f/(Hz)$

(h)

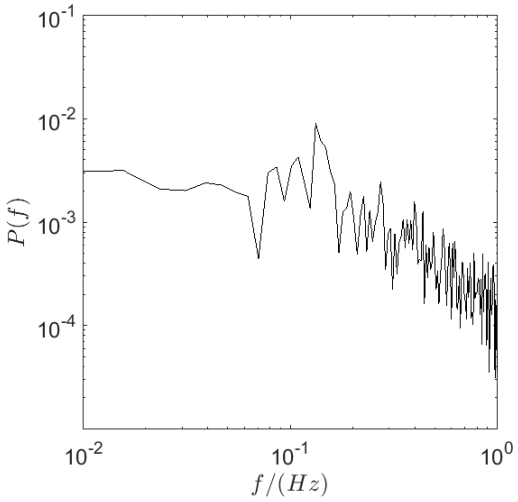

(i)

Figure 6.20: Fourier spectra for the temporal variation of $K.E_{(v_\theta)}$ for different background rotations rates for a jet with Re_0 = 2300; the rotation rates, in units of rad s^{-1}, associated with sub figures are: (a) 0.2, (b) 0.31, (c) 0.41, (d) 0.52, (e) 0.63, (f) 0.73, (g) 0.83, (h) 0.94, (i) 1.05.

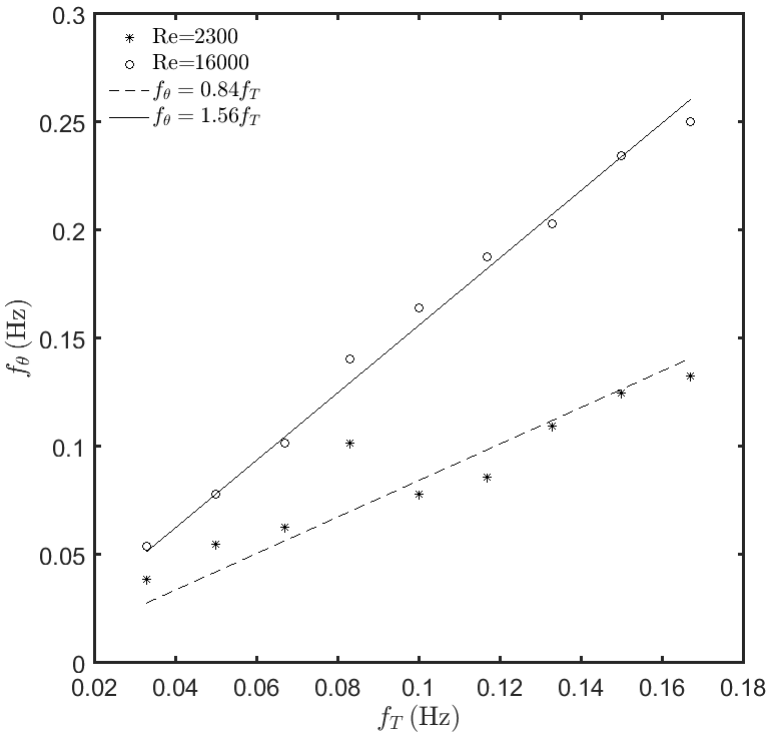

Figure 6.21: Formation-breakdown frequency, f_θ, of the jets as a function of the background-rotation frequency, $f_T = \Omega/2\pi$, of the turntable.

6.4.4 Kinetic Energy Associated with the Radial Velocity

The temporal variation of the kinetic energy associated with the radial velocity component is also investigated. Figures 6.22 (a) - (i) show the temporal fluctuations of $K.E_{(v_r)}$. The graphs in the figure qualitatively show, the same periodic, behaviour as in figure 6.19. But when the two figures, 6.19 & 6.22, are compared, it is clear that the data associated with the temporal variation of $K.E_{(v_\theta)}$ are less noisy than that of $K.E_{(v_r)}$. Therefore these data were not subjected to further analysis.

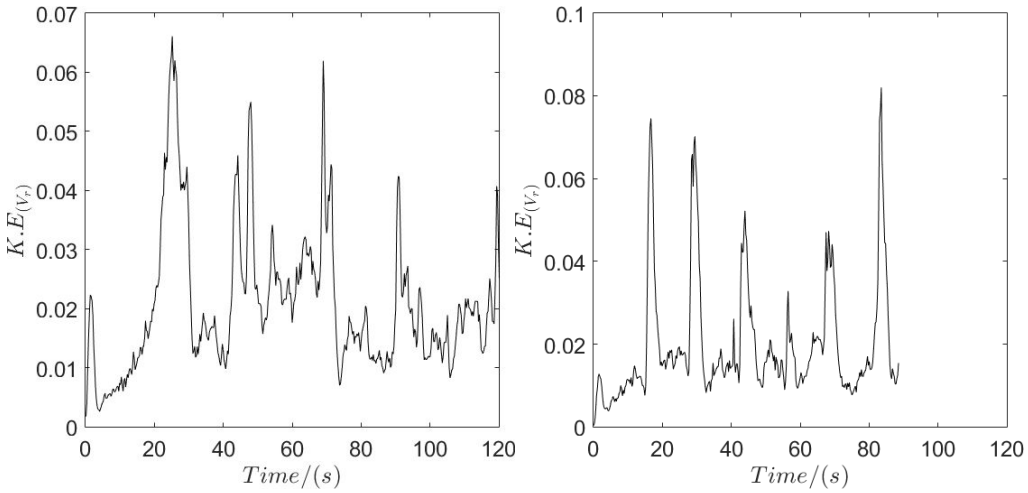

(a) (b)

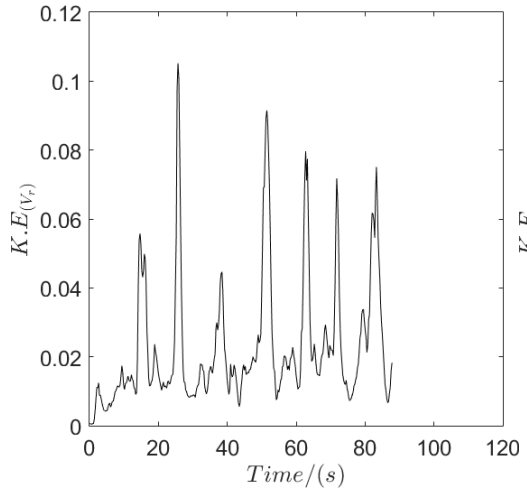
0.12
0.1
0.08
0.06
0.04
0.02
0
$K.E_{(V_r)}$
0
20
40
60
80
100
120
$Time/(s)$

(c)

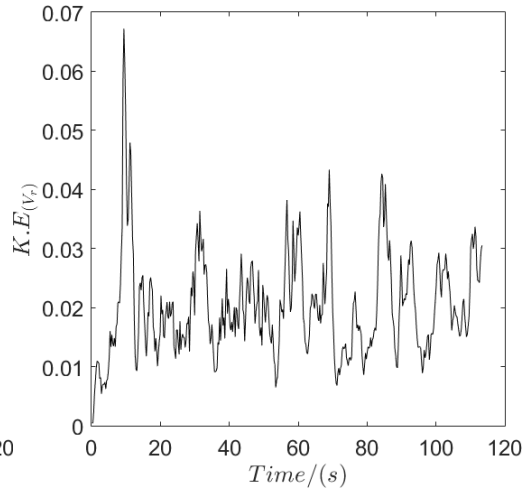
0.07
0.06
0.05
0.04
0.03
0.02
0.01
0
$K.E_{(V_r)}$
0
20
40
60
80
100
120
$Time/(s)$

(d)

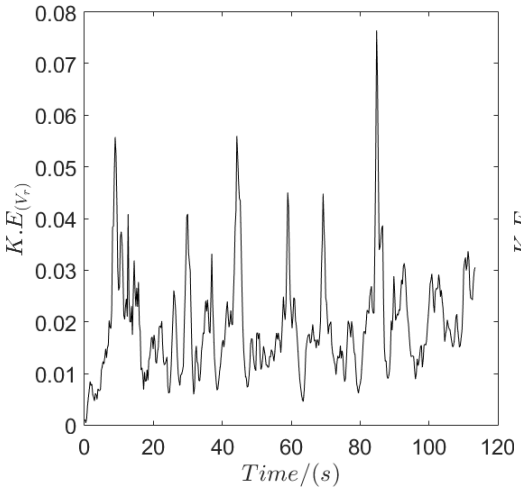
0.08
0.07
0.06
0.05
0.04
0.03
0.02
0.01
0
$K.E_{(V_r)}$
0
20
40
60
80
100
120
$Time/(s)$

(e)

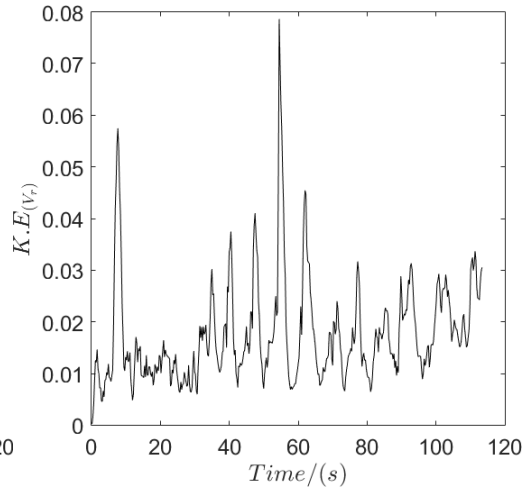
0.08
0.07
0.06
0.05
0.04
0.03
0.02
0.01
0
$K.E_{(V_r)}$
0
20
40
60
80
100
120
$Time/(s)$

(f)

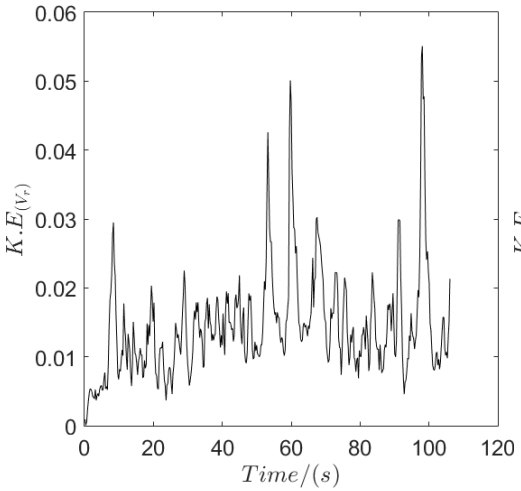

(g)

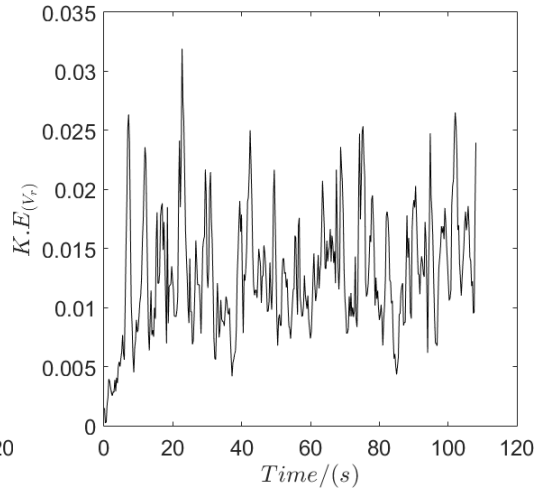

(h)

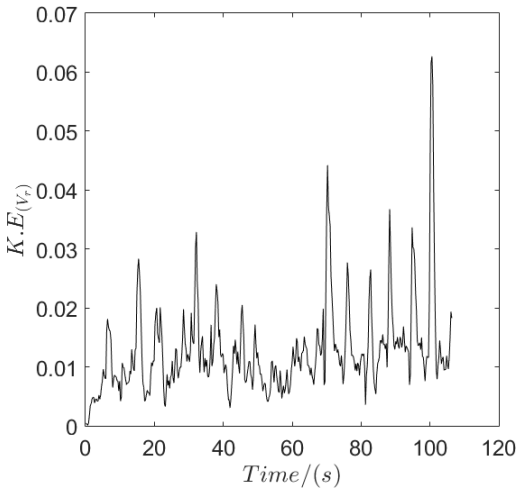

(i)

Figure 6.22: Temporal variation of the kinetic energy associates with the radial velocity component for different background rotations rates, for a jet with Re_0 = 2300 at z/d = 0.5; the rotation rates, in units of rad s^{-1}, associated with the photos which are: (a) 0.2, (b) 0.31, (c) 0.41, (d) 0.52, (e) 0.63, (f) 0.73, (g) 0.83, (h) 0.94, (i) 1.05.

6.4.5 Azimuthal Wave Number

Figure 6.2 revealed that the stem region of the jets develops into two, sometimes sporadically three, separate upward spiralling strands during the formation-breakdown cycle. This issue is investigated in more detail in this section to

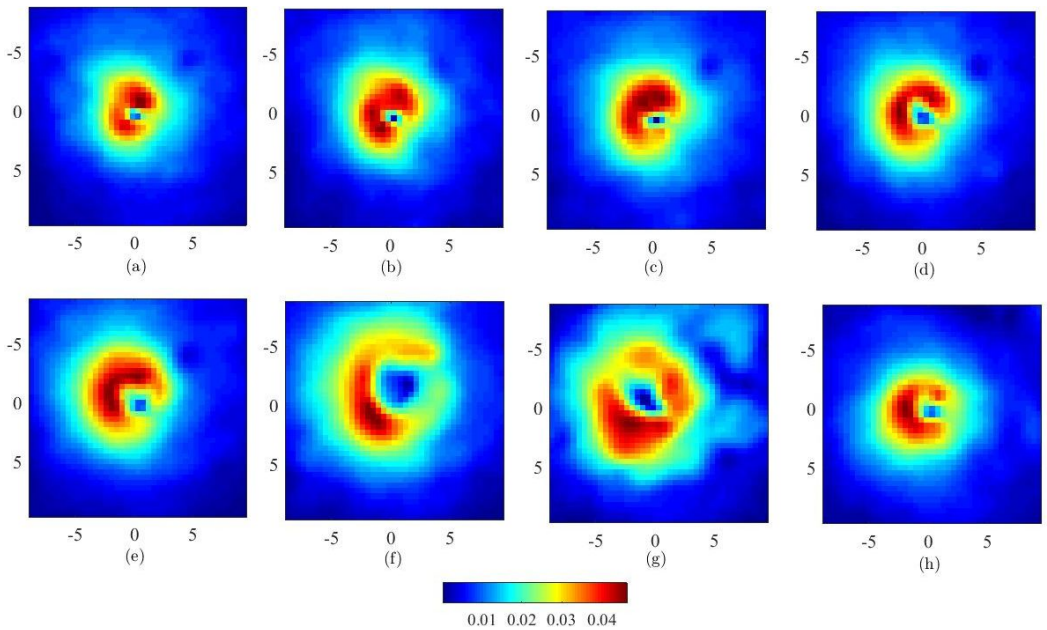

Figure 6.23: Temporal variation of magnitude of the instantaneous velocity for a jet with $Re_0 = 2300$ at $z/d = 0.5$ and $\Omega = 0.21$ rad s^{-1} for times: (a) 6 s, (b) 10 s, (c) 14 s, (d) 18 s,(e) 22 s, (f) 26 s, (g) 30 s, (h) 34 s .

enable a more quantitative characterisation of how frequently these different modes of the jet are observed. Figures 6.23 (a) - (h) show examples for the variation of the instantaneous horizontal velocity field during a formation-breakdown cycle. Here the process of the stem dividing into two strands is identified through a single high-velocity region in the vicinity of the centre of the swirling structure undergoing transition to two separate high-velocity regions. This process of mode transition can be identified in figure 6.23 (b) - (d), at $z/d = 0.5$, where one can see two high-velocity regions in figure 6.23 (b) which have combined into a single high-velocity region in figure 6.23 (c) whereas figure 6.23 (d) once again displays two separate high-velocity regions. The number of high velocity regions, characterizes the mode of the jet and is referred to as $m = 1, 2, 3, ...$ The mode m can be obtained from a Fourier transformation of the circumferential instantaneous velocity profiles and as a function of the nondimensionalised distance, r/d, from the centre of the flow structure. These Fourier spectra are shown in figures 6.24 (a) - (h) for eight instants in time and, each time, at eight radial locations in the range $0.5 \leqslant r/d \leqslant 4$. Reference to figure 6.24 reveals a substantial presence of mode $m = 2$ in figure 6.24 (a), (d)

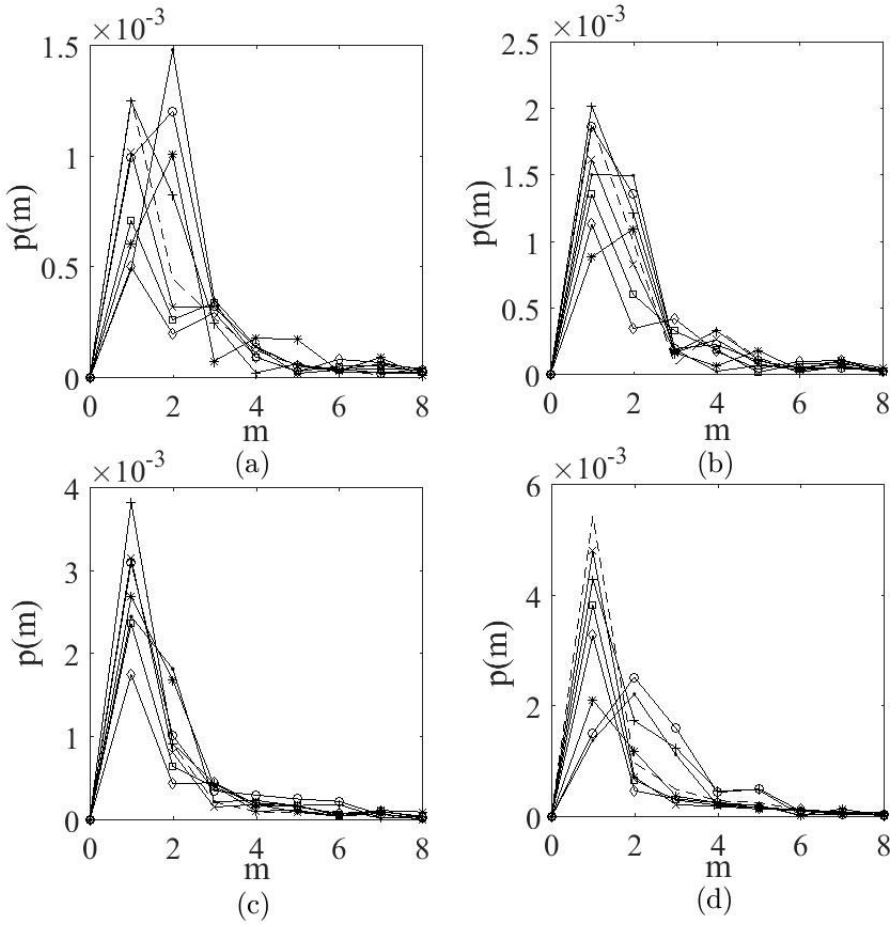

Figure 6.24: Variation of azimuthal wave number, at $z/d = 0.5$, for eight radial locations, $0.5 \leqslant r/d \leqslant 4$, for a jet with $Re_0 = 2300$ at $\Omega = 0.21$ rad s^{-1} for times: (a) 6 s, (b) 10 s, (c) 14 s, (d) 18 s, (e) 22 s, (f) 26 s, (g) 30 s, (h) 34 s.

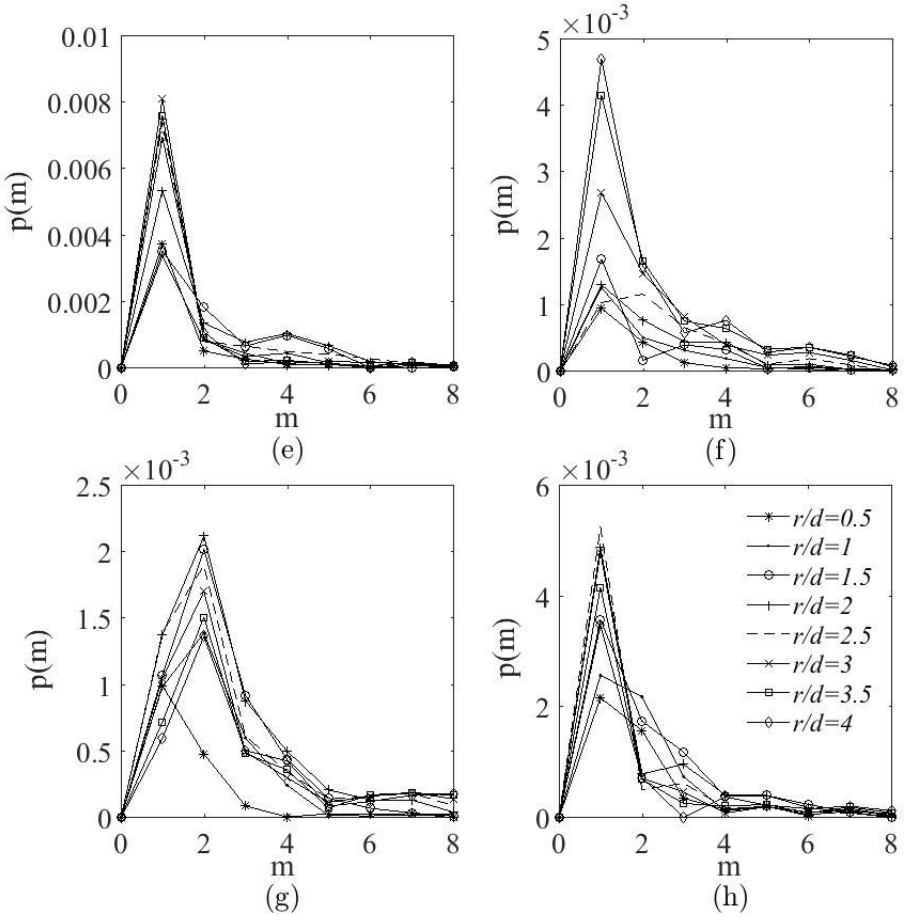

Figure 6.24: Continued.

and, in particular, in (g) whereas cases (b), (c), (e), (f) and (h) are dominated by mode $m = 1$. In summary it is concluded that both the single helical mode, $m = 1$, and the double-helical mode, $m = 2$, coexist but that mode $m = 1$ generally dominates the flow during the formation-breakdown cycles of the jet.

6.4.6 Local Rossby Number

It is reasonable to assume that the dynamics of the jets, at any particular given height above the source, depend on a local velocity scale and a local length scale and that the global value Ro_0 is not the most appropriate, and dynamically relevant, definition for the Rossby number. The analysis of our PIV measurements yielded data for the circumferentially-averaged profiles of the azimuthal velocity component (figure 6.16) throughout the formation-breakdown cycles of the jets. Therewith it is possible to calculate an alternative, dynamically more relevant, instantaneous, local Rossby number analogous to the definition used in Kloosterzielt & Heijst (1991) for vortices in a rotating fluid. This instantaneous, local Rossby number, as in equation 3.23 is based on the radial location, $r^{max}(t)$, where the velocity profiles in figure 6.16 reach their maximum and the maximum velocity value $\overline{v}_\theta^{max}(t)$ at this location. The values of $Ro_l(t)$ must be expected to vary with the height z/d above the source where the profiles of $\overline{v}_\theta(t)$ were measured. In order to characterise the jets we will, therefore, consider the value of $Ro_l(t)$ in the immediate vicinity of the source at $z/d = 0.5$. Figures 6.25 (a) - (i) display the temporal variation of $Ro_l(t)$, at this height for a jet with $Re_0 = 2300$, and for nine background rotation rates. It can clearly be observed that $Ro_l(t)$ has periodic behaviour and the period decreases when rate of the background rotation increases.

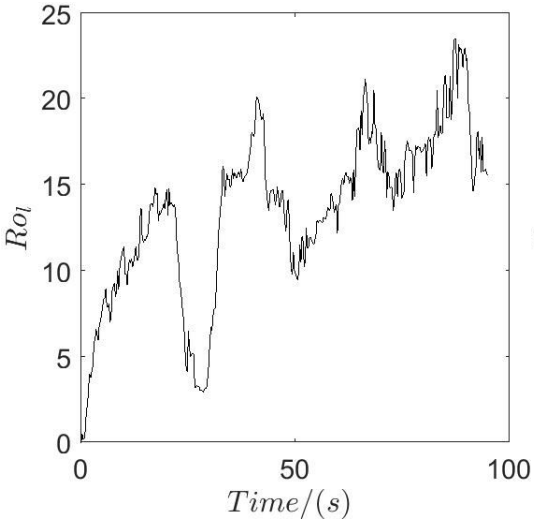
25
20
15
10
5
0
Ro_l
0
50
100
$Time/(s)$

(a)

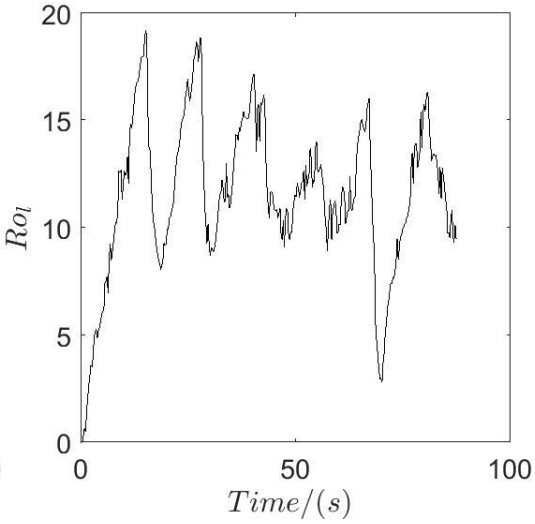
20
15
10
5
0
Ro_l
0
50
100
$Time/(s)$

(b)

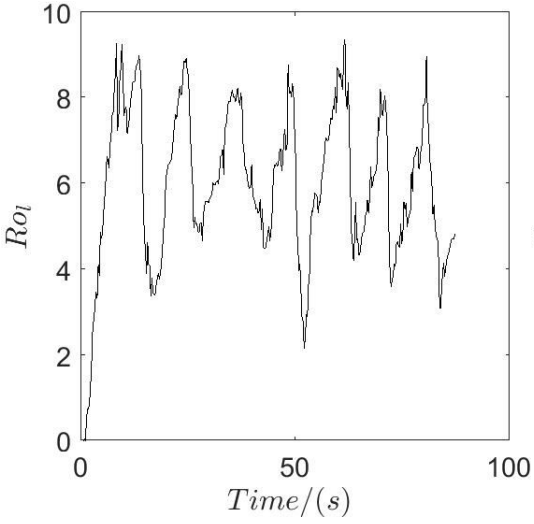
10
8
6
4
2
0
Ro_l
0
50
100
$Time/(s)$

(c)

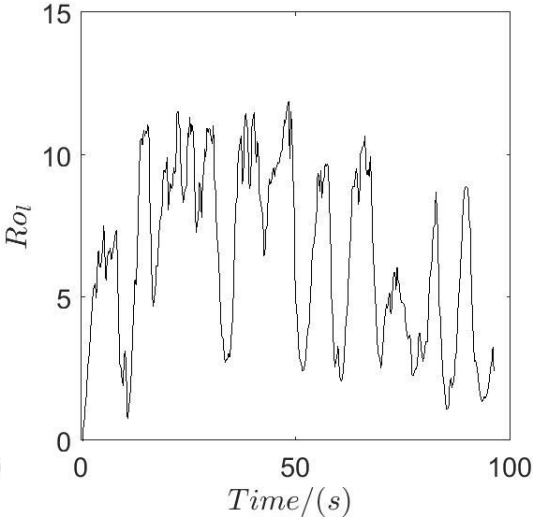
15
10
5
0
Ro_l
0
50
100
$Time/(s)$

(d)

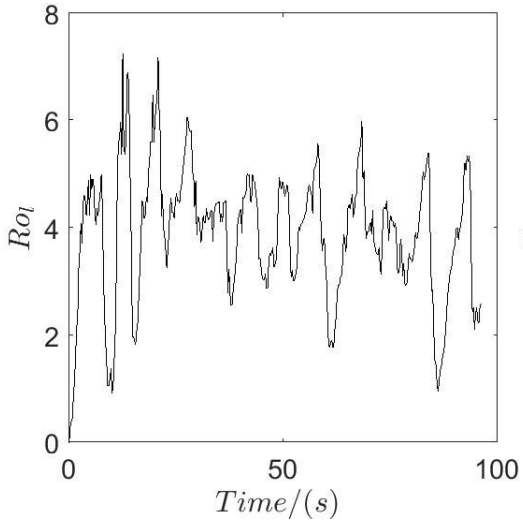
8
6
4
2
0
Ro_l
0
50
100
$Time/(s)$

(e)

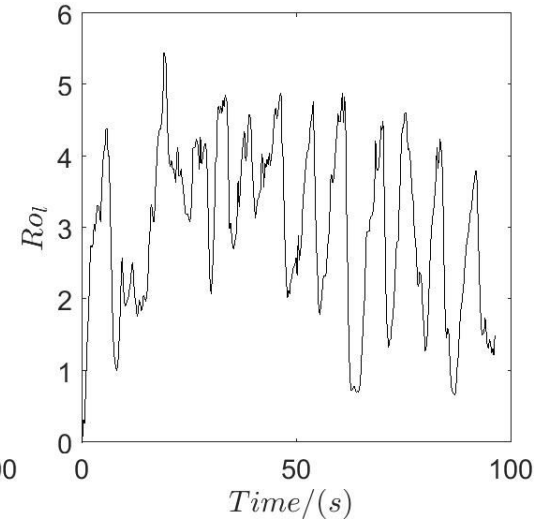
6
5
4
3
2
1
0
Ro_l
0
50
100
$Time/(s)$

(f)

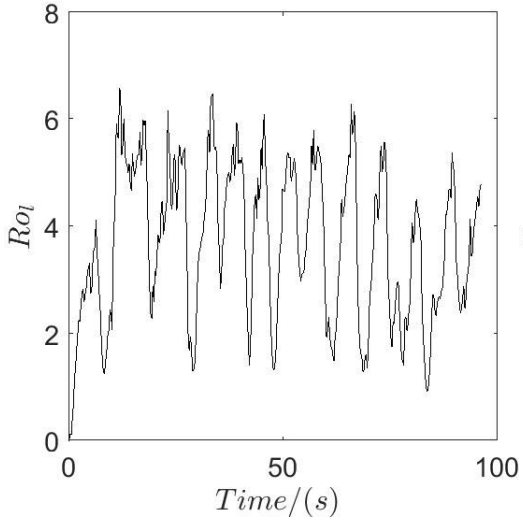
8
6
4
2
0
Ro_l
0
50
100
$Time/(s)$

(g)

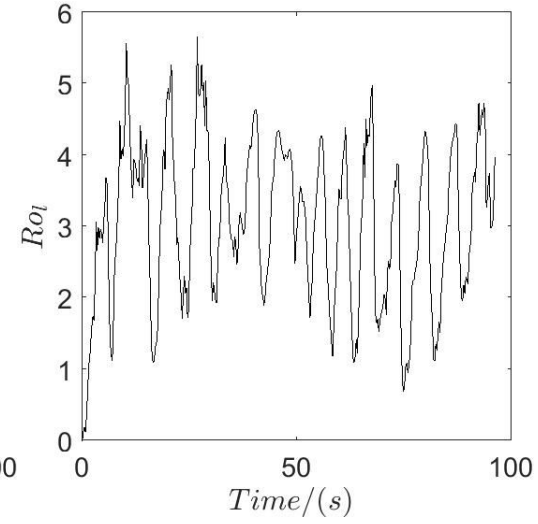
6
5
4
3
2
1
0
Ro_l
0
50
100
$Time/(s)$

(h)

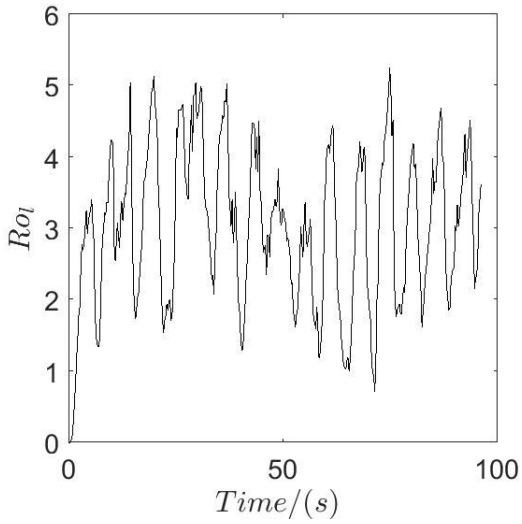

(i)

Figure 6.25: Variation of the instantaneous, local Rossby number Ro_l with time for a jet with Re = 2300, at z/d = 0.5, with different background rotations rates; the rotation rates, in units of rad s^{-1}, associated with the sub figures are: (a) 0.2, (b) 0.31, (c) 0.41, (d) 0.52, (e) 0.63, (f) 0.73, (g) 0.83, (h) 0.94, (i) 1.05.

The two quantities, Ro_l^U & Ro_l^L, were calculated from the data associated with figures 6.25 (a) - (i). Ro_l^U is the mean value of all the maxima for each graph whereas Ro_l^L is the mean value of all the minima for each graph in the figure. Figure 6.26 displays the variation of Ro_l^U and Ro_l^L with background rotation rate Ω. The solid line curve and the dashed line curve respectively represent the least square power curve fit for Ro_l^U and Ro_l^L. The least square fits led to two relationships $Ro_l^U = 4.65\Omega^{-1.05}$ and $Ro_l^L = 1.51\Omega^{-1.24}$. Moreover the mean value of the local Rossby number, $\overline{Ro_l}$, at each height was also calculated to see the variation of $\overline{Ro_l}$ with both background rotation rate and the vertical axial distance from the source. Figure 6.27 displays the variation of $\overline{Ro_l}$ with background rotation for heights $z/d = 0.5, 5$ & 10. The solid line curve represents the least-squares power-law curve fit, for $\overline{Ro_l}$ at z/d = 0.5, which gives the relationship $\overline{Ro_l} = 3.06\Omega^{-1.11}$. The dashed-line curve represents the least-squares power-law curve fit for $\overline{Ro_l}$ at z/d = 5 which gives the relationship $\overline{Ro_l} = 0.26\Omega^{-1.61}$, whereas the dotted line curve represents the least-squares power-law curve fit for $\overline{Ro_l}$ at z/d = 10 which gives the relationship $\overline{Ro_l} = 0.26\Omega^{-1.61}$. The figure reveals that the mean value of local Rossby number

does not vary drastically within the horizontal planes of the jet at heights $z/d = 5$ and $z/d = 10$. But values of $\overline{Ro_l}$ at these two heights are comparatively lower than that of the horizontal plane at $z/d = 0.5$, for every background rotation rate.

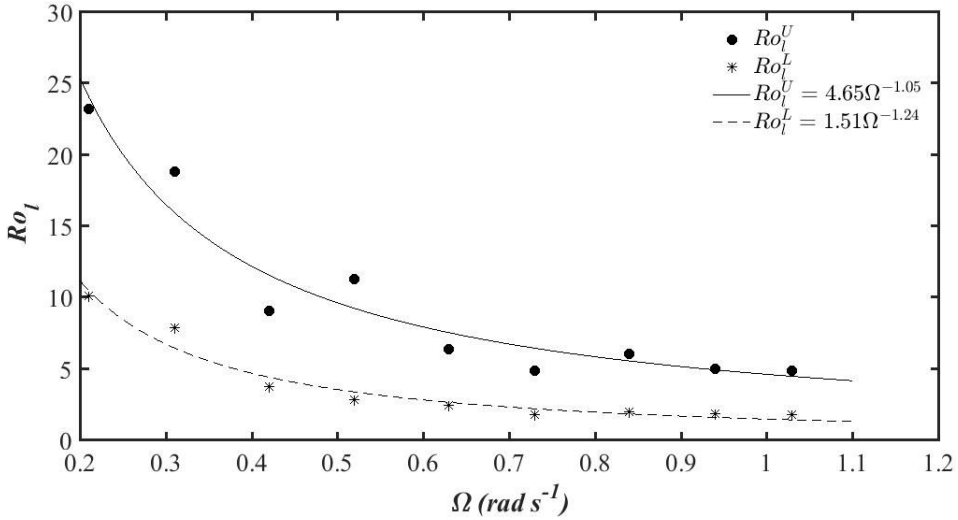

Figure 6.26: Variation of the mean maximum and minimum local Rossby number with background rotation for a jet with $Re = 2300$, at $z/d = 0.5$.

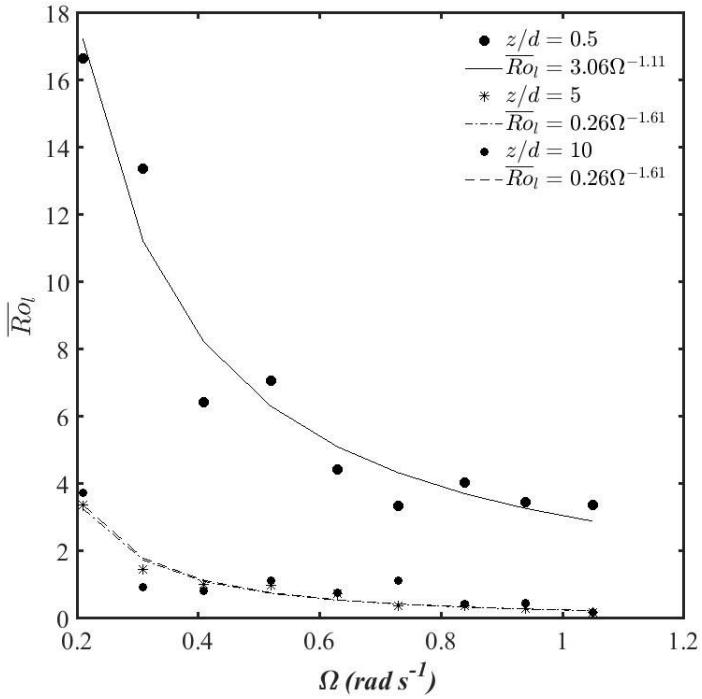

Figure 6.27: Variation of the mean local Rossby number $\overline{Ro_l}$ with background rotation for a jet with Re = 2300, at z/d = 0.5, z/d = 5 & z/d = 10.

Figure 6.28 summarizes the available data for Ro_l^U and Ro_l^L at the two Reynolds numbers Re_0 = 2300 and Re_0 = 16000 over the associated ranges of values for the global Rossby number, Ro_0, for which experiments were conducted. The data for Re = 2300 are displayed as the squares at the lower end of the range of Ro_0 in figure 6.28 where Ro_l^U corresponds to the black squares while Ro_l^L is identified by the open squares. Correspondingly the data for Re = 16000 are displayed as circles, where black circles identify Ro_l^L and open circles Ro_l^U. The lines interpolating the data for Re = 2300 in figure 6.28 are linear least-squares fits given by $Ro_l^U = 0.011Ro_0 - 4$ and $Ro_l^L = 0.05Ro_0 - 0.21$. The additive constants for both these data interpolations are small, compared to Ro_l^U and Ro_l^L. Moreover, it is evidently required that both Ro_l^U and Ro_l^L approach zero as $Ro_0 \to 0$, that is when the ejection velocity, u_0 vanishes and when there exists no jet. Consequently one can assume that the additive constants reflect measurement errors and, therefore, neglect them. Therewith one can conclude that $Ro_l^U \propto \Omega^{-1}$ and $Ro_l^L \propto \Omega^{-1}$.

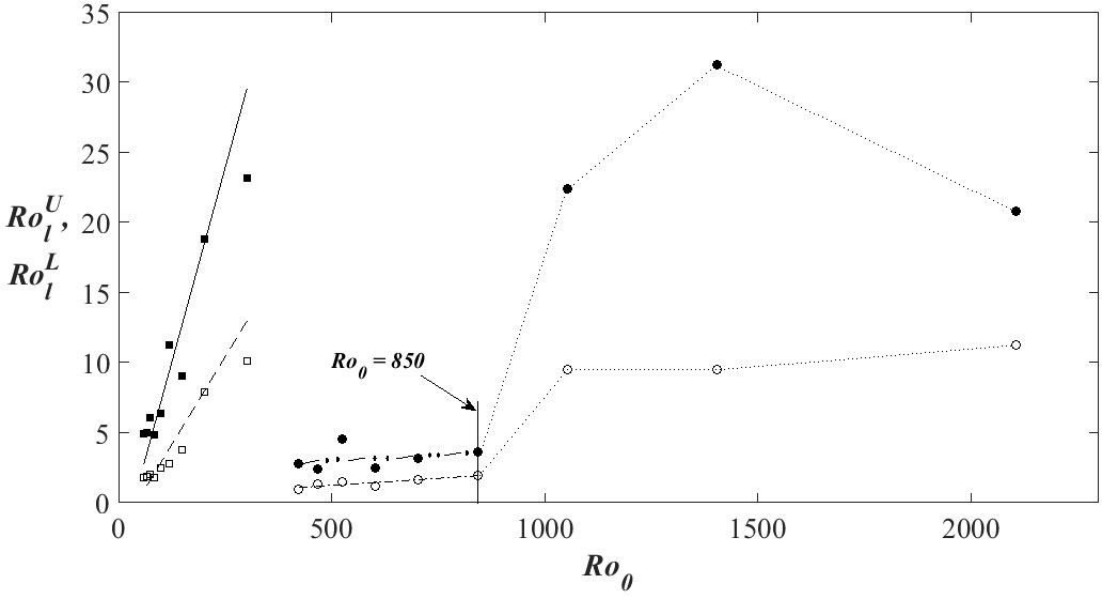

Figure 6.28: The mean values of the maximum and minimum local Rossby number, Ro_l^U and Ro_l^L, as a function of the global Rossby number, Ro_0 at height $z/d = 0.5$ above the source. For $Re_0 = 2300$: Upper Limit, ■, $-, Ro_l^U = 0.011Ro_0 - 4$; Lower Limit, □, $--, Ro_l^L = 0.05Ro_0 - 0.21$. For $Re_0 = 16000, Ro_0 \leq 850$: Upper Limit, •, $-..-, Ro_l^U = 0.0015Ro_0 + 2.27$; Lower Limit, ∘, $. - ., Ro_l^L = 0.002Ro_0 + 0.27$.

6.5 Behaviour of the Jet in the Horizontal Plane after Continuation of the Jet for Long Time

After revealing the formation-breakdown nature of the jet subjected to background rotation, it was decided to investigate the behaviour of the jet after comparatively long time of ejection of liquid from the source had started. Therefore the PIV measurements were conducted at the horizontal plane, z/d = 5, after continuing the liquid ejection from the source, approximately for 30 minutes. Figures 6.29 (a) - (p) show the development of the instantaneous velocity fields in the horizontal plane at height z/d = 5 above the source, for a jet with Re_0 = 2300 and background rotation Ω = 0.21 rad s^{-1}. Figure 6.29 (a) shows the jet, approximately 1800 s after ejection of liquid from the source had commenced. Due to the fact that the entrainment velocity gets affected by the Coriolis force, a cyclonic vortex has formed. Thus the figure appears to suggest that the jet is propagating through the horizontal plane. Around 184 s, in figure 6.29 (b), the radius of the vortex has further increased. But in figure 6.29 (c) the vortex starts to break from a point at the outer circumference and this break up further develops as can be seen in figures 6.29 (d), (e) and (f). Thereafter, in figures 6.29 (g), (h) and (i), the vortex is reforming for a time interval of 12 s. The same breaking up of the vortex as earlier can be observed again in figures 6.29 (j), (k), (l) and (m) and also reforming of the vortex can be observed in figures 6.29 (n), (o), and (p). The observations from these figures prove that the breaking-reformation cycle of the jet continues after comparatively long time of ejection of the liquid from the source had started. In figures 6.29 (a) - (p), there is an anticyclonic motion surrounded by the vortex can be seen. But the velocity, of the anticyclonic motion is much less than that of the cyclonic vortex motion. Therefore one can not observe the anticyclonic motion clearly.

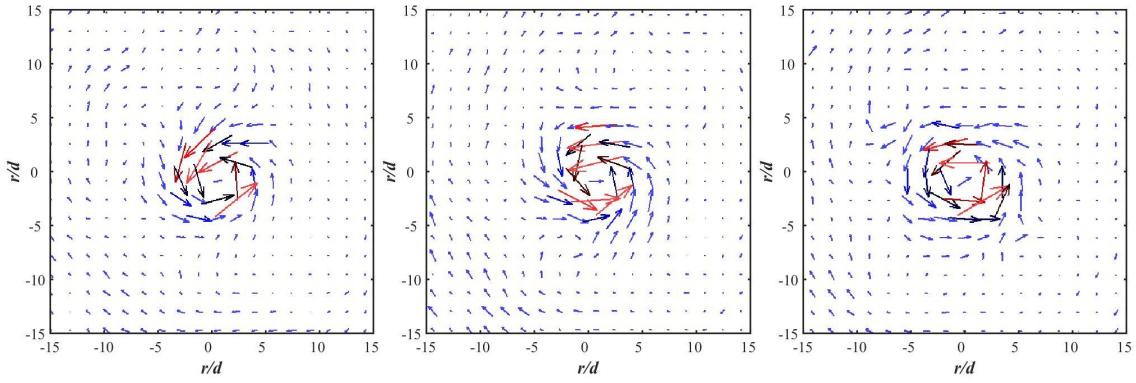

(a) (b) (c)

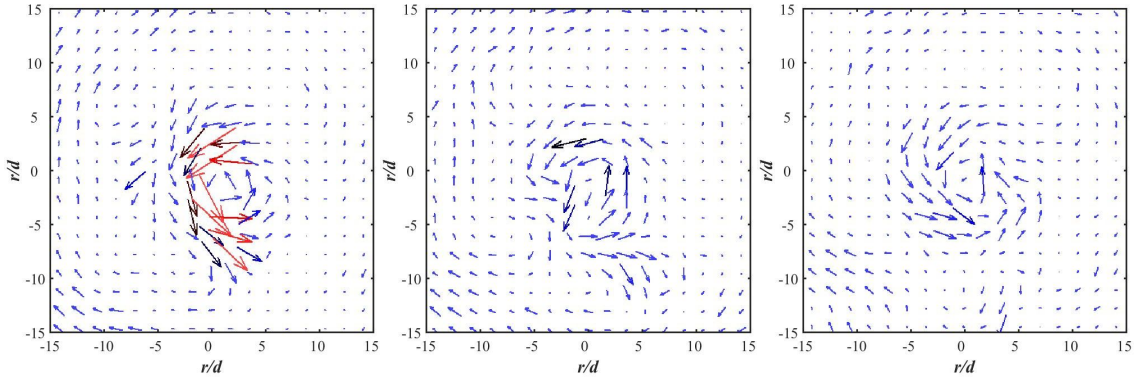

(d) (e) (f)

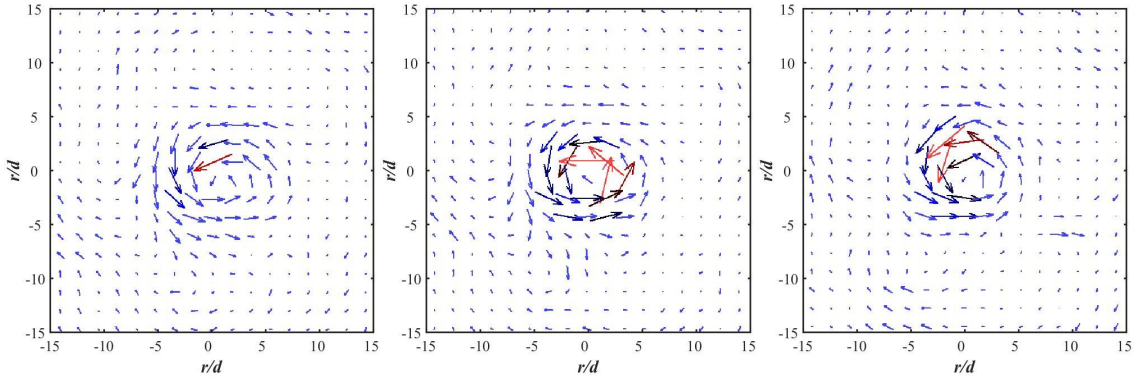

(g) (h) (i)

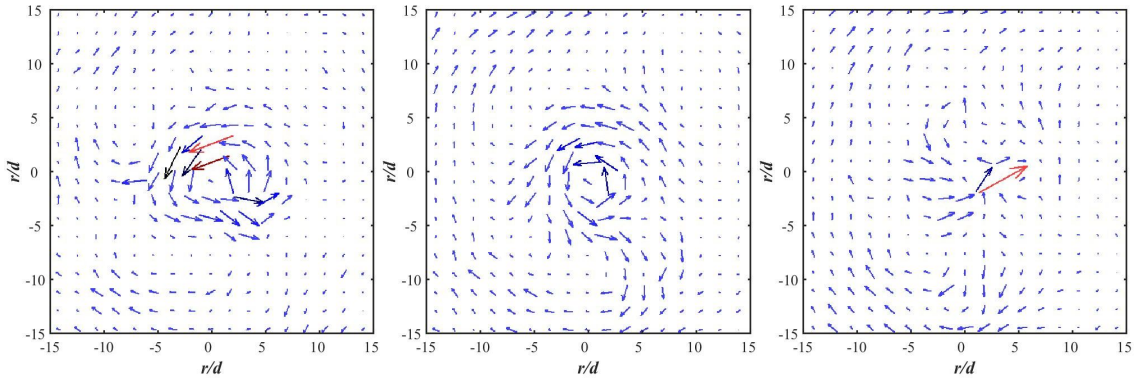

(j) (k) (l)

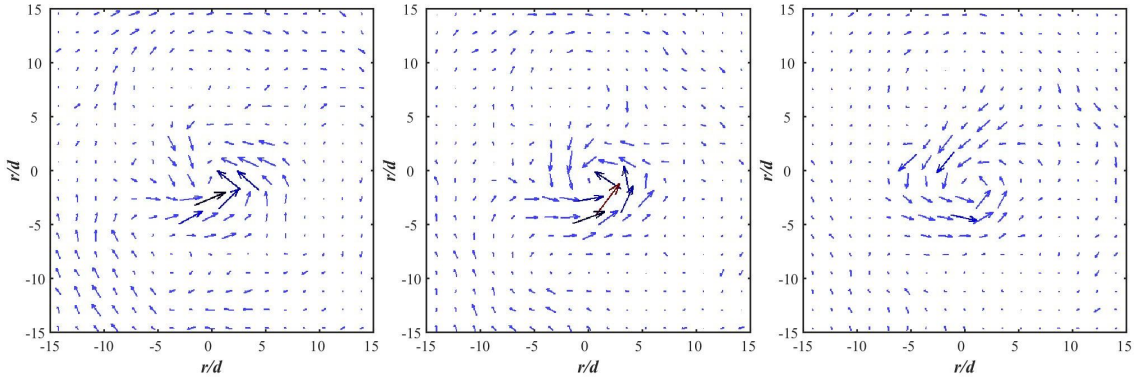

(m) (n) (o)

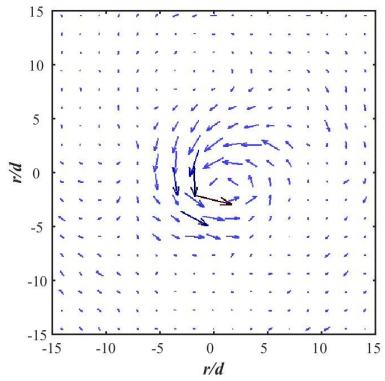

(p)

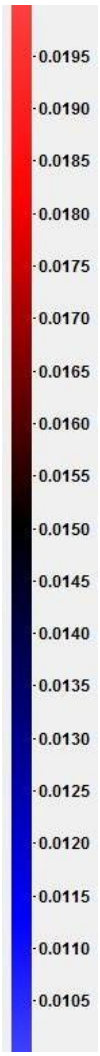

(q)

Figure 6.29: Instantaneous vector fields of the velocity components, u_r & u_θ for a jet with Re_0 = 2300 at Ω = 0.21 rad s^{-1} at times t for (a) 1800 s, (b) 1804 s, (c) 1808 s, (d) 1812 s, (e) 1816 s, (f) 1820 s, (g) 1824 s, (h) 1828 s, (i) 1832 s, (j) 1836 s, (k) 1840 s, (l) 1844 s, (m) 1848 s, (n) 1852 s, (o) 1856 s, (p) 1860 s at z/d = 5.

In order to clearly display the anticyclonic flow surrounding the jet a series of instantaneous velocity vector fields of the jet subjected to a higher background rotation rate was selected. Figure 6.30 (a) - (p) shows the instantaneous velocity-vector fields in the horizontal plane at z/d = 5, for a jet with Re_0 = 2300 and background rotation 0.63 rad s^{-1}. Figure 6.30 (p) shows the colour map for the velocity vectors. Figure 6.30 (a) displays the instantaneous velocity-vector field approximately 180 s after ejection of liquid had started. The cyclonic vortex, appear in the figure due to the entrainment velocity of the jet, implies that the jet is propagating through this horizontal plane. In addition to that the figure reveals an anti-cyclonic flow surrounding the cyclonic vortex. In figure 6.30 (b) the velocity of the fluid within the vortex has reduced, implying that the strength of the cyclonic vortex has reduced. At the same time some velocity vectors in the outer circumference of the vortex show radially outward flow. Therefore one can conclude that the jet is breaking up. In figure 6.30 (c), the cyclonic vortex can be seen again implying that the jet has reformed. But again in figure 6.30 (d) the vortex appears to be breaking whereas in figure 6.30 (e) three co-rotating vortices can be seen with comparatively low velocity vectors. Therefore it can be assumed that there is no entrainment velocity is present in this plane. Hence it can be concluded that at this instance, which is 196 s after starting the jet, the jet is not propagating through this plane. The jet reappears in figure 6.30 (f), and one can clearly see that it breaks in figure 6.30 (g) and completely disappears in figure 6.30 (h). Note that these figures correspond to a comparatively higher background rotation rate and the formation-breakdown frequency of the jet is much higher than that of the jet shown in figures 6.29 (a) - (p). It is evident from the figure that a strong anticyclonic motion has developed around the jet after comparatively long times after ejection of liquid from the source had started.

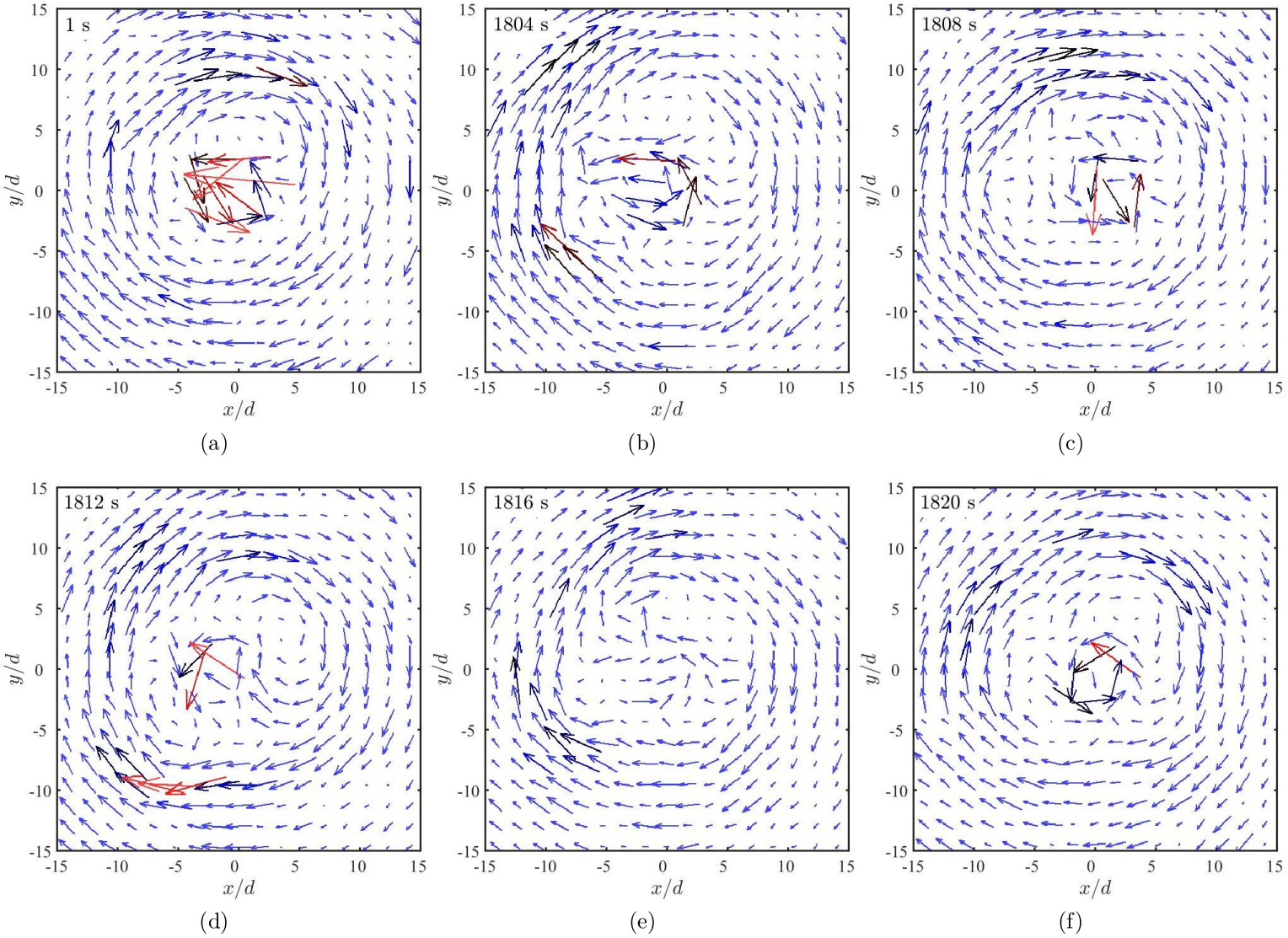

Figure 6.30: Instantaneous vector fields of the velocity components, u_r & u_θ for a jet with $Re_0 = 2300$ at $\Omega = 0.63$ rad s^{-1} at times t for at $z/d = 15$.

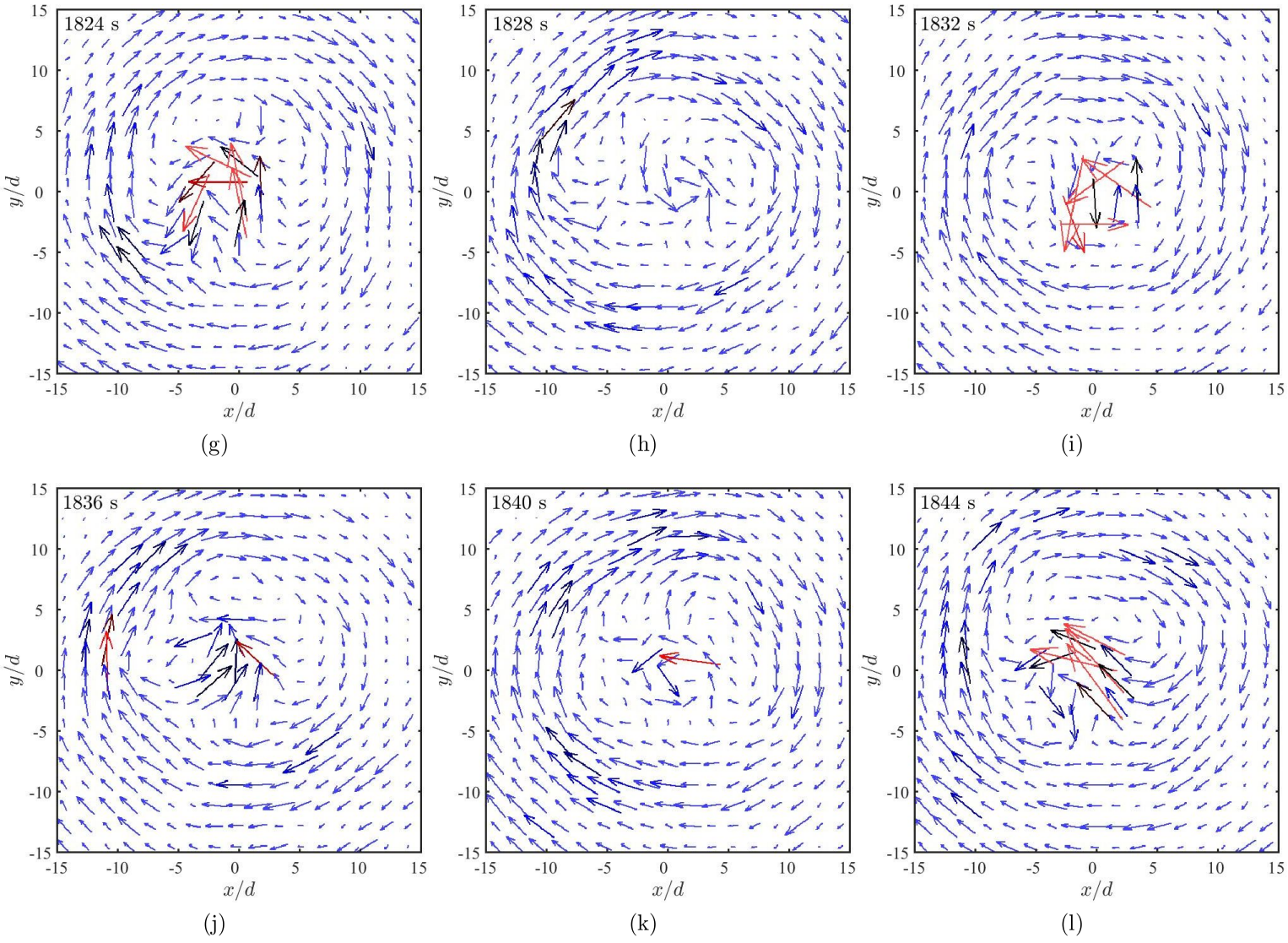

Figure 6.30: Continued.

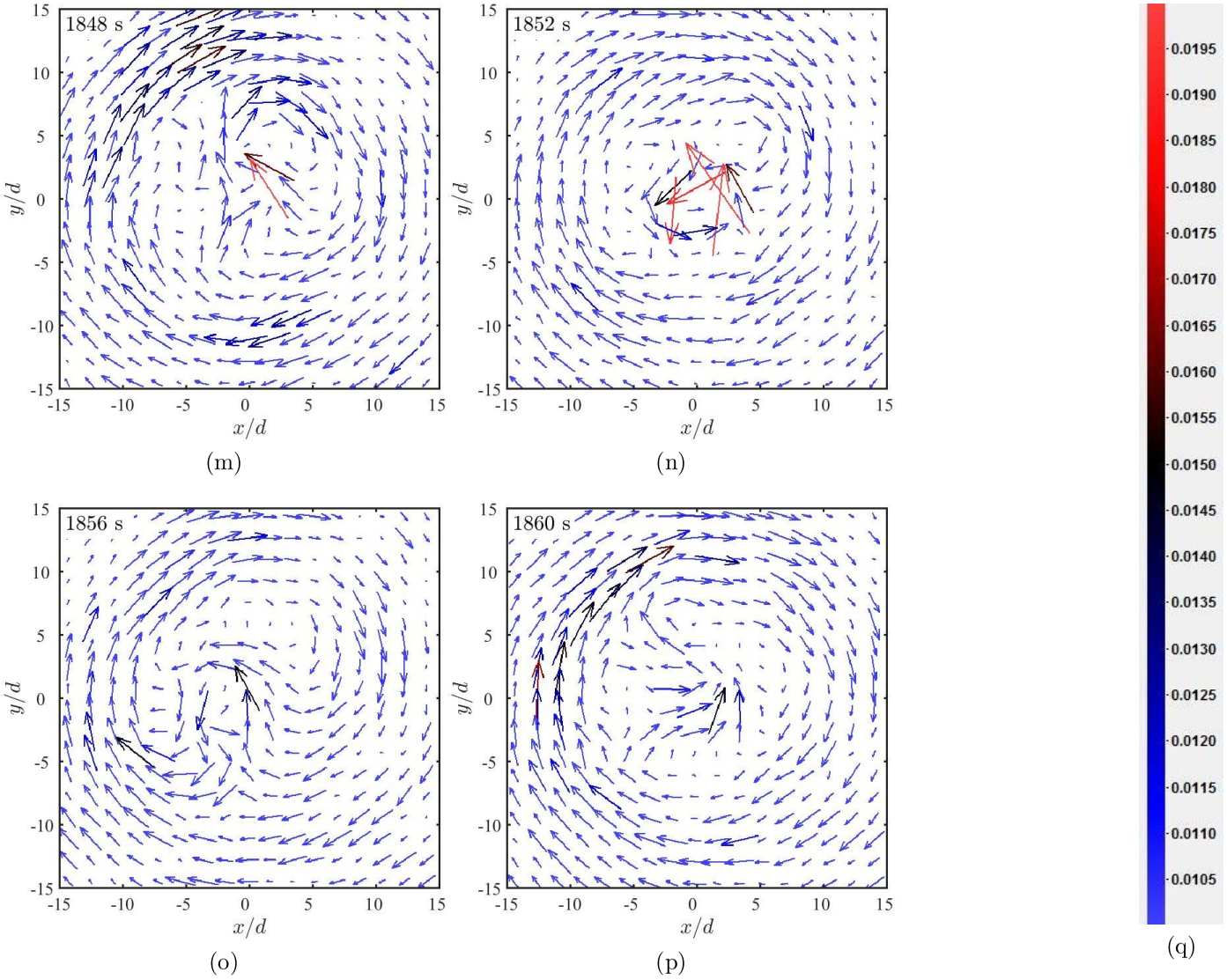

Figure 6.30: Continued.

Chapter 7

Proper Orthogonal Decomposition Analysis

7.1 Introduction

Turbulent flows are characterised by both large scale motions and small scale motions even though turbulent flow motions itself is incoherent. However, it is well established that large-scale organized motions are present and these are referred to as 'coherent structures'. Proper Orthogonal Decomposition (POD) represents a tool to identify such coherent structures in turbulent flow (Patte-Rouland *et al.*, 2001; Vanierschot *et al.*, 2014). Therefore the data obtained from the PIV measurements were analyzed by means of this method. The POD technique was first used in the study of turbulent flows by Lumley (1967). It is also known as Principal Component Analysis (PCA). According to the review written by Berkooz *et al.* (1993), the POD analysis was independently discovered by Kosambi (1943), Loeve (1945), Karhunen (1946), Pougachev (1953), and Obukhov (1954). Details of the POD analysis method are described in Joliffe (2002).

There exist two different variations of the POD analysis technique. One method is referred to as classical POD and this was introduced for turbulent flows by Lumley (1967). The second technique is the snapshot methodology which was introduced by Sirovich (1987). The classical method is normally

applied to problems with low spatial resolution whereas the snapshot method finds its applications in the context of problems with high spatial resolution and lower temporal resolution. This is due to the fact that the dimension of the eigenvalue problem in each POD method strictly depends on either spatial resolution or temporal resolution (refer equation 3.31). In the present study the snapshot POD method was adopted for analysis.

7.2 POD Modes of the Jet with Background Rotation

7.2.1 Horizontal Plane

The data discussed in this section were obtained close to the source, at a height of $z/d = 0.5$. The vector fields from the PIV measurements were obtained, at a rate of 90 frames per second and they were averaged over successive periods of $\Delta t = 0.25$ s. This series of averaged vector fields was then subjected to the POD analysis. The total number of averaged frames used for the POD analysis was approximately 450, for each experiment, containing several formation-breakdown cycles. This number is sufficiently larger than the minimum of around four hundred frames required to capture the statistics of the first three POD modes for these types of flows (Patte-Rouland *et al.*, 2001; Vanierschot *et al.*, 2014). Figures 7.1 (a) - (i) show the first POD mode for nine background rotations as identified in the figure caption. Figures 7.2 (a) - (i) show the variation of corresponding temporal coefficients for the first POD modes shown in figures 7.1 (a) - (i). It can be seen that the time coefficients of the first POD mode corresponds to each background rotation rate, display regular temporal fluctuations occurring over approximately equal time intervals. This represents evidence for the regular occurrence and disappearance of the coherent structures associated with the POD modes and it therewith represents evidence for the existence of the formation-breakdown cycle described in Chapter 6. Furthermore figures 7.3 (a) - (c) display typical results obtained for the velocity-vector field, with superposed associated vorticity field, of the first three POD modes for a jet at $Re_0 = 2300$ with $\Omega = 0.21$ rad s^{-1}. In the figure the magnitude of the vorticity and velocity are identified by means of

the colour maps. Figure 7.3 (a) shows the first mode which reflects a Coriolis-induced circumferential, cyclonic flow velocity which is established when the primary, upward flow results in radial flow motion due to entrainment of ambient liquid into the jet. Figure 7.3 (b) and (c) additionally show the second and third POD modes where flows are more closely aligned with the radial direction. It can be concluded that these modes correspond to vortex break down that occurs when the jet breaks up.

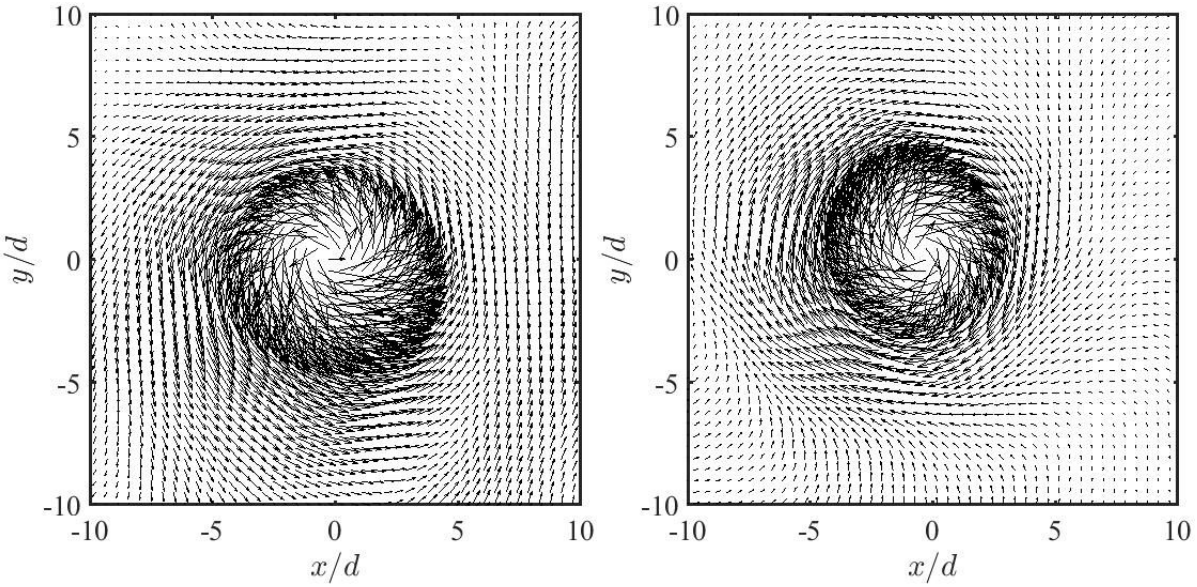

(a) (b)

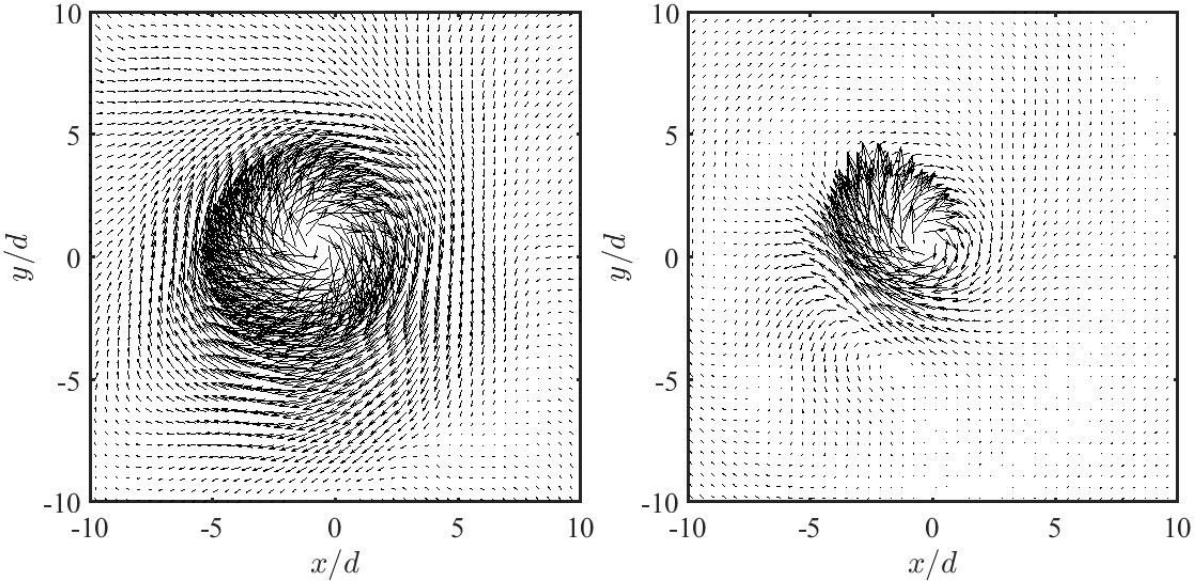

(c) (d)

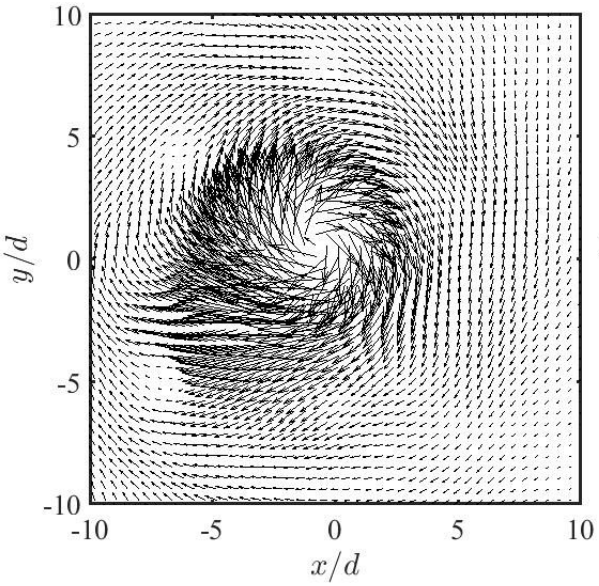
10
5
0
-5
-10
-10
-5
0
5
10
y/d
x/d

(e)

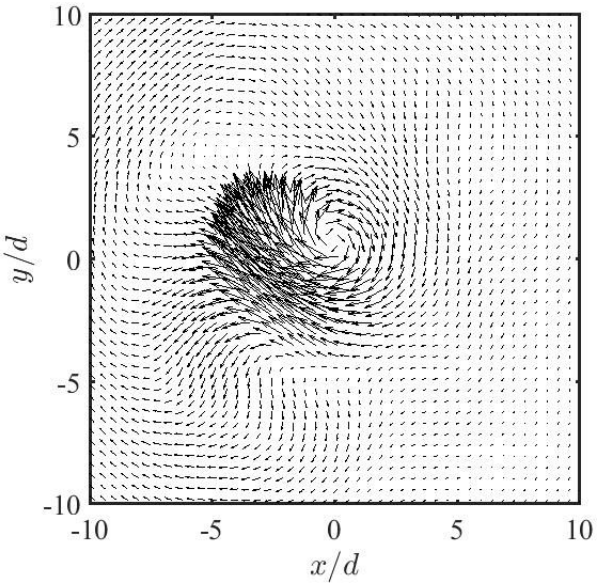
10
5
0
-5
-10
-10
-5
0
5
10
y/d
x/d

(f)

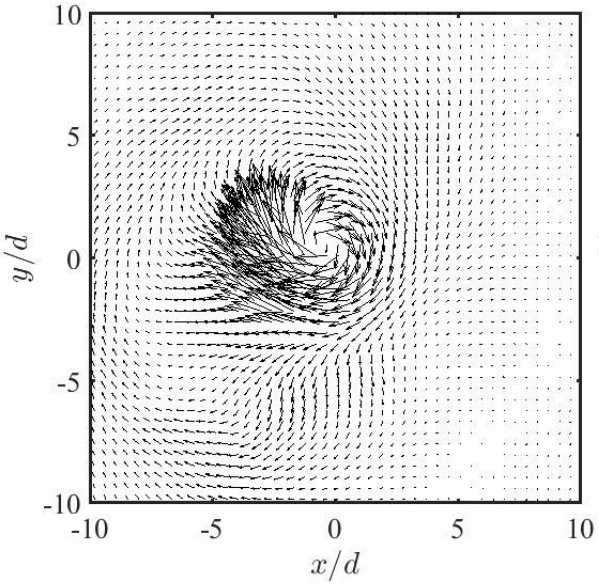
10
5
0
-5
-10
-10
-5
0
5
10
y/d
x/d

(g)

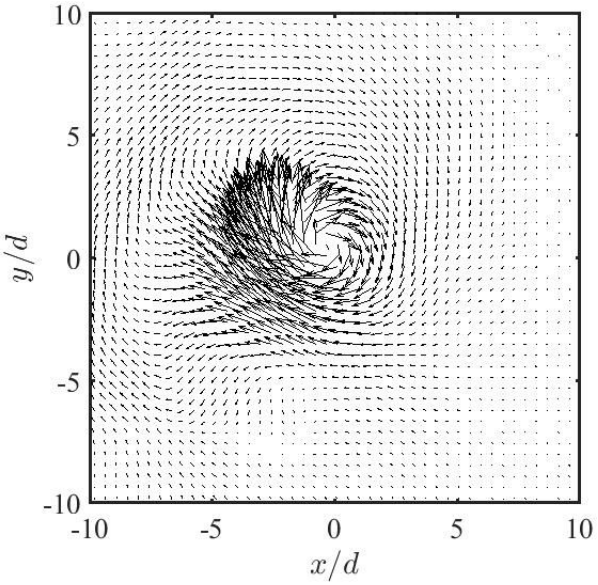
10
5
0
-5
-10
-10
-5
0
5
10
y/d
x/d

(h)

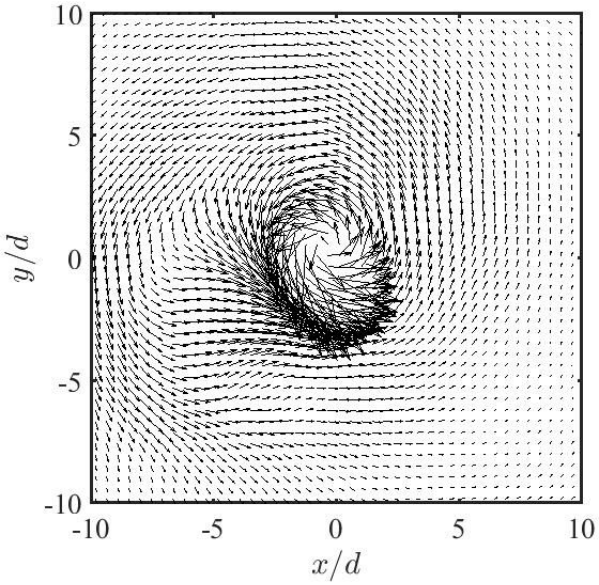

(i)

Figure 7.1: Velocity vector fields of the first POD mode: the rotation rates, in units of rad s^{-1}, associated with sub figures are: (a) 0.2, (b) 0.31, (c) 0.41, (d) 0.52, (e) 0.63, (f) 0.73, (g) 0.83, (h) 0.94, (i) 1.05.

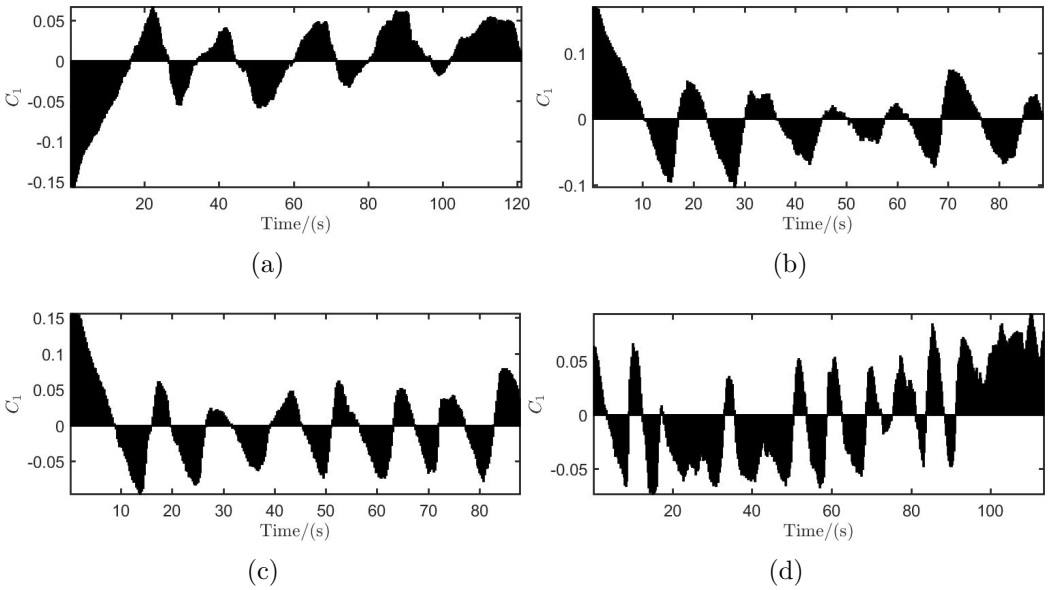

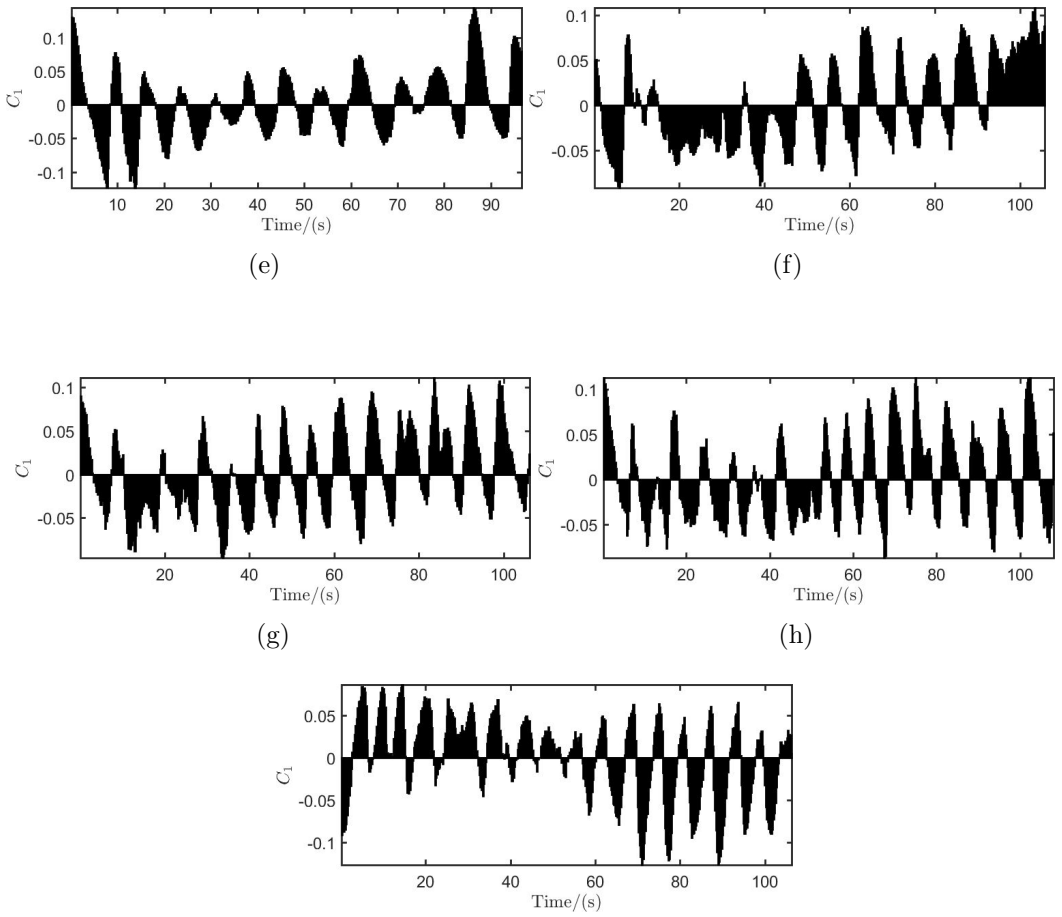

Figure 7.2: Temporal coefficients of POD mode 1: the rotation rates, in units of rad s^{-1}, associated with sub figures are: (a) 0.2, (b) 0.31, (c) 0.41, (d) 0.52, (e) 0.63, (f) 0.73, (g) 0.83, (h) 0.94, (i) 1.05.

Subjecting the time coefficient $C_1(t)$ of the first POD mode, i.e. the energetically dominant mode, to a Fourier analysis yields the repetition frequency, f_θ, associated with the formation-breakdown scenario of the jet structure. Figures 7.4 (a) - (i) display the Fourier spectra for $C_1(t)$ for experiments with nine different background rotation rates. For each spectrum of figure 7.4 (a) - (i) the dominant peak identifies f_θ for each of the nine associated rotational speeds of the turntable. The frequencies for these peaks, for jets at Re_0 = 2300 and Re_0 = 16000, at different rotational frequencies f_T, are displayed in figure 7.5. The two least-squares interpolations of the two data set for Re_0 = 2300 and Re_0 = 16000 are given by, respectively, $f_\theta = 0.84 f_T$ and $f_\theta = 1.55 f_T$ and they

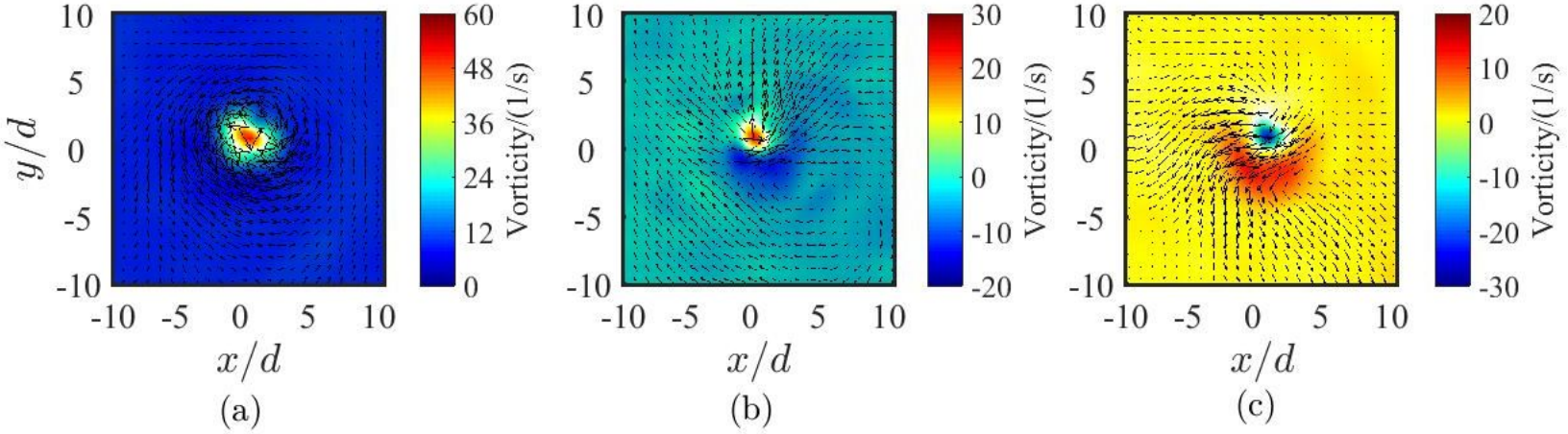

Figure 7.3: Velocity vectors and vorticity field of (a) first, (b) second and (c) third POD mode for a jet with $Re_0 = 2300$, at $\Omega = 0.21$ rad s^{-1}, for $z/d = 0.5$.

are identified by the solid line and the dashed line, respectively. The figure reveals that f_θ increases approximately linearly with f_T within the explored range of 0.067 Hz $\leqslant f_T \leqslant$ 0.17 Hz (corresponding to the range 2 – 10 rpm) for both Reynolds numbers. Figure 7.5 also shows that the formation-breakdown frequency also increases with the Reynolds number.

Moreover figure 7.6 displays the combined results obtained for f_θ using both the POD and the analysis of the kinetic energy of azimuthal velocity component. Hence in figure 7.6 the superposed dotted lines shown in very close proximity of each one of these two least-squares data interpolations represent the corresponding interpolations obtained by analysing kinetic energy associated with azimuthal velocity component, that is shown in figure 6.21. Figure 7.6 reveals that, at both Reynolds numbers, the results from the POD analysis and from the analysis of the azimuthal kinetic energy are in very good quantitative agreement. Note that the range obtained for f_θ/f_T is close to the value of $f_\theta/f_T \approx 2$ which one infers from the information provided in the abstract of Niino (1980) for the residual damped oscillations which he observed near the forcing region in his simulations - when consulting the paper by Niino note that he uses f to refer to the Coriolis parameter, 2Ω.

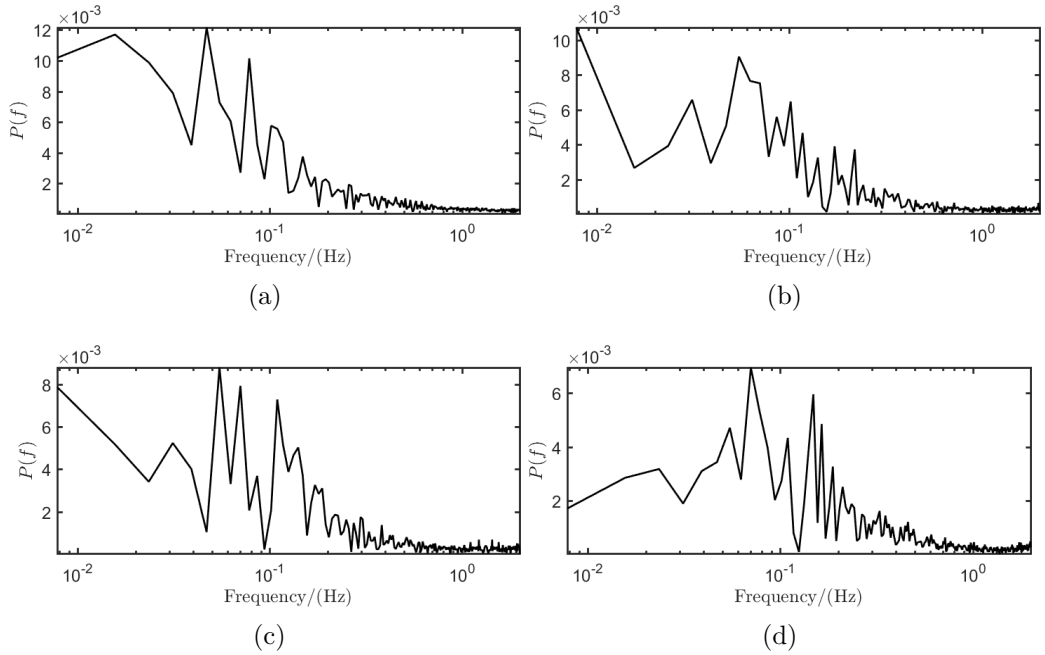

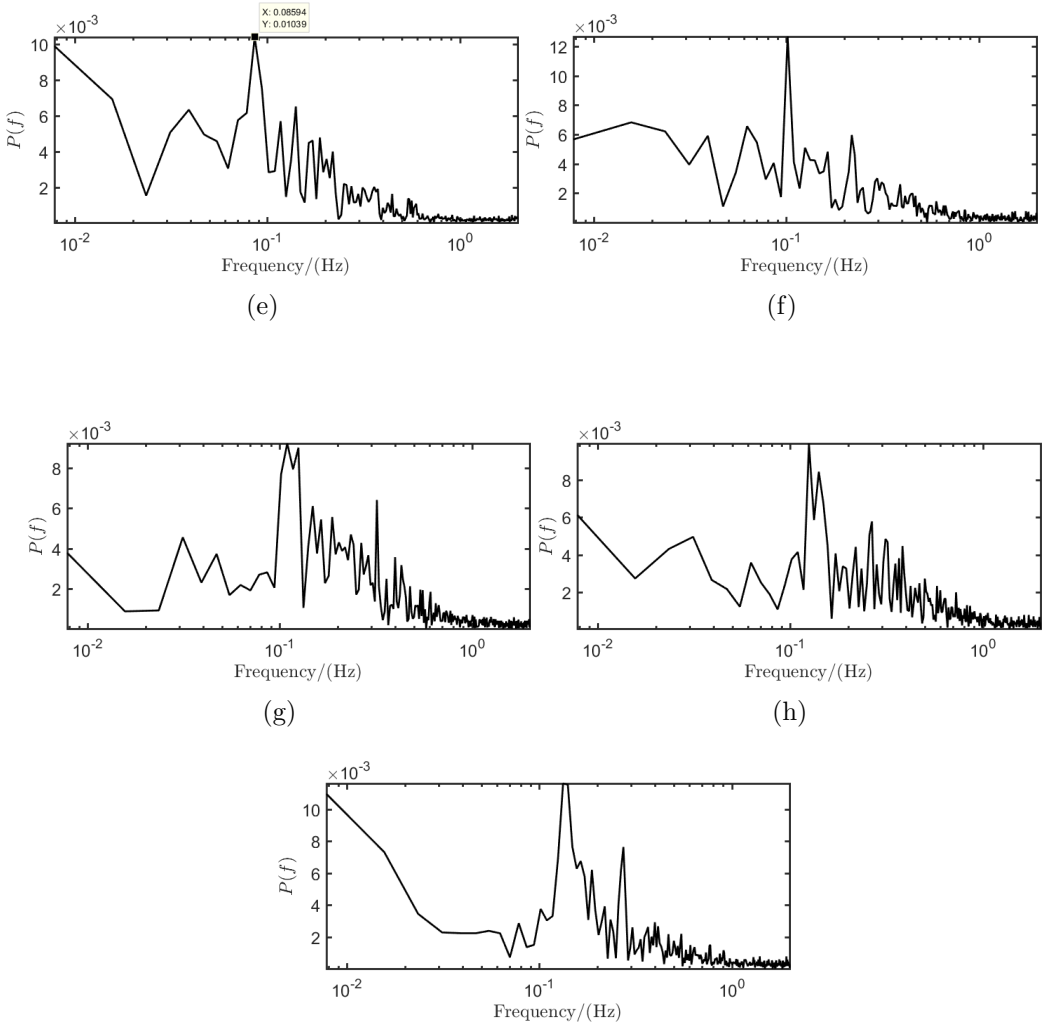

Figure 7.4: Fourier spectra for the time coefficient, $c_1(t)$, of the first POD mode for a jet with Re = 2300 for different rotation rates;the rotation rates, in units of rad s^{-1}, associated with sub figures are: (a) 0.2, (b) 0.31, (c) 0.41, (d) 0.52, (e) 0.63, (f) 0.73, (g) 0.83, (h) 0.94, (i) 1.05.

The data obtained from the PIV measurements in the horizontal planes at heights z/d = 5, 10, 15 & z/d = 20, were also subjected to the POD analysis. Figure 7.7 shows the three dimensional view of the first POD mode at each vertical height of the jet, for a jet with Re = 2300 and background rotation 0.21 rad $^{-1}$. The magnitude of the velocity is given by the height of the surface. It can be seen from this figure that the strongest first mode occurs at height z/d = 0.5 and the strength of the velocities of the POD first mode decreases as

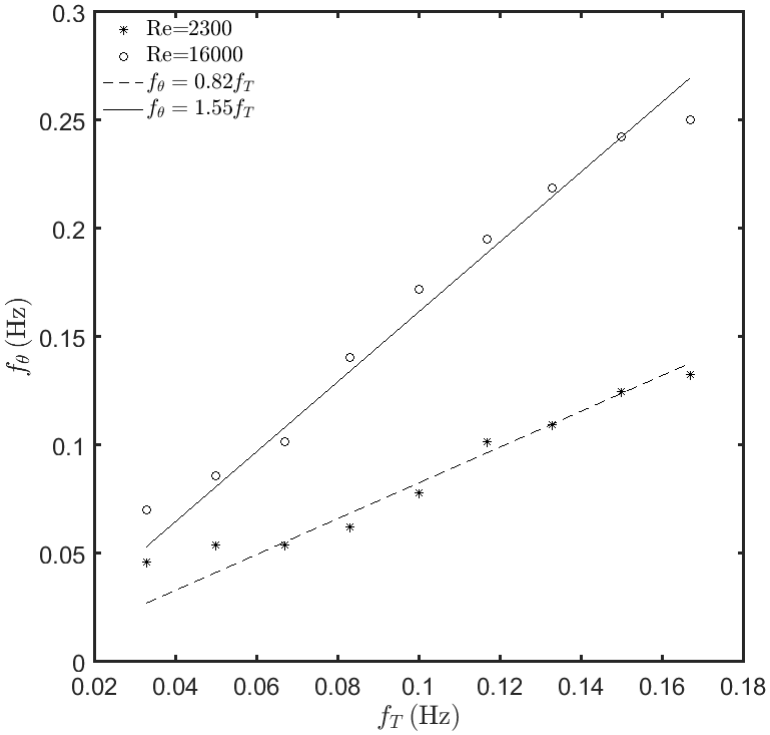

Figure 7.5: Formation-breakdown frequency, f_θ, of the jets as a function of the background-rotation frequency, $f_T = \Omega/2\pi$, of the turntable.

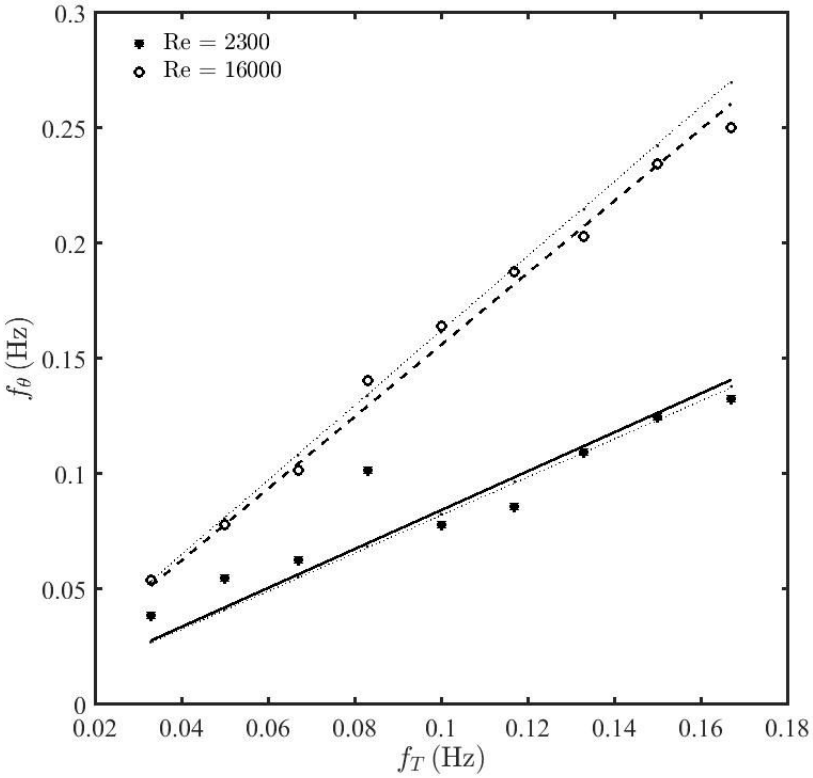

Figure 7.6: Formation-breakdown frequency, f_θ, of the jets as a function of the background-rotation frequency, $f_T = \Omega/2\pi$, of the turntable; $\bullet, -, Re = 2300$, $f_\theta = 0.84 f_T$; $\circ, --, Re = 16000, f_\theta = 1.57 f_T$. The dotted lines in the immediate vicinity of the two least-squares interpolations in this figure are the corresponding data interpolations from figure 6.21 obtained from the analysis of kinetic energy of the azimuthal component.

the distance above the source increases.

Figure 7.8 shows the dependence of the formation-breakdown frequency on the Reynolds number, Re_0, for three different rotation rates Ω = 0.21 rad s^{-1} , Ω = 0.52 rad s^{-1} and Ω = 1.05 rad s^{-1} corresponding to f_T = 0.033, f_T = 0.083 and f_T = 0.167, respectively. Since the diameter of the source was constant throughout the present study, the increase of the Reynolds number reflects increasing fluid ejection rates at the source. In addition to the results in figure 7.6, figure 7.8 reveals that f_θ increases approximately linearly with Re_0 for the regime of Reynolds numbers explored.

7.2.2 Vertical Plane

Figures 7.9 (a) - (f) show the vector fields of the first POD mode in the vertical plane, for a jet with Re_0 = 2300, for six different rotation rates as identified in the figure caption. As shown in figures 7.9 (a), (c) & (d), the velocity vectors of the first POD mode, that is the most energetic mode, show reverse or downward flow. In figures 7.9 (b), (e) & (f) velocity vectors of the first POD mode show, proper streamwise, upward flow. It is a known fact that at the beginning, the jet flow is upward. When the time characteristics, are carefully inspected for each rotation rate, shown in figures 7.10 (a) - (f), it can be seen that in figures 7.10 (a), (c) & (d), the time characteristic coefficient remains negative for the first half of each period. It was discussed in section 3.4 that for the reconstruction of the actual image of the vector field the POD modes are multiplied by their respective time coefficients. Therefore, when the first POD modes in figures 7.9 (a), (c) & (d), are multiplied by their respective (negative) time coefficients the resulting velocity vector fields show upward motion. From the plots that represent time characteristics for different background rotations shown in figure 7.2 reveal clearly a periodic behaviour even though it is not as regular as the time characteristics of the POD modes in the horizontal plane. This is because the jet was subjected to a slight precession and it moved out of the laser plane. Hence the time characteristics of the POD modes in the vertical plane were not used to calculate any further quantities.

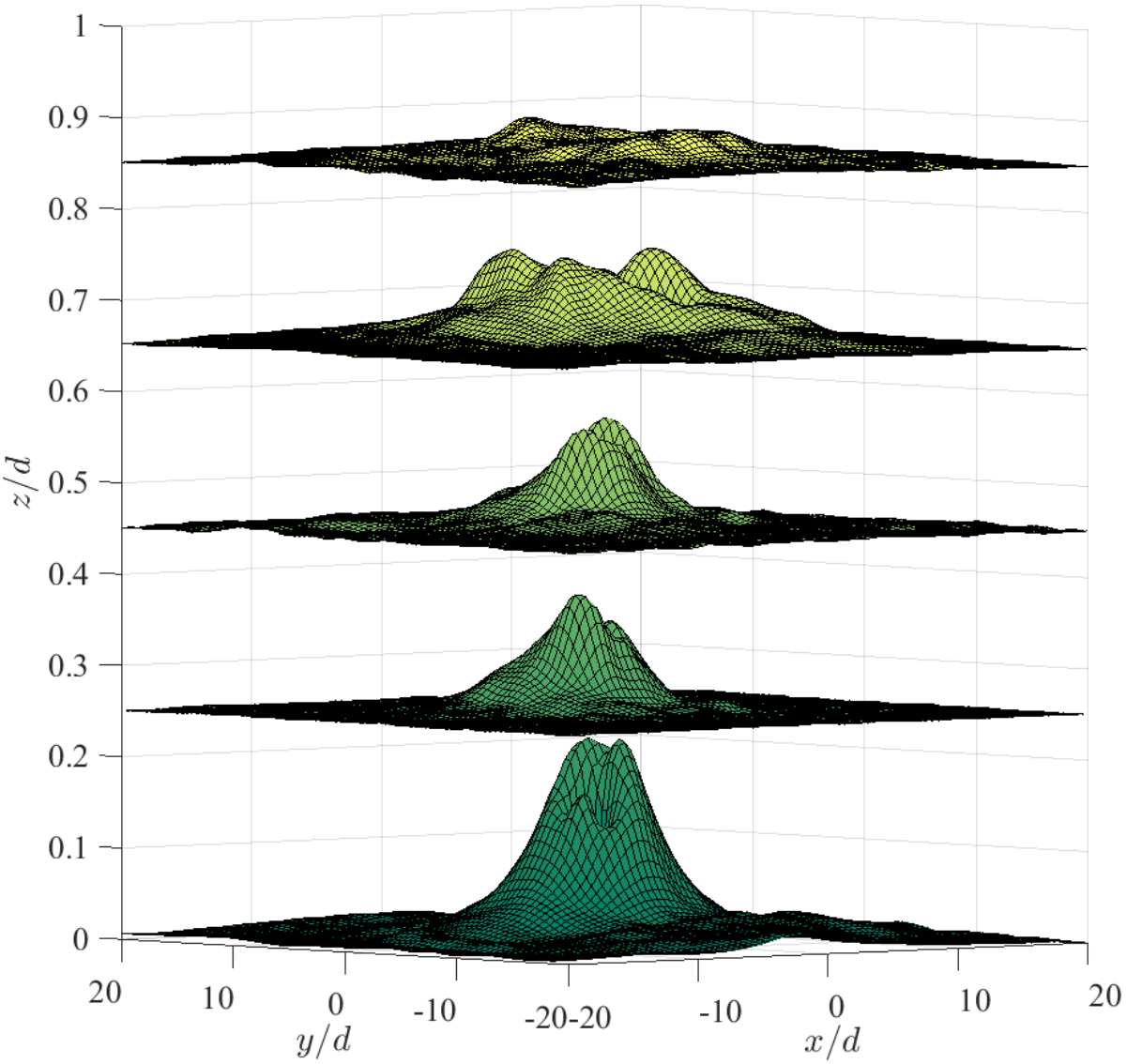

Figure 7.7: The first POD mode at each nondimensionalised vertical height of the jet for a jet with Re = 2300, and background rotation 0.21 rad $^{-1}$.

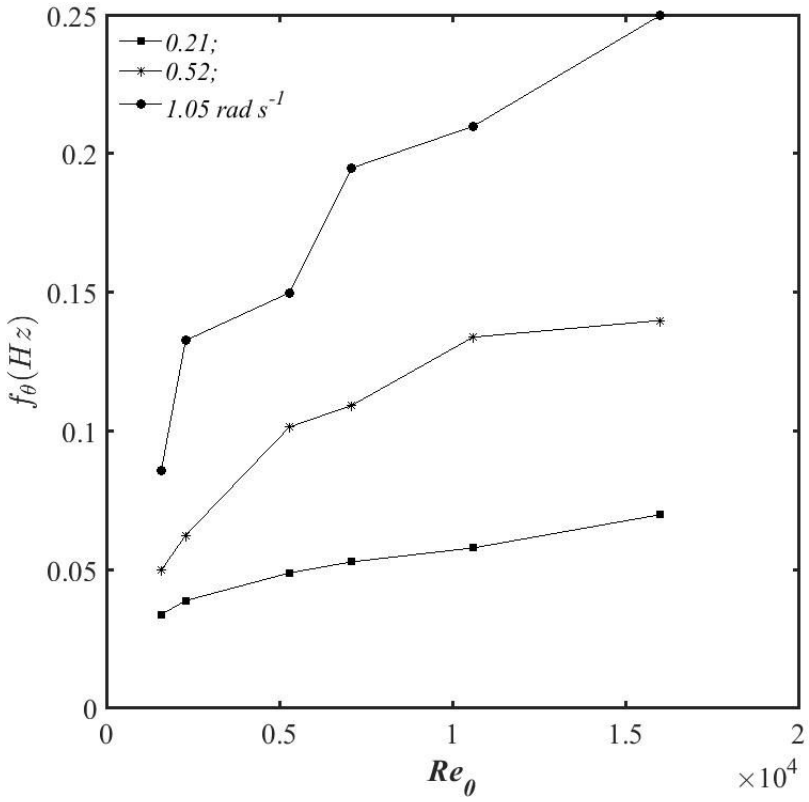

Figure 7.8: Variation of formation-breakdown frequency, f_θ, of the jets as a function of the Reynolds number Re_0 .

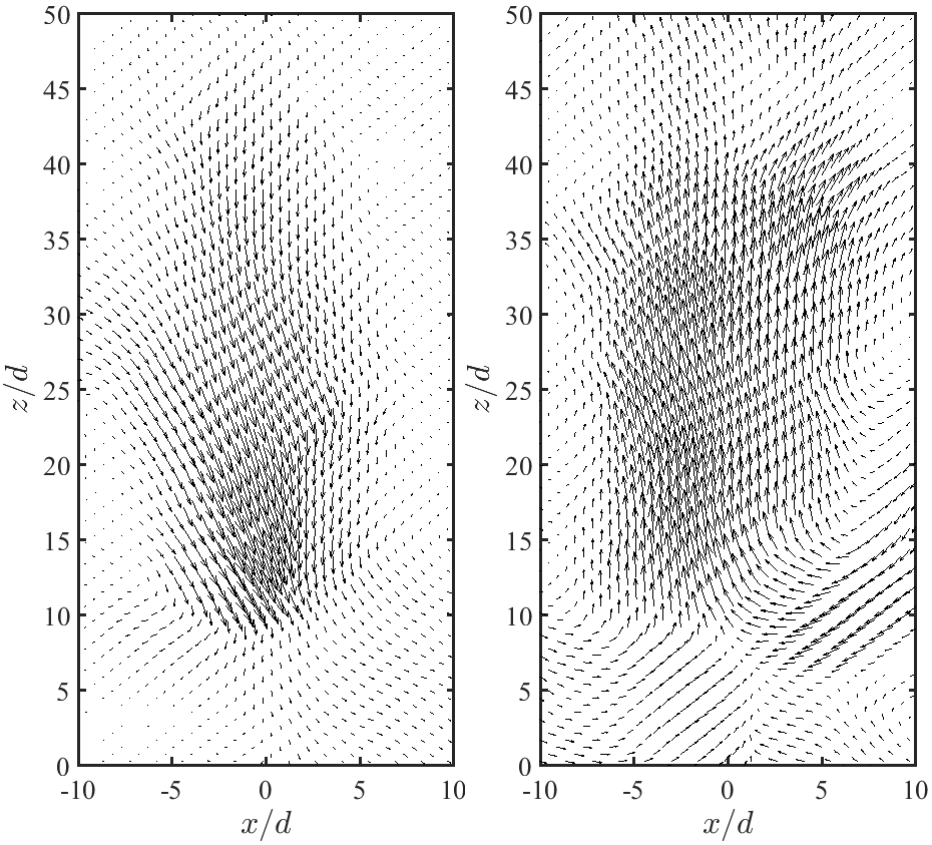
50
45
40
35
30
25
20
15
10
5
0
z/d
-10
-5
0
5
10
x/d

(a) (b)

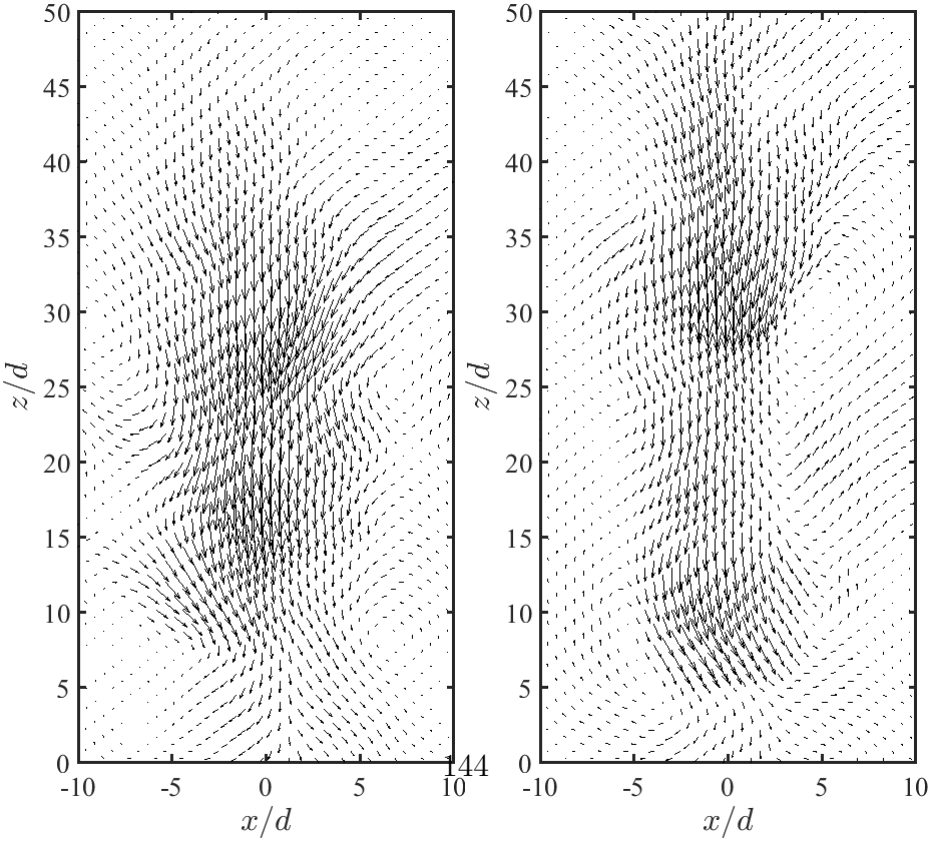
50
45
40
35
30
25
20
15
10
5
0
z/d
-10
-5
0
5
10
x/d

(c) (d)

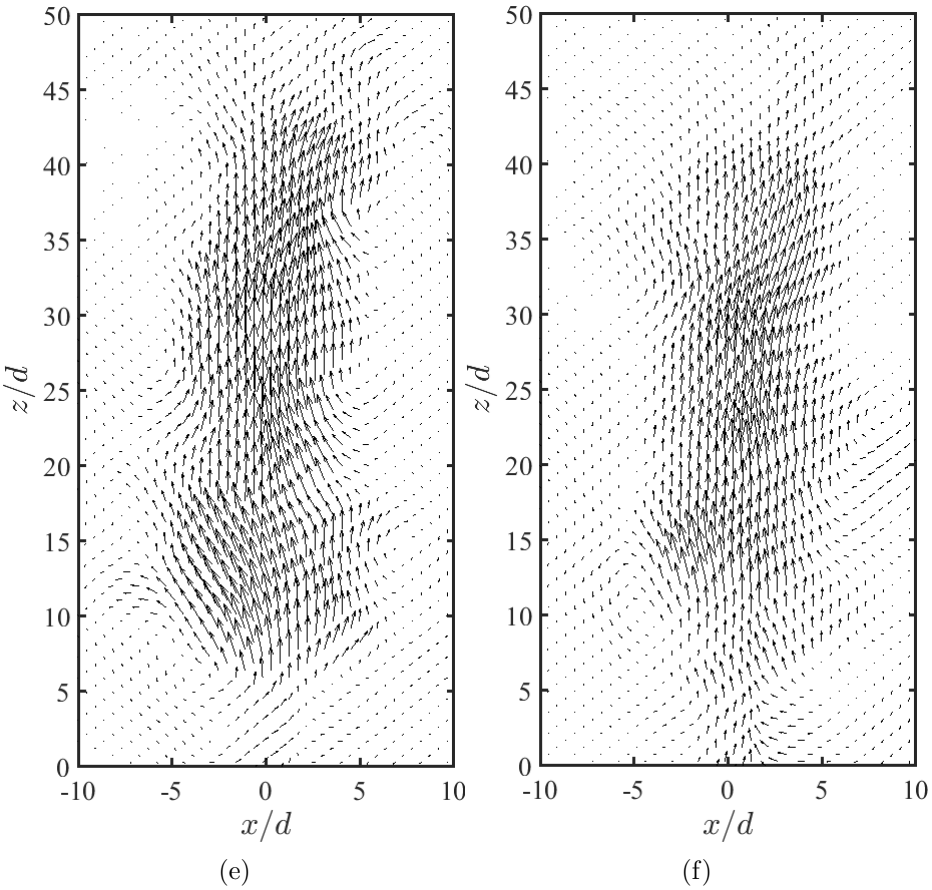

Figure 7.9: First POD mode in the vertical plane for jet with Re_0 = 2300 and z/d = 0.5. The rotation rates, in units of rad s^{-1}, associated with sub figures are: (a) 0.21, (b) 0.31, (c) 0.41, (d) 0.52, (e) 0.73, (f) 0.83.

7.3 Image Reconstruction Using the POD Modes

The original image reconstruction from the calculated POD modes improves the reliability of the conclusions drawn from the study. Therefore a number of original images were reconstructed using the POD modes to check the accuracy of them. Figure 7.11 (a) shows the original instantaneous velocity vector field of the jet in the horizontal plane after 40 s of ejection of the liquid had commenced and Figure 7.11 (b) shows the reconstructed image using the first five POD modes. These two figures represent the vector fields in the area approximately five diameters away from the center in each direction. Figures

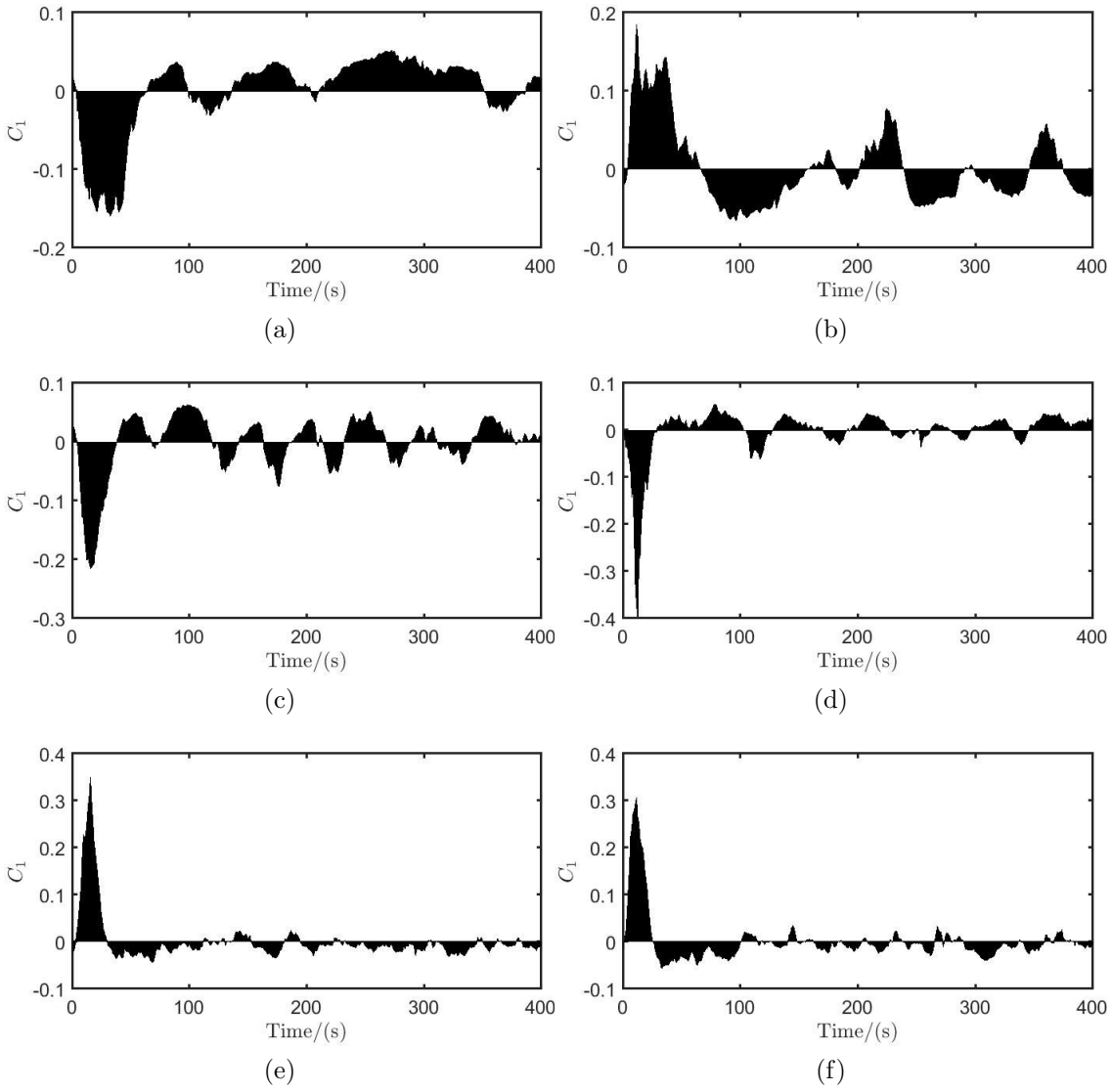

Figure 7.10: Time characteristics of first POD mode in the vertical plane (a) for jet with $Re_0 = 2300$ and $z/d = 0.5$. The rotation rates, in units of rad s^{-1}, associated with sub figures are: (a) 0.21, (b) 0.31, (c) 0.41, (d) 0.52, (e) 0.73, (f) 0.83.

7.11 (a) & (b) look qualitatively similar in terms of the arrangement of the velocity vectors. Figure 7.12 (a) shows a much wider area of the same original velocity field shown in figure 7.11 (a). Figure 7.12 (b) shows the corresponding reconstructed vector field from the first five POD modes. Now if one compares these two figures, it is clear that the two figures are qualitatively different and almost all the vectors are not captured by the first five POD modes. Nevertheless figure 7.13 (a) shows the original velocity vectors of the same vector field in the horizontal plane as in figure 7.11 (a), and figure 7.13 (b) shows the corresponding reconstructed velocity field using the first thirty POD modes. The figures 7.13 (a) & (b) look very similar. Even when a wider area of the reconstructed vector field was inspected as shown in figure 7.14 (b), it agrees well with the corresponding original vector field that is shown in figure 7.14 (a). Reconstruction of images of the vertical plane is also carried out using thirty POD modes and figures 7.15 (a) and (b) show an original vector field and the corresponding reconstructed vector field respectively. Moreover figure 7.16 (a) and (b) show the cumulative percentage energy variation against POD modes for the vertical plane and the horizontal plane respectively. The figures clearly show that, 90% of energy is captured by, thirty modes in the vertical plane and twenty modes in the horizontal plane.

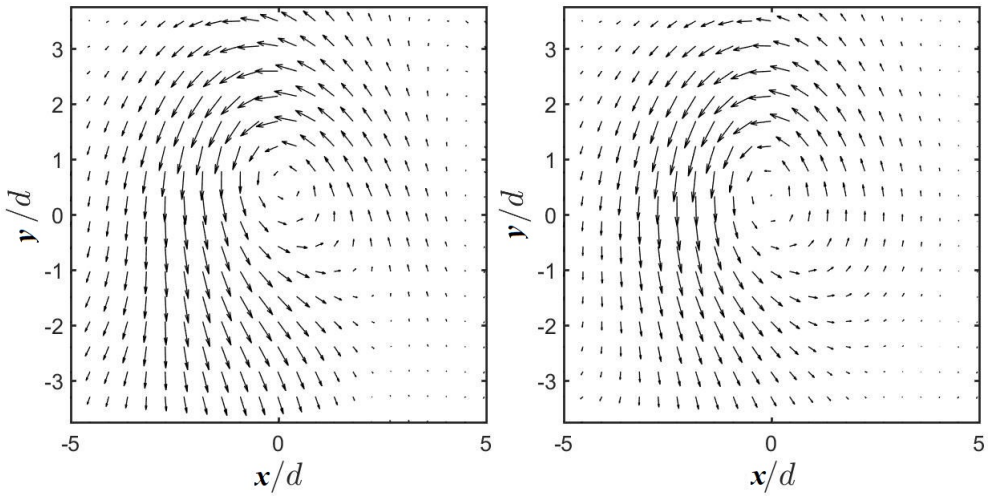

Figure 7.11: (a) The original vector field in the horizontal plane after $40s$ of the jet development and (b) reconstructed vector fields using first 5 POD modes, for jet with $Re = 2300$ and $z/d = 0.5\ d$, $-5 \leqslant x/d \leqslant 5$ and $-5 \leqslant y/d \leqslant 5$.

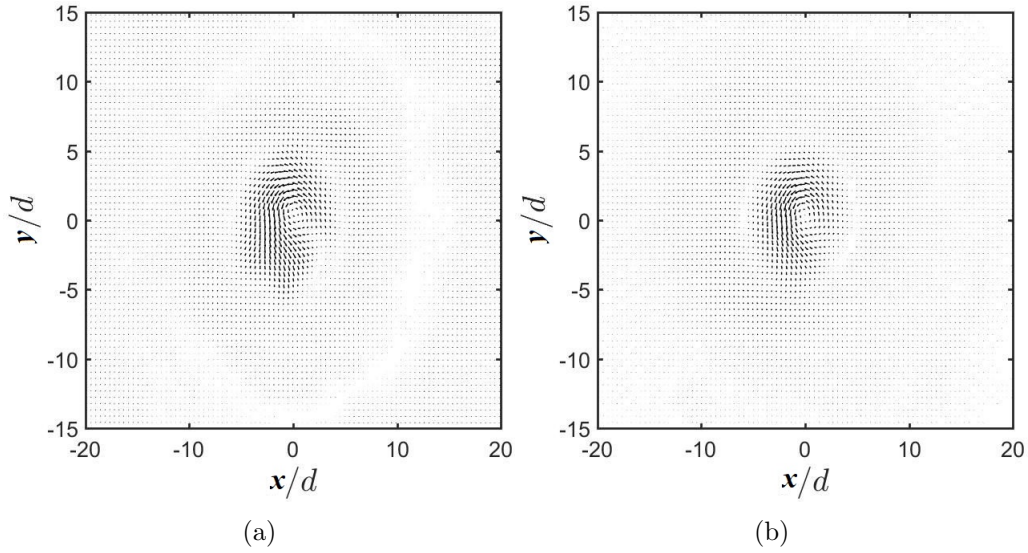

Figure 7.12: (a) The original vector field in the horizontal plane after $40s$ of the jet development and (b) reconstructed vector fields using first 5 POD modes, for jet with $Re = 2300$ and $z/d = 0.5\ d$, $-15 \leqslant x/d \leqslant 15$ and $-15 \leqslant y/d \leqslant 15$.

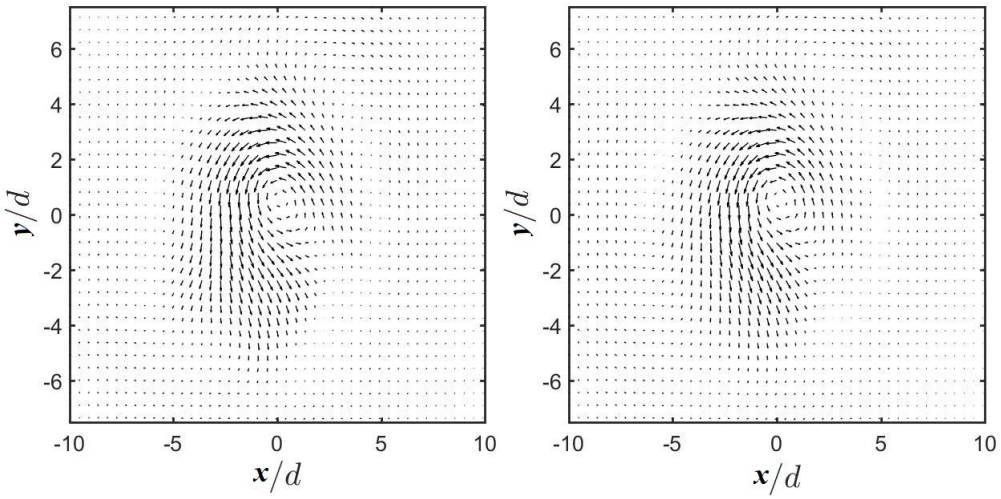

Figure 7.13: (a) Original vector field in the horizontal plane after $40s$ of jet development and (b) reconstructed vector fields using first 30 POD modes, for jet with $Re = 2300$ and $z/d = 0.5d$, $-10 \leqslant x/d \leqslant 10$ and $-10 \leqslant y/d \leqslant 10$.

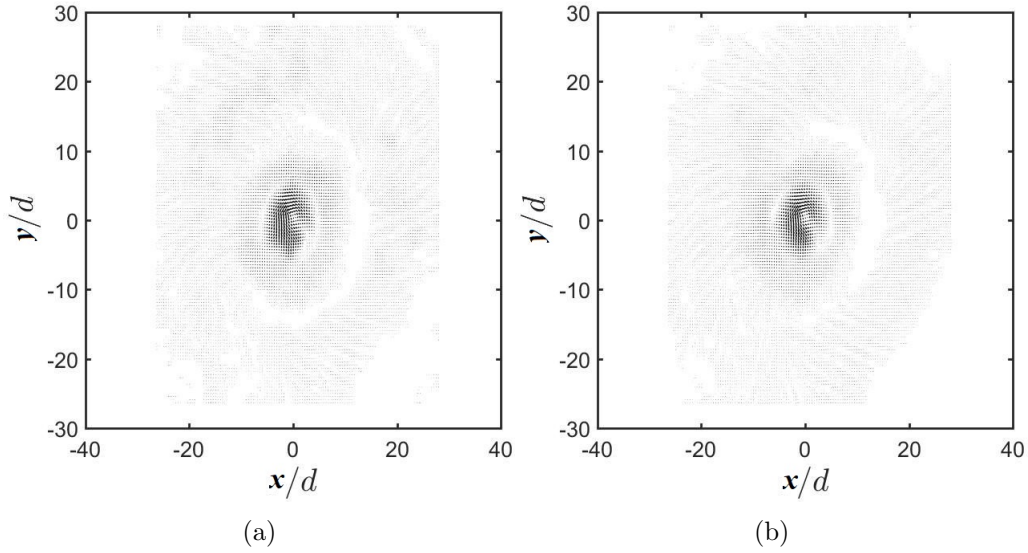

Figure 7.14: (a) Original vector field in the horizontal plane after $40s$ of jet development and (b) reconstructed vector fields using first 30 POD modes, for jet with $Re = 2300$ and $z/d = 0.5d$, $-40 \leqslant x/d \leqslant 40$ and $-40 \leqslant y/d \leqslant 40$.

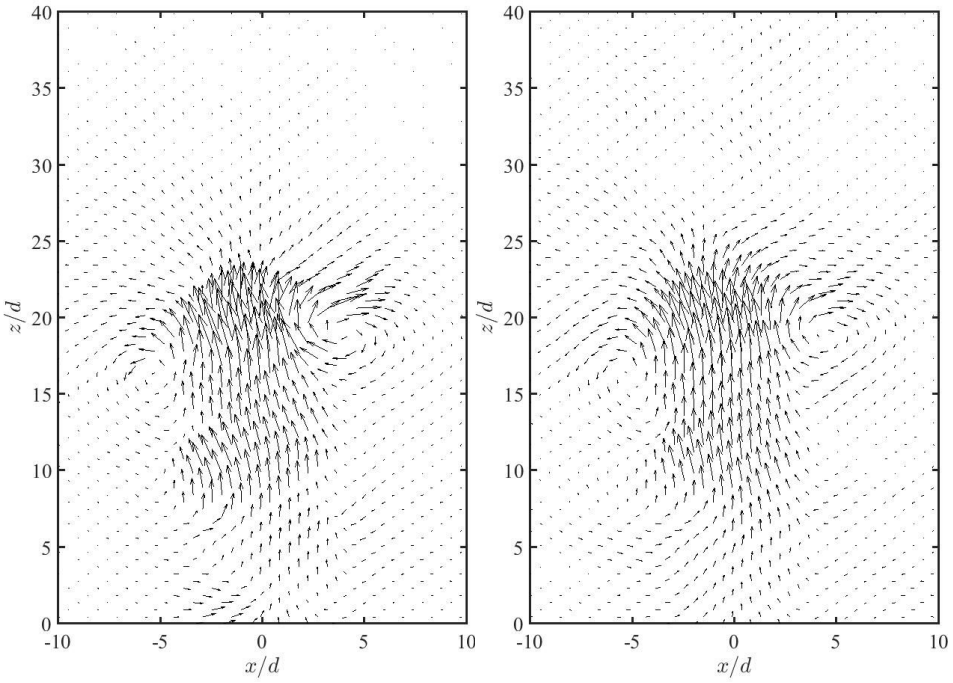

Figure 7.15: (a) The original vector field in the vertical plane after $2s$ of jet development and (b) reconstructed vector fields using first 30 POD modes, for a jet with Re = 2300.

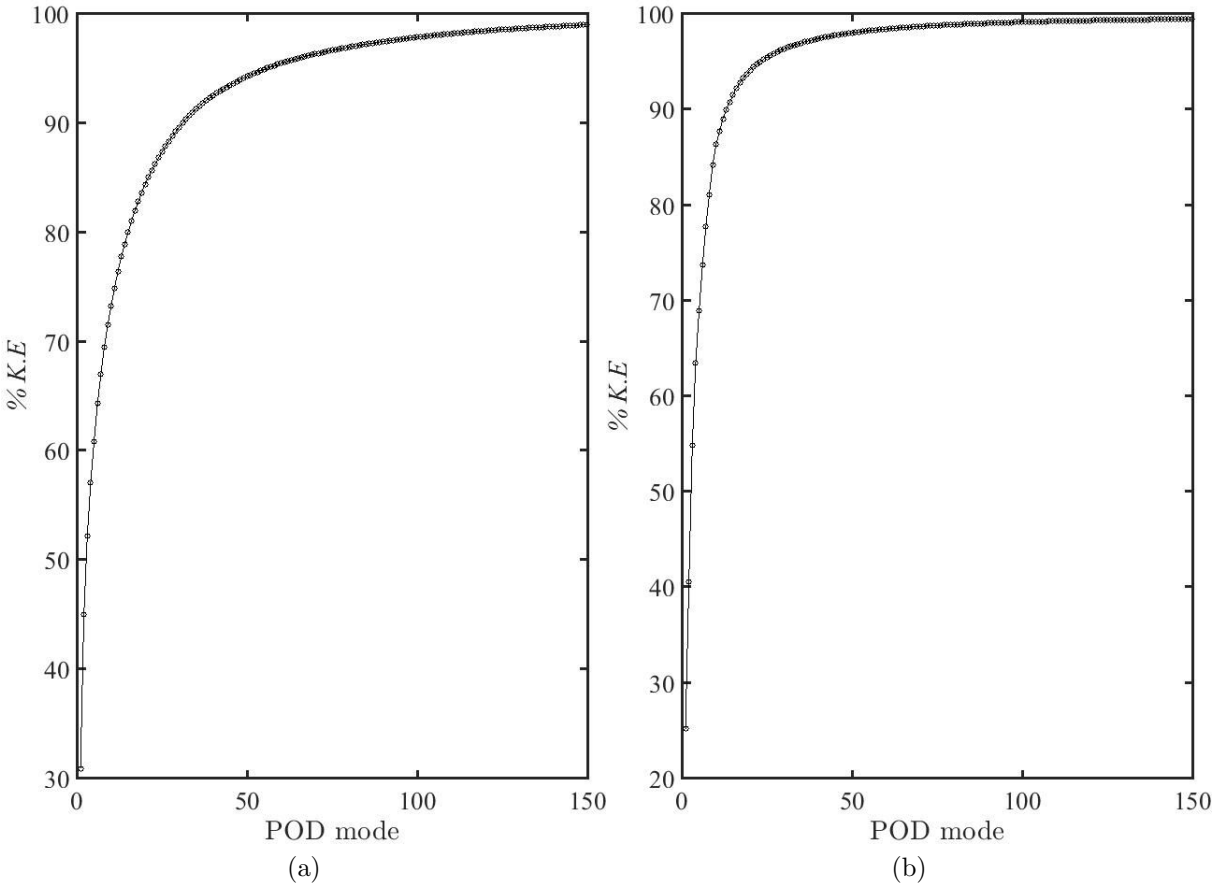

Figure 7.16: Variation of cumulative percentage of kinetic energy with POD mode number in the: (a) vertical plane (b) horizontal plane for a jet with Re = 2300.

Chapter 8

Centrifugal Instability

In this chapter the possible cause underlying the development of the formation-breakdown cycle of the jets considered in this study is discussed. The upward motion of the liquid, forming the jets leads to radial flow and radial entrainment of ambient liquid. This process induces a rotary cyclonic flow within the jets due to the action of the Coriolis force on the radially entrained liquid. Thus, the flow that is established is qualitative somewhat similar to the flow of swirling jets in a non-rotating reference frame. Swirling jets are known to develop helical instabilities arising from a combination, or competition, of Kelvin-Helmholtz (K-H) instability and the generalized centrifugal instability (Liang & Maxworthy, 2005). For the jets considered in this study, the effects of shear between the liquid forming the jet and the ambient are small compared to the case of a swirling jet in a non-rotating environment. Therefore we suspected that the formation-breakdown cycle discussed here might arise as a consequence of centrifugal instability. This hypothesis will be tested in the remainder of this chapter on the basis of four criteria discussed in Kloosterzielt & Heijst (1991) and Nagarathinam *et al.* (2015).

Figures 8.1, 8.2 and 8.3 display spatio-temporal representations of the results obtained for experimental data of the current study for the Rayleigh instability criterion ($d(\overline{v_\theta}r)^2/dr \leq 0$), for a jet with Re_0 = 2300 and Ω = 0.21 rad s^{-1}, at heights z/d = 0.5, z/d = 5 & z/d = 10 respectively. Figures 8.4, 8.5 and 8.6 display the corresponding plots for the modified Rayleigh criterion ($d(\overline{v_\theta}r + \Omega r^2)^2/dr \leq 0$) by Kloosterzielt & Heijst (1991). Reference to fig-

ures 8.1, 8.2 and 8.3, reveals that it is easy to see that, formally, the Rayleigh instability criterion is satisfied after regularly recurring intervals in time for radial locations roughly within the interval $0 \leqslant r/d \leqslant 5$ where minimum values are around $d(\overline{v_\theta}r)^2/dr \approx -2 \times 10^{-6}$ m^{3}s^{-2} at $z/d = 0.5$, $d(\overline{v_\theta}r)^2/dr \approx -4 \times 10^{-7}$ m^{3}s^{-2} at $z/d = 5$ and $d(\overline{v_\theta}r)^2/dr \approx -5 \times 10^{-7}$ m^{3}s^{-2} at $z/d = 10$, are adopted. However, since the Rayleigh criterion does not account for the background rotation Ω, it can evidently not be the appropriate criterion to apply to the data of the present experiments. The background rotation is accounted for in figures 8.4, 8.5 and 8.6 for the modified Rayleigh criterion by Kloosterzielt & Heijst (1991). Due to the nature of the data set, and due to the viewing angle, in figures 8.4, 8.5 and 8.6 it is slightly less obvious that this modified stability criterion is marginally satisfied after regularly recurring temporal intervals since values of only $d(\overline{v_\theta}r + \Omega r^2)^2/dr \approx -0.5 \times 10^{-6}$ m^{3}s^{-2} are adopted over much narrower radial intervals within $0 \leqslant r/d \leqslant 5$. Nevertheless, the regions where the instability criterion is satisfied can be identified as the five small protrusions extending downwards into the region of negative values in figure 8.4, and four small protrusions in figures 8.5 and 8.6. The substantial increase in magnitude of the values of $d(\overline{v_\theta}r + \Omega r^2)^2/dr$ for increasing r/d in figures 8.4, 8.5 and 8.6, is due to the contribution of the term Ωr^2.

Checking the two instability criteria by Nagarathinam *et al.* (2015) which account for rotation and, additionally, for axial flow is more complex. This necessitates calculating the parameter χ_1 and χ_2 by means of equations 3.45 and 3.46, respectively. This, however, requires experimental input data for the circumferential flow velocity, v_θ, as well as for the axial velocity, w. Nevertheless, our 2D PIV set up did not allow measuring both these velocity components simultaneously in each experiment. This is due to the measurement of v_θ requiring a laser-light sheet in the $\theta - r$ plane (refer figures 4.6 & 4.3) whereas the measurement of w requires a light sheet in the $z - r$ plane. Since these two planes are perpendicular to each other the simultaneous measurement of both components in a single experiment is not possible. Therefore the required data for v_θ and w had to be extracted from two separate experimental runs conducted under identical conditions.

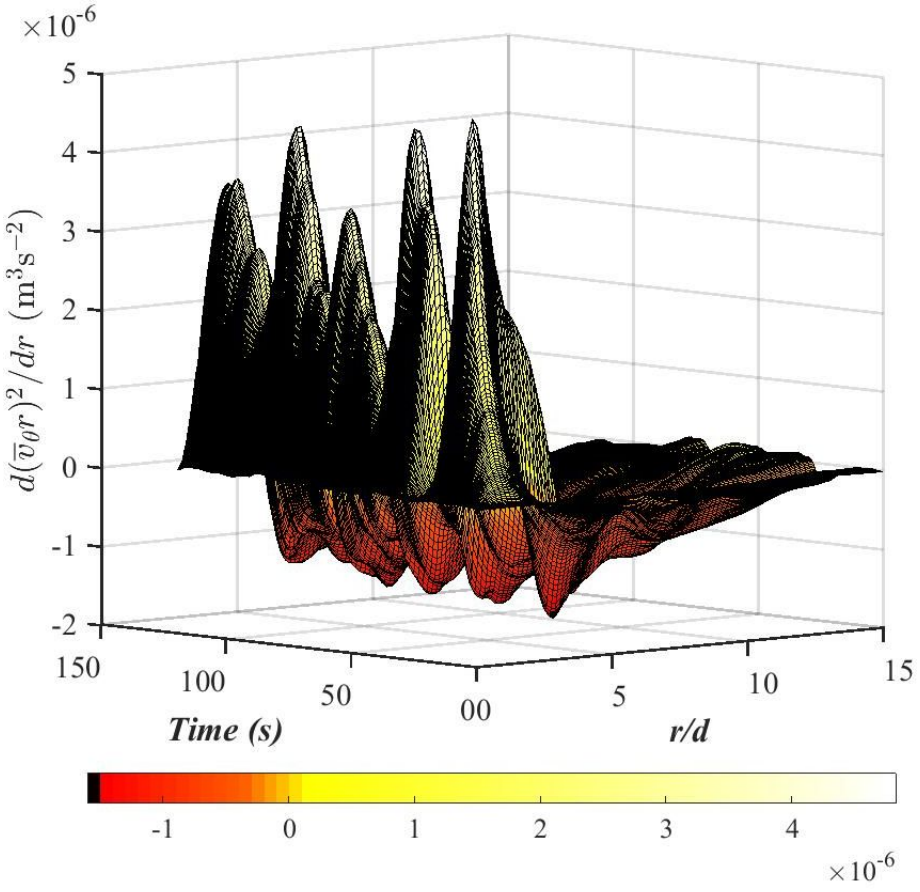

Figure 8.1: Variation of $d(\overline{v_\theta}r)^2/dr$ with time and r/d at z/d = 0.5, for a jet with Re_0 = 2300 at Ω = 0.21 rad s^{-1}.

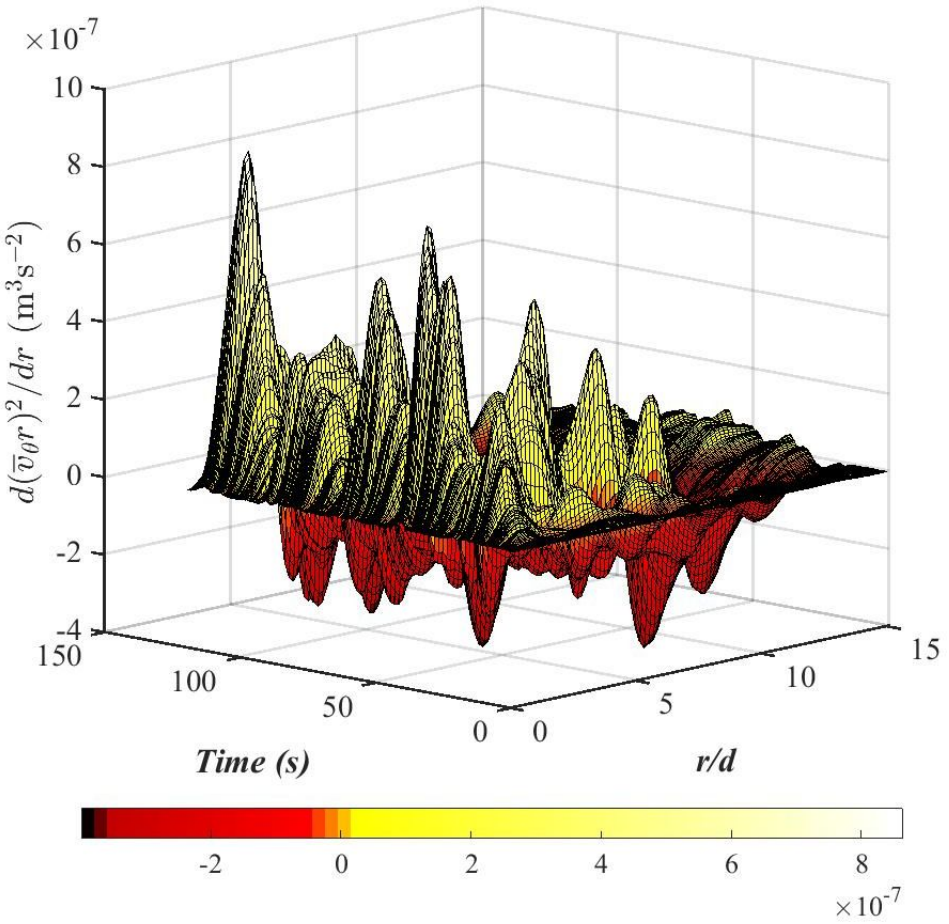

Figure 8.2: Variation of $d(\overline{v_\theta} r)^2/dr$ with time and r/d at $z/d = 5$, for a jet with $Re_0 = 2300$ at $\Omega = 0.21$ rad s^{-1}.

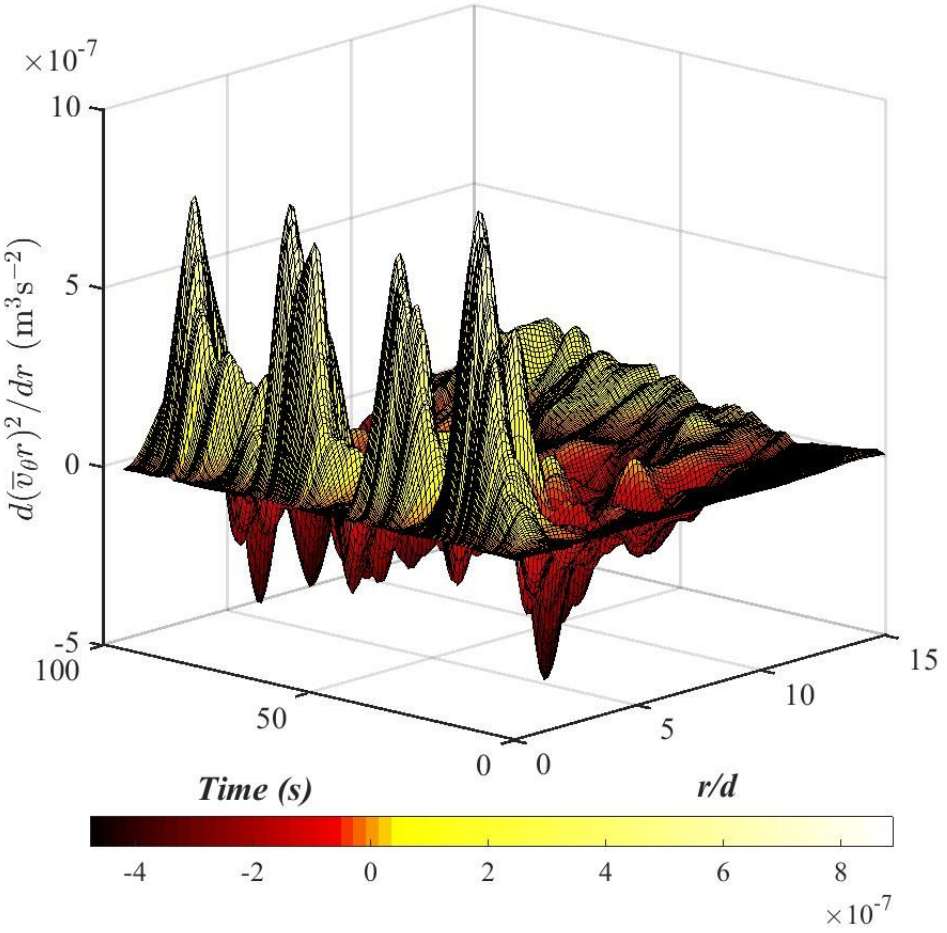

Figure 8.3: Variation of $d(\overline{v_\theta}r)^2/dr$ with time and r/d at z/d = 10, for a jet with Re_0 = 2300 at Ω = 0.21 rad s^{-1}.

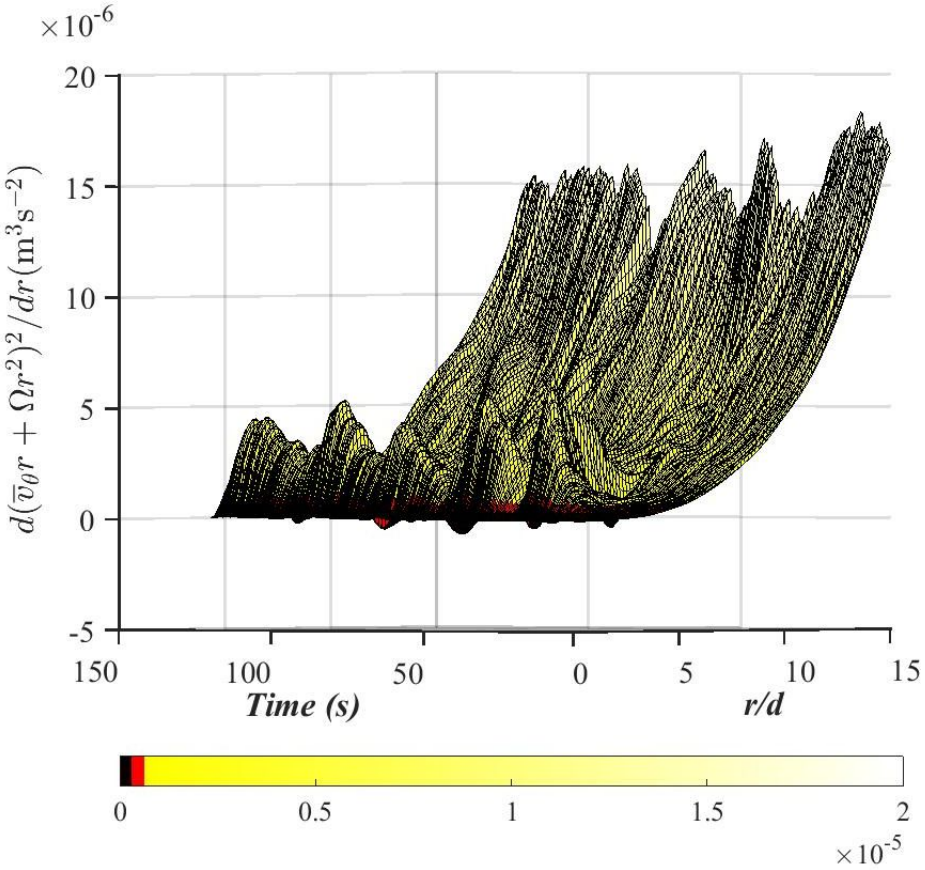

Figure 8.4: Variation of $d(\overline{v_\theta}r + \Omega r^2)^2/dr$ with time and r/d at $z/d = 0.5$, for a jet with $Re_0 = 2300$ at $\Omega = 0.21$ rad s^{-1}.

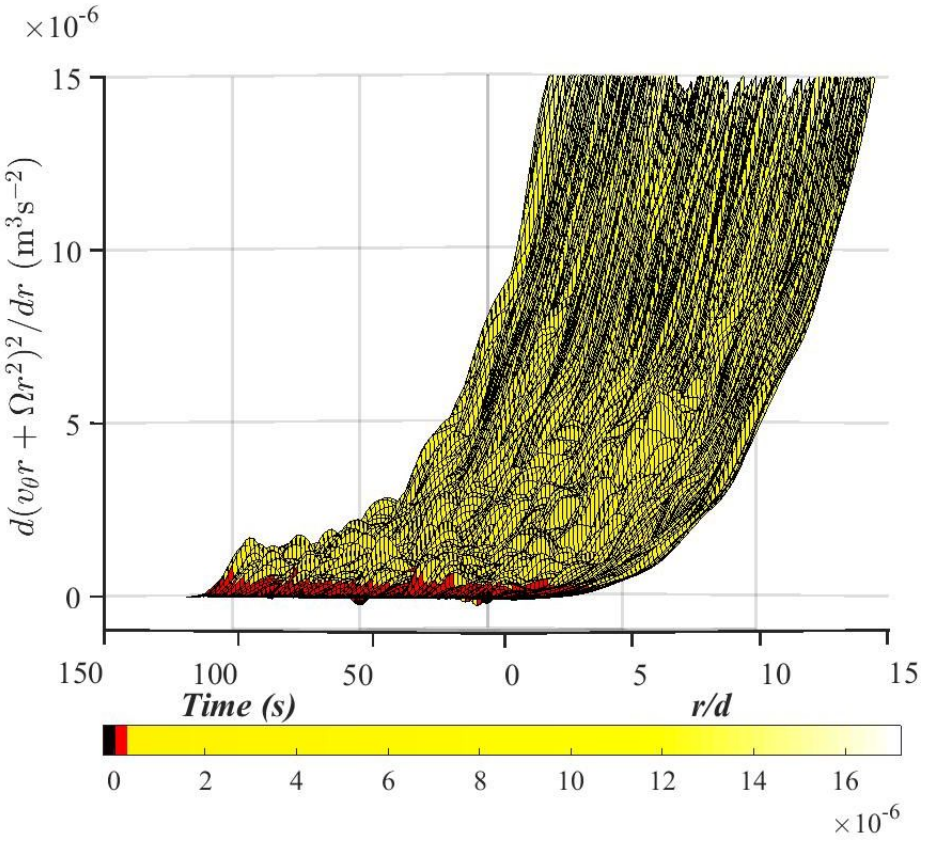

Figure 8.5: Variation of $d(\overline{v_\theta}r + \Omega r^2)^2/dr \leq 0$ with time and r/d at $z/d = 5$, for a jet with $Re_0 = 2300$ at $\Omega = 0.21$ rad s^{-1}.

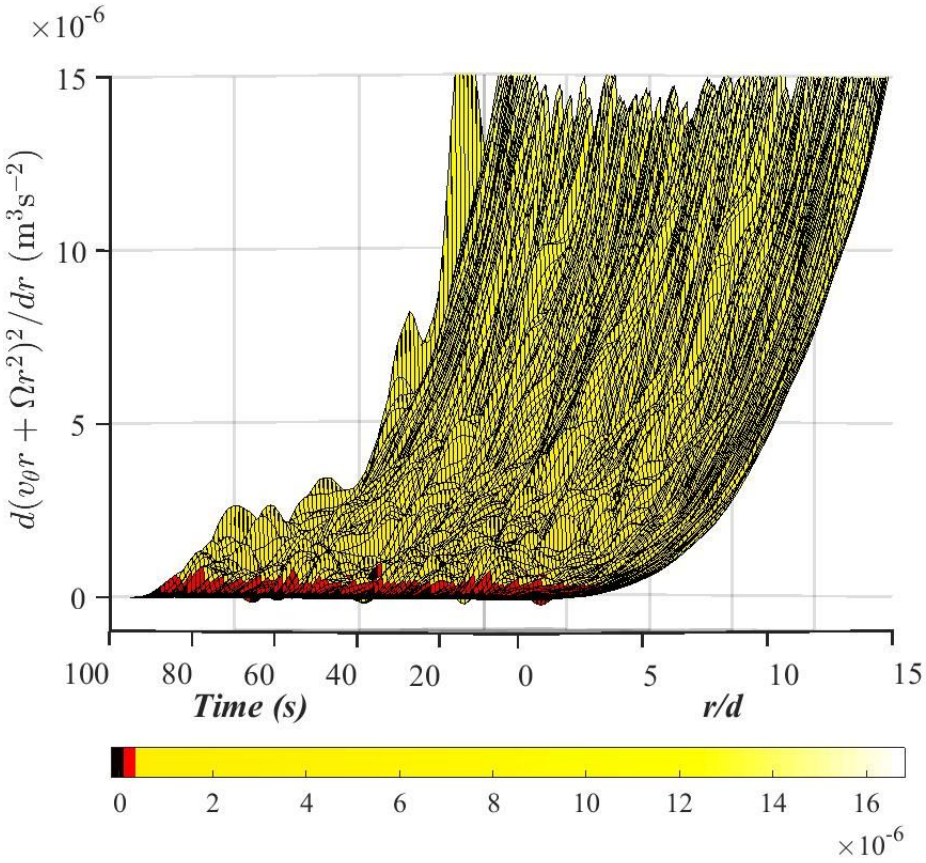

Figure 8.6: Variation of $d(\overline{v_\theta}r + \Omega r^2)^2/dr \leq 0$ with time and r/d at z/d = 10, for a jet with Re_0 = 2300 at Ω = 0.21 rad s^{-1}.

The situation regarding v_θ and w is further complicated by the fact that in-phase data for the two fluctuating quantities during the formation-decay cycles are required. Therefore an algorithm had to be devised to enable the required phase correction of these fluctuating data measured independently in the two separate realizations of the experiment. To this end the radial component of the flow velocity, $v_r(t)$, was considered which is available from measurements in both the $\theta - r$ and the $z - r$ measurement planes. The magnitude of the temporal data shift required to synchronize the data from the two independent experiments was obtained from a cross correlation of the two data sets for the radial component of the flow velocity, $v_r(t)$, in the $\theta - r$ plane and the $z - r$ planes. For the data obtained from the $\theta - r$ plane circumferentially-averaged velocity data for $v_r(t)$ were used. For the data from the $z - r$ plane circumferential averaging is evidently not possible, due to the non-availability of data from outside the $z - r$ plane. In this case the data for $v_r(t)$ were, therefore, averaged within a vertical interval $\Delta z/d = \pm 0.5$ around the measurement height $z/d = 10$. The algorithms used to calculate the two quantities χ_1 & χ_2 were first tested against the calculated boundary limits (see Appendix), in order to ensure that the algorithms are reliable to perform further calculations. Moreover in order to evaluate χ_2 the stream function value at each radial location in the $\theta - r$ plane had to be evaluated. The method adopted for evaluating criterion χ_2 is given in the appendix.

Figures 8.7 and 8.8 display the results obtained from the data analysis for χ_1 and χ_2 associated with, respectively, axisymmetric and non-axisymmetric flow. In these two figures green iso-surface lines were included which identify $\chi_1 = 0$ and $\chi_2 = 0$. These lines enclose regions of the flow field where $\chi_1 > 0$, $\chi_2 > 0$, that is regions where the criterion for instability is satisfied. Figure 8.7 reveals that the results for χ_1 are very inconclusive. There are only some very small, randomly distributed, islands in the flow field where the instability criterion $\chi_1 > 0$ is, in most cases only marginally, satisfied. On most of the flow domain $\chi_1 \approx 0$ and it approaches negative values, indicating stability, for $r/d \to 0$. Since χ_1 is associated with axisymmetric flow this result probably indicates that this parameter is not the appropriate stability criterion for the

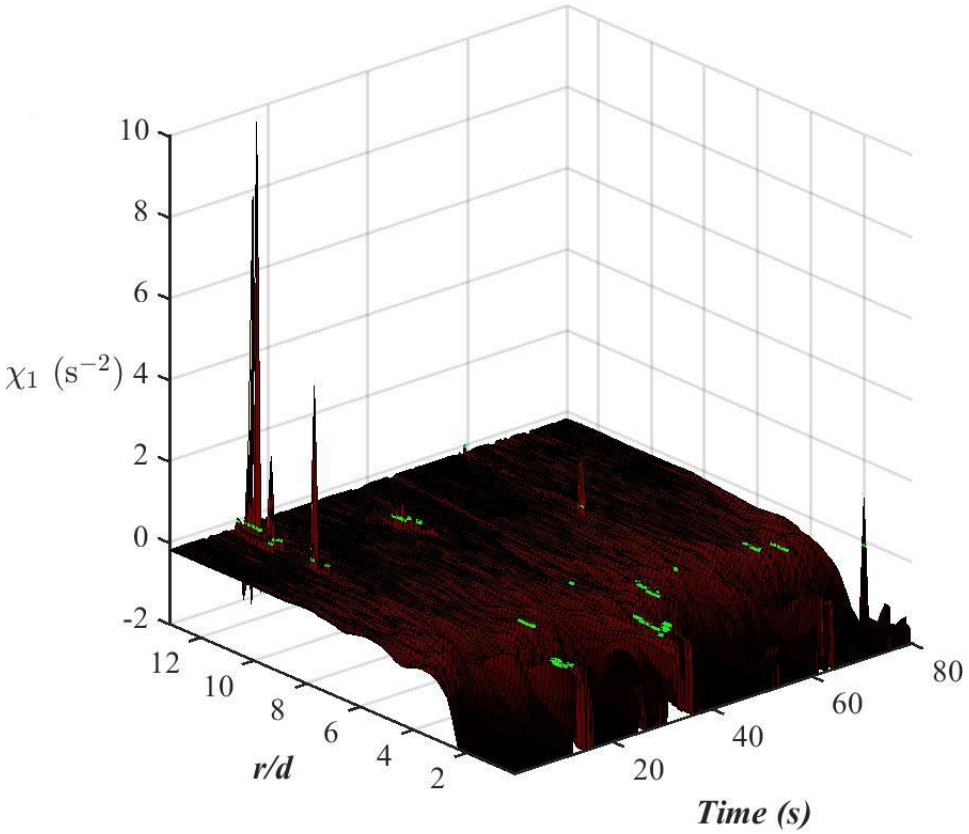

Figure 8.7: Variation of χ_1 with time and r/d at z/d = 10, for a jet with Re_0 = 2300 at Ω = 0.21 rad s^{-1}.

flow field during the formation-decay cycles of the jet.

However, the situation is fundamentally different when considering χ_2 for non-axisymmetric flow in figure 8.8. In this figure clear time-periodic regions of strong instability ($\chi_2 > 0$) exist. This suggests that the criterion for non-axisymmetric flow of Nagarathinam *et al.* (2015) is a suitable parameter to characterize centrifugal jet instability in the presence of background rotation and axial flow. In this context also note that Nagarathinam *et al.* (2015) stated that, to the best of their knowledge, their criterion, here referred to by χ_2, represented the first effort to characterize centrifugal instability in non-axisymmetric vortices with an axial flow and background rotation. The present study is the first experimental corroboration of the theoretical results of Nagarathinam *et al.* (2015).

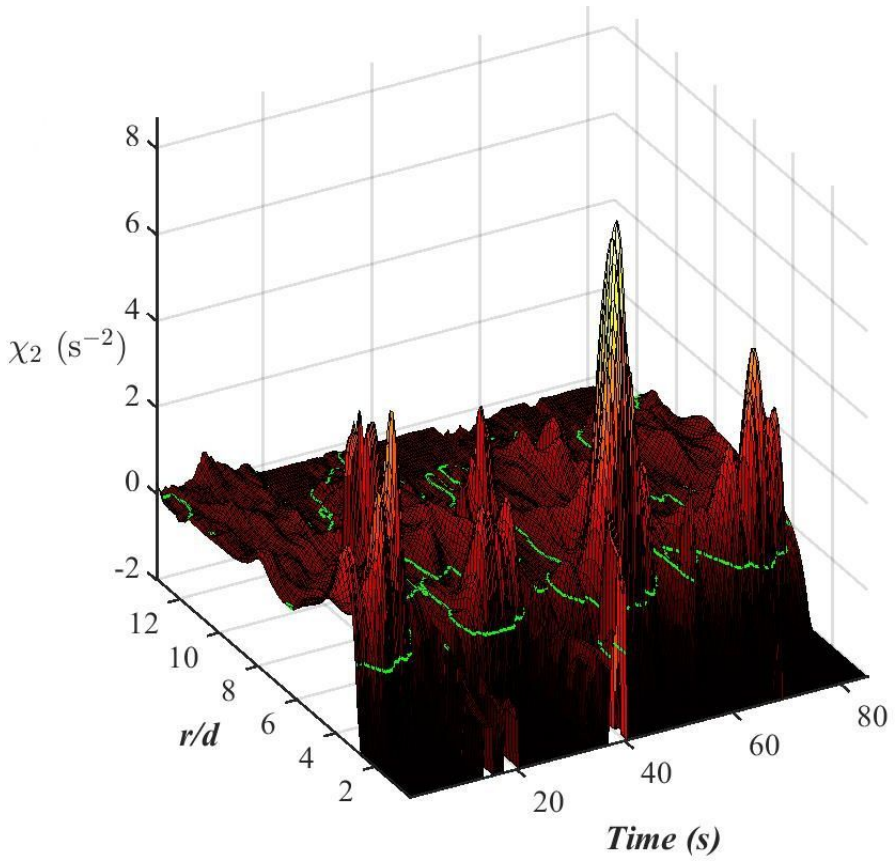

Figure 8.8: Variation of χ_2 with time and r/d at z/d = 10, for a jet with Re_0 = 2300 at Ω = 0.21 rad s^{-1}.

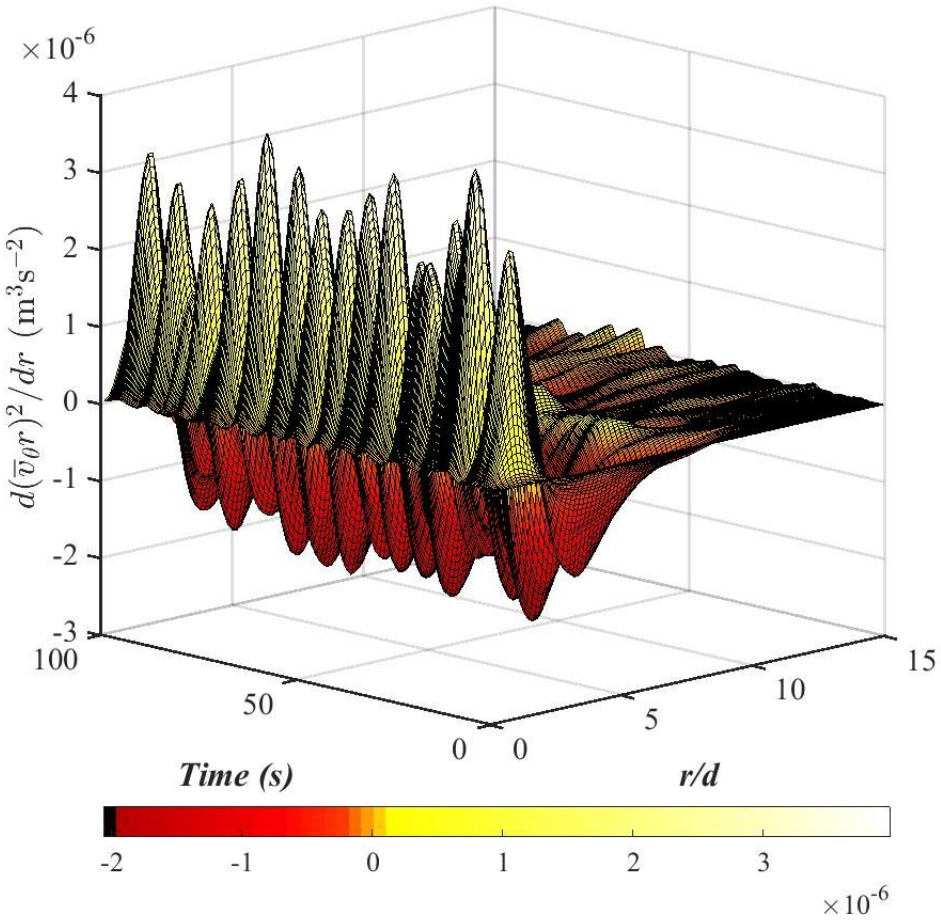

Figure 8.9: Variation of $d(\overline{v_\theta}r)^2/dr$ with time and r/d at z/d = 0.5, for a jet with Re_0 = 2300 at Ω = 0.83 rad s^{-1}.

Figures 8.9, 8.10, 8.11,8.12, 8.13, 8.14, 8.15, and 8.16 shows experimental results which correspond to those of figures 8.1, 8.2, 8.3,8.4, 8.5, 8.6, 8.7 and 8.8, but for the experiments conducted with background rotation of Ω = 0.84 rad s^{-1}, which is comparatively higher compared to Ω = 0.21 rad s^{-1} in the former case. In comparison to figures 8.4, 8.5, 8.6, 8.7, and 8.8, the data in figures 8.12, 8.13, 8.14, 8.15, and 8.16 for the higher rotation rate reveal an important result. Reference to data represent in figures 8.12, 8.13 and 8.14, for background rotation 0.21 rad s^{-1} and figures 8.4, 8.5 and 8.6, for background rotation 0.84 rad s,$^{-1}$, for the modified Rayleigh criterion of Kloosterzielt & Heijst (1991), reveal that regions of instability ($d(\overline{v_\theta}r + \Omega r^2)^2/dr \leq 0$) are now no longer present at all, at the higher rotation rate for all three heights (i.e.

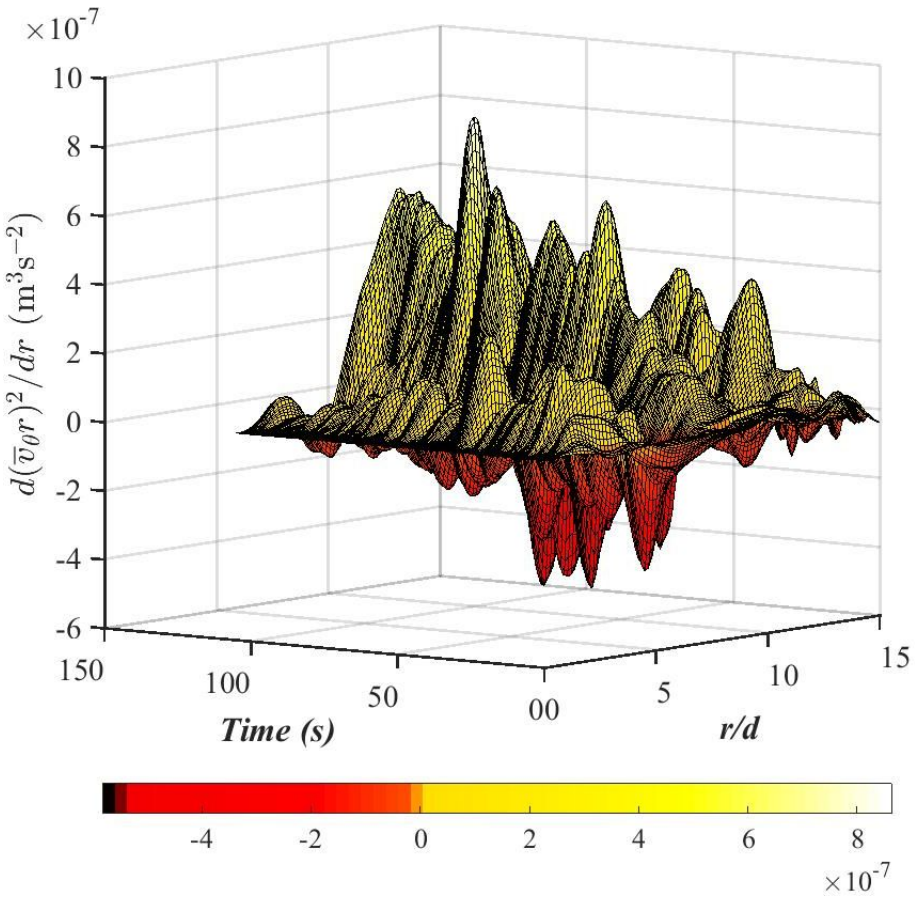

Figure 8.10: Variation of $d(\overline{v_\theta}r)^2/dr$ with time and r/d at z/d = 5, for a jet with Re_0 = 2300 at Ω = 0.83 rad s^{-1}.

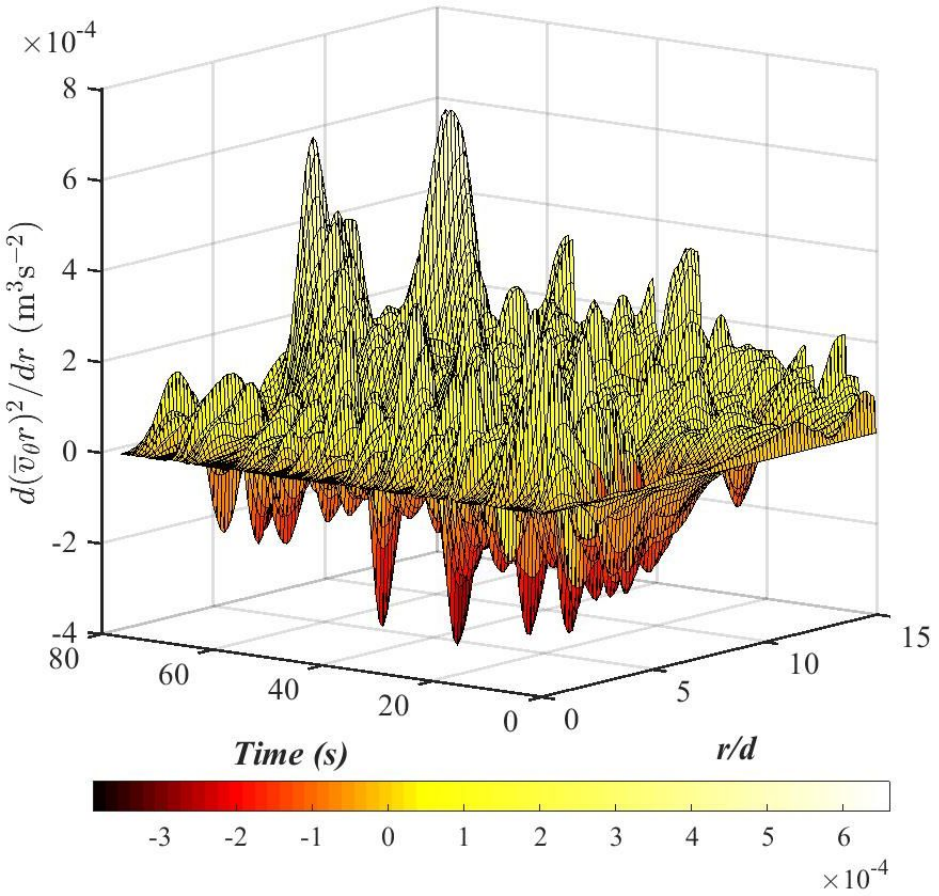

Figure 8.11: Variation of $d(\overline{v_\theta}r)^2/dr$ with time and r/d at z/d = 10, for a jet with Re_0 = 2300 at Ω = 0.83 rad s^{-1}.

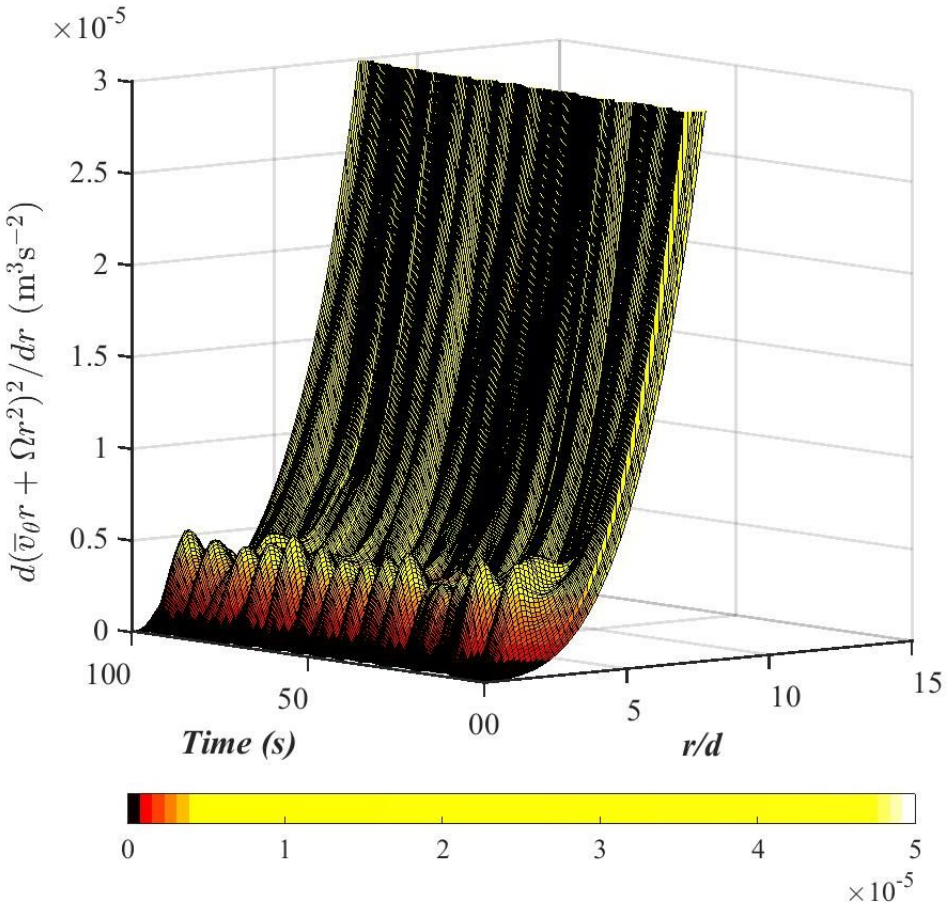

Figure 8.12: Variation of $d(\overline{v_\theta}r + \Omega r^2)^2/dr$ with time and r/d at $z/d = 0.5$, for a jet with $Re_0 = 2300$ at $\Omega = 0.83$ rad s^{-1}.

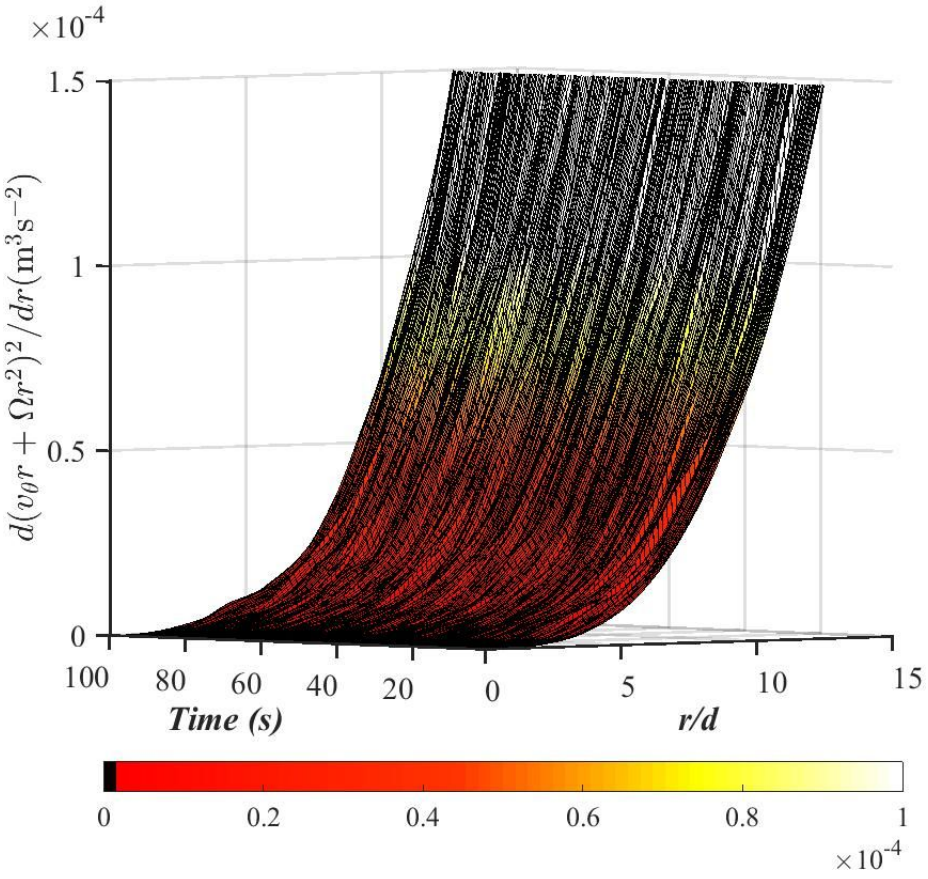

Figure 8.13: Variation of $d(\overline{v_\theta}r + \Omega r^2)^2/dr$ with time and r/d at $z/d = 5$, for a jet with $Re_0 = 2300$ at $\Omega = 0.83$ rad s^{-1}.

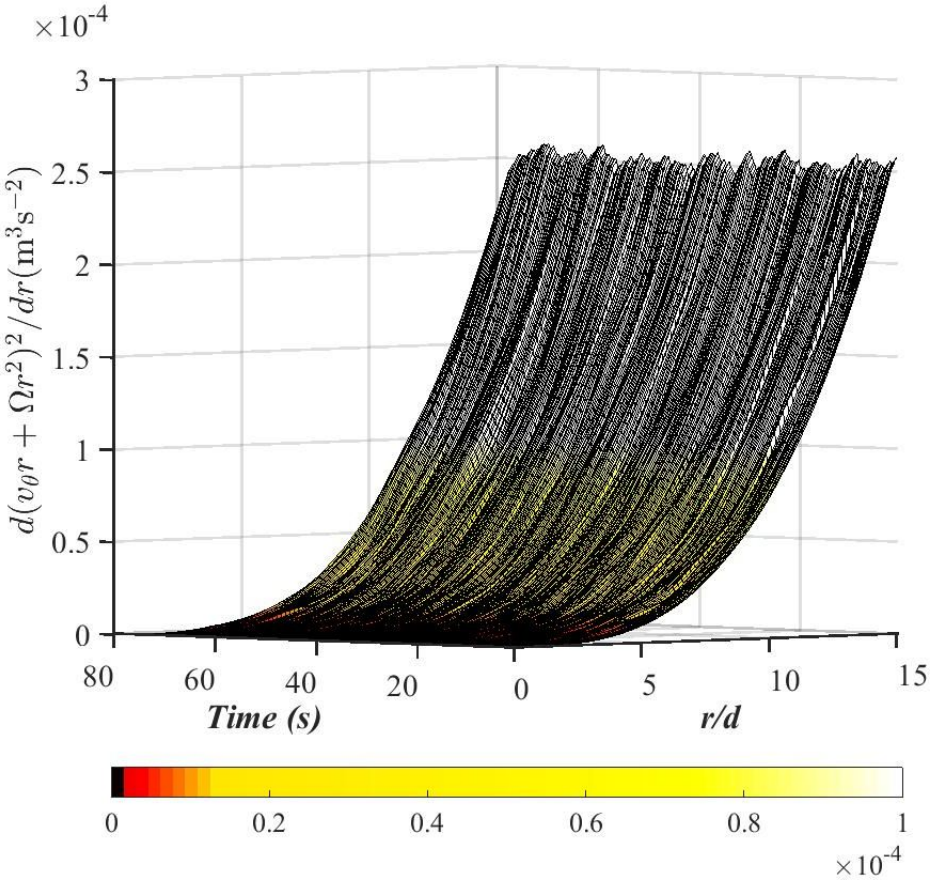

Figure 8.14: Variation of $d(\overline{v_\theta}r + \Omega r^2)^2/dr0$ with time and r/d at $z/d = 10$, for a jet with $Re_0 = 2300$ at $\Omega = 0.83$ rad s^{-1}.

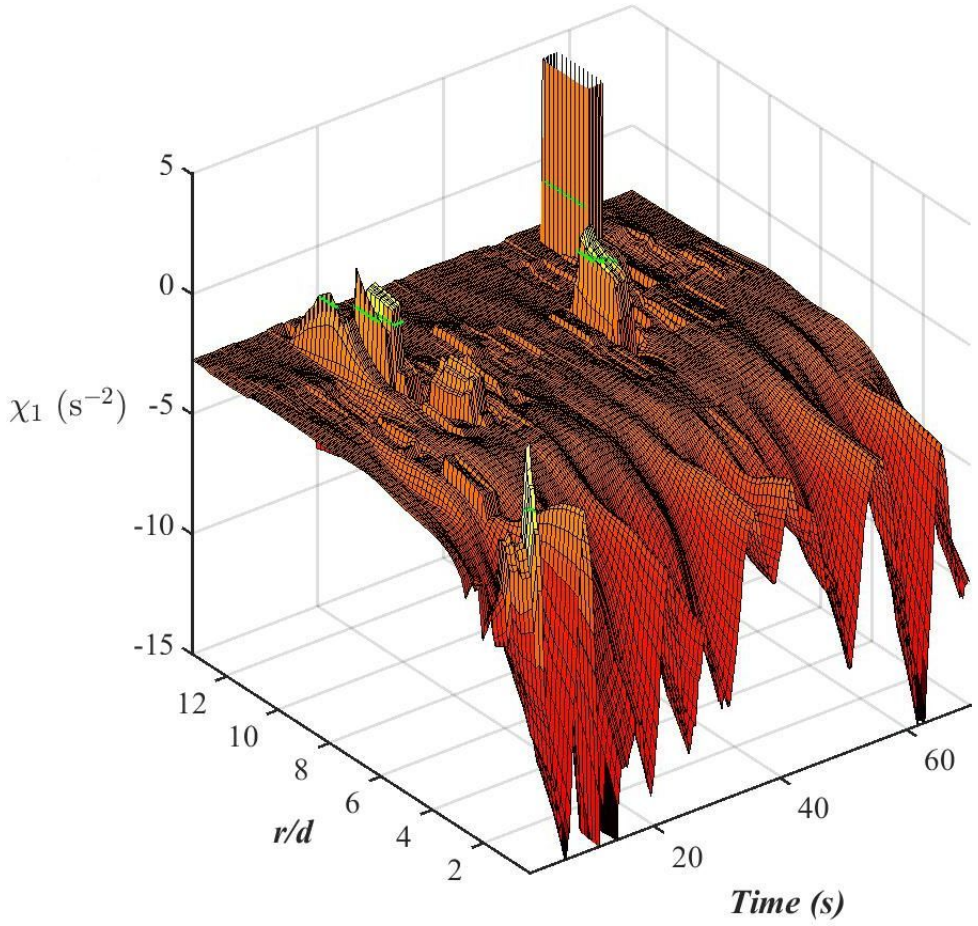

Figure 8.15: Variation of χ_1 with time and r/d at z/d = 10, for a jet with Re_0 = 2300 at Ω = 0.83 rad s^{-1}.

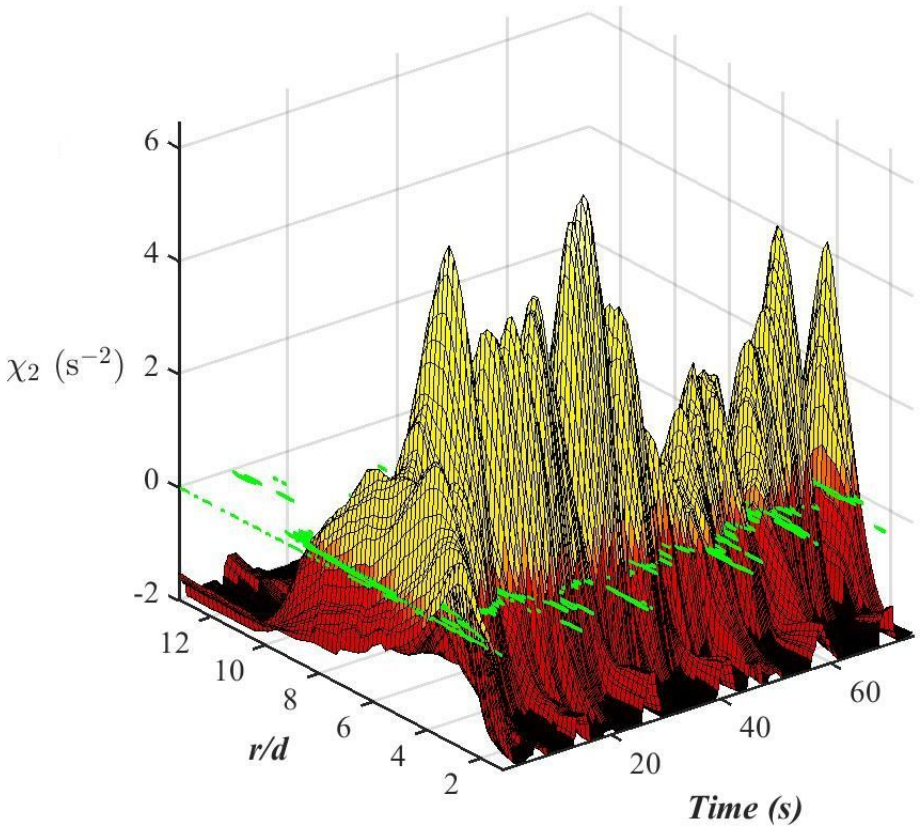

Figure 8.16: Variation of χ_2 with time and r/d at z/d = 10, for a jet with Re_0 = 2300 at Ω = 0.83 rad s^{-1}.

$z/d = 0.5, 5, 10$). Yet the jet was observed to be unstable in the experiments. Nevertheless, as revealed by figure 8.16 the criterion for instability ($\chi_2 > 0$) of Nagarathinam *et al.* (2015) remains to be satisfied as it was in the case for experiments at the lower rotation rate. This result implies that the axial flow is a crucial factor effecting the stability of the jets.

Figure 8.17 (a) - (d) summarizes the temporal variation of quantities relevant in the context of the instability criterion of Nagarathinam *et al.* (2015) at height $z/d = 10$ for the particular radial location $r/d = 3.5$. The purpose of this final figure is to help elucidate the qualitative nature of the flow dynamics throughout the formation-decay cycles of the jets. Figure 8.17 (a) displays the radial component $\overline{v}_r$ of the flow velocity for the two successive runs of the experiments used to determine the magnitude of the time shift required to synchronize the data for the vertical velocity component $\overline{w}_{z-r}$ in the $z-r$ plane and the azimuthal flow velocity, $\overline{v}_\theta$ in the $z-\theta$ plane. In figure 8.17 (a) one of the two data curves begins at $t = 0$ s whereas the other one has been shifted to the right to start at $t = 15$ s. Figure 8.17 (a) reveals that for this time shift of $t = 15$ s the maxima and the minima of the two data sets in the figure approximately overlap. This data shift of $\Delta = 15$ s was then applied to synchronize the required data for the mean circulation $\overline{\Gamma}_{\theta-r}$, obtained from data measured in the $\theta-r$ plane in one experiment, and the data for the mean axial velocity $\overline{w}_{z-r}$ in the $z-r$ plane, measured in the repetition of the experiment, These synchronized data were then used to calculate the instability parameters χ_1 and χ_2 in figure 8.17 (d) and (e).

Figures 8.7, 8.8, 8.15 and 8.16 had already revealed that χ_1 and χ_2 fluctuate with time. The parameter χ_1, in figure 8.17 (d), only marginally extends into positive values during its fluctuation cycles and, as is known from the discussion above, it is not the appropriate parameter to characterize the instability. Nevertheless, a comparison of χ_1 and χ_2 in figures 8.17 (d) and (e) shows that their fluctuations are synchronized. Moreover, that their fluctuations are also in phase with the circulation, $\overline{\Gamma}_{\theta-r}$ in figure 8.17 (b) and with the mean axial velocity, $\overline{w}_{z-r}$ in figure 8.17 (c). The comparison of the plots shows that $\chi_2 \geq 0$ when $\overline{\Gamma}_{\theta-r}$ and $\overline{w}_m$ reach their maxima. This implies that the decay of the jet

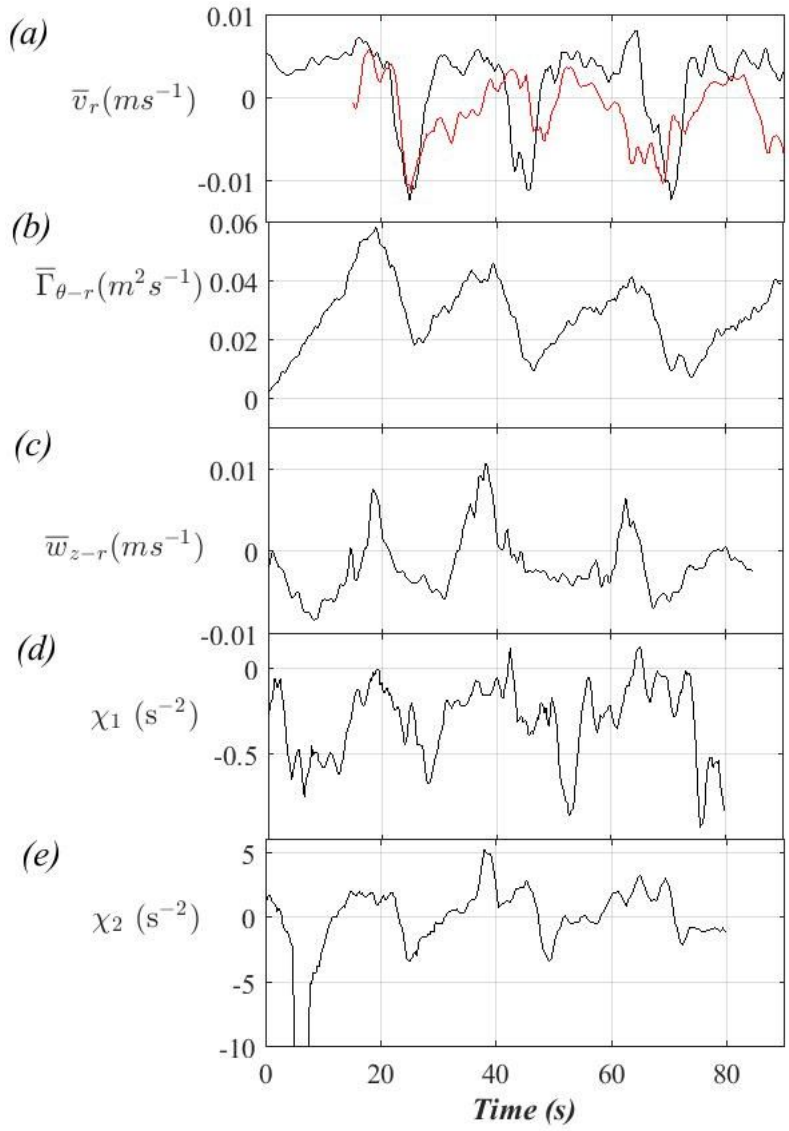

Figure 8.17: (a) Phase synchronized, mean radial velocity component $\overline{v}_\theta$ obtained for two separate experimental runs from $\theta - r$ plane and from $r - z$ plane; (b) circumferentially and radially averaged mean circulation $\overline{\Gamma}_{\theta-r}$ (c) radially averaged mean vertical flow component $\overline{w}_{\theta-r}$; (d) parameter χ_1, from (3.45) & (e) parameter χ_2, from (3.46) , for instability criterion of Nagarathinam *et al.* (2015) for a jet with $Re_0 = 2300$, at $\Omega = 0.21$ rad s^{-1}, for $z/d = 10$, $Ro_0 = 302$.

is initiated when both the upward flow motion and the internal swirling motion of the jet are most pronounced. As the mean circulation in figure 8.17 (b) and the mean axial flow in figure 8.17 (c) begin to reduce in value so does the mean radial velocity $\overline{v}_r$ in figure 8.17 (a). However, it is this flow directed radially inwards which, in association with the Coriolis force resulting from the background rotation, is responsible for the development of swirl. Simultaneously the instability parameter χ_2 in figure 8.17 (e) decreases until it adopts a value, around $\chi_2 \approx -3$, that is low enough for a new formation cycle of the jet to be initiated. The renewed rise of χ_2 is associated with a rise of the mean axial velocity as well as an increased radial entrainment, reflected through a simultaneous increase of $\overline{v}_r$ which, in turn, leads to a concurrent increase of the mean circulation. This process continues until χ_2 once again reaches values sufficiently above zero such that another breakdown cycle is initiated.

Chapter 9

Forced Plumes in the Presence of Background Rotation

The main focus of this chapter is to investigate the behaviour of plumes developing subject to the effects of background rotation and compare their behaviour with that of jets affected by corresponding levels of background rotation. To this end experiments with plumes for nine different background rotation rates were conducted and analysed. Corresponding to the earlier experiments with jets the horizontal PIV laser-sheet measurement plane was at a height z/d = 10 above the ejection nozzle. The main motivation for these additional experiments involving plumes were the very recent observations by (Deremble, 2016; Tomàs *et al.*, 2016; Frank *et al.*, 2017) who reported that plumes developing subject to background rotation display a precession around the axis of rotation. Note again that we only conducted measurements in the horizontal plane for the experiments performed for this short comparative investigation.

9.1 Behaviour in the Horizontal Plane

Figures 9.1 (a) - (p) show the development of the plume in the horizontal plane at height z/d = 10 above the source and for a time interval of 60 s. The Reynolds number associates with the plume is Re = 1800. Figure 9.1 (q) shows the colour map for velocity vectors. Also this colour map is the same as that used in figure 6.12, in which the development of the jet in the horizontal plane,

$z/d = 10$, above the source is shown. The background rotation associated with figures 9.1 (a) - (p) is 0.52 rads^{-1}. A reasonably higher background rotation rate was selected for displaying the data in figures 9.1 (a) - (p), so that the considered time interval for displaying the velocities extends over five table revolutions. This choice was motivated by the observations of Frank *et al.* (2017) who reported that precession is initiated after approximately one rotation period when the plume tilts laterally and starts to precess anticyclonically. Also note that the velocity vectors are displayed in the interval $-15 \leqslant x/d \leqslant 15$ and $-15 \leqslant y/d \leqslant 15$ in the horizontal plane for figures 9.1 (a) - (p). As displayed in figure 9.2 the circumferentially averaged azimuthal velocity($\overline{v}_\theta$) approaches zero ($\overline{v}_\theta \to 0$) as $r/d \to 15$. Therefore $r/d = 15$ was selected as the cut off radius for any calculation and any display purposes.

Figure 9.1 (a) reveals that a cyclonic vortex has formed due to the entrainment velocity and in association with the action of the Coriolis force. After 8 s, in figure 9.1 (b), the radius of the vortex has increased and the shape of the vortex is elliptical. In figure 9.1 (c), the shape of the vortex remains elliptical. As in figures 9.1 (d) - (p), as time passes, there is no drastic change in the vector fields that can be observed other than a slight change of the radius. When the temporal development of the jet in the horizontal plane, at height $z/d = 10$, in figure 6.12 is compared with that of the plume at the same height in figure 9.1 one can clearly see that there is no indication of breaking of the vortex at any time instance for the plume. Instead the maximum velocity of the plume, in the horizontal plane, changes its location more randomly compared to the jets. This enables two conclusions. One is that, only the location of the maximum entrainment velocity changes its position or the whole plume itself changes its position. But if the maximum velocity changes its location and the plume is still, it should change around a one circumference of the plume which it is not in this case, as it can be seen in figures 9.1 (a) - (p). Moreover figures 9.3 (a) - (o) show a much closer view of a series of vector fields of the plume in the horizontal plane, $z/d = 10$. The figures display the time development of the vortex beginning 24 s after ejection of liquid had commenced. Note that the vortex that has formed due to the entrainment of ambient fluid into the plume spins cyclonically. The background rotation associated with the figures

is 0.52 rad s^{-1}. In each one of the sub figures the superposed crosshair-style lines identify the center of the source at distance $z/d = 10$ below the measurement plane. These lines serve to provide a clear visualisation of the movement of the centre of the vortex with respect to the centre of the source. An inspection of the series of figures reveals that the centre of the vortex, that is the centre of the plume, precesses anticyclonically around the centre of the source.

Moreover figure 9.4 displays the temporal variation of non dimensionalised radial coordinate of the location of the maximum velocity, that shows a periodic behaviour. The radial coordinate for the location of the maximum velocity varies in between $-5 \leqslant r/d \leqslant 5$. Further more figure 9.5 shows the temporal variation of the radial coordinate for the location of the maximum vorticity, which is again periodic and vary in between $-5 \leqslant r/d \leqslant 5$.

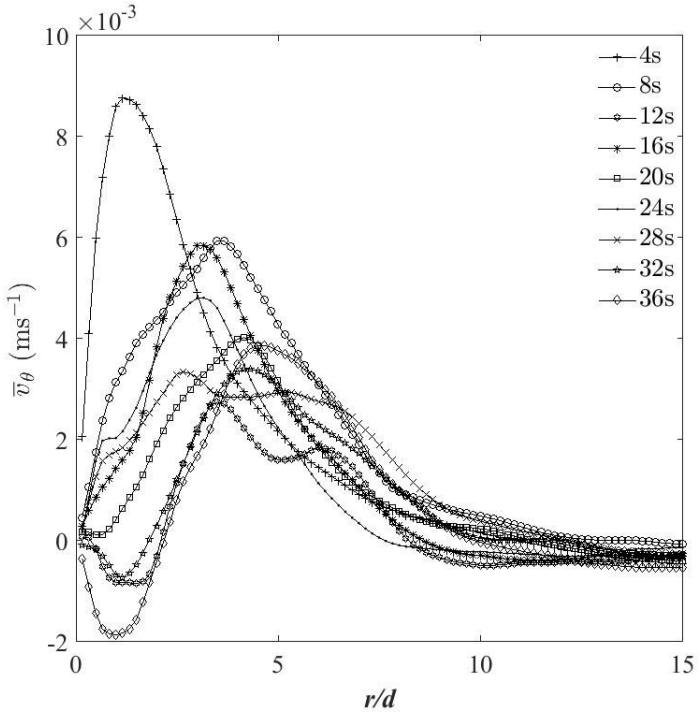

Figure 9.2: Profiles of the circumferentially-averaged azimuthal velocity component $\overline{v}_\theta$ as a function of nondimensionalised distance r/d from the centre for different instances in time, for a plume with $Re_0 = 1800$ at $\Omega = 0.52$ rad s^{-1}, $z/d = 10$.

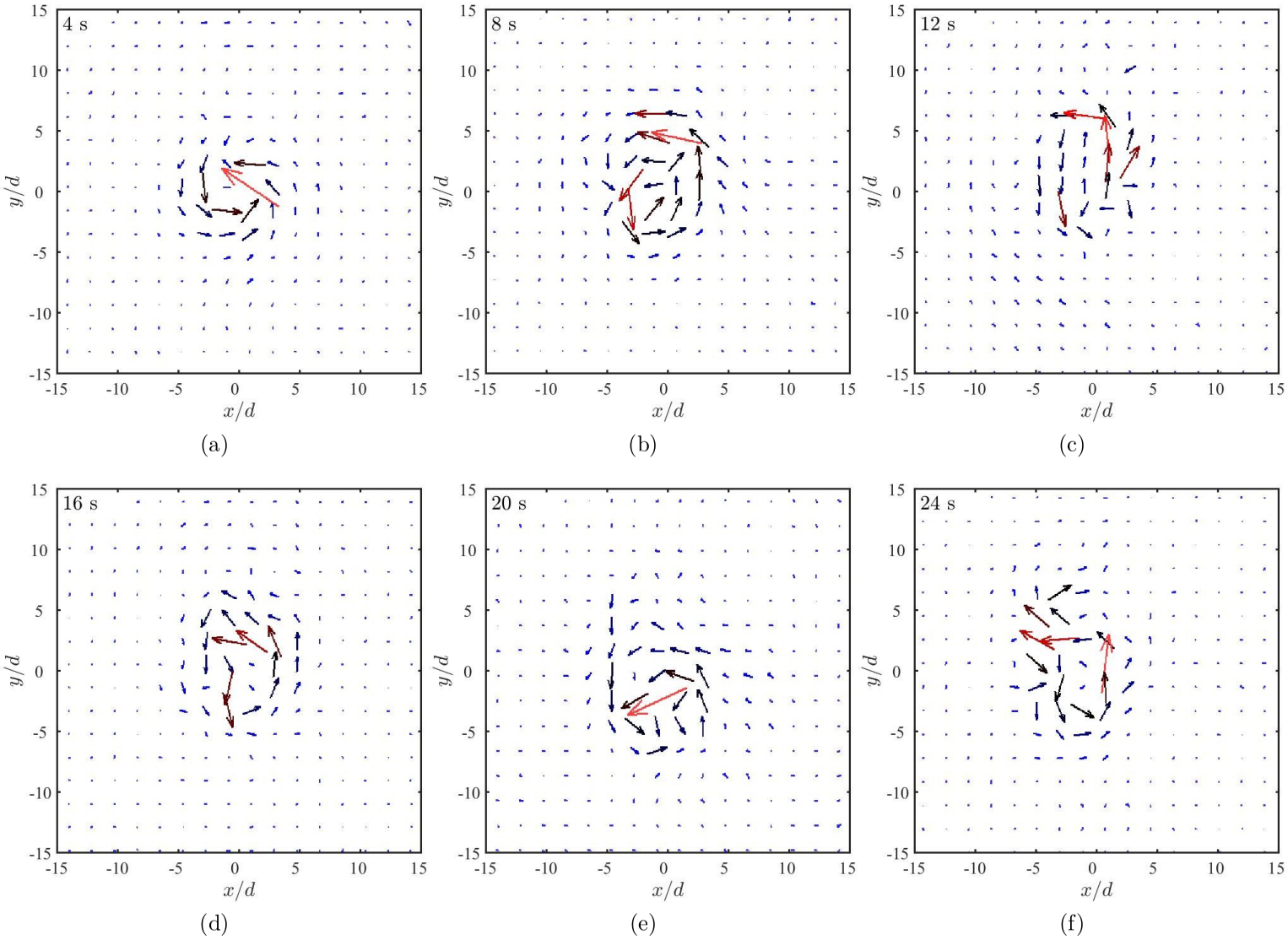

Figure 9.1: Instantaneous vector fields of the velocity components, u_r & u_θ for a plume with Re_0 = 1800 at Ω = 0.21 rad s^{-1} at times t for at z/d = 10

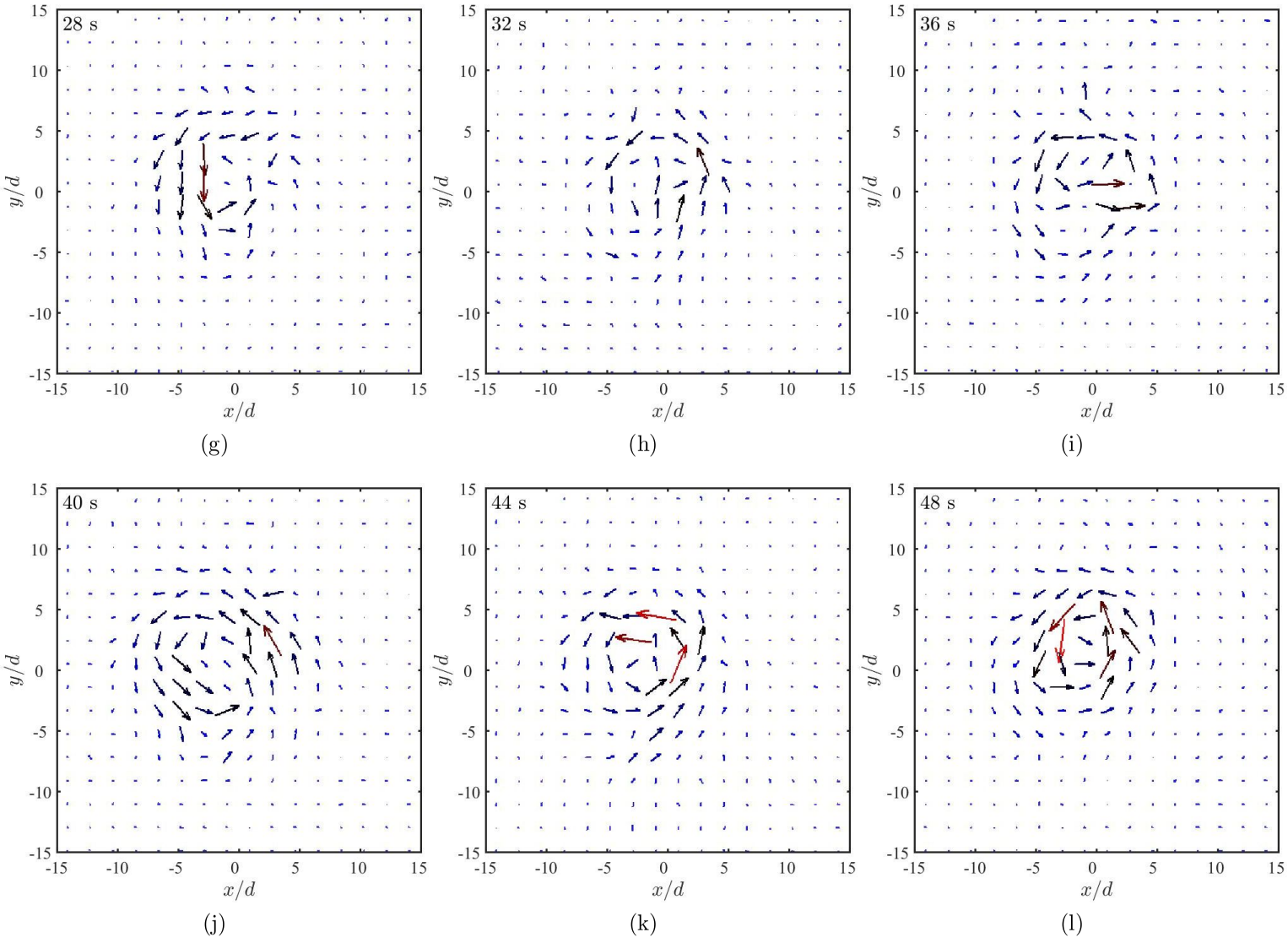

Figure 9.1: Continued

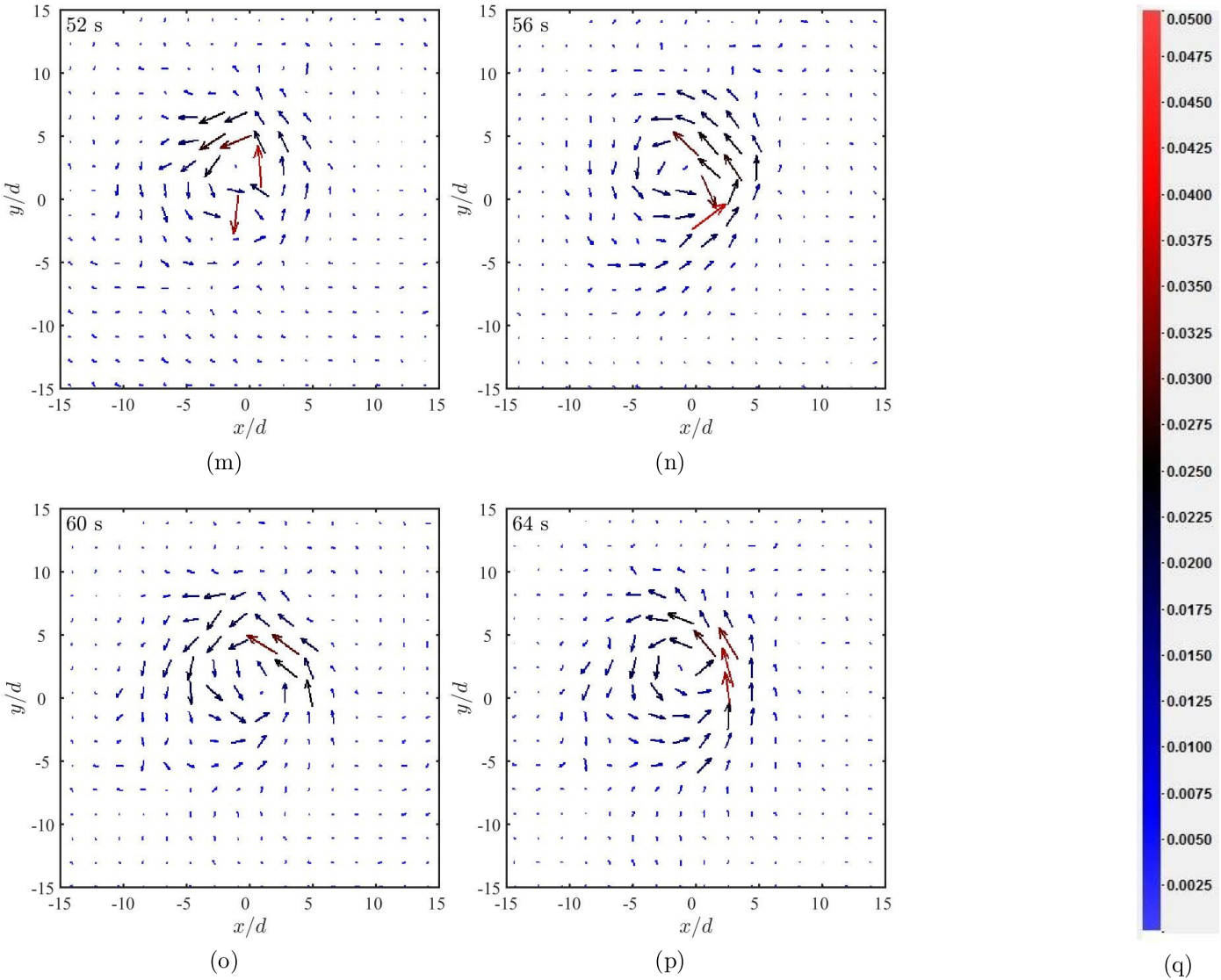

Figure 9.1: Continued

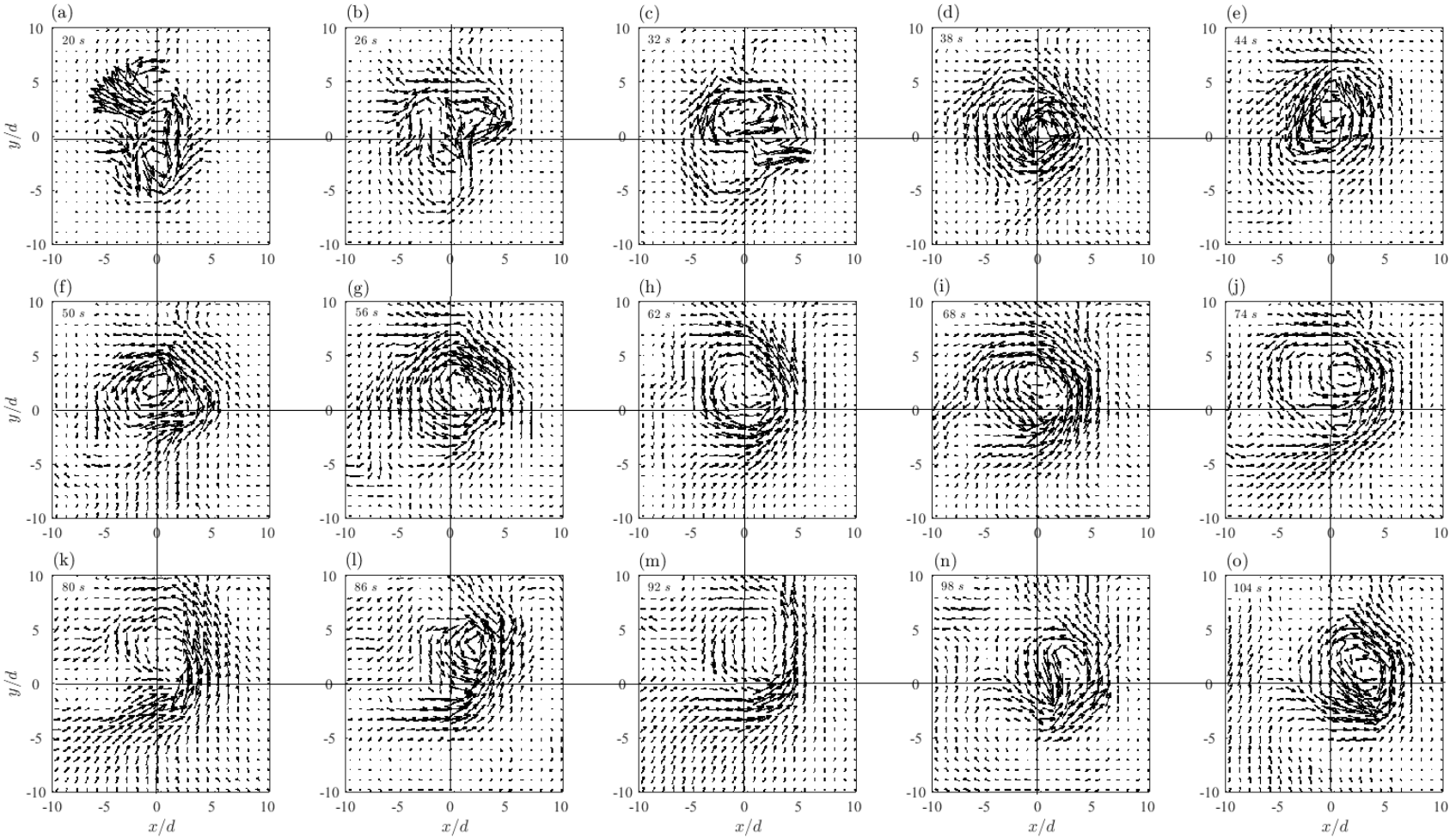

Figure 9.3: Instantaneous velocity vectors field of the plume at (a) 20 s, (b) 26 s (c) 32 s (d) 38 s (e) 44 (f) 50 s (g) 56 s (h) 62 s (i) 68 s (j) 74 s (k) 80 s (l) 86 s (m) 92 s (n) 98 s (o) 104 s for a plume with $Re_0 = 1800$, at $\Omega = 0.52$ rad s^{-1}, for $z/d = 10$.

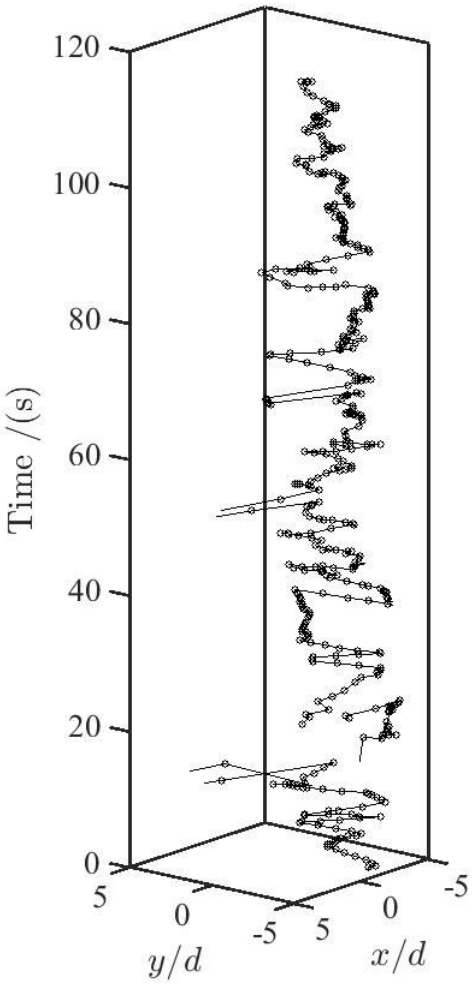

Figure 9.4: Temporal variation of the nondimensionalised radial coordinate for the location of the maximum velocity for the plume of $Re_0 = 1800$ at $z/d = 10$ at background rotation 0.52 rad s^{-1}.

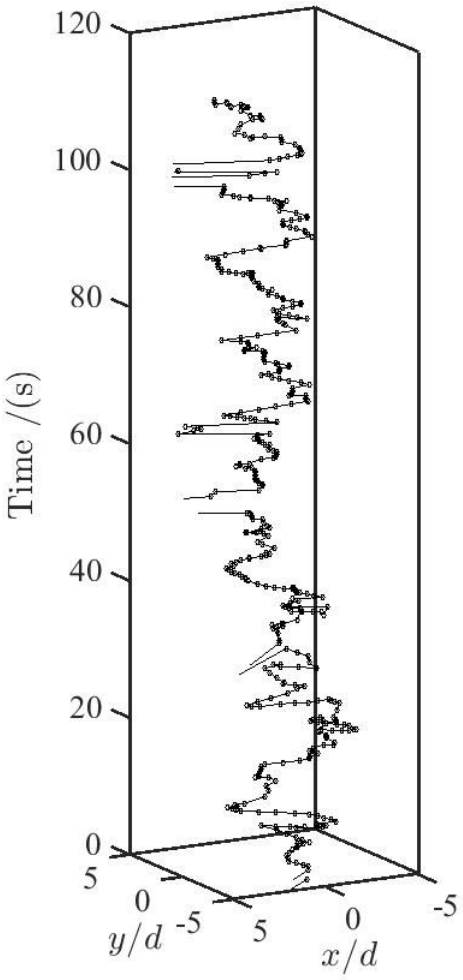

Figure 9.5: Temporal variation of the nondimensionalised radial coordinate for the location of the maximum vorticity for the plume (Re_0 = 1800) at height z/d = 10 with background rotation 0.52 rad s^{-1}.

9.2 First POD Mode

Figures 9.6 (a)-(i) display the velocity vectors of the first POD mode for nine different background rotation rates for the plume (Re_o = 1800), at height z/d = 10d. A comparison of these figures with those for the corresponding first POD modes of the jets shown in figures 7.1 (a) - (i) reveals that both are qualitatively different. For the jets the first POD mode vector arrangement is such that it forms a cyclonic or anticyclonic vortex. However, in the case of the plumes the vector fields display two or three co-rotating or counter-rotating

vortices. Moreover figures 9.7 & 9.8 show the first three POD modes of the plume (Re_0 = 1800) and the jet (Re_0 = 2300) respectively, with vorticity in the background. When the first mode of the plume and jet displayed in 9.7 (a) & 9.8 (a) are compared one can see that the vector field arrangement and the background vorticity values fundamentally differ from each other. This also applies to the second POD mode of the plume & the jet, where two co-rotating vortices can be seen in the second POD mode of the plume(refer figure 9.7 (b)) and two counter-rotating vortices are visible for the second POD mode of the jet (refer figure 9.8 (b)). However, when the third POD mode of the plume and the jet are compared they are qualitatively similar as revealed by figures 9.7 (c) & 9.8 (c) respectively. It is clear from the comparison of these POD modes that the plume and the jet behave differently when subjected to background rotation.

Figures 9.9 (a) - (i) display the temporal variation of the time coefficient (c_1) of the first POD mode of the plumes. The background rotation rate for each plume is given in the figure caption. Unlike for their counterparts for the time coefficient of the first POD mode of jets in figures 7.2 (a) - (i), a clear qualitative period can not be observed in figure 9.9 (a) - (h) except for the graph in figure 9.9 (i). The graphs plotted in figures 9.9 (a) - (h) reveal that they correspond to non stationary processes for which statistical properties vary with time. Therefore Fourier analysis can not be used to find the frequency of the data given in 9.9 (a) - (i). Following Frank *et al.* (2017) the Hilbert-Huang transformation is therefore used to calculate the precession frequency of the plume.

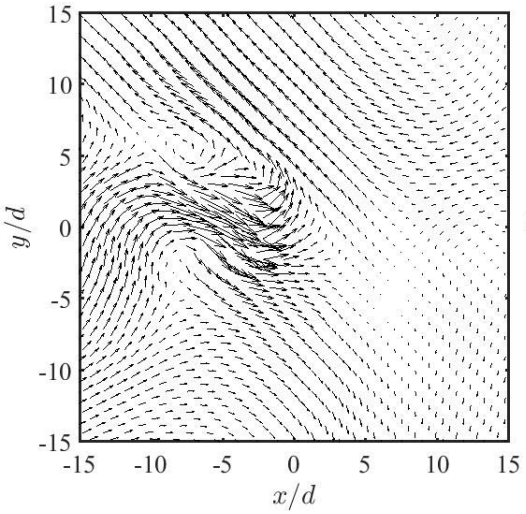
15
10
5
0
-5
-10
-15
y/d
-15 -10 -5 0 5 10 15
x/d

(a)

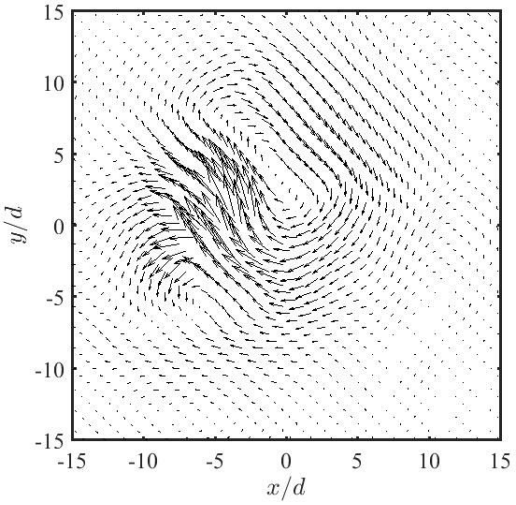
15
10
5
0
-5
-10
-15
y/d
-15 -10 -5 0 5 10 15
x/d

(b)

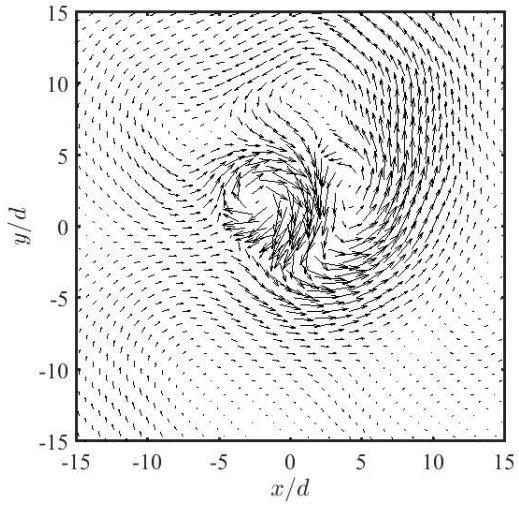
15
10
5
0
-5
-10
-15
y/d
-15 -10 -5 0 5 10 15
x/d

(c)

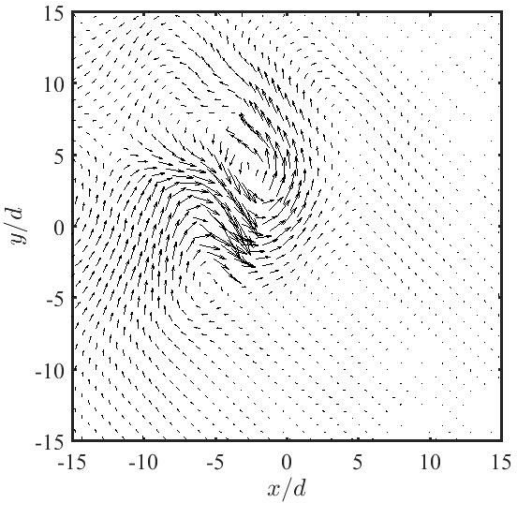
15
10
5
0
-5
-10
-15
y/d
-15 -10 -5 0 5 10 15
x/d

(d)

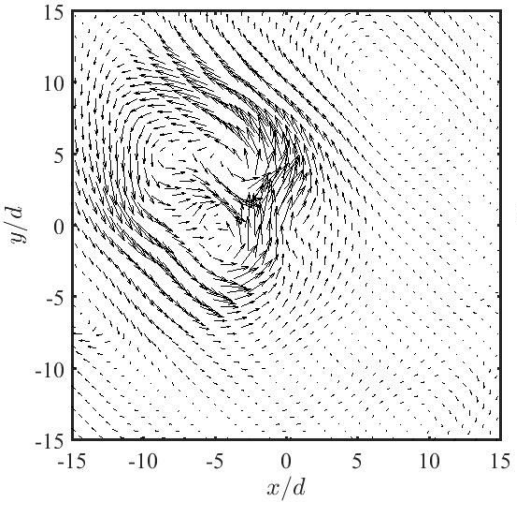
15
10
5
0
-5
-10
-15
y/d
-15 -10 -5 0 5 10 15
x/d

(e)

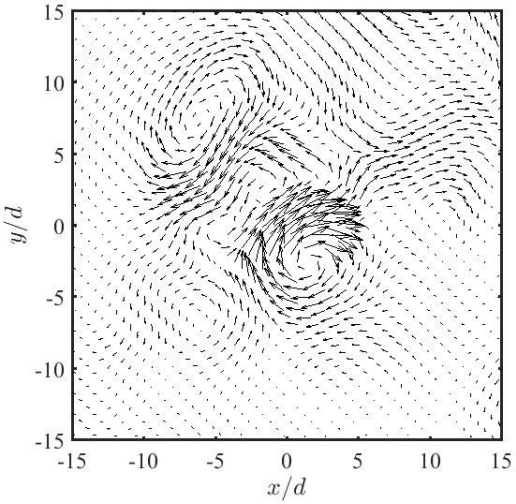
15
10
5
0
-5
-10
-15
y/d
-15 -10 -5 0 5 10 15
x/d

(f)

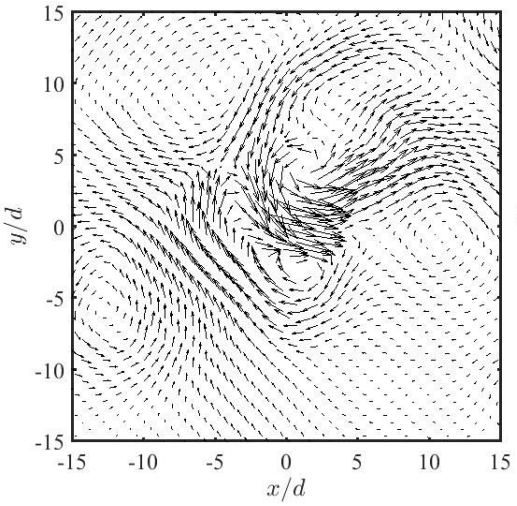
15
10
5
0
-5
-10
-15
y/d
-15 -10 -5 0 5 10 15
x/d

(g)

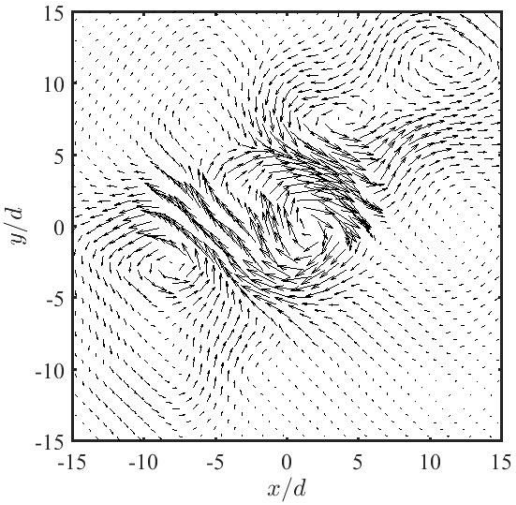
15
10
5
0
-5
-10
-15
y/d
-15 -10 -5 0 5 10 15
x/d

(h)

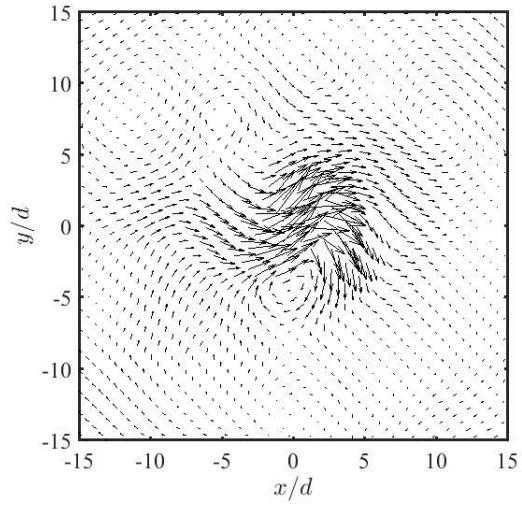

(i)

Figure 9.6: Velocity vectors of first POD mode: the rotation rates, in units of rad s^{-1}, associated with sub figures are: (a) 0.2, (b) 0.31, (c) 0.41, (d) 0.52, (e) 0.63, (f) 0.73, (g) 0.83, (h) 0.94, (i) 1.05.

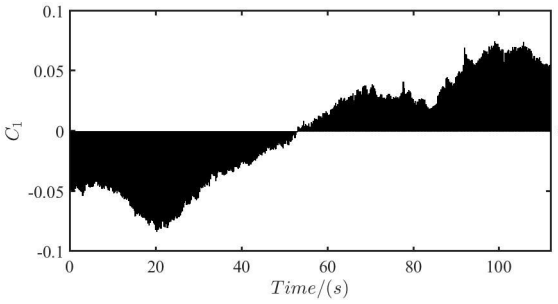

(a)

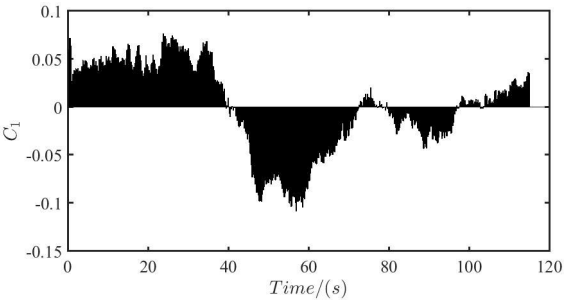

(b)

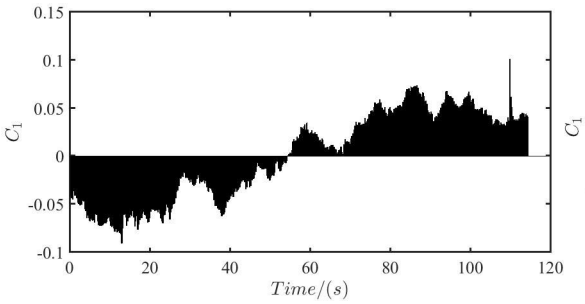

(c)

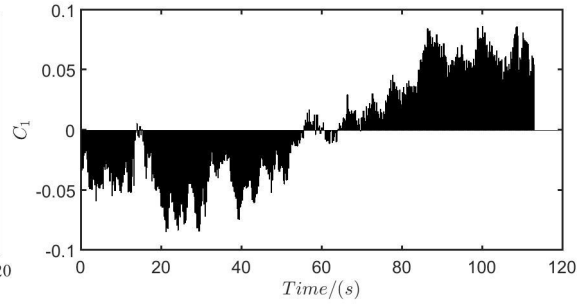

(d)

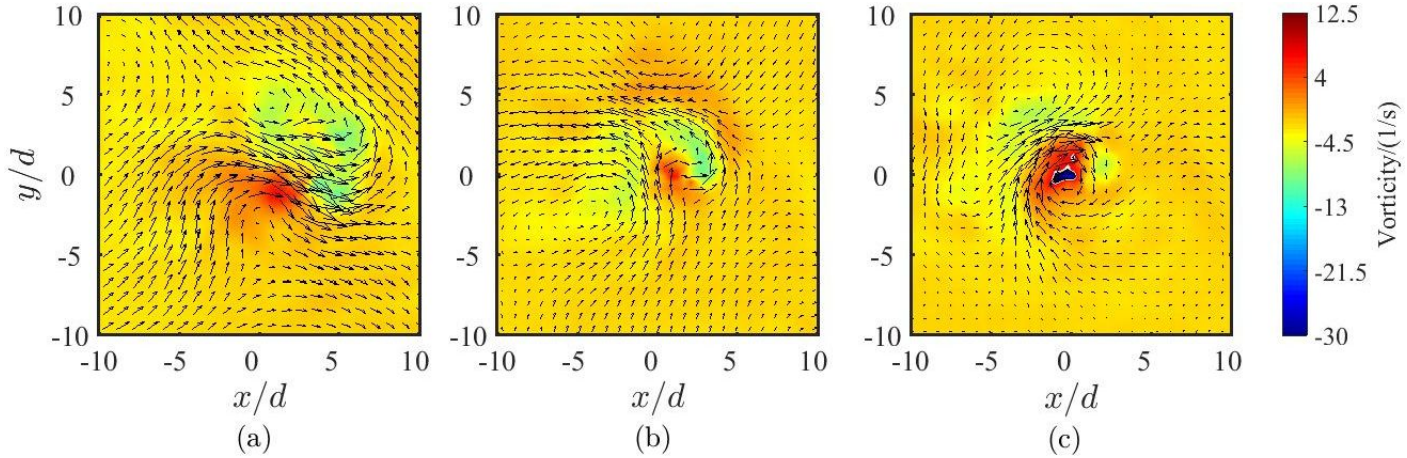

Figure 9.7: Velocity vectors and vorticity field of (a) first, (b) second and (c) third POD mode for a plume with $Re_0 = 1800$, at $\Omega = 0.21$ rad s^{-1}, for $z/d = 10$.

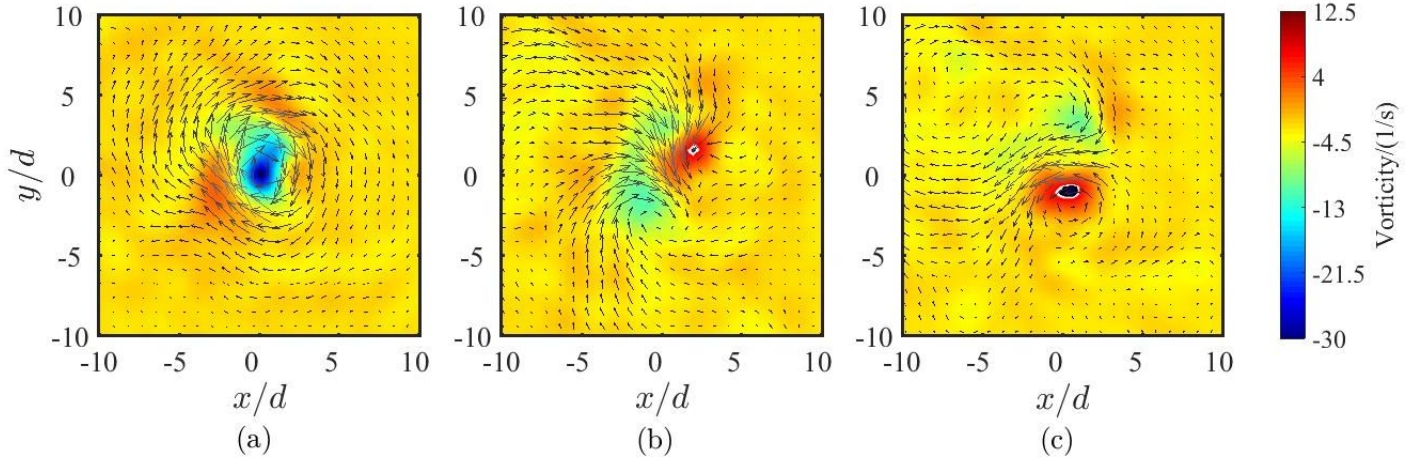

Figure 9.8: Velocity vectors and vorticity field of (a) first, (b) second and (c) third POD mode for a jet with $Re_0 = 2300$, at $\Omega = 0.21$ rad s^{-1}, for $z/d = 10$.

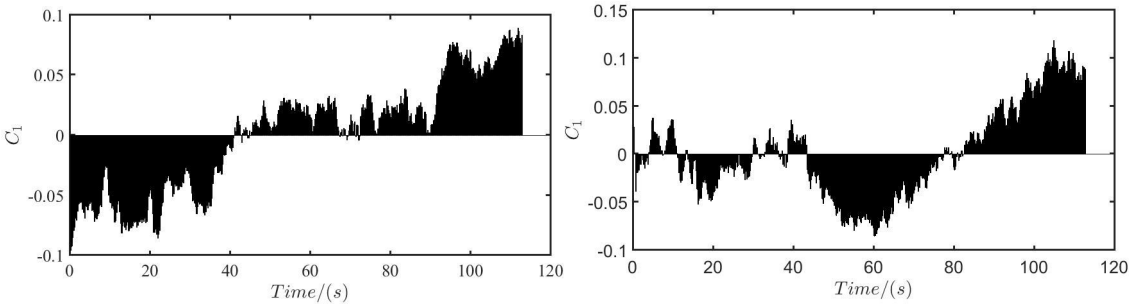

(e)

(f)

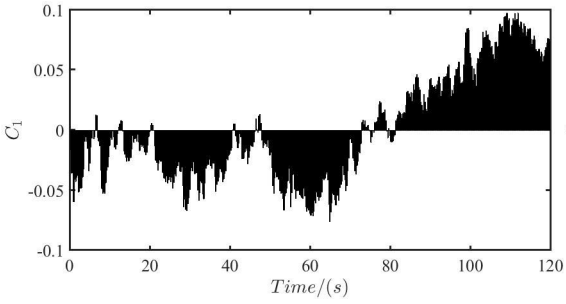

(g)

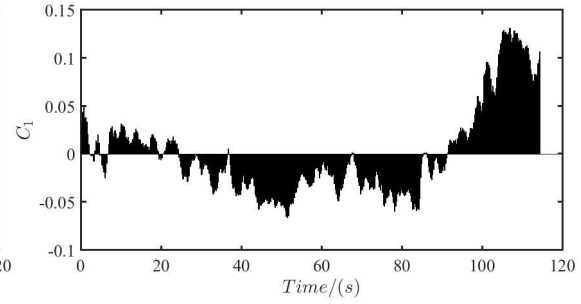

(h)

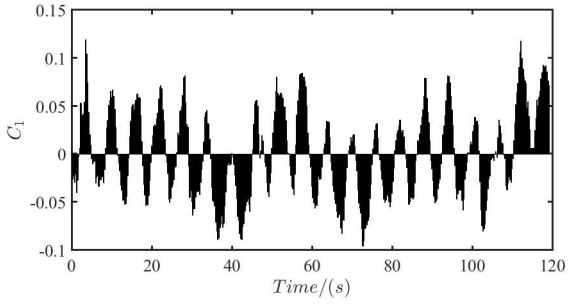

(i)

Figure 9.9: Variation of the time coefficient of the first POD mode: the rotation rates, in units of rad s^{-1}, associated with sub figures are: (a) 0.2, (b) 0.31, (c) 0.41, (d) 0.52, (e) 0.63, (f) 0.73, (g) 0.83, (h) 0.94, (i) 1.05.

9.3 The Precession Frequency of the Plume

In order to find the precession frequency of the plumes, the time characteristics of the first POD mode were subjected to the Hilbert-Huang transformation.

The first step of the Hilbert-Huang transformation is to find IMFs using empirical mode decomposition (EMD). To perform this at first, the local extrema should be identified and then the local maxima and the local minima should be connected by two separate splines. Figure 9.10 shows the temporal variation of the time characteristics (C_1) of the first POD mode for a plume subjected to background rotation of 0.52 rad s^{-1}, together with the splines for the maxima and the minima. The figure also shows the temporal variation of the local mean. The local mean was calculated considering the values along the two splines for maxima and minima. Next the mean was subtracted from the original data (C_1) and those values are used to calculate a new local mean after fitting new splines to the local extrema as done previously. This process is called sifting. Figure 9.11 shows the splines and the temporal variation of the new local mean after first sifting. Note that the data within time interval 0 – 40 s was only displayed in order to made the details clear in figure 9.11. The sifting process was continued until the first IMF was found.

Figure 9.12 shows the first IMF (IMF_1) found after 40 sifting processes. Then this procedure was continued to find IMF_2 and so on. To find IMF_2 the sifting process was started with a new data set, obtained by subtracting IMF_1 from the original data C_1. Moreover figure 9.13 displays IMF_2. As by the definition of an IMF, it should have a zero local mean as in two figures 9.12 & 9.13. For finding the next IMF, the data was obtained by subtracting IMF_2 by initial data used to find IMF_2. The IMF finding process was continued until further IMFs cannot be found. Figure 9.14 displays all the IMFs found for C_1. When the last IMF was subtracted from the initial data that used to find it, the remainder is called 'residue'. Figure 9.15 displays temporal variation of the residue and the original data (C_1). The next step is to find the most relevant IMF from all IMFs. This was achieved by calculating the correlation coefficient between each IMF and original data. The IMF with highest correlation coefficient has been selected as the most relevant IMF for the considered process and the instantaneous frequencies were calculated using the Hilbert transform.

Figures 9.16 (a) - (f) show the instantaneous frequency variation with time for the first six IMFs from IMF_1 to IMF_6 respectively. As figure 9.16 (a)

reveals the first IMF has a comparatively high instantaneous frequencies of around 1 – 2 (Hz). The second IMF has an instantaneous frequencies around the same values. But in the case of IMF_3 the instantaneous frequencies are within 0 – 1 (Hz). For the first three IMFs the instantaneous frequencies vary significantly within the considered time interval as displayed by figures 9.16 (a)-(c). However, for the fifth, sixth & seventh IMF the instantaneous frequencies do not change much with time when compared to the first three IMFs. The correlation coefficient calculated with the original data and each IMF were 0.1, 0.13, 0.11, 0.11, 0.09, and 0.3 for IMF_1, IMF_2, IMF_3, IMF_4, IMF_5 and IMF_6 respectively. Therefore IMF_6, which has the highest correlation coefficient was selected to find the precession frequency and the mean value of the instantaneous frequencies of IMF_6 was taken as the precession frequency at background rotation 0.51 rad s^{-1}. The same procedure was followed for analysing the precession frequencies for other values of background rotations within 0.21-1.05 rad s^{-1}. Figure 9.17 shows the variation of the plume precession rate (ω_p) in rad s^{-1} with background rotation Ω. The linear least-squares fit to the data is $\omega_p = 0.7\Omega$ and it is represented by the solid line interpolating the data points. Figure 9.18 shows the variation of precession rate with the background rotation for plumes for nine different experimental data sets by Frank *et al.* (2017). The nine different data series shown in the figure are for nine different Rossby number ranges. The least square fit shown by green line suggests $\omega_p \approx 0.4\Omega_0$. Further Frank *et al.* (2017) considered pure plumes ($\Gamma \approx 1$). But the plume that we considered in our study is a forced plume of which $\Gamma \approx 0.003$. Therefore in summary it can be concluded that even with a initial momentum at the source, plumes do precess around the axis of background rotation.

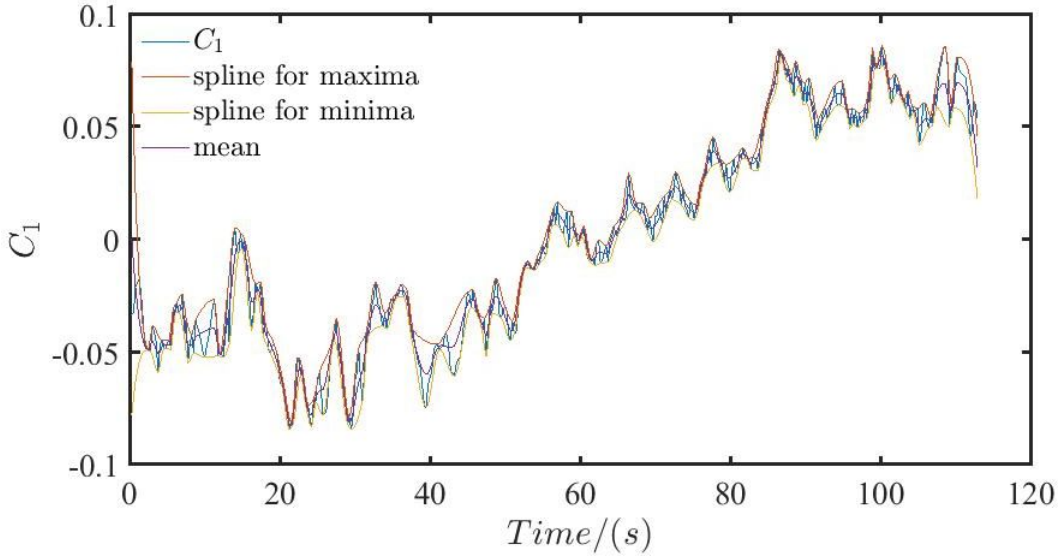

Figure 9.10: Splines for extrema and mean for the time characteristics (C_1) of POD mode 1 of the plume at background rotation 0.52 rad $^{-1}$.

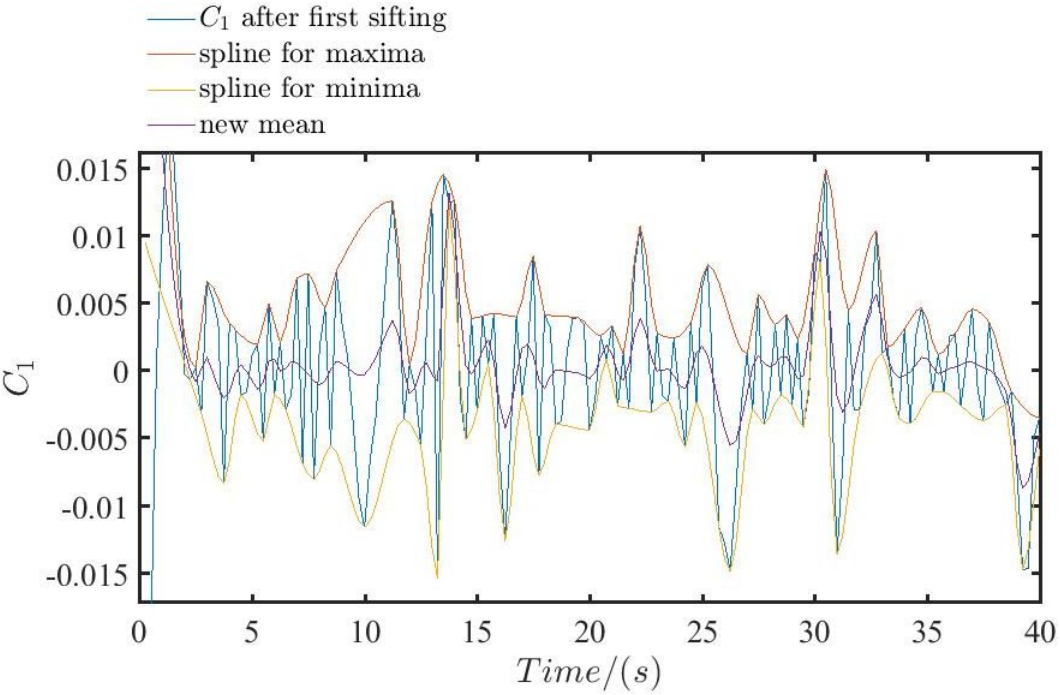

Figure 9.11: Splines for extrema and mean for the time characteristic (C_1) of POD mode 1 of the plume after first sifting, at background rotation 0.52 rad $^{-1}$

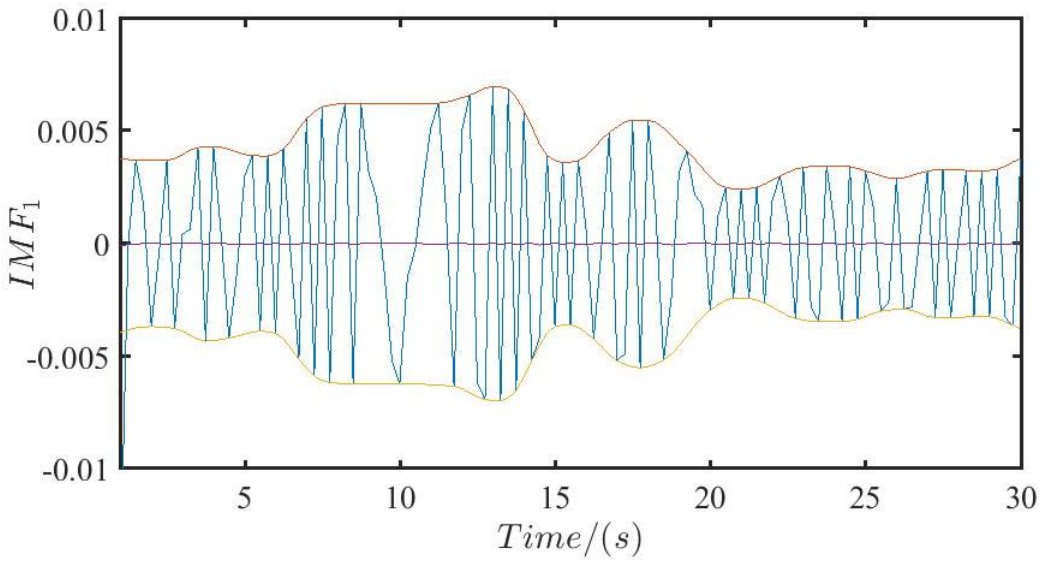

Figure 9.12: IMF_1 calculated from the time characteristic (C_1) of POD mode 1 of the plume after twenty siftings. Splines for extrema and mean is shown in yellow and purple lines respectively. The background rotation associate with data is 0.52 rad s^{-1}.

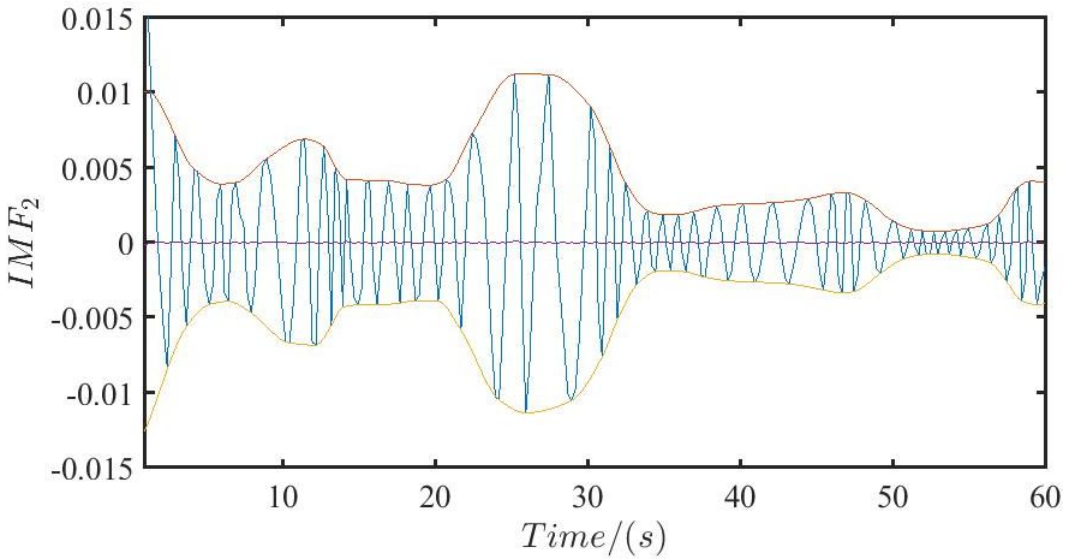

Figure 9.13: IMF_2 calculated from the time characteristic (C_1) of POD mode 1 of the plume after ten siftings. Splines for extrema and mean is shown in yellow and purple lines respectively. The background rotation associate with data is 0.52 rad s^{-1}.

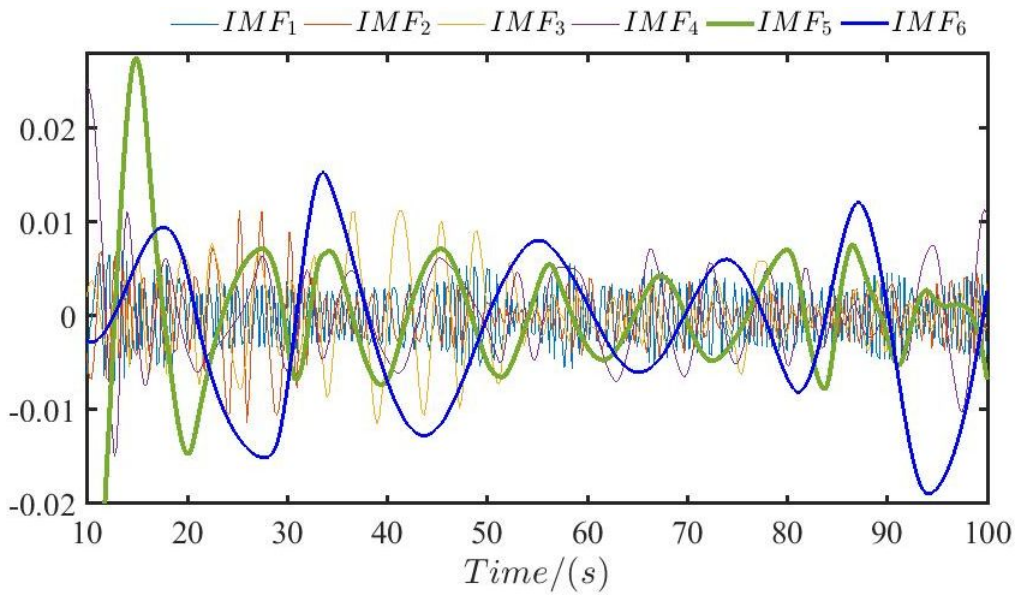

Figure 9.14: All IMFs calculated from the time characteristic (C_1) of POD mode 1 of the plume. The background rotation associate with data is 0.52 rad s^{-1}.

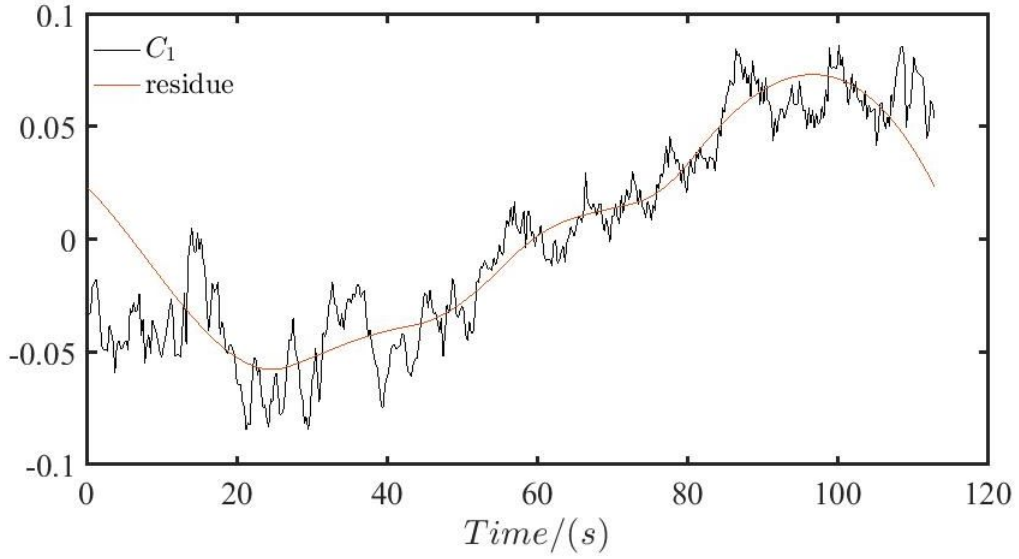

Figure 9.15: All IMFs calculated from the time characteristic (C_1) of POD mode 1 of the plume. The background rotation associate with data is 0.52 rad s^{-1}.

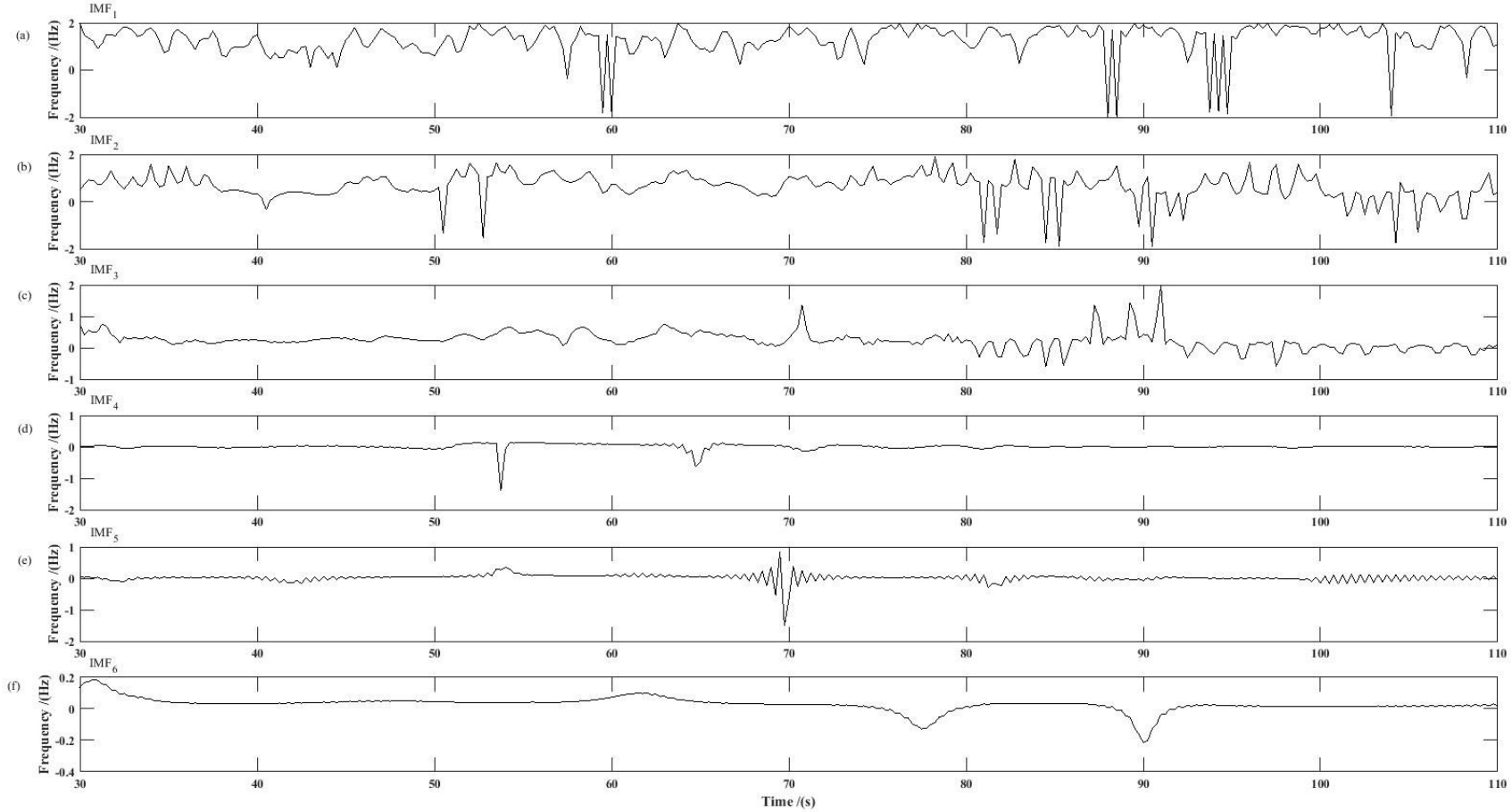

Figure 9.16: Variation of the instantaneous frequency with time for the plume at $\Omega = 0.52$ rad s^{-1}, for $z/d = 0.5$: (a) IMF$_1$, (b) IMF$_2$, (c) IMF$_3$, (d) IMF$_4$, (e) IMF$_5$, (f) IMF$_6$.

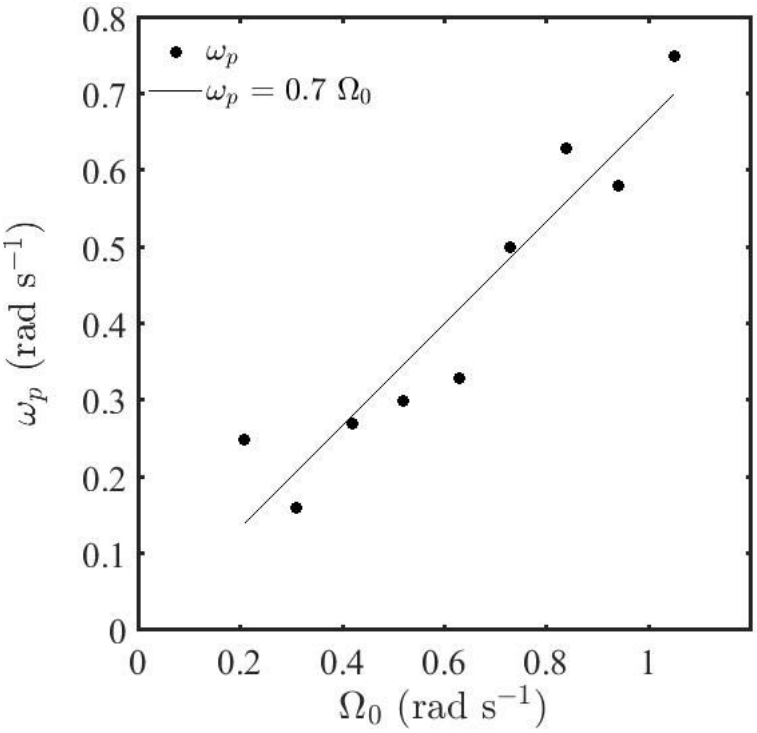

Figure 9.17: Variation of the plume precession rate ω_p with background rotation rate Ω.

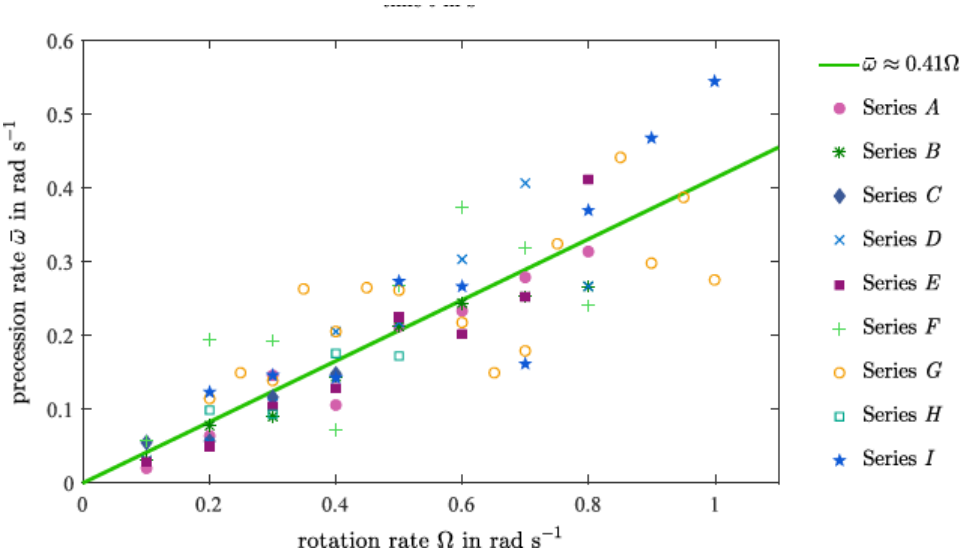

Figure 9.18: Mean plume precession frequency $\overline{\omega}$ as a function of the rotation rate of the environment Ω by Frank *et al.* (2017).

Chapter 10

Conclusion

An experimental study investigating the dynamics of turbulent jets developing subject to background rotation was conducted. Data from comprehensive PIV measurements were presented, analyzed and discussed. From the concurrent literature review it appears that the present investigation represents the first study of jets in rotating systems that utilized PIV technology, rather than relying on the analysis of data obtained from dye visualizations only. The absence of previous PIV studies on the subject is probably related to the fact that a rather large-scale rotating-tank facility is required, together with an on board PIV system mounted within the rotating frame of reference, to successfully perform such an investigation with sufficient accuracy. Initial experiments on jets in non-rotating systems were performed to demonstrate the capabilities of the experimental arrangement in comparison to relevant data available in the literature. The analysis has shown that the results of the current study for water jets in a non-rotating environment agree very well with the corresponding data that Ezzamel *et al.* (2015) recently obtained from PIV measurements investigating jet flow in air and with data of other authors such as Papanicolaou *et al.* (2008), Panchapakesan & Lumley (1993), Hussein *et al.* (1994) and Wang & Law (2002).

The study of the investigation of the effects of background rotation on the dynamics of the jets was originally motivated partly by a short summary of computational results of Lawrie *et al.* (2011) who found, and qualitatively discussed, that their simulations revealed that the jets develop a helical in-

stability, whereby the jet initially grows, entrains ambient fluid and that this leads to helical displacement of the jet from the axis. At large displacement amplitudes the jet beaks down upon which the associated entrainment ceases. They argued that with nothing to drive further radial convergence of material contours, the azimuthal velocity decays sufficiently for the jet to reform, whereby a periodic formation-breakdown cycle is established. The experimental PIV data discussed here have corroborated that jets subject to background rotation behave precisely as described in Lawrie *et al.* (2011). The quantitative analysis of our PIV data has revealed that the formation-breakdown frequency of the jets increases linearly with both the rotational velocity of the turntable and the volumetric ejection rate of liquid from the source. It was further revealed that the formation-breakdown cycle existed when the fluid ejection at the source was continued long time compared to the period of formation - breakdown cycle of the jet. The data have moreover shown that the initiation of the formation-breakdown cycle is associated the development of an axial back flow. The existence of such a back flow for jets subject to background rotation was first described in the summary of the numerical simulations of Niino (1980) but it had hitherto not been corroborated experimentally.

The breakdown of the jets proceeds via an instability whereby the initially circular cross section of the jets splits up into two separate, helically upward winding strands; where the sense of winding is predominantly cyclonic with regard to the background rotation. The analysis has shown that both the onset of breakdown of the jet and the onset of the reformation process can be characterized in terms of a critical value of a local Rossby number that scales linearly with the global Rossby number; up to a certain critical value of the global Rossby number.

As part of the data analysis, the first experimental test was performed to corroborate the very recent theoretical instability criterion of Nagarathinam *et al.* (2015) for non-axisymmetric centrifugal instability of vortices subject to background rotation and in the presence for axial flow. The discussion has revealed that this criterion appears to represent a suitable means to characterize our experimental data. The results in particular confirm that the axial flow plays

a very prominent role in the context of the centrifugal instability of vortices subject to background rotation.

It was found that each formation-breakdown cycle proceeds as follows. At the start of the cycle axial flow develops. This axial flow results in radial entrainment of ambient liquid. This necessitates the development of a radially inward flow. The radial flow component is subject to the action of Coriolis forces. Thereby a swirling motion within the jet develops. When the circulation and the axial flow concurrently reach maxima characterized by the instability criterion of Nagarathinam *et al.* (2015) for non-axisymmetric flow the breakdown phase of the cycle begins. During this phase the circulation as well as the axial and the radial flow diminish. This continues until a critical level is reached that is low enough such that, aided by the continuous supply of fluid being ejected from the source, a new formation cycle can be established.

Finally the behaviour of jets developing subject to background rotation was briefly compared to the corresponding behaviour displayed by plumes. This short concluding set of experiments was motivated by the two very recent computational studies of Tomàs *et al.* (2016) and Deremble (2016) and the experimental study of Frank *et al.* (2017) involved with the effect of background rotation on plumes. Neither one of the two computational studies reported any fluctuating behaviour similar to the formation-breakdown cycle observed in the simulations of Lawrie *et al.* (2011) for jets and corroborated here experimentally. However, Frank *et al.* (2017) reported that the plumes in their study precessed around the axis of rotation. This is unlike the behaviour displayed by the jets in the current study where no such precession was observed. Therefore a number of PIV experiments with plumes at nine different rotation rates was conducted to investigate if it was possible to reproduce the precession phenomenon for plumes in our experimental facility.

The analysis of the PIV data for the plumes revealed that these do not display a recurrent formation-breakdown cycle such as that observed for the jets. However, it was possible to confirm the existence of the precession phenomenon that was first described by Frank *et al.* (2017). The instantaneous velocity

measurements were analysed by means of the POD analysis. The first POD mode was compared with that of the jet at corresponding background rotation and at the corresponding horizontal plane (z/d = 10). It was found that the first POD mode of the jet is different from that of the plume for all background rotations. The precession frequency for each background rotation was calculated by subjecting the time characteristics of the first POD mode to a Hilbert-Huang transformation. It was found that the precession frequency, f_p, of the plumes increases linearly with the background rotational frequency, f_T of the turntable $f_p \approx 0.111 f_T$. In comparison the dye-visualization experiments on plumes conducted by Frank *et al.* (2017) yielded $f_p \approx 0.0644 f_T$. Since Frank *et al.* (2017) conducted experiments for dye visualization only more in-depth comparisons with the PIV data of the present study are not possible. Note that Tomàs *et al.* (2016) also observed a plume precession in their numerical simulations. Nevertheless they considered a stratified ambient and rotating environment whereas the ambient liquid in Frank *et al.* (2017) was not stratified. Moreover the plumes considered by Frank *et al.* (2017) are pure plumes of which $\Gamma \approx 1$ and the plumes considered in the present study are forced plumes of which $\Gamma \approx 0.003$.

Appendix A

A.I Limits of instability criterion χ_1

In order to see the accuracy of the values from the experimental analysis the limits of chi_1 was calculated.

$$\chi_1 = \left(\frac{4w'^2(r\Omega + v_\theta)^2}{(rv'_\theta - v_\theta)^2 + r^2w'^2} - 2\Big(\frac{v_\theta}{r} + \Omega\Big)\Big(v'_\theta + \frac{v_\theta}{r} + 2\Omega\Big)\right). \tag{A.1}$$

When $r = 0$ (at the center of the jet), since vertical velocity profiles show Gaussian behaviour at $r = 0$, it can be assumed that $w' = 0$. $v_\theta = (\Omega + \Omega')r$ where Ω' is the additional rotation rate created by jet flow. Therefore;

$$\chi_1 = -2\left(\frac{(\Omega + \Omega')r}{r} + \Omega\right)\left(\frac{d(\Omega + \Omega')r}{dr} + \frac{(\Omega + \Omega')r}{r} + 2\Omega\right). \tag{A.2}$$

$$\chi_1 = -2(2\Omega + \Omega')(4\Omega + 2\Omega'). \tag{A.3}$$

when $r \longrightarrow \infty$, there is no vertical or axial velocity therefore $w' \longrightarrow 0$.

$$\chi_1 = -2(\Omega)(v'_\theta + 2\Omega). \tag{A.4}$$

$$\chi_1 = -2(\Omega)(v'_\theta + 2\Omega). \tag{A.5}$$

$$\chi_1 = -2(\Omega)(\Omega'' + 3\Omega). \tag{A.6}$$

A.II Limits of instability criterion χ_2

$$\chi_2 = \left(\frac{4(dw/d\psi)^2(\Omega + 2\pi/T)^2}{(\Gamma/T^3)(dT/d\psi)^2 + (dw/d\psi)^2} - 2\Big(\frac{2\pi}{T} + \Omega\Big)\Big(\frac{1}{T}\frac{d\Gamma}{d\psi} + 2\Omega\Big)\right). \tag{A.7}$$

since $T = 2\pi r/\psi'$,
when $r \to \infty$,

$T \to \infty$ substituting in equation 3.46,

$$\chi_2 = \left(\frac{4(dw/d\psi)^2(\Omega + 2\pi/\infty)^2}{(\Gamma/\infty)(dT/d\psi)^2 + (dw/d\psi)^2} - 2\Big(\frac{2\pi}{\infty} + \Omega\Big)\Big(\frac{1}{\infty}\frac{d\Gamma}{d\psi} + 2\Omega\Big)\right), \tag{A.8}$$

$$\chi_2 = \left(\frac{4(dw/d\psi)^2(\Omega + 0)^2}{0 + (dw/d\psi)^2} - 2\Big(0 + \Omega\Big)\Big(0 + 2\Omega\Big)\right), \tag{A.9}$$

$$\chi_2 = 4\Omega^2 - 4\Omega^2 = 0, \tag{A.10}$$

since $\Gamma = 2\pi r\psi'$, when $r \to 0$, $\Gamma \to 0$

$$\chi_2 = \left(\frac{4(dw/d\psi)^2(\Omega + 2\pi/T)^2}{0 + (dw/d\psi)^2} - 2\Big(\frac{2\pi}{T} + \Omega\Big)(0 + 2\Omega)\right). \tag{A.11}$$

$$\chi_2 = \left(4(\Omega + 2\pi/T)^2 - 2\Big(\frac{2\pi}{T} + \Omega\Big)2\Omega\right). \tag{A.12}$$

$$\chi_2 = 4(\Omega + 2\pi/T)(\Omega + 2\pi/T - \Omega). \tag{A.13}$$

$$\chi_2 = 4(\Omega + 2\pi/T)(2\pi/T), \tag{A.14}$$

Again $T = 2\pi r/\psi'$,

$$\chi_2 = 4(\Omega + \frac{2\pi}{2\pi r/\psi'})(\frac{2\pi}{2\pi r/\psi'}). \tag{A.15}$$

$$\chi_2 = 4(\Omega + \frac{\psi'}{r})(\frac{\psi'}{r}), \tag{A.16}$$

$\psi' = (\Omega + \Omega')r$

$$\chi_2 = 4(\Omega + \frac{(\Omega + \Omega')r}{r})(\frac{(\Omega + \Omega')r}{r}), \tag{A.17}$$

$$\chi_2 = 4(2\Omega + \Omega')(\Omega + \Omega'). \tag{A.18}$$

A.III Evaluation of instability criterion χ_2

The azimuthal velocity(v_θ) at any radial point(r) close to the radial point r_0 can be written as

$$v_\theta = \gamma_0(r - r_0), \tag{A.19}$$

where γ_0 is the azimuthal velocity gradient at the radial point r_0. Then the stream function ψ can be written as

$$\varphi = \frac{1}{2}\gamma_0(r - r_0)^2. \tag{A.20}$$

$$T = \frac{2\pi r}{v_\theta}. \tag{A.21}$$

$$T = \frac{2\pi r}{\gamma_0(r - r_0)}. \tag{A.22}$$

$$\Gamma = 2\pi r v_\theta. \tag{A.23}$$

$$\Gamma = 2\pi r\gamma_0(r - r_0). \tag{A.24}$$

$$\frac{dw}{d\varphi} = \frac{dw/dr}{d\varphi/dr} = \frac{\kappa}{\gamma_0(r - r_0)}. \tag{A.25}$$

$$\frac{dT}{d\varphi} = \frac{dT/dr}{d\varphi/dr}. \tag{A.26}$$

$$\frac{dT}{dr} = \frac{2\pi}{\gamma_0}\frac{1}{(r - r_0)^2}\{(r - r_0) - r\} = -\frac{2\pi r_0}{\gamma_0(r - r_0)^2}. \tag{A.27}$$

$$\frac{dT}{d\varphi} = -\frac{2\pi r_0}{\gamma_0(r - r_0)^2\gamma_0(r - r_0)}. \tag{A.28}$$

$$\frac{dT}{d\varphi} = -\frac{2\pi r_0}{\gamma_0^2(r-r_0)^3}. \tag{A.29}$$

$$\frac{d\Gamma}{d\varphi} = \frac{d\Gamma/dr}{d\varphi/dr} = \frac{2\pi\gamma_0(r+r-r_0)}{\gamma_0(r-r_0)} = \frac{2\pi(2r-r_0)}{r-r_0}. \tag{A.30}$$

$$\chi_2 = \frac{4\frac{\kappa^2}{\gamma_0^2(r-r_0)^2}\{\Omega + \frac{2\pi}{\frac{2\pi r}{\gamma_0(r-r_0)}}\}^2}{\frac{2\pi\gamma_0 r(r-r_0)}{(\frac{2\pi r}{\gamma_0(r-r_0)})^3}(-\frac{2\pi r_0}{\gamma_0^2(r-r_0)^3})^2 + (\frac{\kappa}{\gamma_0(r-r_0)})^2} - 2(\frac{2\pi}{\frac{2\pi r}{\gamma_0(r-r_0)}} + \Omega)(\frac{1}{\frac{2\pi r}{\gamma_0(r-r_0)}}\frac{2\pi(2r-r_0)}{r-r_0} + 2\Omega). \tag{A.31}$$

$$\chi_2 = \frac{4\frac{\kappa^2}{\gamma_0^2(r-r_0)^2}\{\Omega + \frac{2\pi}{\frac{2\pi r}{\gamma_0(r-r_0)}}\}^2}{\frac{r(r-r_0)}{(\frac{r}{(r-r_0)})^3}(\frac{r_0}{(r-r_0)^3})^2 + (\frac{\kappa}{\gamma_0(r-r_0)})^2} - 2(\frac{2\pi}{\frac{2\pi r}{\gamma_0(r-r_0)}} + \Omega)(\frac{1}{\frac{2\pi r}{\gamma_0(r-r_0)}}\frac{2\pi(2r-r_0)}{r-r_0} + 2\Omega). \tag{A.32}$$

$$\chi_2 = \frac{4\frac{\kappa^2}{\gamma_0^2(r-r_0)^2}\{\Omega + \frac{2\pi}{\frac{2\pi r}{\gamma_0(r-r_0)}}\}^2}{\frac{1}{r^2}\frac{r_0^2}{(r-r_0)^2} + \frac{\kappa^2}{\gamma_0^2(r-r_0)^2}} - 2(\frac{2\pi}{\frac{2\pi r}{\gamma_0(r-r_0)}} + \Omega)(\frac{1}{\frac{2\pi r}{\gamma_0(r-r_0)}}\frac{2\pi(2r-r_0)}{r-r_0} + 2\Omega). \tag{A.33}$$

$$\chi_2 = \frac{4\frac{\kappa^2}{\gamma_0^2}\{\Omega + \frac{\gamma_0(r-r_0)}{r}\}^2}{\frac{1}{r^2}\frac{r_0^2}{} + \frac{\kappa^2}{\gamma_0^2}} - 2(\frac{2\pi}{\frac{2\pi r}{\gamma_0(r-r_0)}} + \Omega)(\frac{1}{\frac{2\pi r}{\gamma_0(r-r_0)}}\frac{2\pi(2r-r_0)}{r-r_0} + 2\Omega). \tag{A.34}$$

$$\chi_2 = \frac{4\kappa^2\{\Omega r + \gamma_0(r-r_0)\}^2}{r_0^2\gamma_0^2 + \kappa^2 r^2} - 2(\frac{\gamma_0(r-r_0) + \Omega r}{r})(\frac{\gamma_0(2r-r_0) + 2\Omega r}{r}). \tag{A.35}$$

$$\chi_2 = \frac{4\kappa^2\{\Omega r\}^2}{r_0^2\gamma_0^2 + \kappa^2 r^2} - 2(\Omega)(\frac{\gamma_0(2r-r_0) + 2\Omega r}{r}). \tag{A.36}$$

$$\chi_2 = \frac{4\kappa^2\Omega^2}{\gamma_0^2 + \kappa^2} - 2\Omega(\gamma_0 + 2\Omega). \tag{A.37}$$

Bibliography

Adrian, R.J. & Yao, C.S. 1984 Development of pulsed laser velocimetry (PLV) for measurement of fluid flow. In *8th biennial symposium on turbulence* (ed. G. Patterson & J. Zakin), pp. 170–186. Rolla, Missouri.

Adrian, R. J. 1991 Particle-imaging techniques for experimental fluid mechanics. *Annual Review of Fluid Mechanics* **23**, 261–304.

Adrian, R. J. 2005 Twenty years of particle image velocimetry. *Experiments in Fluids* **39**, 159–169.

Afanasyev, Y. & Peltier, W. 1998 Three-dimensional instability of swirling flow in rotating fluid: Laboratory experiments and related theoretical predictions. *Physics of Fluids* **10**, 3194.

Afanasyev, Y.D., Rhines, P.B. & Lindahl, E.G. 2009 Velocity and potential vorticity fields measured by altimetric imaging velocimetry in the rotating fluid. *Experiments in Fluids* **47**, 913–926.

Baines, W.D. & Chu, V.H 1996 *Environmental Hydraulics*, , vol. 19. Dordrecht: Springer.

Ball, C.G., Fellouah, H. & Pollard, A. 2012 The flow field in turbulent round free jets. *Progress in Aerospace Sciences* **50**, 1–26.

Barcilon, A. 1967b A theoretical and experimental model for a dust devil. *Journal of Atmospheric Science* **24**, 453–466.

Bayly, B. J. 1988 Three dimensional centrifugal type instabilities in inviscid two dimensional flows. *Physics of Fluids* **31**, 56–64.

Berkooz, G., Holmes, P. & Lumley, J. L. 1993 The proper orthogonal decomposition in the analysis of turbulent flows. *Annual Review of Fluid Mechanics* **25** (1), 539–575.

Bush, John W. M. & Woods, Andrew W. 1998 Experiments on buoyant plumes in a rotating channel. *Geophysical & Astrophysical Fluid Dynamics* **89** (1-2), 1–22.

Cambon, C. 1994 Turbulent flows undergoing distortion and rotation. A report on EUROMECH 288. *Fluid Dynamics Research* **13**, 231–266.

Carazzo, G., Kaminski, E. & Tait, S. 2006 The route to self-similarity in turbulent jets and plumes. *Journal of Fluid Mechanics* **547**, 137–148.

Chia, F., Griffiths, R. W. & Linden, P. F. 1982 Laboratory experiments on fronts. *Geophysical & Astrophysical Fluid Dynamics* **19** (3-4), 189–206.

Cowen, N. L. & Monismith, S. G. 1997 A hybrid digital particle tracking velocimetry technique. *Journal of Experimental Fluids* **22**, 199–211.

Cushman-Roisin, B. 1994 *Introduction to Geophysical Fluid Dynamics*. Englewood Cliffs, New Jersey, USA: Prentice Hall Inc.

Deremble, B. 2016 Convective plumes in rotating systems. *Journal of Fluid Mechanics* **799**, 27–55.

Elrick, J. R. 1979 Interaction between a discrete downdraft and a rotating environment. *Journal of the Atmospheric Sciences* **36** (2), 306–312.

Elsinga, G. E., Scarano, F., Wieneke, B. & van Oudheusden, B. W. 2006 Tomographic particle image velocimetry. *Experiments in Fluids* **41**, 933–947.

Etling, D. & Fernando, H. J. S. 1993 On the influence of background rotation on turbulent jets. *NATO Advanced Research Workshop on Recent Research Advances in the Fluid Mechanics of Turbulent Jets and Plumes* .

Ezzamel, A., Salizzoni, P. & Hunt, G. R. 2015 Dynamical variability of axisymmetric buoyant plumes. *Journal of Fluid Mechanics* **765**, 576–611.

Fernando, H. J. S., Chen, R. R. & Ayotte, B. A. 1998 Development of a point plume in the presence of background rotation. *Physics of fluids* **10**, 2369–2383.

Forstall, W. & Gaylord, E. W. 1955 Momentum and mass transfer in a submerged water jet. *Journal of Applied Mechanics* **22**, 161–164.

Frank, D., Landel, J. R., Dalziel, S. B. & Linden, P. F. 2017 Precession of a single-phase plume in a rotating environment. *Geophysical Research Letters* **44**.

Gallaire, F. & Chomaz, J.-M. 2003a Instability mechanisms in swirling flows. *Physics of Fluids* **15** (9), 2622–2639.

Gaydon, M., Raffel, M., Willert, C., Rosengarten, M. & Kompenhans, J. 1997 Hybrid stereoscopic particle image velocimetry. *Journal of Experimental Fluids* **23**, 331–334.

George, W. K., Alpert, R. L. & Tamanini, F. 1977 Turbulence measurements in an axisymmetric buoyant plume. *International Journal of Heat Mass Transfer* **20**, 1145–1154.

Godeferd, F. S., Cambon, C. & Leblanc, S. 2001 Zonal approach to centrifugal, elliptic and hyperbolic instabilities in stuart vortices with external rotation. *Journal of Fluid Mechanics* **449**, 137.

Graftieaux, L., Michard, M. & Grosjean, N. 2001 Combining piv, pod and vortex identification algorithms for the study of unsteady turbulent swirling jets. *Measurement Science and Technology* **12** (3), 1422–1429.

Greenspan, H. P. 1968 *The Theory of Rotating Fluids*. Cambridge, UK: Cambridge University.

Hassa, C., Paul, P. H. & Hanson, R. K. 1987 Laser-induced fluorescence modulation techniques for velocity measurements in gas flows. *Journal of Experimental Fluids* **5**, 240–246.

Helfrich, Karl R. & Battisti, Thomas M. 1991 Experiments on baroclinic vortex shedding from hydrothermal plumes. *Journal of Geophysical Research: Oceans* **96** (C7), 12511–12518.

Hesselink, L. 1988 Digital image processing in flow visualization. *Annual Review of Fluid Mechanics* **20**, 421–485.

Hopfinger, E.J. & Linden, P.F. 1990 The effect of background rotation on fluid motions: a report on euromech 245. *Journal of Fluid Mechanics* **211**, 417–435.

Huang, N. E., Long, S. R. & Shen, Z. 1996 The mechanism for frequency downshift in nonlinear wave evolution. *Advances in Applied Mechanics* **32**, 59111.

Huang, N. E., Shen, Z., Long, S. R., Wu, M. C., Shih, H. H., Zheng, Q., Yen, N.-C., Tung, C. C. & Liu, H. H. 1998 The empirical mode decomposition and the hilbert spectrum for nonlinear and non-stationary time series analysis. In *Proceedings of Royal Society of London : A*, , vol. 454, p. 903995.

Huang, N. E. & Wu, Z. 2008 A review on hilbert-huang transform: Method and its applications to geophysical studies. *Reviews of Geophysics* **46** (2).

Hunt, G. R. & Kaye, N. G. 2001 Virtual origin correction for lazy turbulent plumes. *Journal of Fluid Mechanics* **435**, 377–396.

Hussein, J., Capp, S. P. & George, W. K. 1994 Velocity measurements in a high-reynolds-number, momentum-conserving, axisymmetric, turbulent jet. *Journal of Fluid Mechanics* **258**, 31–75.

John, W. M. Bush & Andrew, W. Woods 1998 Experiments on buoyant plumes in a rotating channel. *Geophysical & Astrophysical Fluid Dynamics* **89** (1-2), 1–22.

Joliffe, I. T. 2002 *Principal Component Analysis (2nd edition)*. Springer.

Kam, K. M. 2014 Stationary and non stationary time series prediction using state space model and pattern based approach. PhD thesis, The university of Texas at Arlington.

Kaminsky, E., Tait, S. & Carazzo, G. 2005 Turbulent entrainment in jets with arbitrary buoyancy. *Journal of Fluid Mechanics* **526**, 361–376.

Karhunen, K. 1946 Zur spektral theorie stochastischer prozesse. *Ann. Acad. Sci. Fennicae Set* **AI** (34).

Kloosterzielt, R. C. & Heijst, G. J. F. Van 1991 An experimental study of unstable barotropic vortices in a rotating fluid. *Journal of Fluid Mechanics* **223**, 1–24.

Kosambi, D. D. 1943 Statistics in function space. *Journal of the Indian Mathematical Society* **7**, 76–88.

Lawrie, A. G. W., Duran, M., Scott, J. F., Godeferd, F., Floe, J. B., Cambon, C. & Daniaila, L. 2011 The axisymmetric jet in a rotating reference frame. *Journal of Physics :Conference Series* (318), 32–48.

Leblanc, S. & Cambon, C. 1998 Effects of the coriolis force on the stability of stuart vortices. *Journal of Fluid Mechanics* **356**, 353–379.

Lee, J. H. & Chu, V. H. 2012 *Turbulent Jets and Plumes: A Lagrangian Approach*. Springer US.

Leibovich, S. & Stewartson, K. 1983 A sufficient condition for the instability of columnar vortices. *Journal of Fluid Mechanics* **126**, 335–356.

Liang, H. & Maxworthy, T. 2005 An experimental investigation of swirling jets. *Journal of Fluid Mechanics* **525**, 115–159.

List, E. J. 1982 Turbulent jets and plumes. *Annual review of Fluid Mechanics* **14**, 189–212.

Lloyd, P. M., Stansby, P. K. & Ball, D. J. 1995 Unsteady surface-velocity field measurement using particle tracking velocimetry. *Journal of Hydraulic Research* **33** (4), 519533.

Loeve, M. 1945 Functions aleatoire de second ordre. p. 220. C. R. Academy of Science, Paris.

Lumley, J. L. 1967 The structure of inhomogeneous turbulence. In *Atmospheric Turbulence and Wave Propagation* (ed. A. M. Yaglom & V. I. Tatarski), pp. 166–78. Moscow: Nauka.

Mathur, M., Ortiz, S., Dubos, T. & Chomaz, J. M. 2014 Effects of an axial flow on the centrifugal, elliptic and hyperbolic instabilities in stuart vortices. *Journal of Fluid Mechanics* **758**, 565–585.

Mi, J., Xu, M. & Zhou, T. 2013 Reynolds number influence on statistical behaviors of turbulence in a circular free jet. *Physics of Fluids* **25**, 075101.

Mininni, P.D., Alexakis, A. & Pouquet, A. 2009 Scale interactions and scaling laws in rotating flows at moderate Rossby numbers and large Reynolds numbers. *Physics of Fluids* **21**, 015108.

Morton, B. R., Taylor, G. I. & Turner, J. S. 1956 Turbulent gravitational convection from maintained and instantaneous sources. *Proceedings of the Royal Society of London A* **A** (234), 1–23.

Muste, M., Fuijta, I. & Kruger, A. 1998 Experimental comparison of two laser-based velocimeters for flows with alluvial sand. *Journal of Experimental Fluids* **24**, 273–284.

Nagarathinam, D., Sameen, A. & Mathur, M. 2015 Centrifugal instability in non-axisymmetric vortices. *Journal of Fluid Mechanics* **769**, 26–45.

Niino, H. 1978 Turbulent jet in a rotating fluid. *Journal of the Meteorological Society of Japan* **56**, 527–547.

Niino, H. 1980 Evolutions of a laminar jet in a homogeneous rotating fluid: a linear theory. *Journal of the Meteorological Society of Japan* **58**, 33–51.

Nishino, K., Kasagi, N. & Hirata, M. 1989 Three-dimensional particle tracking velocimetry based on automated digital image processing. *Journal of Fluids Engineering* **111**, 384–391.

Obukhov, A. M. 1954 Statistical description of continuous fields. *Tr. Geophys. Int. Akad. Nauk. SSSR* **24**, 3–42.

Panchapakesan, N. R. & Lumley, J. L. 1993 Turbulence measurements in axisymmetric jets of air and helium. part 1. air jet. *Journal of Fluid Mechanics* **246**, 197–223.

Papanicolaou, P. N., Ilias, G. P. & Christodoulou, G. C. 2008 On the entrainment coefficient in negatively buoyant jets. *Journal of Fluid Mechanics* **614**, 447–470.

Papanicolaou, P. N. & List, E. J. 1988 Investigations of round vertical turbulent buoyant jets. *Journal of Fluid Mechanics* **195**, 341–391.

Patte-Rouland, B., Lalizel, G., Moreau, J. & Rouland, E. 2001 Flow analysis of an annular jet by particle image velocimetry and proper orthogonal decomosition. *Meas. Sci. Tech.* **12** (9), 1404–1412.

Pedlosky, J. 1987 *Geophysical Fluid Dynamics*, 2nd edn. New York, USA: Spinger-Verlag.

Potylitsin, P. G. & Peltier, W. R. 1999 Three-dimensional destabilization of stuart vortices: the influence of rotation and ellipticity. *Journal of Fluid Mechanics* **387**, 205–226.

Pougachev, V. S. 1953 General theory of the correlations of random functions. *Izv. Akud. Nauk. SSSR. Set. Mat.* **17** (5), 401–420.

Prasad, A. K. & Adrian, R. J. 1993 Stereoscopic particle image velocimetry applied to liquid flows. *Journal of Experimental Fluids* **15**, 49–60.

Priestley, C. H. B. & Ball, F. K. 1955 Continuous convection from an isolated source of heat. *Quarterly Journal of the Royal Meteorological Society* **81** (348), 144–157.

Proudman, J. 1916 On the motion of solids in a liquid possessing vorticity. *Proceedings of the Royal Society of London A* **92** (642), 408–424.

Quénot, G., Rambert, A., Lusseyran, F. & Gougat, P. 2001 Simple and accurate piv camera calibration using a single target image and camera focal length. In *4 th International symposium on particle image velocimetry*. Göttingen, Germany.

Raffel, M., Willert, C. E., Wereley, S. T. & Kompenhans, Jrgen 2007 *Particle Image Velocimetry : A Practical Guide*, 2nd edn. Springer.

Rayleigh, L. 1917 On the dynamics of revolving fluids. *Proceedings of the Royal Society of London A* **93**, 148–154.

Rosensweig, R. E., Hottel, H. C. & Williams, G. D. 1961 Smoke-scattered light measurement of turbulent concentration fluctuations. *Chemical Engineering Science* **15**, 111129.

Shabbir, A. & George, W. K. 1994 Experiments on a round turbulent buoyant plume. *Journal of Fluid Mechanics* **275**, 1–32.

Sirovich, L. 1987 Turbulence and the dynamics of coherent structures. *Quarterly of Applied Mathematics* **45** (3), 561–590.

Sutton, M. M., Wolters, W.J., Peters, W.H., Ranson, W.H. & Macneill, S. R. 1983 Determination of displacements using an improved digital correlation method. *Optical Engineering* **1**, 113139.

Taylor, G. I. 1917 Motion of solids in fluids when the flow is not irrotational. *Proceedings of the Royal Society of London A* **93** (648), 99113.

Thomas, P. J. 2014 Personal Communication.

Tomàs, A. F., Poje, A. C., Özgökmen, T. M. & Devar, W. K. 2016 Effects of rotation on turbulent buoyant plumes in stratified environments. *J. Geophys. Res.* **121**, 5397–5417.

Uddin, M. & Pollard, A. 2007 Self-similarity of coflowing jets the virtual origin. *Physics of Fluids* **19**, 068103.

Vanierschot, M., Dyck, K. Van, Sas, P. & den Bulck, E. Van 2014 Symmetry breaking and vortex precession in low-swirling annular jets. *Physics of Fluids* **26** (10), 105110.

Vanyo, J. P. 1993 *Rotating Fluids in Engineering and Science*. Mineola, New York, USA: Dover Publications Inc.

Wang, H. & Law, A. W. K. 2002 Second-order integral model for a round turbulent buoyant jet and adrian wing-keung law. *Journal of Fluid Mechanics* **459**, 397–428.

Westerweel, J., Dabiri, D. & Gharib, M. 1997 The effect of a discrete window offset on the accuracy of cross- correlation analysis of digital piv recordings. *Experiments in Fluids* **23**, 20–28.

Wilkins, E. M., Sasaki, Y., Friday, E. M., McCarthy, J. & McIntyre, J. R. 1969 Properties of simulated thermals in a rotating fluid. *Journal Geophysics Research* **74**, 4472–4486.

Wilkins, E. M., Sasaki, Y. & Schauss, R.H. 1971a Interaction between the velocity fields of successive thermals. *Monthly Weather Review* **99**, 215–226.

Wilkins, E. M., Sasaki, Y. & Schauss, R.H. 1971b Vortex formation by successive thermals: a numerical simulation. *Monthly Weather Review* **99**, 577–592.

Willert, C. E. & Gharib, M. 1991 Digital particle image velocimetry. *Experiments in Fluids* **10**, 181–193.

Wygnanski, I. & Fiedler, H. 1969 Some measurements in the self preserving jet. *Journal of Fluid Mechanics* **38**, 577–612.

Zel'dovich, Y. B. 1937 The asymptotic laws of freely-ascending convective flows. *Journal of Experimental and Theoretical Physics* **7**, 1463–1465.